Localization Precise in Urban Area

Yu Wang

THÈSE

En vue de l'obtention du

DOCTORAT DE L'UNIVERSITÉ DE TOULOUSE

Délivré par :

Institut National Polytechnique de Toulouse (Toulouse INP)

Discipline ou spécialité :

Signal, Image, Acoustique et Optimisation

Présentée et soutenue par :

Mme YU WANG

le vendredi 10 mai 2019

Titre :

Localization Precise in Urban Area

Ecole doctorale :

Mathématiques, Informatique, Télécommunications de Toulouse (MITT)

Unité de recherche :

Laboratoire de Télécommunications (TELECOM-ENAC)

Directeur(s) de Thèse :

M. CHRISTOPHE MACABIAU

Rapporteurs :

M. MANUEL HERNANDEZ PAJARES, UNIV POLITECNICA DE CATALUNYA BARCELONA
Mme SANDRA VERHAGEN, UNIVERSITE DE DELFT

Membre(s) du jury :

M. MANUEL HERNANDEZ PAJARES, UNIV POLITECNICA DE CATALUNYA BARCELONA, Président
M. CARL MILNER, ECOLE NATIONALE DE L'AVIATION CIVILE, Membre
M. CHRISTOPHE MACABIAU, ECOLE NATIONALE DE L'AVIATION CIVILE, Membre

Abstract

Nowadays, stand-alone Global Navigation Satellite System (GNSS) positioning accuracy is not sufficient for a growing number of land users. Sub-meter or even centimeter accuracy is becoming more and more crucial in many applications. Especially for navigating rovers in the urban environment, final positioning accuracy can be worse as the dramatically lack and contaminations of GNSS measurements. To achieve a more accurate positioning, the GNSS carrier phase measurements appear mandatory. These measurements have a tracking error more precise by a factor of a hundred than the usual code pseudorange measurements. However, they are also less robust and include a so-called integer ambiguity that prevents them to be used directly for positioning.

While carrier phase measurements are widely used in applications located in open environments, this thesis focuses on trying to use them in a much more challenging urban environment. To do so, Real-Time-Kinematic (RTK) methodology is used, which is taking advantage on the spatially correlated property of most code and carrier phase measurements errors. Besides, the thesis also tries to take advantage of a dual GNSS constellation, GPS and GLONASS, to strengthen the position solution and the reliable use of carrier phase measurements. Finally, to make up the disadvantages of GNSS in urban areas, a low-cost MEMS is also integrated to the final solution.

Regarding the use of carrier phase measurements, a modified version of Partial Integer Ambiguity Resolution (Partial-IAR) is proposed to convert as reliably as possible carrier phase measurements into absolute pseudoranges. Moreover, carrier phase Cycle Slip (CS) being quite frequent in urban areas, thus creating discontinuities of the measured carrier phases, a new detection and repair mechanism of CSs is proposed to continuously benefit from the high precision of carrier phases.

Finally, tests based on real data collected around Toulouse are used to test the performance of the whole methodology.

Résumé

Récemment, la précision qu'on peut obtenir avec le GNSS-autonome positionnement est insatisfaisant pour de plus en plus d'utilisateurs au terrain. Une précision au-dessous de mètre ou encore de niveau centimètre est devenue plus cruciale pour pleine d'applications. Surtout pour des véhicules dans le milieu urbain, la précision finale est considérablement pire comme les manques et les contaminations des GNSS signaux sont présentes. Afin d'avoir un positionnement plus précis, les mesures carrier phases sont dispensables. Les erreurs associés à ces mesures sont plus précises de factor centaine que les mesures pseudoranges. Cependant, un paramètre de nature entière, appelée ambiguïté, empêche les mesures phases de comporter comme les pseudoranges 'précises'.

Pendant que les mesures carrier phases sont largement utilisées par les applications localisées dans un environnement ouvert, cette thèse s'intéresse sur les exploitations dans un environnement urbain. Pour cet objectif, la méthodologie RTK est appliquée, qui est principalement basée sur les caractéristiques que les erreurs sur les mesures pseudoranges et phases sont corrélées spatialement. De plus, cette thèse profite de la double GNSS constellation, GPS et GLONASS, pour renforcer la solution de position et l'utilisation fiable des mesures carrier phases. Enfin, un low-cost MEMS est aussi intégré pour compenser des désavantages de GNSS dans un milieu urbain.

A propos des mesures phases, une version modifiée de Partial-IAR (Partial Ambiguity Resolution) est proposée afin de faire comporter de la façon la plus fiable possible les mesures phases comme les pseudoranges. Par ailleurs, les glissements de cycle sont plus fréquents dans un milieu urbain, qui introduisent des discontinuités des mesures phases. Un nouveau mécanisme pour détecter et corriger les glissements de cycle est du coup mise en place, pour bénéficier de la haute précision des mesures phases.

Des tests basés sur les données collectées autour de Toulouse sont faits pour montrer la performance.

Acknowledgements

First of all, I would like to thank my supervisor, Prof. Olivier Julien, for his patient guidance and kindly support during the whole PhD project. He was the first ever tutor who led me into the academic research area and showed me the wonderfulness of rigorous and logic thinking.

Same thanks are expressed to Prof. Christophe Macabiau, who takes over the whole responsibility without hesitation at the end of my PhD project. Without his encouragement and guidance over the main direction, I would never accomplish my study.

Thanks to my colleagues and friends inside the ENAC Telecom team. Thank you, Paul Thevenon, Amani Ben Afia and Jérémy Vezinet, for all your technical supports and detailed responses to my questions. Thank you, Yiping Jiang, for your being supportive and listener to my story. Thank you, Hang Zhou and Xiao Hu, for your generous help at those annoying matters. Thank you all, Anne-Christine Escher, Anaïs Martineau, Antoine Blais, Axel Javier Garcia Pena, Carl Milner, Alexandre Chabory, Rémi Douvenot, Christophe Morlass, Hélène Galiègue, Capucine Amielh, Quentin Tessier, Sara Bouterfas, Ikhlas Selmi, Eugene Bang, Johan Duplouy and others who have left for another adventure, thank you for making the time spent memorable and happy.

Last but not least, grateful thanks to my husband, without whose priceless love and continuous support I would never come to the end. Nothing would matter without him.

Dedication

To my love, Zihan!

Table of Contents

List of Figures

List of Tables

List of Abbreviations

ADC	Analog-to-Digital Converter
AFSCN	Air Force Satellite Control Network
AGC	Automatic Gain Controller
ASDF	Air and Space Defense Forces
CC	Central clocks
CDMA	Code division multiple access
CS	Cycle slip
CS-DR	CS detection and repair
DD	Double-differencing
DGNSS	Differential-GNSS
DLL	Delay Lock Loop
DOP	Dilution of precision
DSSS	Direct sequence spread spectrum
ECEF	Earth-Centered Earth-Fixed
ECI	Earth-Centered Inertial
EMLP	Early-power-minus-Late-power
ENU	East-North-Up
FDMA	Frequency division multiple access
FT-RT	Fixed Threshold Ratio Test
GLONASS	Global'naya Navigatsionnaya Sputnikovaya Sistema
GLOT	GLONASS time
GNSS	Global Navigation Satellite System
GPS	Global Positioning System
GPST	GPS time
IAE	Integer Aperture Estimator
IAR	Integer Ambiguity Resolution
ICBs	Inter-channel biases
IERS	International Earth Rotation and Reference Systems Service
IGS	International GNSS Service
ILS	Integer least-squares
INS	Inertial Navigation System
IRNSS	Indian Regional Navigation System
ITU	International Telecommunication Union
LAMBDA	Least-squares AMBiguity Decorrelation adjustment
LNA	Low Noise Amplifier
LOS	Line-Of-Sight
LSE	Leas-Squares estimation
MEMS	Micro-Electro-Mechanical System
NCO	Numerically-Controlled Oscillator
NGA	National Geospatial-Intelligence Agency
NHC	Non-Holonomic Constraint
NLOS	Non-line-of-sight
OCXO	Ovenized crystal oscillator
Partial-IAR	Partial-Integer Ambiguity Resolution
PLL	Phase Lock Loop
PPP	Precise Point Positioning
PRN	Pseudo random noise
PZ	Parametry Zemli

QZSS	Quasi-Zenith Satellite System
RF-FE	Radio-Frequency Front End
RNSS	Radio Navigation Satellite Services
RT	Ratio Test
RTK	Real Time Kinematic
SD	Single-differencing
SLR	Satellite laser ranging
SU	Soviet Union
TAI	International Atomic Time
TC	Tight Coupling
TCXO	Temperature compensated crystal oscillator
TDMA	Time division multiple access
TEC	Total electron content
TOA	Time of arrival
TT&C	Telemetry, Tracking and Control
UERE	User equivalent range error
USNO	United States Naval Observatory
UTC	Coordinated Universal Time
VC-matrix	Variance-covariance matrix
WGS	World Geodetic System

1 Introduction

1.1 Background and Motivation

Navigation, the process of determining the position, velocity and sometimes the attitude of an object, has always been a technology that people have strived to conquer [1], [2]. Since the advent of Global Navigation Satellite Systems (GNSS), especially with the most important utility Global Positioning System (GPS), precise navigation went from professional skilled navigators to the mass market public [3]. Over the past decade, the universal GNSS has been dramatically utilized in various domains, such as aviation, marine, precise agriculture, geodesy and surveying, automotive, etc. However, the accuracy or integrity that a low-cost GNSS receiver can provide in a constrained urban or indoor environment is far from satisfactory for applications where decimeter or centimeter accuracy and error bounds are mostly envisioned.

The higher precision of raw carrier phase measurements compared to pseudorange measurements have made them essential for high accuracy techniques [4], [5]. Nevertheless, carrier phase integer ambiguities and losses of lock called cycle slips creating sudden changes of these ambiguities increase the difficulty to consider these ambiguities.

Confronting the mass market customers until 2017, a market of single-frequency (single- or multi-constellation) equipment is persistent although precise positioning technologies have been developed for high-end multiple-frequency receivers [6]. Besides, the quality of raw measurements collected with low-cost systems, typically a low-cost receiver and a patch antenna, is not sufficient to achieve a reliable integer ambiguity resolution, without mentioning the quality degradations in the dynamic conditions [7].

Many precise positioning techniques have been devised to improve the positioning accuracy, such as the Real-Time Kinematic (RTK) and the Precise Point Positioning (PPP) techniques [6], [8], [9]. PPP takes advantages of precise corrections of ephemeris and clock errors affecting raw measurements provided by IGS or other organizations. Nevertheless, a long convergence period is required as single-frequency ambiguities are estimated float while residual errors are lumped into integer ambiguities, such that these are not integer anymore. RTK eliminates most measurements errors, which are spatially correlated, by differencing measurements with a reference station. Typically, a centimeter-level accuracy is achievable with RTK with only a few seconds of convergence time, in a short-baseline configuration under an open-sky condition [7].

What's more, to enhance the performance of ambiguity resolution, i.e. convergence time and reliability, a lot of scientific efforts have been put into the study of the integer ambiguity resolution techniques. The whole integer ambiguity resolution process is composed of two basic parts: estimation and validation [10]–[12]. In terms of maximizing the ambiguity success rate, the estimation technique Integer Least-Squares (ILS) is considered the most optimal one compared to other popular techniques, e.g. integer rounding, integer bootstrapping [13]–[16]. For instance, the Least-squares AMBiguity Decorrelation adjustment (LAMBDA), as a specific implementation algorithm of ILS, has been widely approved and applied facing IAR (Integer Ambiguity Resolution) problems. Ratio test as a popular validation technique is widely implemented for its good performance in practical applications. However, there lacks a theoretical knowledge of performance indicator, e.g. the probability of failure P_f. Some fixed failure validation tests are proposed whilst practical implementations become more complex and computationally burdened.

The application of interest in this dissertation is achieving precise positioning for road users in practical driving environment. Facing the challenges of a benign environment, for example the frequent signal blockages, multipath/NLOS signals, poor availability of GPS measurements, the precise positioning for low-cost single receiver is always an issue. The full operational capacity of GLONASS (Global'naya Navigatsionnaya Sputni kovaya Sistema) reveals the advantages of multi-constellation positioning [17].

The performance of satellite-based positioning schemes is highly dependent on user-satellite geometry even in a difficult environment, like semi-urban or urban areas. Along with the consideration of another GLOT receivers, i.e. GLONASS code and carrier phase inter-channel biases (ICB) [18]–[22]. Aside from the poor signal availability, another consequence that GNSS carrier phase observations may suffer from is frequent cycle slips (CS). A cycle slip is referring to the loss of continuous lock of satellite signal carrier phase tracking and an integer number should be added to update the integer carrier phase ambiguities.

Unlike GNSS, vulnerable to various outliers due to signal propagation especially in a constrained environment, the Inertial Navigation System (INS) is completely autonomous from signal reception. An INS provides the position, velocity and attitude information of the rover with the help of a set of inertial sensors (also known as an inertial measurement unit (IMU)), and a navigation processor [1], [23]. Despite the immunity to outliers, the stand-alone position quality of IMUs degrades quickly due to the sensor inaccuracies. Apparently, high-grade IMUs bear slower degradation but at an extreme high cost that mass market can not afford. At a low cost, the miniaturization, low power consumption and mass-production capacity have made the micro-electro-mechanical system (MEMS) sensors more and more attractive for automotive applications [2], [24]. Given the complimentary characteristics of INS and GNSS, but the overall performance in an urban environment remains an unknown.

In this thesis, the performance of applying precise positioning technique RTK in semi urban or urban areas, with raw GNSS measurements collected by a low-cost single-frequency multi-constellation receiver coupled with MEMS is investigated.

1.2 Objectives and Contributions of this Dissertation

The fundamental objective of this dissertation is to explore the navigation performance that a low-cost system, taking full advantages of low-cost GNSS receiver, low-cost INS, and precise positioning technology RTK, can achieve in the areas that are current GPS harsh in terms of signal reception. The process of achieving the global objective is divided into following sub-objectives:

- Code and Doppler measurement outliers are detected and excluded based on an Innovation test, which also keeps watch on carrier phase measurements subject to miss-detected cycle slips;
- Along with GPS DD (Double Differenced) ambiguities, included GLONASS DD ambiguities are conserving integer natures by isolating associative GLONASS inter-channel biases;
- A Cycle-Slip detection and repair (CS-DR) scheme detects and repairs cycle slips, which enables the continuous estimation of GNSS ambiguities;
- With a view to lower the fatal wrong fixing probability P_f regarding GNSS ambiguities, an Integer Ambiguity Resolution (IAR) scheme capable of controlling P_f and making use of the best subgroup of DD ambiguities is proposed;
- Further more, a low-cost MEMS is tightly-integrated to explore its benefits pertaining to the performance of the CS-DR scheme, the operation of IAR and finally the positioning performance;
- Testing of the proposed algorithm is based on real collected data during two campaigns in typical semi-urban/urban areas in Toulouse.

1.3 Dissertation Outline

This dissertation is composed of eight chapters and four appendices. The detailed organization is described as following.

Chapter 1 describes the background, objectives and contributions of this dissertation. Under the constraint of low cost, single-frequency multi-constellation RTK is integrated with MEMS to conquer at most the difficulties a road user may experience.

Chapter 2 provides an overview of GNSS principles including the system structure, the reception of GNSS signals and the production of GNSS raw measurements. The single point positioning with GPS code measurements is briefly illustrated at last.

In Chapter 3 the general precise positioning techniques are reviewed. The RTK methodology and Integer Ambiguity Resolution (IAR) schemes have been paid full attention to. However, evident challenges still exist in urban environments.

Chapter 4 reveals implemented precise positioning methodologies to improve GNSS positioning performance, including the pre-processing of GNSS measurements, the Innovation test for further outliers elimination, the CS-DR (Cycle slip detection and repair) scheme and the proposed modified partial integer ambiguity resolution (Partial-IAR) technique.

Chapter 5 presents the 2 data collections and the performance of the proposed RTK methodology. Different adjustments of the CS-DR scheme are tested to explore its best performance.

Chapter 6 starts with the overview of INS, and ends with the INS/GNSS tight coupling theory. To better represent the system, the applied MEMS unit is previously modelled and all possible motion constraints are implemented.

Chapter 7 explores the impacts of the integration with INS namely on CS-DR, IAR and the positioning performance.

Chapter 8 concludes the major results and makes a list of recommended directions that the research can proceed in the future.

In appendices are various information helpful for a complete understanding of this dissertation.

2 Overview of GNSS Principles

Global Navigation Satellite System (GNSS), is nowadays widely used in various applications such as civil aviation, agriculture, leisure activities, etc., thanks to its ability to provide users' position and time information anytime anywhere.

GPS (Global Positioning System), the US GNSS, is the most popular and widely used of such systems. It is also the only GNSS that provided continuous positioning service since its full operational capability declared in 1995. The Russian GNSS, GLONASS (Global'naya Navigatsionnaya Sputnikovaya Sistema), although originally declared operational in 1995 as GPS, went through a period of time in the years 2000s during which it was not fully operational. It became fully operational again in 2011 [6].

More recently, initiatives have led to the development of other GNSS, most notably in Europe with Galileo and in China with BeiDou. These two systems have already reached intermediate milestones in their program development and are planned to be fully operational in 2020.

Finally, other initiatives have led to the development of regional systems only meant at covering a specific geographical area with positioning and timing services. This is the case of IRNSS (Indian Regional Navigation System) in India, and QZSS (Quasi-Zenith Satellite System) in Japan [2].

In the frame of this manuscript, only GPS and GLONASS have been used since both BeiDou and Galileo were not yet operational and since most of the testing perform could not rely on a significant number of satellites from these systems. As a consequence, only GPS and GLONASS systems are described.

2.1 Structure of GNSS

A space system such as a GNSS is generally divided into three segments: space segment, control segment, and user segment. Each plays a key role in ensuring a reliable GNSS service. In this sub-section, the principles of positioning with GNSS will be firstly introduced, followed by the high-level description of the three segments of GNSS.

2.1.1 Principles of GNSS

GNSS is a system based on the continuous transmission of signals from a constellation of satellites to GNSS users typically located near the Earth surface. The system is thus a one-way system in the sense that GNSS users do not send any signal to the satellites. The localization of a GNSS user is basically a process of resolving a system based on the knowledge of the location of the visible satellites and the distance separating the user receiver antenna from these satellites. A (simplified) depiction of the GNSS positioning principle is showed in Figure 2-1.

The estimate of the range between the satellite location and the user is computed by the user receiver via the estimation of the time-of-flight of the GNSS signal in space. This time-of-flight (TOF), also referred as time-of-arrival (TOA), is typically obtained by differencing the time of emission and the arriving time of the received signal. Assuming that the signal travels at the speed of light, this time-of-flight can be translated in a distance. A precise measure of the TOA is thus very important as a bias of 1 millisecond can give rise to a range error of 300 km. More details on the GNSS signal are addressed in Section 2.3 and 2.4.

It is easy to understand that the computed range based on this principle will be biased by the mis-synchronization of the satellites' and user clock. This is why the measurements made using the above principle are referred to as pseudoranges. To compensate for the satellite mis-synchronization, the satellites transmit as part of their useful message their clock bias and drift with respect to a reference

time, known as GNSS time. All satellite clocks can thus be referenced to a unique clock. This means that all corrected pseudoranges are now only biased by the user clock, common to all measurements.

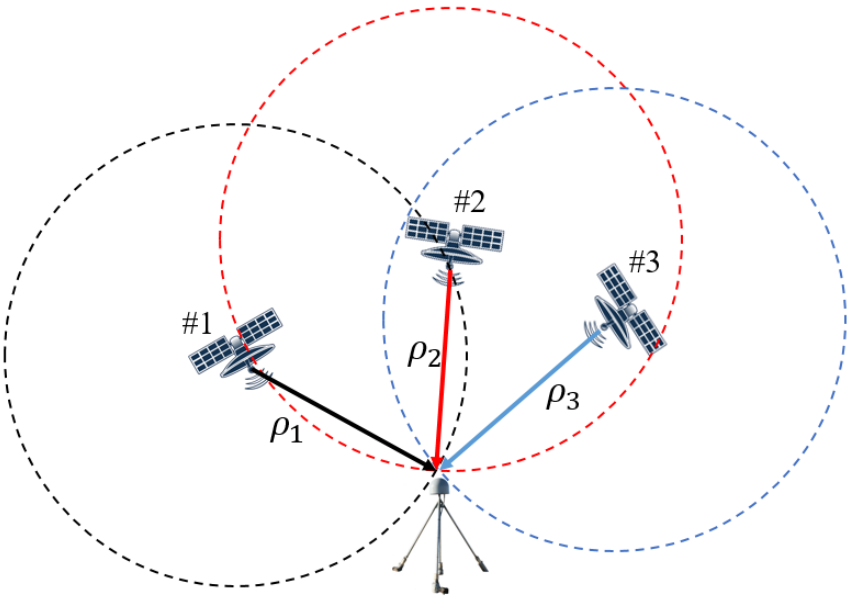

Figure 2-1. GNSS Positioning with Sphere Intersection [6]

As part of the satellite transmitted message is the precise satellite orbit, also referred to as ephemeris, that allows the user to access the satellite location at the time of transmission. Therefore, to obtain the position of the user receiver, the user receiver will have to solve a system composed of the collected pseudoranges and their mathematical model (that include 4 unknowns – the receiver 3-D location and the receiver clock offset with respect to the GNSS time). To solve for this system, there is thus a need to have at least 4 pseudoranges from 4 different satellites. The user position can then be calculated and is fully linked to the estimation of the receiver clock bias. The latter is the reason why GNSS is also a time-transfer system.

2.1.2 GPS and GLONASS Space Segments

The GNSS space segment is composed of the satellite constellation. This constellation is made to ensure a very high availability of the computed position and time at the user level. It is thus built so that at least 4 satellites are tracked anywhere on the Earth surface.

The space segment of the GPS consists in a minimum guaranteed constellation of 24 satellites distributed in 6 Earth-centered medium altitude earth orbital planes (altitude around 20,180 km above the Earth surface), with 55 degrees inclination relative to the equator, and 4 satellites within each plane. However, the current (updated to January 9, 2019 [25]) GPS constellation is well above this number with 31 operational satellites. The orbital period of each satellite is approximately 11 hours 58 minutes, meaning that their ground trace repeats every sidereal day. From 1978, the first launch of GPS satellite, until now, the payload technology has evolved (i.e. the modernization of GPS) resulting in different GPS satellite families referred to as Block: Block I, Block II/IIA, Block IIR/IIR-M, Block IIF, and Block III [6], [26]. In particular, satellites are now equipped with more stable atomic clocks, rubidium and/or cesium category, and have a longer design life-time. For more information on clock characteristics, refer to Section 2.2.2.3.

The 24 operational GLONASS satellites are evenly distributed over 3 orbital planes (altitude around 19,100 km above the Earth surface), 120 degrees apart. The orbital inclination of each plane is about 65 degrees, higher than that of GPS, which provides a better satellite visibility over the high latitude areas. The orbital period is about 11 hours 15 minutes 44 seconds. After the first generation GLONASS satellites launched in the 1980's, the developed generations GLONASS-M, GLONASS-M+, GLONASS-K1, GLONASS-K1+ and GLONASS-K2 were subsequently launched in following decades [6], [27].

2.1.3 GPS and GLONASS Control Segments

The control segment of a GNSS consists of a network of stations around the world which are responsible for monitoring, commanding and controlling the GNSS constellation. GNSS signals are collected at stations to ensure the quality of the signal transmitted by the satellites, and to generate accurate models of the satellite orbits and clock biases. This information is then uploaded to the satellites to be included in their useful message sent to the user, known as navigation message.

The GPS control segment is comprised of a master control station, which is located at Schriever Air Force Base (formerly Falcon AFB) in the State of Colorado, USA, and a global network of monitor stations and ground antennas, as illustrated in Figure 2-2 [2]. Among those monitor stations, some are operated by Air Force, others are operated by the National Geospatial-Intelligence Agency (NGA). Although not dedicated to the GPS constellation, Air Force Satellite Control Network (AFSCN) stations can be utilized if needed to conduct data links with GPS satellites.

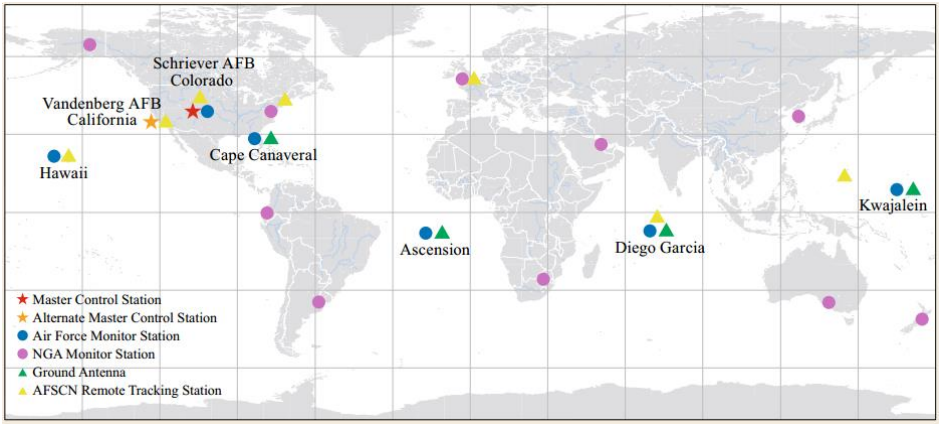

Figure 2-2. GPS Control segment [6]

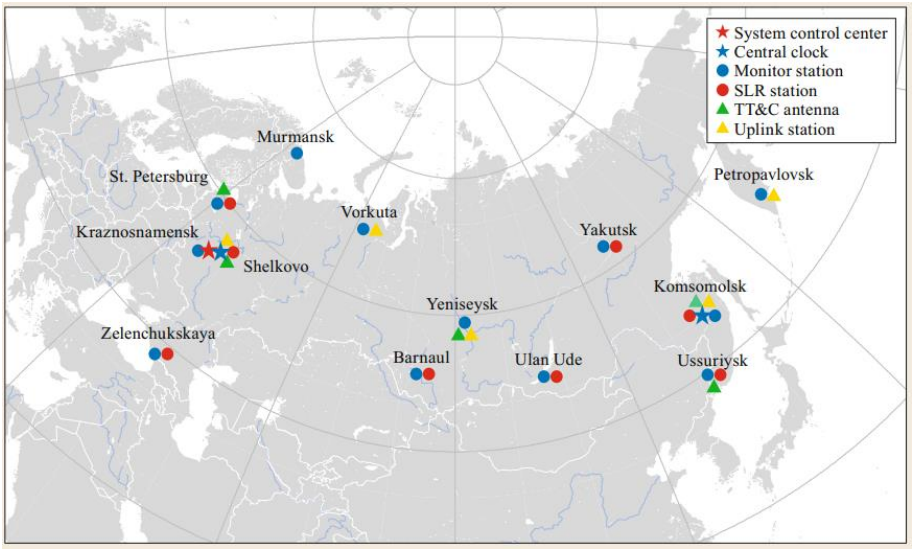

Figure 2-3. GLONASS Control segment [6]

The GLONASS ground-based control segment includes a system control center, central clocks (CC), monitor stations, the Telemetry, Tracking and Control (TT&C) stations, the up-link stations, and satellite laser ranging (SLR) stations [2], [6] (Figure 2-3). All components are located at Air and Space Defense Forces (ASDF) sites within the Russian territory. Each component has its own specific operations to finally ensure the full-operation of GLONASS.

2.1.4 User Segment

Different categories of users, i.e. civilian and military, are benefiting from GNSS in various fields, such as geological research, marine/avigation navigation, agriculture, automobile navigation, automatic driving, etc. Different levels of accuracy are needed in different applications and so will be the user receiving technologies. Even so, a user receiving equipment, i.e. GNSS receiver, generally consists of the same key elements (Figure 2-4):

- the antenna,
- the Radio-Frequency Front End (RF-FE),
- the signal processor and
- the data processor.

More details on the receiver design will be presented in Section 2.4.

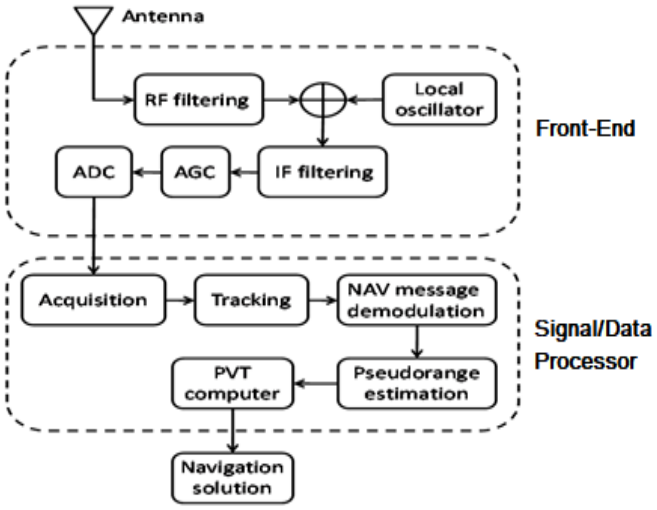

Figure 2-4. Architecture of a digital receiver [2]

2.2 Reference Systems

In GNSS navigation, the reference system in which any navigation state, i.e. the position, the velocity or the clock delay, has to be defined carefully in order to avoid confusion. In this section, various relevant coordinate frames are firstly described, followed by time reference frames.

2.2.1 Coordinate System

To represent the position of the user or of the GNSS satellites, it is necessary to primarily define the reference coordinate systems in which these positions will be expressed. In the first part, introductions of several general coordinate systems are provided. Then, the specific ones adopted by GPS and GLONASS are presented and their comparison is then drawn.

2.2.1.1 General Coordinate Systems

Earth-Centered Inertial frame

The Earth-Centered Inertial frame (ECI, denoted by *i-frame*) is defined with:

- its origin at the mass center of the Earth,
- the z^i-axis parallel to the Earth's spin axis,
- the x^i-axis pointing to the vernal equinox, and
- the y^i-axis completing the right-handed orthogonal frame defined by (x^i, z^i).

The computation of the satellite's position and velocity in orbit entails mostly an inertial frame. The measurements outputted by inertial sensors are also usually obtained with reference to an inertial frame.

Earth-Centered Earth-Fixed frame

The Earth-Centered Earth-Fixed frame (ECEF, denoted by *e-frame*) is defined with:

- an origin at the center of mass of the Earth,

- the x^e-axis pointing towards the mean meridian of Greenwich,
- the z^e-axis parallel to the mean spin axis of the Earth, and
- the y^e-axis completing a right-handed orthogonal frame.

For ground-navigating users, a position expressed relative to the Earth can be more interesting. This is the reason why the ECEF frame, rotating in accordance with the Earth, is of interest. Sometimes instead of having the position expressed in Cartesian form $\boldsymbol{X^e}(x^e, y^e, z^e)$, another alternative for ground navigation is to use the Geodetic coordinates (latitude φ, longitude λ and height h) [2], [28]. The relation between the ECEF frame and the Geodetic coordinates is displayed in Figure 2-5. By drawing a line orthogonal to the surface of the Earth ellipsoid from the point $\boldsymbol{P}$, the height h is the distance between $\boldsymbol{P}$ and the intersection point on the ellipsoid surface. The latitude φ is defined as the angle of intersection of the line to the equatorial plane ($x^e y^e$). The longitude λ is denoted as the angle from the x^e-axis to the intersection plane. To perform the transformation between the Cartesian coordinates and the Geodetics coordinates, the ellipsoidal model of the Earth need be properly defined. Refer to Section 2.2.1.2 for slightly different Earth ellipsoid models defined by the GPS and GLONASS.

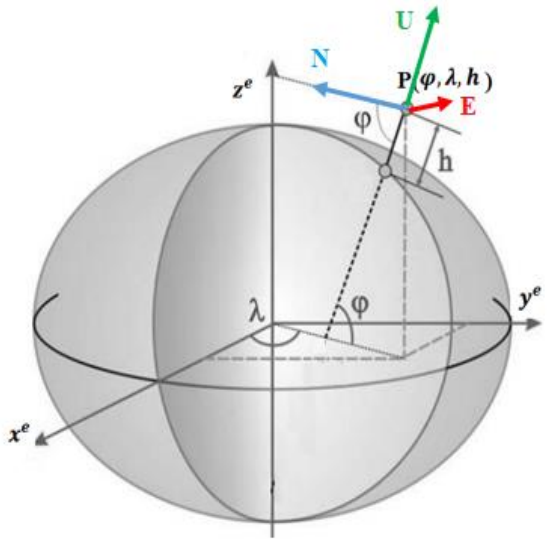

Figure 2-5. ECEF frame, Geodetic coordinates and Local frame [29]

Local Navigation frame

The local navigation frame of type East-North-Up (ENU, denoted by *n-frame*) is defined with

- An origin at the center of the navigation frame,
- the e-axis pointing towards geodetic East,
- the u-axis pointing Up orthogonal to the reference ellipsoid, and
- the n-axis pointing towards geodetic North, completing the right-handed orthogonal frame.

A local frame is important when users need to know their attitudes. However, there exists an important drawback of the *n-frame* that is that a singularity at each pole is generated by the impossibility to define north and east axes. Refer to Section 6.1.3 for further details.

2.2.1.2 GPS and GLONASS Coordinate Systems

Both GPS and GLONASS have their own ECEF coordinate systems in which broadcast parameters related to the position and velocity of satellites in orbit are expressed. GPS uses the World Geodetic System (WGS) 84 as its terrestrial reference system, while GLONASS uses Parametry Zemli (PZ, in

English 'Earth Parameters')-90 [27], [30], [31]. These two systems are both ECEF coordinate frames, while slightly different Earth geodetic datum is applied [32]–[34]. The fundamental parameters of the WGS84(G1762) and PZ-90.11 Earth model are listed in Table 2-1.

Since 1987 when the WGS 84 was developed by the US Department of Defense, successive refinements have been made. The current refined frame WGS84(G1762) was introduced in October 2013. As for GLONASS, according to its modernization plan, all satellites have been broadcasting in the PZ-90.11, a progressively refined version of the initially proposed PZ-90, from 3:00 pm on December 31, 2013.

Table 2-1. Ellipsoidal Parameters of the Earth ellipsoid in WGS 84 and PZ-90.11

Parameter	**WGS84(G1762)**	**PZ-90.11**
Semi-major axis $a_{\oplus}$ [m]	6378137.0	6378136.0
Earth's rotation rate $w_{\oplus}[\frac{rad}{s}]$	$7.2921151467\times 10^{-5}$	7.292115×10^{-5}
Earth's gravitational constant $\mu_{\oplus}[\mathrm{m}^3\mathrm{s}^{-2}]$	3.986005×10^{14}	$3.986004418\times 10^{14}$
Flattening factor $f_{\oplus}$	1/298.257223563	1/298.25784
2nd zonal harmonic J_2	-484.16685×10^{-6}	1082625.75×10^{-9}

For a point expressed in WGS84 and PZ-90.11, the relation between the two Cartesian coordinates is now [32]:

$$(x,y,z)_{WGS} = (x,y,z)_{PZ-90.11} + (-0.3cm, -0.1cm, 0cm) \quad (2\text{-}1)$$

2.2.2 Time Reference Frame

The determination of a user's position with the GNSS is based on the concept TOA of the signals transmitted by all the satellites in view. TOA describes the duration it takes for the signal to go from the satellite emitter to the receiver antennas. Therefore, it is critical that the relation between the two time reference frames used respectively for the measurement of the transmission and reception times is explicit. In this section, before presenting the specific times frames adopted by GPS and GLONASS, the notations of several international time scales are first explained. In the end are depicted the characteristics of different clock technologies, which are practically used in GNSS.

2.2.2.1 International Time Scales

In 1967/1968, the adoption of the SI second by the 13th General Conference of Weights and Measures opened the way towards the formal definition of International Atomic Time (TAI) [35]. TAI is a uniform time scale based on the atomic SI second, and is realized today by the Bureau International des Poids et Mesures.

The Coordinated Universal Time (UTC) provides the compatibility for time synchronization of users worldwide. UTC is a stepped atomic time scale adopted in 1972 on the recommendation of the Radiocommunication Sector of International Telecommunication Union (ITU). A so-called leap second is regularly added to the UTC time to keep it in line with the irregular Earth's rotation when the International Earth Rotation and Reference Systems Service (IERS) recommends it based on astronomical observations.

The difference between UTC and the continuous TAI has amounted to 37 seconds in January 2017 [6]. Similar to TAI, UTC is also a 'paper' time scale that is not physically represented by clocks. However, it is approximated by local physical representations. For example, the United States Naval Observatory (USNO) maintains its own version of UTC, denoted as UTC(USNO). UTC(SU) is the Russian (formerly Soviet Union, SU) realization of UTC. It is maintained by the Institute of Metrology for Time and Space in Moscow. According to years' records, the drifts of the two realizations have always been kept within 30 ns from UTC [6].

2.2.2.2 GPS and GLONASS Reference Time Frames

GPS system time (GPST) is a continuous time scale that is broadcast by the GPS satellites. The GPST and the UTC(USNO) were coincident at 0 hr January 6, 1980 UTC(USNO). This corresponds to the week 0 of the GPST. The steering of the GPST is required to be within 1 μs of UTC(USNO) modulo 1 s. The leap second between GPST and UTC is always broadcast in the GPS navigation message [36]. For example, the GPST is always 19 s behind TAI, and in July 2015, 17 s ahead of UTC(USNO) .

Different from GPST, GLONASS time (GLOT) choses to follow UTC(SU), with a drift less than 1 ms modulo 1 s, as a stepped time scale. The origin of GLOT is at 0 hr January 1, 1996 UTC(SU). With the presence of the constant 3-hour offset of the Moscow time to the Greenwich time according to the Terrestrial Control Complex operational principles, the UTC(SU) is always 3 h ahead of the UTC.

The relations (in entire second) between TAI, UTC, GPST and GLOT are represented in Figure 2-6. The remaining time difference (modulo second) between GPST and GLOT can reach up to several hundreds of nanoseconds (or several hundreds meters in range) [6], [17].

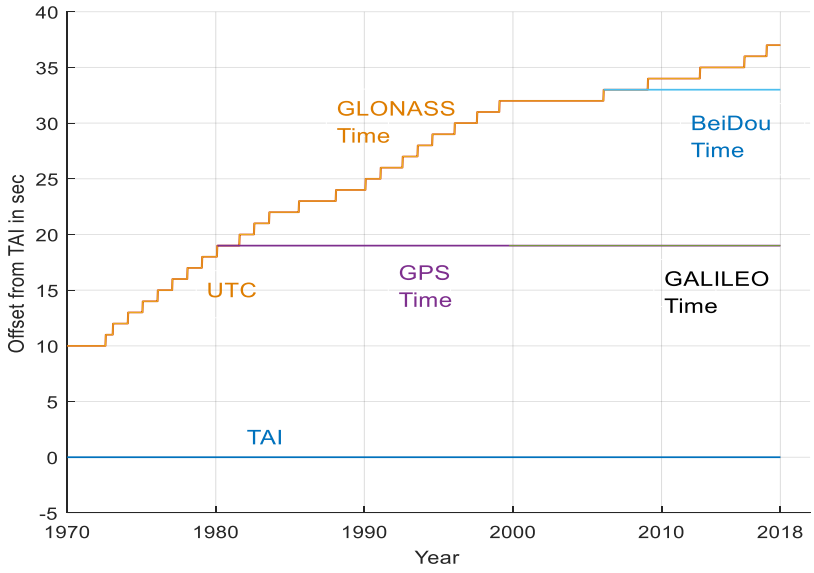

Figure 2-6. Offset in Seconds from TAI for UTC, GPS Time and GLONASS Time (as well as Galileo and BeiDou Time)

2.2.2.3 Clock Categories

Clock is physically a time-keeping device and its core component is the oscillator whose frequency is used as the inverse of the time-recording interval. However, oscillators are not perfect and problems like

clock drifts and phase noise arise. The main types of oscillators are, from the most stable to the least, hydrogen maser atomic clocks, rubidium, cesium and crystal oscillators [6], [37]. To maintain the accuracy of clocks, different technical requirements and technologies are required for different areas. For example, high-precision rubidium and cesium are massively used on GNSS satellites; with constraints of the cost and the size, crystal oscillators are preferred in mobile applications.

In terms of navigation with the GNSS, clocks drifts need be corrected on both the satellite side and the receiver side. Practical clock corrections of satellites are provided in Appendix 0. The receiver clock drift is estimated along with the user's position and a dynamic model will be presented in Section 4.2.3.

2.3 GNSS Signal Model at Antenna Input

GNSS satellites are continuously transmitting signals in at least one carrier frequency and each system has specific signal characteristics. To enable good data reception and synchronization accuracy in most operational conditions while preventing interference between GNSS signals, cautious choices should be made on the signal design and the signal processing. In this part, a general view of GNSS signal structure will first be provided. Then the effect of the propagation channel on GNSS signals is modeled.

2.3.1 GNSS Signal Structure for GPS and GLONASS

Most GNSS signals consist of three components [2]:

- a carrier
- a navigation data message D,
- a spreading code C.

The signal transmitted is typically modeled as following using a direct sequence spread spectrum modulation (DSSS):

$$s(t) = \sqrt{2A}D(t)C(t)cos(2\pi f_0 t) \tag{2-2}$$

where

- A is the signal average power,
- f_0 is the radio frequency.

A depiction of GNSS signal structure is illustrated in Figure 2-7.

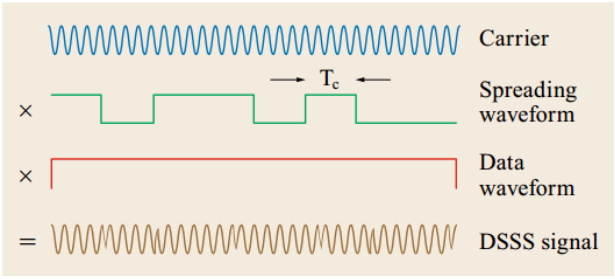

Figure 2-7. GNSS signal structure (adapted from [6])

2.3.1.1 Carrier Frequency

The carrier frequency is the central frequency or frequency channels allocated to each GNSS signal. The ITU has allocated to the Radio Navigation Satellite Services (RNSS), where GNSS belongs to, two frequency bands, the Upper and the Lower L-band. Other frequency bands have been discussed, but the

L-band was chosen as the best compromise between frequency availability, propagation effects, and system design [8].

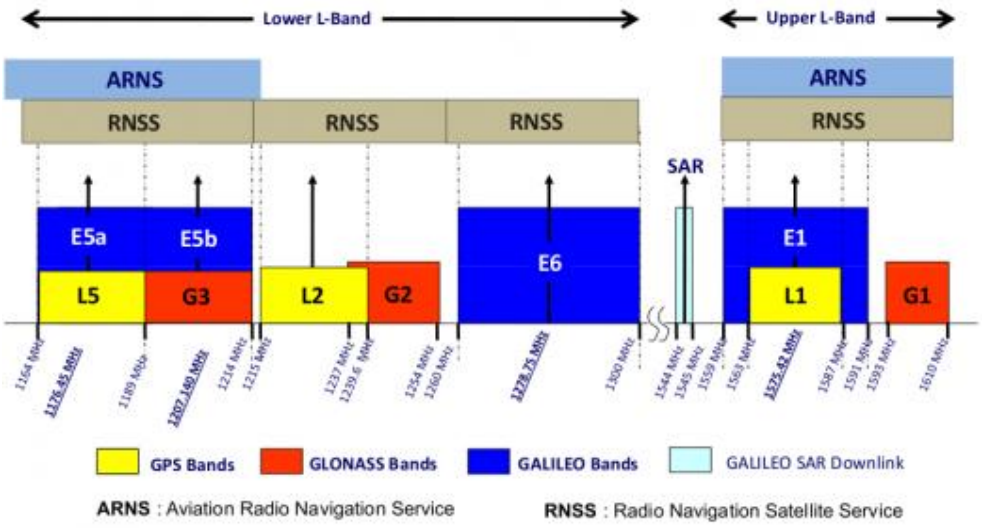

Figure 2-8. GNSS signal carrier frequency bands (adapted from [38])

Historically, the open GNSS signals have been located in the upper L-band. As a consequence, most of the civilian receivers process the signals in this band. Even today, most of the mass market receivers are still only processing these signals. As illustrated in Figure 2-8, GPS L1 and GLONASS G1 are located in the Upper L-band (1559-1610 MHz). Detailed descriptions of these signals will be in following section. In this band:

- GPS transmits three signals that have a common central frequency at 1575.42 MHz:
  - GPS L1 C/A which is an open signal that can be freely used. It is the only open GPS signal that is transmitted by the whole GPS constellation
  - GPS L1 P(Y) and GPS M-code that are encrypted signals for military/restricted use
- GLONASS transmits two signals that have a central frequency spread over the G1 band:
  - GLONASS G1 OF (also known as GLONASS G1 C/A), which is an open signal that can be freely used
  - GLONASS G1 SF, which is a secured signal.

In the frame of this PhD thesis, the GNSS signals considered are GPS L1 C/A and GLONASS G1 C/A.

In the Lower L-band (1151-1350 MHz) are located GPS L2 (1227.60 MHz), GPS L5 (central frequency at 1176.45 MHz), GLONASS G3 (central frequency at 1207.14 MHz) and GLONASS G2 (14 channels ranging from 1242.9375 MHz to 1248.625 MHz).

2.3.1.2 Navigation Data

The navigation data is a binary sequence carrying all the useful information from the system infrastructure to the user. This data, periodically updated by the control segment, includes information such as satellite clock bias, satellite ephemeris, satellite health status, constellation almanac, etc.

However, the structures of the navigation data differs between GPS L1 C/A and GLONASS G1 C/A.

- For GPS L1 C/A, the navigation message uses a basic format of 25 frames with each frame containing 1500 bits and each frame is subdivided into 5 sub-frames with 300 bit [31]. The data

is transmitted at a rate of $R_d = 50$ bit/s (per second). Therefore, a total time of 12.5 mins is needed to transmit the whole navigation message.

- For GLONASS G1 C/A signal, the navigation message uses the same bit rate of 50 bit/s. A duration of 2.5 mins is required to transmit the whole message in 5 frames with each frame containing 1500 bits and each frame consisted of 15 strings of 100-bit length [27].

Besides the structure, the data content also differs between GPS to GLONASS. This is the case, for instance, of the satellite orbit information: satellite positions, velocities, and accelerations are directly contained in the GLONASS G1 C/A navigation message, while parameters (such as the sine/cosine harmonic correction to the orbit radius, eccentricity of the orbit, etc) describing the satellite position in orbit are provided by the GPS L1 C/A signal. Refer to Appendix A for more information on the navigation data and the RINEX, a specified exchange format used nowadays to restore navigation data.

2.3.1.3 Spreading Code

The spreading code, also known as pseudo random noise (PRN) sequence, is a binary periodic code that is used for both identification of the transmitted signal and for finely synchronizing the receiver with the received signal. In order to distinguish the bits of the PRN sequence from the bits of the navigation message transmitted by the satellite, the PRN code bits are referred to as chips.

Two main parameters are used to characterize a spreading code: the chipping rate R_c and the length N_c. Thus, the duration of the spreading code sequence T_p is

$$T_p = N_c T_c = N_c / R_c$$

The chipping rate R_c is typically much higher than the useful data rate R_d. As a consequence, the multiplication of the useful signal with the speading code leads to a significant increase of the signal spectrum bandwidth. This means of communication is therefore known as spread spectrum technique. For example, the GPS L1 C/A signals are using a spreading code, known as Gold code, with a chipping rate R_c of 1.023 Mchips/s ($N_c = 1023, T_p = 1\ ms$), while the data rate is only 50 bit/s. The GLONASS G1 C/A signals are using a spreading code of chipping rate R_c =0.511 Mchips/s $\left(N_c = 511, T_p = 1\ ms\right)$, while the data rate is 50 bit/s.

Responding to the demands of transmitting multiple signals with minimum interference from each single satellite, and even upon a single carrier, three basic multiple access techniques can be used [39]: Time division multiple access (TDMA), Frequency division multiple access (FDMA), and Code division multiple access (CDMA).

GPS uses CDMA, which means that each signal is associated to a different PRN ranging sequence, each PRN code being as orthogonal as possible to the other PRN codes of the other satellites.

GLONASS uses FDMA, which means that a slightly different carrier frequency is allocated to each satellite in order to discriminate between the different signals coming from different satellites. Take the GLONASS G1 band for example, the nominal carrier frequencies allocated to satellites are:

$$f_i = f_{0,G1} + k_i \Delta f_{G1} \tag{2-3}$$

where

- $f_{0,G1} = 1602\ MHz$ the central frequency for GLONASS G1 band,
- $\Delta f_{G1} = 562.5\ kHz$ the frequency separation, and $k_i \in [-7, 6]$ the frequency number [27].

Note however that for a given signal (e.g. GLONASS G1), the same PRN sequence is used for all satellites.

2.3.2 Signal Propagation and Reception

GNSS signals, once transmitted by the satellites, need to travel to the near Earth users. In this section, the effects of the propagation channel on the GNSS signal will be briefly described, followed by the reception of signal through the antenna and the RF-FE.

2.3.2.1 Atmospheric Effects

Rather than a simple propagation delay brought by the vacuum, the effects of the Earth's atmosphere on radio waves are much more complex. Generally, the propagation speed of radio waves is related to the index of refraction n of the medium, which gives its definition as following:

$$n = c/v \tag{2-4}$$

with c the speed of light in vacuum, v the propagation speed of the radio waves. What's more, in terms of the GNSS signals, the phase velocity v_{ph} of the signal's carrier phase need be distinguished from the group velocity v_{gr} associated with the waves carrying the signal information, as well as the indexes of refraction. A formula describing the relation between the phase refractive index n_{ph} and the group refractive index n_{gr} is provided [8]

$$n_{gr} = n_{ph} + f\frac{dn_{ph}}{df} \tag{2-5}$$

with f the carrier frequency, $\frac{dn_{ph}}{df}$ the derivative of n_{ph} with respect to f.

Ionosphere Effect

With respect to the atmosphere effect on GNSS signal propagation, the atmosphere is usually divided in 2 layers: the ionosphere and the troposphere. The ionospheric layer is roughly located from 50 to 1000 km above the Earth's surface. With the presence of free electrons in this layer that impacts the refractivity index of the medium, GNSS signals are refracted. The ionosphere is a dispersive medium, meaning that its effect depends upon the signal carrier frequency. Two equations are used to approximate in first order the phase refractive index n_{ph} and the group refractive index n_{gr}:

$$n_{ph} = 1 + \frac{c_2}{f^2} \tag{2-6}$$

$$n_{gr} = 1 - \frac{c_2}{f^2} \tag{2-7}$$

with the coefficient c_2 frequency independent but a function of the electron density [2], [8].

This results finally in a group delay and a phase advance of the signal (with respect to propagation in vacuum) of the same magnitude. The derivation process is omitted but the simplified formulas of the group delay (positive value as convention) and the phase advance in meter are presented in relation to the total electron content (TEC) along the propagation path [8]:

$$I_{ph} = -\frac{40.3}{f^2}TEC \tag{2-8}$$

$$I_{gr} = \frac{40.3}{f^2}TEC \tag{2-9}$$

Thus, the estimate and the reduction of the ionosphere effect rely on the complicated determination of TEC which depends on various quantities, i.e. the sunspot activities, the line of sight, etc. GPS offers a simple method, the Klobuchar model, for single-frequency users to estimate the ionospheric effect. The Klobuchar model, firstly proposed in 1986, offers an ionospheric reduction at L1 of at least 50% by using the ionospheric coefficients broadcast in GPS navigation message. The slant ionospheric time delay is modeled by a half-cosine function in following form [6], [8], [31]:

$$\tau_{ion,gr} = M(E) * \tau_{ion,gr,v} = M(E) * \left\{ A_1 + A_2 \cos\left[\frac{2\pi(t - A_3)}{A_4}\right]\right\} \quad (2\text{-}10)$$

where

- $M(E) = 1 + 16(0.53 - E)^3$ is the obliquity factor or the mapping function transforming the $\tau_{ion,gr,v}$, the vertical ionospheric time delay, to the slant ionospheric time delay $\tau_{ion,gr}$;
- E is the elevation angle in semicircles;
- $A_1 = 5\ ns,$ the constant vertical ionospheric time delay during night time;
- $A_3 = 14h$ local time, the center of the half-cosine function*;*
- $A_2 = \alpha_0 + \alpha_1\phi_m + \alpha_2\phi_m^2 + \alpha_3\phi_m^3$ is the amplitude of the cosine function, $A_4 = \beta_0 + \beta_1\phi_m + \beta_2\phi_m^2 + \beta_3\phi_m^3$ is the period;
- $\alpha_{i,i\in[0,3]}$, $\beta_{i,i\in[0,3]}$ are broadcast ionospheric coefficients; ϕ_m is the geomagnetic latitude of the Earth projection of the ionospheric piercing point whose computation steps are not addressed here.

However, the performance of this model is limited and only first-order atmosphere delays are corrected. Albeit, as these effects are depending on the propagation path of GNSS signal, a spatial correlation is naturally expected.

Troposphere Effect

Extending to about 12 km above the Earth's surface, the troposphere, a non-dispersive medium for radio waves of frequency up to 15 GHz, creates both a group and phase (of same magnitude) delay. The delay depends on the local temperature, pressure, relative humidity, etc. To compute the tropospheric delay, typically ranging from 2 to 20 m, other than relying on the refractive index n, the refractivity N_{trop} is instead used:

$$N_{trop} = 10^6(n - 1) \quad (2\text{-}11)$$

This refractivity is possible to be divided into two parts, a dry (hydrostatic) and a wet (nonhydrostatic) component. While the dry component, composing about 90% of the whole tropospheric delay, can be predicted precisely, the wet component is more difficult to predict as the water vapor holds plenty variations. Approximation methods like Hopfield model, Saastamoinen model, Marini mapping function, and the most widely applicable UNB3M model, have been proposed to eliminate the troposphere delays [6], [8], [40], [41]. Referred to UNB3M, the dry and wet are both functions of the meteorological parameters, i.e. pressure, temperature, water vapor pressure, temperature lapse rate and water vapor lapse rate. Unable to obtain the current atmosphere condition without meteorological sensors, a look-up table is used to predict the meteorological parameters. Detailed implementation steps of the UNB3M model are referred to [39], [40, p. 3], [42].

2.3.2.2 Multipath

The GNSS receiver antenna can receive several signals coming from the same satellite that have gone through different paths, typically created by reflections. These signals coming from a single origin are

known as multipath. An illustration of the multipath is provided in Figure 2-9. The amplitude, delay and phase of the multipath depends on the specific propagating paths followed by each signal. Because the receiver needs to get synchronized with the direct, also known as Line-Of-Sight (LOS) signal, to extract a precise TOA measurement, multipath are a source of errors. This is particularly true since they share the same PRN code as the LOS signal.

Specific situations, known as the non-line-of-sight (NLOS) event, can occur in which only indirect signals arrives at the receiver (the LOS being blocked, for instance by a building). This situation will tend to make the receiver track the first arriving signal, thus creating a positive bias on the pseudorange measurements.

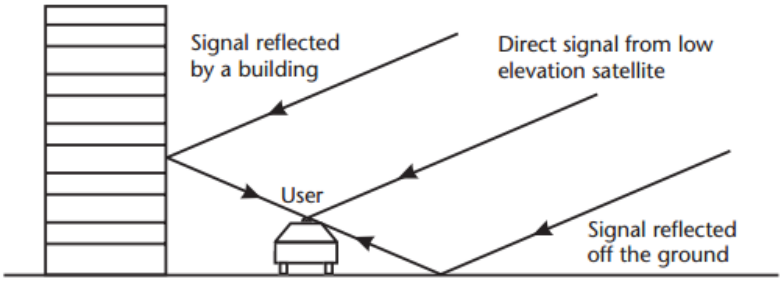

Figure 2-9. Multipath [2]

2.3.2.3 Interference

Other than the expected GNSS signals, the presence and reception of interferences may however degrade the GNSS performance. The interference is referring to RF signals coming from undesired sources, intentional or unintentional. Unintentional interferences are mostly signals from other services, intersystem interference, or other system both regulated by ITU, intersystem interference.

Intentional interferences are often categorized into jamming, spoofing and meaconing [8], [39]. Jamming is denoting the intent of drowning the desired GNSS signals in high-power interferences to cause loss of lock. Spoofing is similar to meaconing. While spoofing is referring to the operation of broadcasting false locally-generated GNSS signals to make the receiver produce a false position, meaconing is concerned about a reception of GNSS signals and re-broadcasting a delayed version.

2.3.2.4 Antenna and Receiver RF Front-End

Antennas receive signals and transform the energy of electromagnetic waves into electric currents. The ability of an antenna to focus on certain elevation or azimuth is measured by its gain. An isotropic antenna has an uniform gain pattern in all directions. However, with the aim to reject multipath and interference, the antenna gain is often a function of the azimuth and the elevation. For example, as the GNSS receivers only need to focus on signals from above the user's horizon, an antenna gain growing with the elevation angle would be more appropriate. The location of the user that "captures" the signals is referred to as the antenna phase center. Depending upon the antenna technology, this phase center can vary with azimuth, elevation and frequency. It can thus create different delays, usually fairly small, between the received GNSS signals.

The RF-FE is typically composed of a Low Noise Amplifier (LNA), filters, a down-conversion and an Analog-to-Digital Converter (ADC), the later being coupled with an Automatic Gain Controller (AGC). The RF-FE creates delays in the signal propagation (compared to vacuum propagation). This delay is

typically dependent upon the spectrum of the incoming signal as well as its carrier frequency. For instance, all GPS signals will be delayed and phase-shifted similarly by the RF front-end while this might not be the case for GLONASS FDMA signal (that are at different carrier frequencies). The amount of hardware delays, depending on the specific processing channel, is overall receiver and frequency dependent. Refer lately to Section 2.4.4 for detailed modeling of those delays. The electronic components of the antenna and the RF front-end also create a background noise also known as thermal noise that will superimpose the received signal.

2.3.2.5 Received Signal Model

The continuous received analog signal can be modeled as:

$$r(t) = f(t) \otimes [h(t) \otimes s(t) + w(t)]$$

where

- h is the impulse response of the propagation channel,
- w is an additive white noise,
- f is the filtering effect of the RF-FE on the received signal, and
- $\otimes$ denotes the convolution product.

Let's consider that h only introduces a delay and that the RF front-end filter is sufficiently wide with respect to the signal bandwidth, then the received signal can be modeled as:

$$r_f(t) = \sqrt{2P} D(t-\tau) C(t-\tau) cos(2\pi f_{\mathrm{I}} t + 2\pi f_{\mathrm{D}} t + \theta) + n(\mathrm{t})$$

where

- τ is the signal delay,
- P is the signal power,
- f_{I} is the signal carrier frequency after down-conversion,
- f_D is the Doppler frequency due to the relative dynamics, assumed constant during the processing period (i.e., T_{co} the duration of the integrator in Section 2.4),
- θ is the signal phase shift,
- $n(\mathrm{t})$ is the white thermal noise generated in the receiver.

The typical power for GPS C/A-code signal at the transmission is about 14.3 dBW (27 watts), which is collected by a typical receiver on the earth's surface with P ranging from -162.5 dBW to -154.5 dBW [5].

The thermal noise can typically be assumed White. Its typical PSD level can be around approximately -201 dBW/Hz, leading to typical received C/N_0 value around 38.5 dB.Hz to 46.5 dB.Hz in open sky conditions.

2.4 GNSS Receiver Signal Processing and GNSS Measurements

The estimation of the triplet (τ, θ, f_D) of $r_f(t)$ by the receiver will respectively give the pseudorange, the carrier phase and the Doppler measurements as by-products. The signal processing normally proceeds in two stages: the signal acquisition, that provides a rough estimation of the above parameters, and the signal tracking that provides a fine estimation of the above parameters and enables also data demodulation. The expanded components of the GNSS receiver signal processing is provided in Figure 2-10.

In this section, the signal acquisition will be first introduced followed by the signal tracking loops. General models of GNSS measurements are presented in the end.

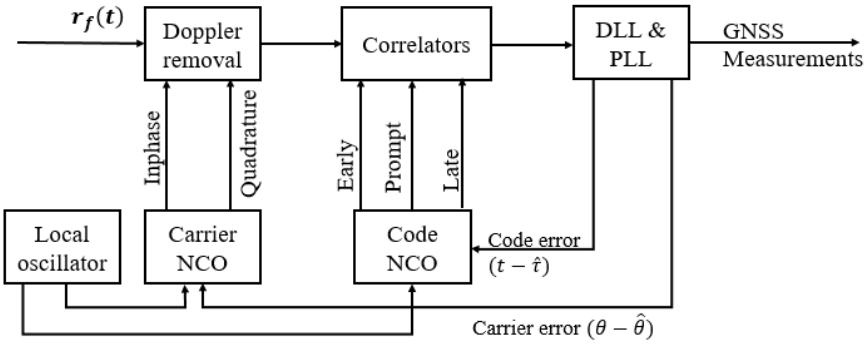

Figure 2-10. GNSS receiver signal processing

2.4.1 Signal Acquisition

The signal acquisition is a global search for the coarse values of (τ, f_D), while subsequently the signal tracking is a local search for accurate values of (τ, f_D) - referred as a non-coherent signal tracking - or of (τ, θ, f_D) - referred as a coherent signal tracking.

Depending on the amount of a-priori information, a cold start or a warm start or a reacquisition is adopted for the signal acquisition [5]

- A cold start is a type of acquisition related to the fact that the receiver does not have any a-priori information about its position, its clock delay, or which satellite could be seen in the sky. In this case, a time-consuming search over all possible satellites and all possible values of (τ, f_D) is required.
- A warm start is when a coarse estimation of the receiver's position and clock delay is known, and recent satellite almanac is accessible. In this case, the search space is much reduced and the acquisition can be much faster.

The signal acquisition proceeds with two blocks in order: the carrier/carrier phase removal and the correlators, as presented in Figure 2-11.

- The Doppler removal is based on the use of a local reference signal $\sqrt{2}cos\left(2\pi f_1 t + 2\pi \hat{f}_D t + \hat{\theta}\right)$ and its $\pi/2$ phase-shifted signal. In this case, $\hat{\theta}$ represents the receiver-controlled carrier phase. These 2 components are multiplied with the received signal to create an in-phase and quadrature-phase branch. The in-phase and quadrature signals r_I and r_Q can then be modeled as (anticipating the filtering of the terms with double frequencies):

$$r_I(t) = \sqrt{P}D(t-\tau)C(t-\tau)cos(2\pi\Delta f_D t + \Delta\theta) \quad (2\text{-}12)$$

$$r_Q(t) = \sqrt{P}D(t-\tau)C(t-\tau)sin(2\pi\Delta f_D t + \Delta\theta)$$

  with $\Delta f_D = f_D - \hat{f}_D$ and $\Delta\theta = \theta - \hat{\theta}$.

- A local replica of the spreading code, with a controlled delay $\hat{\tau}$, is then multiplied with r_I and r_Q, before passing through an integrator $\frac{1}{T_{co}}\int_0^{T_{co}}(\cdot)dt$. T_{co} is known as the integration duration.

This process is known as a correlation process. To take advantage of the correlation properties of the PRN code, T_{co} is typically chosen as a multiple of the PRN code duration.

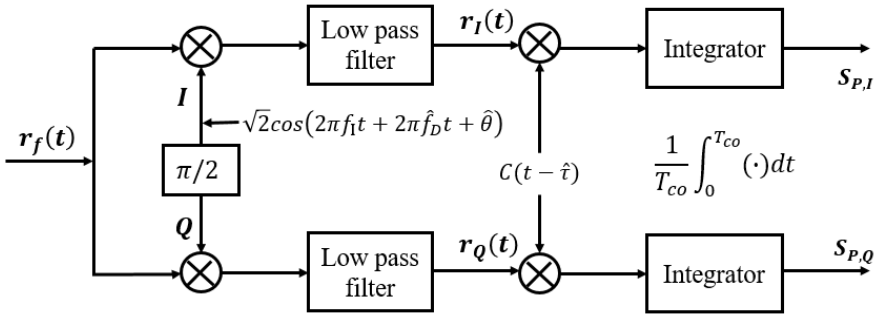

Figure 2-11. Signal acquisition

$S_{P,I}$ and $S_{P,Q}$ can thus be modelled as:

$$S_{P,I}(\Delta\tau, \Delta f_D, \Delta\theta) = \frac{1}{T_{co}}\int_0^{T_{co}} \sqrt{P}D(t-\tau)C(t-\tau)C(t-\hat{\tau})cos(2\pi\Delta f_D t + \Delta\theta)dt \quad (2\text{-}13)$$

$$S_{P,Q}(\Delta\tau, \Delta f_D, \Delta\theta) = \frac{1}{T_{co}}\int_0^{T_{co}} \sqrt{P}D(t-\tau)C(t-\tau)C(t-\hat{\tau})sin(2\pi\Delta f_D t + \Delta\theta)dt$$

which can be simplified, assuming that the signal parameters are constant during T_{co} and that the value of the data message does not change during that interval, into:

$$S_{P,I}(\Delta\tau, \Delta f_D, \Delta\theta) = \sqrt{P}D \cdot R(\Delta\tau)sinc(\pi \cdot \Delta f_D \cdot T_{co})cos(\Delta\theta) + n_I \quad (2\text{-}14)$$

$$S_{P,Q}(\Delta\tau, \Delta f_D, \Delta\theta) = \sqrt{P}D \cdot R(\Delta\tau)sinc(\pi \cdot \Delta f_D \cdot T_{co})sin(\Delta\theta) + n_Q$$

Where

- D is the value of the data bit during the correlation,
- R is the PRN code autocorrelation function,
- $\Delta\tau = \tau - \hat{\tau}$,
- n_I and n_Q are the noise components at the correlator outputs and are assumed Gaussian and independent from each other.

To focus on the estimation of (τ, f_D), the magnitude summation of these two signals are computed:

$$S_P^2(\Delta\tau, \Delta f_D) = S_{P,I}^2(\Delta\tau, \Delta f_D, \Delta\theta) + S_{P,Q}^2(\Delta\tau, \Delta f_D, \Delta\theta) = P * \left|\tilde{R}(\Delta\tau, \Delta f_D)\right|^2 + N_{S_P} \quad (2\text{-}15)$$

where

- $\tilde{R}(\Delta\tau, \Delta f_D) = R(\Delta\tau)sinc(\pi \cdot \Delta f_D \cdot T_{co})$
- N_{S_P} is the noise term.

${S_P}^2$ is a function that will be maximized when $\Delta\tau = 0$ and $\Delta f_D = 0$. The objective of the acquisition algorithm will thus be to find the receiver-controlled $\hat{\tau}$ and $\hat{f}_D$, from a 2-dimensional search grid, that maximize ${S_P}^2$. For more details on practical applications, refer to [5], [6].

Signal acquisition provides rough estimates of the code delay τ and the Doppler frequency f_D. The refinement and continuous tracking of those estimates rely on the signal tracking process. To illustrate

the functioning of the signal tracking, typical structures of DLL and PLL will be introduced in the following sections.

2.4.2 Delay Lock Loop

The common structure of a DLL consists of a code discriminator, which is an estimator of $\Delta\tau$, a low-pass filter and a Numerically-Controlled Oscillator (NCO) to adjust the code delay estimate $\hat{\tau}$.

The detailed structures of DLL is given in Figure 2-12. A simple non-coherent Early-power-minus-Late-power (EML) DLL and a coherent DLL will be expanded in this section as a depiction. For more discuss on the DLL, refer to [2], [5], [8].

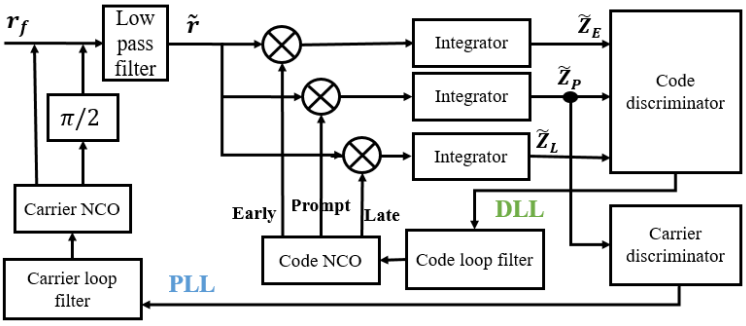

Figure 2-12. Signal tracking (DLL & PLL)

A complex representation is adopted without loss of generality. As mentioned in previous sections, the complex signal at the output of the low pass filter is

$$\tilde{\boldsymbol{r}}(\boldsymbol{t}) = r_I(t) + jr_Q(t) = \sqrt{P}D(t-\tau)C(t-\tau)exp(j2\pi\Delta f_D t + \Delta\theta)$$

Then early and late correlators are implemented by using two code replicas, early and late with respect to $\hat{\tau}$ by a known delay $d/2$. The complex signals obtained at the outputs of correlators are thus in forms

$$\tilde{\boldsymbol{Z}}_{\boldsymbol{E}}(\Delta\tau, \Delta f_D, \Delta\theta) = \sqrt{P}D \cdot exp(j\Delta\theta)\tilde{R}(\Delta\tau - d/2, \Delta f_D) \tag{2-16}$$

$$\tilde{\boldsymbol{Z}}_{\boldsymbol{L}}(\Delta\tau, \Delta f_D, \Delta\theta) = \sqrt{P}D \cdot exp(j\Delta\theta)\tilde{R}(\Delta\tau + d/2, \Delta f_D)$$

To strip out the dependence on $\Delta\theta$ and D, the non-coherent EML DLL constitutes the code discriminator function $\boldsymbol{L}_{\Delta\tau,EML}$ as a square subtraction:

$$\begin{aligned}\boldsymbol{L}_{\Delta\tau,EMLP}(\Delta\tau, \Delta f_D) &= \left|\tilde{\boldsymbol{Z}}_{\boldsymbol{E}}(\Delta\tau, \Delta f_D, \Delta\theta)\right|^2 - \left|\tilde{\boldsymbol{Z}}_{\boldsymbol{L}}(\boldsymbol{k}\Delta\tau, \Delta f_D, \Delta\theta)\right|^2 \\ &= P * \left(\left|\tilde{R}\left(\Delta\tau - \frac{d}{2}, \Delta f_D\right)\right|^2 - \left|\tilde{R}\left(\Delta\tau + \frac{d}{2}, \Delta f_D\right)\right|^2\right) + N_{EMLP}\end{aligned} \tag{2-17}$$

After the signal acquisition, the estimate of the Doppler frequency can be considered as accurate enough to consider that $\Delta f_D = 0$. If we restrain our focus on small values of $\Delta\tau$, $\boldsymbol{L}_{\Delta\tau,EMLP}$ can be approximated as a linear function of $\Delta\tau$:

$$\boldsymbol{L}_{\Delta\tau,EMLP}(\Delta\tau) \approx P * \left(\left|R\left(\frac{\Delta\tau - d}{2}\right)\right|^2 - \left|R\left(\Delta\tau + \frac{d}{2}\right)\right|^2 + N_{EMLP} \approx \frac{2P}{d}\Delta\tau + N_{EMLP}\right. \tag{2-18}$$

The discriminator output then passes through a low-pass filter to limit the influence of noises on the control loop. The output of the low-pass filter is then the command tension for the VCO that will update the code delay in a continuous way. According to the performance analysis with additive noise presence,

the tracking accuracy is highly dependent of the signal-to-noise ratio C/N_0 and the Early-Late time spacing d [5], [6]:

$$var(\Delta\tau_{EMLP}) = \frac{BdT_c}{2C/N_0}(1 + 2T_{co}\,C/N_0)\ [\text{sec}^2] \tag{2-19}$$

where B is the noise equivalent bandwidth of the DLL filter, and normally the inequality $2BT_{co} \ll 1$ holds true. A narrow correlator space d will correspondingly increase the performance.

The code pseudorange measurements are computed based on the synchronization of the receiver local PRN code with the PRN code of the incoming signal of interest, namely the multiplication of the code delay τ by the speed of light in a vacuum. The delays originating from the atmosphere, the hardware, the clock delays, etc., are thus all part in the code delay τ.

2.4.3 Phase Lock Loop

Similar to the DLL, the PLL consists of a phase discriminator, which gives the possibility to extract the phase error $\Delta\theta$, and a low-pass filter that commands the NCO driving the local carrier generation.

The Costas carrier discriminator function is constructed from the prompt correlator $\tilde{\boldsymbol{Z}}_{\boldsymbol{P}}$ (referred to Figure 2-12),

$$\mathbf{L}_{\Delta\theta,\text{Costas}}(\Delta\tau, \Delta\theta) = \text{Re}\{\tilde{\mathbf{Z}}_{\mathbf{P}}(\Delta\tau, \Delta f_D, \Delta\theta)\}\text{Im}\{\tilde{\mathbf{Z}}_{\mathbf{P}}(\Delta\tau, \Delta f_D, \Delta\theta)\} = \frac{1}{2}\text{P} \cdot \text{R}^2(\Delta\tau)\sin(2\Delta\theta) \tag{2-20}$$

with $Re\{\cdot\}$, $Im\{\cdot\}$ for extracting respectively the real part and the imaginary part of a complex value. The need of a-priori information on date massage is obviated here with the Costas PLL as $D^2 = 1$.

By analyzing the discriminator functions, clearly the resolution of $\Delta\theta$ is insensitive to any $\pi/2$ phase shift in $\boldsymbol{L}_{\Delta\theta,Costas}$ which leaves an ambiguity in the phase estimation that will be part of the carrier phase measurements derived from the PLL local phase.

The carrier phase measurement is accumulated as the number of cycles generated or received since a starting point, i.e. the moment when the phase lock is initially achieved with the signal. As the PLL is only sensitive to the fractional part of $\Delta\theta$, only the fractional part of θ is estimated and refined whereas the integer number of cycles N, noted as integer ambiguity, of the starting point remains unknown.

In case of signal blockage, high user dynamics or high noise level, the PLL can be easily disturbed (compared to the DLL), resulting in phase lock is lost. If such an event happens, a new phase lock needs to be established, which will lead in a new value for the carrier phase integer ambiguity. This is referred to as a cycle slip (CS). The detection and resolution of CS thus plays a vital role in carrier phase positioning.

The Doppler measurements are representative of the rate of change of the carrier phase measurements during a certain interval.

2.4.4 GNSS Raw Measurement Models

Three basic GNSS measurements, the pseudorange measurements, the carrier phase measurements and the Doppler measurements, are produced at the output of the signal processor. Accounting for primary error sources, the basic modeling of GNSS measurements is devised in this section.

Classic models of the GPS pseudorange measurements, carrier phase measurements and Doppler measurements are:

$$P_i^{GPS} = \rho_i + c\left(dt_r^{GPS} - dT_i^{GPS}\right) + I_i + T_i + b_{r,P_i}^{GPS} - b_{s,P_i}^{GPS} + m_{P_i}^{GPS} + \epsilon_{P_i}^{GPS} \quad (2\text{-}21)$$

$$\Phi_i^{GPS} = \rho_i + c\left(dt_r^{GPS} - dT_i^{GPS}\right) - I_i + T_i + \lambda_{GPS} N_i + b_{r,\Phi_i}^{GPS} - b_{s,\Phi_i}^{GPS} + m_{\Phi_i}^{GPS} + \epsilon_{\Phi_i}^{GPS} \quad (2\text{-}22)$$

$$D_i^{GPS} = \dot{\rho}_\iota + c\left(\dot{dt}_r^{GPS} - \dot{dT}_i^{GPS}\right) - \dot{I}_i + \dot{T}_i + m_{D_i}^{GPS} + \epsilon_{D_i}^{GPS} \quad (2\text{-}23)$$

where

- The index i stand for the i-th satellite,
- The index P, Φ and D stand for pseudorange-, phase-, Doppler-specific,
- The sub-index r and s stand for user receiver- and satellite-specific,
- ρ_i is the true geometric range between the satellite i and the receiver antenna in meters,
- dt and dT are respectively the rover and the satellite receiver clock delays steered to the GPST,
- I is the ionosphere delay,
- T is the troposphere delay,
- $m_■$ is the multipath effect on ■,
- $b_{r,■}$ and $b_{s,■}$ are correspondingly the user receiver and the satellite hardware delays,
- N_i is the integer ambiguity which remains constant when the tracking continues without loss of lock,
- λ_{GPS} is the wavelength of the GPS L1 signal, common for all GPS satellites broadcasting signals within the same frequency channel, i.e. $\lambda_{GPS,L1} = \frac{c}{f_{GPS,L1}}$,
- ϵ represents the measurement noise.

With the FDMA modulation, the modeling of the GLONASS measurements is slightly different from GPS,

$$P_j^{GLO} = \rho_j + c\left(dt_r^{GLO} - dT_j^{GLO}\right) + I_j + T_j + b_{r,P_j}^{GLO} - b_{s,P_j}^{GLO} + m_{P_j}^{GLO} + \epsilon_{P_j}^{GLO} \quad (2\text{-}24)$$

$$\Phi_j^{GLO} = \rho_j + c\left(dt_r^{GLO} - dT_j^{GLO}\right) - I_j + T_j + \lambda_j N_j + b_{r,\Phi_j}^{GLO} - b_{s,\Phi_j}^{GLO} + m_{\Phi_j}^{GLO} + \epsilon_{\Phi_j}^{GLO} \quad (2\text{-}25)$$

$$D_j^{GLO} = \dot{\rho}_J + c\left(\dot{dt}_r^{GLO} - \dot{dT}_j^{GLO}\right) - \dot{I}_j + \dot{T}_j + m_{D_j}^{GLO} + \epsilon_{D_j}^{GLO} \quad (2\text{-}26)$$

where

- the wavelength λ_j of the satellite indexed j is not common among the GLONASS G1 satellites, each satellite has its own specific frequency channel (see Eq(2-3)),
- the receiver and satellite clock delays (dt_r^{GLO}, dT_j^{GLO}) are referred to the GLOT, and the discrepancies between the two time references GLOT and GPST need be carefully handled in the multi-GNSS navigation,
- the receiver biases are now signal dependent since each signal is transmitted at a slightly different frequency.

2.4.5 GNSS Corrected Measurement Model

The above models correspond to the so-called raw measurements output by the receiver. Before using the raw measurements for computing its position and time, the receiver will first correct them based on known models and/or information contained in the navigation message.

First of all, the satellite clock delay is corrected using a curve-fit and the relevant steering parameters are contained in the navigation message. Detailed satellite clock correction methodology is provided in

Appendix B. Typically, the residual clock errors result in rang errors from 0.3-4 m, depending on the type of satellite and the age of broadcast data [39].

The ephemerids of all involving satellites are estimated as in the case of the satellite clock correction. A curve-fit is defined to provide the best prediction of the satellite' position and velocity, referred to Appendix B for more details. A normal range error of 1-6 meters is expected due to the residual position error.

Atmosphere delays are corrected using previously mentioned correction models. In terms of the ionosphere delay, the simple Klobuchar model is applied. As for the troposphere delays, it's the UNB3M model finally used. However, the performance of those models is limited, especially with the ionospheric correction model only first-order delays are corrected. Residual atmosphere errors may result range errors from 1-10 meters.

The theoretical model for the corrected measurements is then:

$$P_i^{GPS} = \rho_i + cdt_r^{GPS} + b_{r,P_i}^{GPS} - b_{s,P_i}^{GPS} + m_{P_i}^{GPS} + \epsilon_{P_i}^{GPS} \quad (2\text{-}27)$$

$$\Phi_i^{GPS} = \rho_i + cdt_r^{GPS} + \lambda_{GPS}N_i + b_{r,\Phi_i}^{GPS} - b_{s,\Phi_i}^{GPS} + m_{\Phi_i}^{GPS} + \epsilon_{\Phi_i}^{GPS} \quad (2\text{-}28)$$

$$D_i^{GPS} = \dot{\rho}_i + c\dot{dt}_r^{GPS} + m_{D_i}^{GPS} + \epsilon_{D_i}^{GPS} \quad (2\text{-}29)$$

$$P_j^{GLO} = \rho_j + cdt_r^{GLO} + b_{r,P_j}^{GLO} - b_{s,P_j}^{GLO} + m_{P_j}^{GLO} + \epsilon_{P_j}^{GLO} \quad (2\text{-}30)$$

$$\Phi_j^{GLO} = \rho_j + cdt_r^{GLO} + \lambda_j N_j + b_{r,\Phi_j}^{GLO} - b_{s,\Phi_j}^{GLO} + m_{\Phi_j}^{GLO} + \epsilon_{\Phi_j}^{GLO} \quad (2\text{-}31)$$

$$D_j^{GLO} = \dot{\rho}_J + c\dot{dt}_r^{GLO} + m_{D_j}^{GLO} + \epsilon_{D_j}^{GLO} \quad (2\text{-}32)$$

where the noise terms $\epsilon_{\blacksquare}$ now includes also the residual correction errors.

2.5 Single Point Positioning with GPS Pseudoranges

Mass market GNSS receivers tend to only use pseudorange measurements for position and time offset computation due to the difficulty to use carrier phase measurements (low robustness of tracking mechanism, cycle slipping, ambiguous measurement, etc.). As a consequence, in this section, the estimation of a stand-alone user's position using only GPS pseudorange measurements is illustrated to provide an overview of GNSS navigating. The performance of a single-frequency standard positioning GPS user can observe better than 10 m, 95% positioning and 20-ns, 95% timing accuracy worldwide autonomously using broadcast orbits and clocks [2], [5], [39]. In this section, the basic technique of Leas-Squares estimation (LSE) is implemented.

2.5.1 Least Squares Estimation

Let us define a generic linear system in the form of

$$Y_k = H_k X_k + \epsilon_k$$

where

- Y_k represents the observables vector at instant k,
- X_k represents the states vector to be estimated at instant k,
- H_k is the design matrix linking Y_k and X_k,

- ϵ_k represents the Gaussian white observation noise, with R_k the variance-covariance (VC-) matrix.

LSE is an optimal estimation process to find the best solution which fits the above linear system when the observation noise is Gaussian [37]. It uses the criterion of minimizing the sum of squared residuals:

$$\min_{\hat{X}_k} \|Y_k - \hat{Y}_k\|^2 \tag{2-33}$$

Inside the equation, $\hat{Y}_k = H_k \hat{X}_k$ is the estimation of observables based on states estimates $\hat{X}_k$.

The weighted version of LSE gives the best solution in the form:

$$\hat{X}_k = \left(H_k^T W_k H_k\right)^{-1} H_k^T W_k Y_k \tag{2-34}$$

where W_k is the weighting matrix which modulates the importance of each observation.

A common option is to use the inverse of the VC-matrix R_k of measurements as weights: $W_k = R_k^{-1}$. Measurements with lower noise level should be highly weighted. In such case, the VC-matrix of the solution $\hat{X}_k$ is finally given by

$$P_k = \left(H_k^T W_k H_k\right)^{-1} \tag{2-35}$$

The measurements residuals, r_k, are thus formulated as:

$$r_k = Y_k - \hat{Y}_k = Y_k - H_k \hat{X}_k \tag{2-36}$$

In the quality assessment of an estimation, the measurement residuals play an important role.

2.5.2 Estimation of Position and Time

The previous estimation theory is based on the construction of a linear system. However, the measurement models between GNSS observables and the desired states, i.e. the user position and clock, is not a linear system. Therefore, an extended form of LSE should be applied in which a linearization is needed.

We denote P_u^j the measured pseudorange between the j-th satellite and the receiver u, with $j \in [1, K]$. K is the total number of satellites visible in view of the receiver u. Let vectors $\boldsymbol{X_u}(x, y, z)$ and $\boldsymbol{X^j}(x^j, y^j, z^j)$, represent respectively the ECEF coordinates of the receiver's phase center and the ECEF coordinates of the j-th satellite in orbit. The true user-to-satellite geometric range is thus

$$\rho_u^j = \sqrt{(x - x^j)^2 + (y - y^j)^2 + (z - z^j)^2} = \left\|\boldsymbol{X_u} - \boldsymbol{X^j}\right\| \tag{2-37}$$

After applying the correction of the atmosphere effects and the satellite clock delays, the simplified form of the pseudorange then becomes

$$P_u^j = \rho_u^j + clk_u + \epsilon_{P_u^j} \tag{2-38}$$

with

- clk_u the receiver clock delay in meter with respect to the time reference system and
- $\epsilon_{\mathrm{P}_u^j}$ the combined effect of the residual errors including the residual satellite clock delays, the residual atmosphere delays, the potential multipath errors, etc. Note that due to the model now

using the estimated satellite position in ρ_u^j, $\epsilon_{\mathrm{P}_u^j}$ now also includes the satellite position estimation error.

Clearly, the relation between P_u^j and $\boldsymbol{X_u}$ is non-linear. The basic idea is to linearize the system around an approximate value of the state parameters, solve for the system, and then adjust the system in an iterative way. As a consequence, let us define $\boldsymbol{X_0}(x_0, y_0, z_0)$ and clk_0 the first state guesses. The difference between the true and the approximated values are denoted as

$$\boldsymbol{\delta X_{u,0}} = \boldsymbol{X_u} - \boldsymbol{X_0} \tag{2-39}$$

$$\delta clk_0 = clk - clk_0 \tag{2-40}$$

The position bias $\boldsymbol{\delta X_{u,0}}$ is generally negligible compared to the distance $\left\|\boldsymbol{X_u} - \boldsymbol{X^j}\right\|$ between the satellite and the rover on the ground which is usually of order 1000 km. According to the first-order approximation, the residual measurement $\delta \mathrm{P}_{u,0}^j$ is expressed as

$$\begin{aligned}
&\delta \mathrm{P}_{u,0}^j = \mathrm{P}_u^j - \mathrm{P}_{u,0}^j \\
&= (\left\|\boldsymbol{X_0} + \boldsymbol{\delta X_{u,0}} - \boldsymbol{X^j}\right\| + clk) - (\left\|\boldsymbol{X_0} - \boldsymbol{X^j}\right\| + clk_0) + \tilde{\varepsilon}_{P,u}^j \\
&\approx -\frac{\boldsymbol{X^j} - \boldsymbol{X_0}}{\|\boldsymbol{X^j} - \boldsymbol{X_0}\|} . \boldsymbol{\delta X_{u,0}} + \delta clk_0 + \tilde{\varepsilon}_{P,u}^j \\
&= -\boldsymbol{e^j} . \boldsymbol{\delta X_{u,0}} + \delta clk_0 + \tilde{\varepsilon}_{P,u}^j
\end{aligned}$$

where $\boldsymbol{e_0^j}$ is the estimated line-of-sight (LOS) unit vector along the direction pointing from the initial estimate user position to the satellite, $\boldsymbol{e_0^j} = \frac{\mathbf{1}}{\|\boldsymbol{X^j} - \boldsymbol{X_0}\|}\left(x^j - x_0, y^j - y_0, z^j - z_0\right)$.

A set of K linear equations, representing the K measurements, can be presented as:

$$\boldsymbol{\delta P_0} = \begin{bmatrix} \delta P_{u,0}^1 \\ \delta P_{u,0}^2 \\ . \\ . \\ \delta P_{u,0}^K \end{bmatrix} = \begin{bmatrix} -\boldsymbol{e_0^1} & \mathbf{1} \\ -\boldsymbol{e_0^2} & \mathbf{1} \\ \vdots & \vdots \\ -\boldsymbol{e_0^K} & \mathbf{1} \end{bmatrix} \begin{bmatrix} \boldsymbol{\delta X_{u,0}} \\ \delta clk_0 \end{bmatrix} + \tilde{\varepsilon}_P = \boldsymbol{H} \begin{bmatrix} \boldsymbol{\delta X_{u,0}} \\ \delta clk_0 \end{bmatrix} + \tilde{\varepsilon}_P \tag{2-41}$$

The matrix $\boldsymbol{H}$ is referred to be the geometry matrix describing the user-satellite geometry. The bias state vector $\left[\boldsymbol{\delta X_{u,0}}, \delta clk_0\right]^T$ is then resolved according to Eq.(2-34) and added to the first state guess $[\boldsymbol{X_0}, clk_0]^T$ to refine new state estimate $[\boldsymbol{X_1}, clk_1]^T$. The whole estimation process iterates with the new state estimate until the solution converges, e.g. norm($\left[\boldsymbol{\delta X_{u,0}}, \delta clk_0\right]$) $\leq 1e$-5.

The stochastic performance of the GNSS positioning highly depends on two factors:

- The number and distribution of the tracked satellites in the sky with respect to the user position, which is referred to as the dilution of precision (DOP);
- The quality of the generated GNSS measurements, which is referred to as user equivalent range error (UERE). UERE is the total error budget representing the measurement model errors with respect to this system..

Consider a simplified case that the measurement VC-matric R_k has only diagonal components identical to the square of the satellite UERE, noted $\sigma^2{}_{UERE}$. The VC-matrix of states P_X is then expressed as stated in Eq.(2-35):

$$P_X = \sigma^2{}_{UERE}\left(\boldsymbol{H^T H}\right)^{-1}$$

Note that under the consumption that $\sigma^2{}_{UERE}$ related to satellites is invariant, the state quality is determined by the matrix $\boldsymbol{P} = \left(\boldsymbol{H}^{\boldsymbol{T}}\boldsymbol{H}\right)^{-1} = \left(P_{ij}\right)_{i,j\in\{x,y,z,t\}}$. $\boldsymbol{P}$ only depends on the number of satellites and the relative geometry between the satellites and the user. To describe the translation of measurement noise level σ_{UERE} to the state noise level, the construction of the DOP terms, i.e. the geometric DOP (GDOP), the position DOP (PDOP) and the time DOP (TDOP), are given by

$$GDOP = \sqrt{P_{x,x} + P_{y,y} + P_{z,z} + P_{t,t}}$$

$$PDOP = \sqrt{P_{x,x} + P_{y,y} + P_{z,z}}$$

$$TDOP = \sqrt{P_{t,t}}$$

Intuitively with the same number of visible satellites, a lower PDOP value and consequently a more accurate solution are expected with a good satellite distribution. In Figure 2-13, an illustration of a good distribution of satellites on the left side and a bad one on the right wide with satellites clustered in one side is provided.

When the position is resolved in a local ENU frame, the horizontal DOP (HDOP) and the vertical DOP (VDOP) describing respectively the precision in the horizontal plane and the vertical plane are introduced,

$$HDOP = \sqrt{P_{e,e} + P_{n,n}};\quad VDOP = \sqrt{P_{u,u}}$$

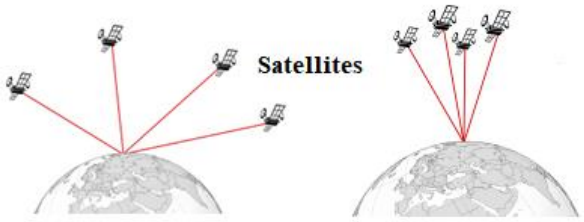

Figure 2-13. Good (left) and bad (right) GDOP cases (adopted from [43])

3 Precise Positioning and the Problem Raised by Urban Environments

The navigation with GNSS is ultimately the process of determining the position of the rover. The accuracy level of the state solution is a key indicator of the navigation performance. To achieve higher accuracy, plenty of efforts have been made for example on both the GNSS constellation side (i.e., the modernization of GNSS signals and satellites, etc.) and the receiver side. In this section, the precise positioning techniques are firstly introduced to show procedures implemented on the receiver side to improve the navigation performance. The influence of the environment where the rover is located is never a negligible factor. Problems that can be raised by the urban environment, a common area for most daily-life users, are presented at the end.

3.1 Precise Positioning Principles and Techniques

In general, a single-frequency standard positioning GPS user can observe better than 10 m, 95% positioning and 20-ns, 95% timing accuracy worldwide [2], [5], [39]. However, these levels of accuracy still cannot satisfy a lot of applications demanding higher performance beyond even the ability of what a single-frequency standard positioning GPS user could provide. According to previous sections, the accuracy level of the PVT (Position-Velocity-Time) solution can be raised by virtue of either decreasing the DOP values or reducing the satellites UERE. On the receiver side, little effort can be made to improve the current satellite geometry except for considering a multi-GNSS constellation. Nevertheless, striving to reduce the UERE, augmentation procedures, like differential GNSS (DGNSS) and the precise point positioning (PPP) are thus brought up.

3.1.1 Differential GNSS

The basic innovation of DGNSS is to benefit from the spatial or time correlation characteristics of most errors contaminating the positioning accuracy for users separated by tens or even hundreds of kilometers away. Thus one or multiple reference station receivers are involved in DGNSS to provide corrections for these sources of errors to the user. The distance between the user and the reference station is referred as the baseline.

DGNSS techniques can be categorized in different ways depending on specific consideration aspects. According to the involved type of GNSS measurements, code-based DGNSS, when only pseudorange measurements are processed, is separated from carrier-phase-based DGNSS when both pseudorange and carrier phase measurements are considered.

Considering the geographic size, the basic categories of DGNSS techniques are [5], [39]:

- local area DGNSS (LDGNSS),
- region-area DGNSS (RDGNSS), and
- wide-area DGNSS (WDGNSS).

The LDGNSS system is expected to serve a region of less than 10-100 km from a reference station, while an area up to 1000 km and a larger functioning area are respectively concerned with the RDGNSS system and the WDGNSS system.

Within each DGNSS category, the number of involved reference stations and the correction data type that the reference station provides are also different. In the case of LDGNSS, majorities of space-correlated errors can be mitigated by using the pseudorange/carrier-phase domain correction from one

reference station, while three or more reference stations are necessary along the perimeter of RDGNSS coverage to provide good performance.

The DGNSS positioning performance highly depends on the length of baseline as the residual errors after correction grow with the baseline. Meter-level or under a better condition a decimeter-level accuracy is achievable with code-based LDGNSS/WDGNSS.

When more accurate positioning is desired, then it is necessary to use carrier-phase measurements. Carrier-phase measurements are very interesting because they contain a very small (compared to pseudorange measurements) tracking jitter, typically below 1cm (1-sigma). As a consequence, once the ionosphere and troposphere errors are efficiently mitigated, they could be used to target centimeter-level positioning. However, to reach this target, there are many hurdles. First, the carrier phase measurements are ambiguous and thus cannot be used directly for absolute positioning. There is thus a required step to estimate correctly the integer ambiguity of each measurements. This is very challenging since the L1 frequency creates carrier wavelength of the order of less than 20 cm. Second, the PLL that is used to generate carrier phase measurements is known to not be very robust. As a consequence, the carrier phase measurements can be unavailable for some time (during high dynamics or low C/N_0 conditions), and when they become available again, the ambiguity will have change, requiring a new ambiguity estimation process. These 2 hurdles explain in part why such methods have mostly been used by applications that take place in fairly open environments.

In the next 2 sections, two types of well-known precise positioning techniques are described: Precise Point Positioning (PPP) and Real-Time Kinematic (RTK). The first one does not require surrounding reference stations, while the second one does. These methods will be looked at in the context of this PhD which only tackles single-frequency GPS/GLONASS receivers.

3.1.2 Precise Point Positioning

The concept of PPP was firstly proposed in 1997 to achieve precise point positioning using undifferenced, dual-frequency, carrier phase and pseudorange measurements, along with precise satellite orbit and clock products [6], [8]. Thanks to the great efforts of the International GNSS Service (IGS), precise satellite orbit and clock solution products for real-time or post-time processing have been available since 1990's. Instead of broadcast ephemerides, precise products are used to reduce satellite orbits and clock noise level.

In order to achieve centimeter level accuracy, additional observation errors need be carefully handled: phase wind-up effect, solid earth tides, ocean loading, antenna phase center offset [5]–[8]. Elaborate modeling is thus required. However, the correction of the atmospheric effects is always a great issue. The low accuracy of the empirical ionosphere delay models (i.e., Klobuchar model, NeQuick) and tropospheric delays models (i.e., Saastamoinen model, Marini mapping function, UNB3M model) have made them inadequate for achieving centimeter-level PPP. Normally, dual-frequency PPP user employ ionosphere-free combinations to achieve the precise estimation of the user's position, clock. Concerning the troposphere delays, in addition to an a-priori troposphere correction model, an extra state (i.e., zenith troposphere delay ZTD) is continuously estimated (at least per hour). This parameter can be mapped to residual troposphere delays through a fairly representative mapping function, i.e. the Niell's mapping function. A positioning accuracy of centimeter level is achievable with dual-frequency PPP, however a long convergence time (more than 15 min) is generally required [44].

Originally developed for dual-frequency users, the generic PPP concept can also be applied to the single-frequency case while additional complexity arises. First of all, as the precise clock correction is based on dual-frequency ionosphere-free combination, for single-frequency users additional correction related to differential code biases (DCB) need be applied [6], [7], [26]. Secondly, the correction of ionosphere

effects becomes essential. Regarding the mitigation of ionosphere delays, two techniques have been introduced in [6], [7], but each has its own drawbacks. One is based on the group and phase ionosphere correction (GRAPHIC) notion to form an ionosphere-free (in first-order) code-phase combination. The mathematical form is provided in Eq.(3-1). The final combination is ionosphere-free but still contains the ambiguous carrier phase ambiguity. Longer observation period is needed to have enough observability of the system. As a consequence, a fairly longer convergence time (15 min longer) is entailed to achieve decimeter-level accuracy. The noise level is half of the original code observables, while on the same time the equivalent wavelength is also decreased by a factor of 2. With a noise level exhibiting the carrier phase wavelength, the detection and handling of small amount cycle clips become more difficult. A remark is made herein that the inseparability between integer ambiguities and hardware delay combinations in Eq(3-1) gives users no choice but estimating an equivalent ambiguity as float.

$$\begin{aligned} \boldsymbol{P_{graphic}} &= \frac{\boldsymbol{P_1 + \Phi_1}}{\boldsymbol{2}} \\ &= \rho_i + c\left(dt_r - dT_{i,s}\right) + T_i + \frac{\lambda_i}{2} N_i + b_{r,P_{Graph}} - b_{s,P_{Graph}} + \epsilon_{P_{Graph}} \end{aligned} \tag{3-1}$$

Another methodology is using total electron content (TEC) maps for ionospheric delay correction. However, a slowly changing residual bias is unneglectable and absorbed by ambiguities. The integer nature of ambiguities that we should make profit from is no longer true.

The profit brought by the fact that the integer-nature ambiguities are resolved or fixed, i.e. Integer Ambiguity Resolution (IAR), is not only the improvement of system accuracy, but also the decrease of system convergence times. This is the reason why multiple-frequency PPP users are striving to come up with new techniques (PPP-AR techniques) to achieve integer ambiguity resolution [6], [44]–[47]. However, for single-frequency PPP users the integer resolution of ambiguities is generally impossible, unless some additional external corrections can be applied. Thus, the carrier-phase-dominated DGNSS technique, Real Time Kinematic methodology, is brought up in next section.

3.1.3 Real Time Kinematic Methodology

Real Time Kinematic (RTK) methodology is devised to achieve fast centimeter-level accuracy positioning with the help of surrounding reference stations. In this case, the integer ambiguities preventing the carrier phase from acting like absolute range measurements should always be resolved. The ability to quickly and correctly resolve the integer ambiguity is one of the key performance indicators of the RTK methodology and a strong differentiator from PPP. In this section, the formation of GNSS differential measurements will firstly be reviewed, followed by the introduction of the core part of the RTK methodology, namely the integer ambiguity resolution (IAR).

3.1.3.1 Differential Measurements

Raw GNSS measurements are broadcast by the reference station. These measurements are used by the user receiver to form so-called difference measurements. Two basic forms of differential observations are typically used:

- SD: “Single–differencing between receivers” refers to the difference of measurements between a pair of receivers, i.e. the rover’s receiver and the reference station’s receiver, sharing a common satellite.
- DD: Double-differencing is the difference between two SD measurements collected from two different satellites, but with the same pair of receivers.

The mathematical construction of GPS differential measurements is separately presented from GLONASS differential measurements which hold different characteristics. Consider two receivers denoted as r and u respectively on the reference station side and the rover side, and the common GPS satellite indexed i. In practice, it is fairly common that no Doppler measurements are provided on the reference station side. Therefore, only the pseudorange and carrier phase measurements are herein studied. The full mathematical formulations of SD GPS measurements are:

$$\Delta P_i^{GPS} = \Delta\rho_i + c\Delta dt_{ru}^{GPS} + \Delta I_i + \Delta T_i + \Delta b_{ru,P_{i,GPS}} + \epsilon_{\Delta P_{i,GPS}} \tag{3-2}$$

$$\Delta \Phi_i^{GPS} = \Delta\rho_i + c\Delta dt_{ru}^{GPS} - \Delta I_i + \Delta T_i + \lambda_{GPS}\Delta N_i + \Delta b_{ru,\Phi_{i,GPS}} + \epsilon_{\Delta\Phi_{i,GPS}} \tag{3-3}$$

where $\Delta\blacksquare$ represents SD terms.

The common satellite-dependent terms (i.e. clock delays and satellite-side hardware delays) are thus eliminated during the single differencing. By virtue of the spatially-correlated property of atmosphere delays, ΔT_i and ΔI_i will be very small when a short baseline is considered. The integer nature of the carrier-phase ambiguities is conserved with the ambiguity term ΔN_i.

Another satellite indexed j is considered as the pivot to form DD measurements,

$$\nabla\Delta P_{ij}^{GPS} = \nabla\Delta\rho_{ij} + \nabla\Delta I_{ij} + \nabla\Delta T_{ij} + \nabla\Delta b_{ru,P_{ij,GPS}} + \epsilon_{\nabla\Delta P_{ij,GPS}} \tag{3-4}$$

$$\nabla\Delta \Phi_{ij}^{GPS} = \nabla\Delta\rho_{ij} - \nabla\Delta I_{ij} + \nabla\Delta T_{ij} + \lambda_{GPS}\nabla\Delta N_{ij} + \nabla\Delta b_{ru,\Phi_{ij,GPS}} + \epsilon_{\nabla\Delta\Phi_{ij,GPS}} \tag{3-5}$$

where $\nabla\Delta\blacksquare$ represents DD terms. The remaining receiver clock term $c\Delta dt_{ru}^{GPS}$ present in the SD measurements is further eliminated when the DD is formed. Holding a common signal frequency between the satellite i and j, the DD hardware delays $\nabla\Delta b_{ru,P_{ij,GPS}}$, $\nabla\Delta b_{ru,\Phi_{ij,GPS}}$ are totally negligible.

As for GLONASS, with FDMA, signals are transmitted at slightly different frequencies for different satellites. Consider the common GLONASS satellite indexed m for instance, SD GLONASS measurements are

$$\Delta P_m^{GLO} = \Delta\rho_m + c\Delta dt_{ru}^{GLO} + \Delta I_m + \Delta T_m + \Delta b_{ru,P_{m,GLO}} + \epsilon_{\Delta P_{m,GLO}} \tag{3-6}$$

$$\Delta \Phi_m^{GLO} = \Delta\rho_m + c\Delta dt_{ru}^{GLO} - \Delta I_m + \Delta T_m + \lambda_m\Delta N_m + \Delta b_{ru,\Phi_{m,GLO}} + \epsilon_{\Delta\Phi_{m,GLO}} \tag{3-7}$$

where the wavelength λ_m differs from satellite to satellite. A remark is made that the remained differential hardware delays $\Delta b_{ru,P_{m,GLO}}$ and $\Delta b_{ru,\Phi_{m,GLO}}$ are frequency-dependent, other than a common value as in GPS case. More characteristics and calibration procedures regarding those hardware terms will be addressed in Section 4.3.

Another satellite indexed k is considered as the pivot to form GLONASS DD measurements,

$$\nabla\Delta P_{km}^{GLO} = \nabla\Delta\rho_{km} + \nabla\Delta I_{km} + \nabla\Delta T_{km} + \nabla\Delta b_{ru,P_{km,GLO}} + \epsilon_{\nabla\Delta P_{km,GLO}} \tag{3-8}$$

$$\nabla\Delta \Phi_{km}^{GLO} = \nabla\Delta\rho_{km} - \nabla\Delta I_{km} + \nabla\Delta T_{km} + (\lambda_m\Delta N_m - \lambda_k\Delta N_k) + \nabla\Delta b_{ru,\Phi_{km,GLO}} + \epsilon_{\nabla\Delta\Phi_{km,GLO}} \tag{3-9}$$

However the integer nature of the ambiguity term is no longer conserved within the GLONASS DD. Extra procedures should thus be taken, or otherwise GLONASS SD measurements should be used [18]–[20].

3.1.3.2 Integer Ambiguity Resolution

Along with the consideration of ambiguous carrier phase measurements, the ambiguities need be resolved to achieve precise positioning. During the formation of differential measurements, the integer nature of the ambiguities are conserved as much as possible. The Integer Ambiguity Resolution (IAR) is the process of benefitting the integer nature to obtain a fast and reliable centimeter-level navigation solution if it succeeds. But also it can lead to unacceptable errors compromising the position integrity when done wrong. As a consequence, there is always a fine line between keeping float ambiguity values that are reliable or accepting fixed ambiguity values that may be corrupted. This is why IAR should strictly be composed of two processes: (1) integer ambiguity estimation to obtain optimal integer ambiguity estimates and (2) validation process to validate the best integer ambiguity candidate [10], [12].

In the first subsection, the notion of Integer Aperture Estimators (IAE) is devised which enables an overall theoretical analysis of IAR. A brief introduction of several popular integer ambiguity estimation techniques is then provided, including the Least-squares AMBiguity Decorrelation adjustment (LAMBDA) method. At the end, integer ambiguity validation procedures are described to provide a discuss on the reliability of the obtained integer ambiguity solution.

Integer Aperture Estimator

To assess the combination of the fixed ambiguity assessment and validation process and provide an overall theoretical basis for IAR, the idea of Integer Aperture Estimator (IAE) is presented in [12]. The general idea of the IAE is the distinction of three situations:

- **success** where the correct integer estimation is accepted;
- **failure** where the false integer estimation is accepted;
- **uncertainty** where integer estimation is rejected.

The related probability parameters are depicted in following table [48]:

Table 3-1. Relevant parameters of Integer Aperture Estimator

		Correct Integers $P_{s,ILS}$		Wrong Integers $P_{f,ILS}$
Accept P_{fix}	=	Success P_s	+	Failure P_f
		+		+
Reject P_{float}	=	False Alarm P_{fa}	+	Detection P_d

Intuitively, the failure case is the most undesired condition that instead of shrinking the float solution uncertainty level, a severely biased fixed solution might be obtained. Therefore, an acceptable upper threshold for the value P_f is recommended. An optimal IAE is thus the one which maximizes the probability of success P_s and on the same time the P_f does not go beyond the predefined limit [11], [49].

Integer Ambiguity Estimation

Any GNSS navigation system can be parametrized in integers $a \in Z^n$ and non-integers $b \in R^{\mathrm{m}}$. A generic representation of the observation model is proposed as the following linear(ized) equation:

$$y = Aa + Bb + \epsilon, \;\; with\; a \in Z^n, b \in R^m \tag{3-10}$$

where

- a is the vector of integer parameters (i.e., integer ambiguities),
- A is the design matrix for integers, and
- b is the vector of non-integer states to be resolved in R (i.e., the baseline increments, receiver clock delay) with B the related design matrix, and $\epsilon \sim N(\Theta, Q_y)$ is the Gaussian observation noise.

The integer ambiguity estimation is mostly accomplished following three steps [50], [51].

- First, the constraint that $a \in Z^n$ is disregarded to obtain the real-valued estimates $(\hat{a}, \hat{b})^T$ from the output of an estimation filter for instance a Kalman Filter (KF) or a LS. The resulting VC-matrix of $\hat{a}$ and the so-called float solution $\hat{b}$ is thereby

$$\begin{bmatrix} \hat{a} \\ \hat{b} \end{bmatrix} \sim \begin{bmatrix} Q_{\hat{a}} & Q_{\hat{a}\hat{b}} \\ Q_{\hat{b}\hat{a}} & Q_{\hat{b}} \end{bmatrix}, \; with\, \hat{a} \in R^n, \hat{b} \in R^m \tag{3-11}$$

- Second, search or calculate the integer ambiguity estimates $\check{a}$ from the float estimates

$$\check{a} = S(\hat{a}) \tag{3-12}$$

  where $S: R^n \rightarrow Z^n$is the integer estimator, a mapping function which directs all float point in R^n into a specific point in Z^n.

- Third, calculate the fixed solution $\check{b}$ by adjusting the float solution in the following way

$$\check{b} = \hat{b}|\check{a} = \hat{b} - Q_{\hat{b}\hat{a}} {Q_{\hat{a}}}^{-1} (\hat{a} - \check{a}). \tag{3-13}$$

Various integer estimators have been proposed since 1980. Among those, the most intuitive and direct integer estimator is the integer rounding estimator [11]. Float ambiguities are rounded to their closest integers. However, the correlation among those ambiguities is then not considered.

A sequential version, the bootstrapped estimator was proposed in [13], [52]. Starting from the first ambiguity term, all following float ambiguities are decorrelated from previous ambiguities before being rounded. Nevertheless, there still lacked a solid theory on the performance evaluation of such integer estimators, until the LAMBDA method and a performance indicator, namely the probability of success fixing P_s, were brought up [14], [15], [53].

Comparisons in terms of computational efficiency and performance between different integer ambiguity estimation techniques are presented in [15], [50], [53], [54]. As a result, the LAMBDA methodology has been acknowledged as the optimal integer estimator in terms of maximizing P_s. A brief introduction of LAMBDA is herein given. For more detailed information, refer to [55], [56].

The LAMBDA is fundamentally an integer least-squares (ILS) estimator as it strives to minimize the following quadratic objective function

$$\min_{a \in Z^n, \hat{b} \in R^m} \|y - Aa - Bb\|^2_{Q_y} = \min_{a \in Z^n, \hat{b} \in R^m} (\|\hat{e}\|^2_{Q_y} + \|a - \hat{a}\|^2_{Q_{\hat{a}}} + \left\|b - \hat{b}|a\right\|^2_{Q_{\hat{b}|a}}) \tag{3-14}$$

In the right side of the previous equation is the orthogonal decomposition of the objective function into three parts. $\hat{e}$ is the measurement residual adhering to the float estimates $(\hat{a}, \hat{b})^T$. $\hat{b}|a$ is the conditional least-squares baseline vector conditioned on $a \in \mathrm{Z}^n$, having $Q_{\hat{b}|a}$ as the VC-matrix. The first part $\|\hat{e}\|^2_{Q_y}$ is irrelevant to the integer estimate $\check{a}$, and the third part can be null by taking the fixed baseline solution as $\check{b} = \hat{b}|\check{a}$. Consequently, the mapping function under the least-squares idea is fundamentally to derive the ILS estimates $\check{a}$ by resolving

$$\min_{a \in Z^n} \|a - \hat{a}\|^2_{Q_{\hat{a}}} = (a - \hat{a})^T Q_{\hat{a}}^{-1} (a - \hat{a}) \tag{3-15}$$

In case of a diagonal $Q_{\hat{a}}$, meaning that integer ambiguities are independent from each other, the search for ILS estimates $\check{a}$ would be quite simple. However, for GNSS applications, all ambiguities are strongly correlated. Hence, a reduction stage by a Z-transformation is primarily settled to simplify the next discrete searching stage. A modified version was brought up in [55] accounting for effectively reducing computational burdens.

The probability of having the final ILS estimates $\check{a}$ equal to the real integer values is quantified by $P_{s,ILS}$. The whole procedure of ILS search makes it impossible to derive a compact theoretical formula of $P_{s,ILS}$. However, a lower bound is provided by the IB estimator [13], [15]

$$P_{s,ILS} \geq P_{s,IB} = \prod_{i=1}^{n}\left(2\Phi\left(\frac{1}{2\boldsymbol{\sigma}_{\hat{\boldsymbol{a}}(\boldsymbol{i}|\boldsymbol{I},\boldsymbol{i}|\boldsymbol{I})}}\right)-1\right) \tag{3-16}$$

where

- $\boldsymbol{\sigma}_{\hat{\boldsymbol{a}}(\boldsymbol{i}|\boldsymbol{I},\boldsymbol{i}|\boldsymbol{I})}$ is the standard deviation of the *i*-th ambiguity obtained through a conditioning on the previous $\boldsymbol{I} = \boldsymbol{1}, \ldots, (\boldsymbol{i}-\boldsymbol{1})$ ambiguities, and

$$\Phi(x) = \int_{-\infty}^{x}\frac{1}{\sqrt{2\pi}}exp(-\frac{1}{2}v^2)dv \tag{3-17}$$

Integer Ambiguity Validation

Theoretically, a parameter estimation should not be considered complete without an appropriate process to validate the solution [11]. Practically, the original intention of fixing the integer parameters in GNSS applications is to decrease the positioning uncertainty on the basis of float solution. A wrong fixing of integer ambiguities may lead to a much severer consequence (i.e., a remarkable positioning bias leading to integrity issues). Therefore, the integer ambiguity validation process is never an omissible part for ensuring a reliable GNSS precise positioning.

The most popular validation methods are the Ratio-test (RT), the F-ratio test (FT) and the Difference test (DT). Comparison between them have been the topic of many publications [48], [57]–[59].

Those three validation methods are all striving to make a reliable discrimination between the best ($\check{a}$) and the second best ($\check{a}_2$) integer candidates of ambiguities, but with different considerations. For its implementation simplicity and well-functioning in practical tests, the detailed implementations of the RT are described herein as an example:

$$\text{Accept } \check{a} \text{ if } \frac{(\check{a}_2-\hat{a})^T Q_{\hat{a}}^{-1}(\check{a}_2-\hat{a})}{(\check{a}-\hat{a})^T Q_{\hat{a}}^{-1}(\check{a}-\hat{a})} \geq c \tag{3-18}$$

where c is a pre-defined threshold or the critical value that the squared norm of ambiguity residuals of the best and second best candidates should overpass to validate the integer estimation.

Regarding the determination of the critical value, a rigorous theoretical analysis of the Eq(3-18) should be done to derive the value. However, it is theoretically too complex and the computation burden is heavy [59]–[61]. Therefore, an empirical fixed value is generally taken (e.g., $c = 3$ as in [7], [62]), namely a Fixed Threshold RT (FT-RT). However, it should be pointed out that it is not the correctness of integer candidates but rather the closeness to the float value that is tested with RT [62], [63]. The popular indicator of IAR performance, the P_f can not be controlled with the FT-RT and the confidence put on the final solution should therefore be relatively low.

3.2 Problems Raised by Urban Environments

An urban environment is generally referred to an area with high density of interfering objects, such as buildings [7], [64]. Signals are more prone to blockages and reflections. As a result, severe local effects are expected such as: significant multipath delays on GNSS observations, especially on pseudoranges and Doppler measurements and NLOS signal tracking. Besides, attenuated signals are received at a lower signal carrier to noise density ratio C/N0. Consequently, cycle slips and loss of lock for carrier phase measurements are more frequent.

As aforementioned, the single-frequency PPP methodology requires longer convergence time to achieve accurate ambiguity resolution compared to RTK. What's more, the handling of frequent cycle slips can furthermore deteriorate the PPP performance. It's finally the RTK methodology chosen in this literature to explore the performance of GNSS navigation in urban environments.

4 Proposed GNSS-only Precise Positioning Algorithm

With the intention to achieve precise positioning in an urban environment, the RTK methodology has been preferred over the PPP methodology. Equipped with single-frequency receiver, the lack of accurate atmosphere correction models indeed restricts the application of the PPP methodology in a constrained area. In this section, the detailed implementations of the RTK algorithm adapted to an urban environment are provided.

In the first place, the Kalman filter is chosen as the estimation technique to take into account the dynamics of the rover and use an epoch-to-epoch geometric link for states refinement .

The RTK measurement model is subsequently presented to reflect considerations over the systematic differences between GPS and GLONASS.

Then, several pre-processing procedures of the GNSS observables are proposed in response to their vulnerabilities to outliers notably in urban area. As an example, an innovation test is implemented to further ensure the reliability of the GNSS navigation solution.

The last part is dedicated to the handling of the precise carrier phase measurements. Procedures to detect and repair cycle slips are devised to continuously benefit from the resolved ambiguities as constants. Elaborations of the integer ambiguity resolution theory are eventually provided.

4.1 Overview of Kalman Filter

4.1.1 Continuous System and Discrete System

A typical system model consists of equations describing the relationships between unknown parameters and system observables. The expected/assumed characteristics of the system observables and the unknown parameters can also be taken into account. Considering the temporal continuity, two categories are introduced: the continuous system and the discrete system. In order to keep the discussion as brief as possible, the following presentation only considers linear systems.

In a 'continuous' system, a continuous process is considered. To have an estimation of a set of parameters of interests $\boldsymbol{x}(t)$ (in case of GNSS positioning, the rover's position, velocity, clock delays, etc.), a functional relationship between the state parameters and the observables must be established. The functional model is typically given in the form:

$$\boldsymbol{y}(t) = \boldsymbol{H}(t) \cdot \boldsymbol{x}(t) + \boldsymbol{e}(t) \tag{4-1}$$

where:

- $\boldsymbol{y}(t)$ is the measurement vector at time t;
- $\boldsymbol{H}(t)$ is the system geometry matrix at time t;
- $\boldsymbol{x}(t)$ is the system state vector at time t;
- $\boldsymbol{e}(t)$ is the measurement noise vector at time t, a zero-mean Gaussian noise with correlation matrix $\boldsymbol{R}(t)$.

Typical system dynamics, when they are taken into consideration, can be represented in the following form:

$$\dot{\boldsymbol{x}}(t) = \boldsymbol{F}(t) \cdot \boldsymbol{x}(t) + \boldsymbol{G}(t) \cdot \boldsymbol{w}(t) \tag{4-2}$$

where:

- $\dot{\boldsymbol{x}}(t)$ the 'dot' represents time derivative;
- $\boldsymbol{F}(t)$ is the dynamic matrix at time t;
- $\boldsymbol{G}(t)$ is the process noise shaping matrix at time t;
- $\boldsymbol{w}(t)$ is the process driving noise at time t, a zero-mean Gaussian noise with a correlation matrix $\boldsymbol{Q}(t)$, assumed to be un-correlated with measurement noise $\boldsymbol{e}(t)$.

In a discrete system, the system is observed at discrete time sequences, which is the case of GNSS PVT. Assuming the sampling time period as $t_s = \frac{1}{f_s}$, the discrete linear system is given as:

$$\begin{aligned} \boldsymbol{Y_k} &= \boldsymbol{H_k X_k} + \boldsymbol{e_k} \\ \boldsymbol{X_k} &= \boldsymbol{\Phi_k X_{k-1}} + \boldsymbol{w_k} \end{aligned} \tag{4-3}$$

where

- $\boldsymbol{Y_k}$, $\boldsymbol{X_k}$ are respectively the vector of measurements and the state vector at epoch k with corresponding time $t_k = t_{k-1} + t_s$;
- $\boldsymbol{H_k}$ is the design/geometry matrix;
- $\boldsymbol{\Phi_k}$ is the state transition matrix from epoch $(k-1)$ to epoch k;
- $\boldsymbol{w_k}$ is the process noise at epoch k, with VC-matrix $\boldsymbol{Q_k}$.

The detailed expressions of $\boldsymbol{\Phi_k}$ and $\boldsymbol{Q_k}$ can be obtained from the following relations [37], [65]–[67]:

$$\boldsymbol{\Phi_k} = e^{\boldsymbol{F}(t_k)t_s} \approx \boldsymbol{I} + \boldsymbol{F_k} t_s + \frac{(\boldsymbol{F_k} t_s)^2}{2} \tag{4-4}$$

$$\boldsymbol{Q_k} \approx \left[\boldsymbol{\Phi_k G}(t_{k-1})\boldsymbol{Q}(t_{k-1})\boldsymbol{G}^T(t_{k-1})\boldsymbol{\Phi}_k^T + \boldsymbol{G}(t_{k-1})\boldsymbol{Q}(t_{k-1})\boldsymbol{G^T}(t_{k-1})\right] t_s/2 \tag{4-5}$$

Approximations made during the propagation interval t_s may not be rigorously correct, but reasonably acceptable when t_s is considerably small enough.

4.1.2 Kalman Filter

During the estimation with LS, only the system measurements are used, which may not take the full advantage of the whole system. Another well-known estimation technique is the Kalman filter (KF), which considers also the state dynamics.

A five-equation operating process of the KF is synthetized here. First step is to develop the properties of the predicted states

$$\widehat{\boldsymbol{X}}_{\boldsymbol{k+1|k}} = \boldsymbol{\Phi_{k+1}} \widehat{\boldsymbol{X}}_{\boldsymbol{k}} \tag{4-6}$$

$$\boldsymbol{P_{k+1|k}} = \boldsymbol{\Phi_{k+1} P_k \Phi_{k+1}^T} + \boldsymbol{Q_{k+1}} \tag{4-7}$$

where

- $\widehat{\boldsymbol{X}}_{\boldsymbol{k+1|k}}$is the states prediction at epoch $(k+1)$ given all measurements until epoch k, and
- $\boldsymbol{P_{k+1|k}}$ is VC-matrix of predicted states based on the state dynamics equation.

The next step is to refine the states prediction based on the information provided by the system observables, which is specifically the difference between predicted observables and measured observables:

$$\boldsymbol{K_{k+1}} = \boldsymbol{P_{k+1|k} H_{k+1}^T}\left[\boldsymbol{H_{k+1} P_{k+1|k} H_{k+1}^T} + \boldsymbol{R_{k+1}}\right]^{-1} \tag{4-8}$$

$$\widehat{\boldsymbol{X}}_{\boldsymbol{k+1|k+1}} = \widehat{\boldsymbol{X}}_{\boldsymbol{k+1|k}} + \boldsymbol{K}_{\boldsymbol{k+1}}(\boldsymbol{Y}_{\boldsymbol{k+1}} - \boldsymbol{H}_{\boldsymbol{k+1}}\widehat{\boldsymbol{X}}_{\boldsymbol{k+1|k}}) \tag{4-9}$$

$$\boldsymbol{P}_{\boldsymbol{k+1|k+1}} = \boldsymbol{P}_{\boldsymbol{k+1|k}} - \boldsymbol{K}_{\boldsymbol{k+1}}\boldsymbol{H}_{\boldsymbol{k+1}}\boldsymbol{P}_{\boldsymbol{k+1|k}} \tag{4-10}$$

where

- $\boldsymbol{K}_{\boldsymbol{k+1}}$ is the Kalman Gain,
- $\widehat{\boldsymbol{X}}_{\boldsymbol{k+1|k+1}}$ is the updated states estimate given all measurements until epoch $(k+1)$and
- $\boldsymbol{P}_{\boldsymbol{k+1|k+1}}$ is the VC-matrix of states.

The difference between predicted and measured observables is known as 'Innovation':

$$\boldsymbol{I}_{\boldsymbol{k+1}} = \boldsymbol{Y}_{\boldsymbol{k+1}} - \boldsymbol{H}_{\boldsymbol{k+1}}\widehat{\boldsymbol{X}}_{\boldsymbol{k+1|k}} \tag{4-11}$$

and its VC-matrix is

$$\boldsymbol{C}_{\boldsymbol{k+1}} = \boldsymbol{H}_{\boldsymbol{k+1}}\boldsymbol{P}_{\boldsymbol{k+1|k}}\boldsymbol{H}_{\boldsymbol{k+1}}^{\boldsymbol{T}} + \boldsymbol{R}_{\boldsymbol{k+1}} \tag{4-12}$$

The Kalman gain $\boldsymbol{K}_{\boldsymbol{k+1}}$ can be seen as a weighing factor striking a compromise between the weights of innovation sequences on the modification of predicted states. The innovation is a key indicator of the consistency among measurements.

4.2 Description of the Proposed RTK KF

4.2.1 Measurement Model

The accuracy performance of a receiver implementing stand-alone GNSS positioning is far from satisfaction for some constrained environment applications, especially when a low-cost receiver is considered. The high noise level, the low quality oscillator, the lack of embedded robust processing techniques can all prevent low cost receivers from providing a stable performance.

As mentioned earlier, 2 main axes are looked at to improve the low-cost receiver performance:

- To take advantage of the temporal and spatial correlation characteristics of most measurements errors (atmosphere delay, ephemeris errors, etc.), differential measurements can be used;
- The high-accuracy carrier phase measurements should be exploitable.

Measurements in a multi-constellation system need extra care given the differences among satellite systems [68]. Various types of differential measurements can be used as inputs in the KF with original GPS/GLONASS code and carrier phase measurements. Herein, to preserve the integer nature of ambiguities and control the measurement noise level at the input, the following measurement combinations are implemented [7], [18], [20]:

- GPS code measurements are single-differenced;
- GPS carrier phase measurements are double-differenced;
- GLONASS code and carrier phase measurements are single-differenced;
- Original GPS and GLONASS Doppler measurements collected by the rover receiver.

In case of a short baseline, the residual atmosphere delays (GPS/GLONASS ΔT, ΔI or GPS $\nabla\Delta T$, $\nabla\Delta I$) are reasonably small to dismiss them in measurement modeling. To avoid the confusion of atmosphere corrected and uncorrected measurements, it is recommended to apply the ionospheric correction model (i.e. the Klobuchar model) and the tropospheric correction model (i.e., the UNB3M model) before using any measurement [7]. Since reference stations do not systematically provide raw Doppler measurements, only Doppler measurements collected by the rover are used.

GPS measurements are finally modeled as:

$$\begin{cases} \Delta P_i^{GPS} = \Delta\rho_i + c\Delta dt_{ru} + \varepsilon_{\Delta P_{i,GPS}} \\ \nabla\Delta\Phi_{ij}{}^{GPS} = \nabla\Delta\rho_{ij} + \lambda_{GPS}\nabla\Delta N_{ij} + \varepsilon_{\nabla\Delta\Phi_{ij,GPS}} \\ D_i{}^{GPS} = \dot{\rho}_\iota + c\dot{dt}_r + \epsilon_{D_{i,GPS}} \end{cases} \quad (4\text{-}13)$$

where

- $\Delta\rho_i$ is the true range difference to a common satellite indexed i between the rover receiver and the reference receiver,
- Δdt_{ru} is the clock delay difference between receivers,
- $\nabla\Delta N_{ij}$, the DD GPS ambiguity with satellite indexed j as the pivot one, is conserving its integer nature, and
- $\dot{dt_r}$ is the clock bias rate of the rover receiver.

Because the GLONASS G1 signals use the FDMA, different carrier frequencies associated to the carrier phase measurements have to be taken into account. In particular, it is well known that the inter-channel biases (ICB) have to be modeled. In the present case, this model assumes that the ICB is a linear function of the channel number [19], [21], [69]. As a consequence, the GLONASS measurements are modeled as:

$$\begin{cases} \Delta P_m^{GLO} = \Delta\rho_m + c\Delta dt_{ru} + b_r + k_m b_{ICB,code} + \varepsilon_{\Delta P_{m,GLO}} \\ \Delta\Phi_m^{GLO} = \Delta\rho_m + c\Delta dt_{ru} + \lambda_m\Delta N_{m,eq} + \varepsilon_{\Delta\Phi_{m,GLO}} \\ D_m^{GLO} = \dot{\rho_m} + c\dot{dt}_r + \epsilon_{D_{m,GLO}} \end{cases} \quad (4\text{-}14)$$

where

- m is the GLONASS satellite index,
- b_r is the between-receivers code hardware bias,
- $b_{ICB,code}$ is the code ICB slope,
- $k_m \in [-7, 6]$ is the GLONASS frequency number,
- $\Delta N_{m,eq}$ is the equivalent ambiguity term consisting of the true integer GLONASS SD ambiguity ΔN_m and the phase ICBs $\Delta b_{ru,\Phi_{m,GLO}}$. The explicit relation is $\lambda_m\Delta N_{m,eq} = \lambda_m\Delta N_m + \Delta b_{ru,\Phi_{m,GLO}}$.

The presence of the phase ICBs makes the integer nature of ΔN_m no longer true for the combination term $\Delta N_{m,eq}$. Due to the float nature of the equivalent GLONASS SD ambiguity $\Delta N_{m,eq}$, different from GPS, a formation of GLONASS DD ambiguities with the pre-calibrated phase ICB information is necessary before passing to the Integer Ambiguity Resolution (IAR) step. The IAR process is the implementation of integer-nature conditions on GNSS DD ambiguities, and thus improve the estimation of other states, i.e. the PVT information.

4.2.2 Linearization Process

The KF theory exposed earlier assumes a linear system while clearly a non-linear relationship exists between the RTK measurement model and the rover's parameters. Therefore, a linearization needs to be done to estimate the rover's station, using the so-called extended KF.

According to the formation of differential measurements, the term $\Delta\rho^i$ describes the range difference between the user receiver and the station receiver from a common satellite indexed by i. It can be linearized around a predicted position of the rover:

$$\Delta\rho^i = \rho_u^i - \rho_r^i = \rho_{u_0}^i - \rho_r^i - \boldsymbol{e_0^i}.(\boldsymbol{X_u} - \boldsymbol{X_{u,0}}) \quad (4\text{-}15)$$

where

- $\boldsymbol{X_u}$ is the estimated position of the rover;
- $\boldsymbol{X_{u,0}} = [x_0, y_0, z_0]^{\boldsymbol{T}}$ is the predicted position of the rover;
- $\boldsymbol{e_0^i}$ is the predicted LOS unit vector along the direction pointing from the approximated user position to the satellite i, $\boldsymbol{e_0^i} = \frac{\mathbf{1}}{\|\boldsymbol{X^i - X_0}\|}\left(x^i - x_0, y^i - y_0, z^i - z_0\right)$ with the satellite position in orbit expressed as $\boldsymbol{X^i} = \left[x^i, y^i, z^i\right]^{\boldsymbol{T}}$.

Therefore, the measurements containing the term $\Delta\rho$ are corrected as follows to obtain a linear system of the rover's position deviation with respect to assumed position. Take the GPS SD pseudorange as an example:

$$\Delta P_{i,corrected}^{GPS} = \Delta P_i^{GPS} - (\rho_{u_0}^i - \rho_r^i) - \boldsymbol{e_0^i X_{u,0}} \tag{4-16}$$

As for the DD range $\nabla\Delta\rho_{ji}$, the difference between $\Delta\rho^i$ and $\Delta\rho^j$, it can be linearized as

$$\nabla\Delta\rho_{ji} = \Delta\rho^i - \Delta\rho^j = \rho_{u_0}^i - \rho_r^i - \rho_{u_0}^j + \rho_r^j - (\boldsymbol{e_0^i} - \boldsymbol{e_0^j}).\left(\boldsymbol{X_u} - \boldsymbol{X_{u,0}}\right) \tag{4-17}$$

The Doppler measurement collected on the rover side is reflecting the rate of the range variation and the clock drift. The rate of the range variation $\dot{\rho}_\iota$ describes the relative motion between the satellite and the rover and can thus be modelled as:

$$\dot{\rho}_\iota = \boldsymbol{e_0^i V^i} - \boldsymbol{e_0^i V_u} \tag{4-18}$$

where

- $\boldsymbol{V^i} = \left[v_x^i, v_y^i, v_z^i\right]^{\boldsymbol{T}}$ is the satellite velocity calculated based on the broadcast ephemeris, and
- $\boldsymbol{V_u} = \left[v_x, v_y, v_z\right]^{\boldsymbol{T}}$ is the rover's velocity.

Therefore, to remove the Doppler shift due to the satellite's motion, the Doppler measurement is corrected by

$$D_{i,corrected} = D_i - \boldsymbol{e_0^i V^i} \tag{4-19}$$

The corrected Doppler measurement is thus directly in a linear relationship with the rover's velocity and receiver clock drift, by neglecting typically smaller atmospheric delay rate.

4.2.3 Description of the State Vector

The goal of GNSS positioning is the estimation of the rover's position and velocity. Nevertheless, the previous analysis of the proposed RTK measurement modeling has showed the presence of other additional parameters to be estimated. In view to obtain a precise positioning, these additional parameters also need be carefully handled.

$$\boldsymbol{X_{GNSS}} = \left(\boldsymbol{X_{PVA}}; c * \Delta dt_{ru};\ c * \Delta\dot{dt}_{ru}; c * \dot{dt}_r; \boldsymbol{\nabla\Delta N_{GPS}}; \boldsymbol{\Delta N_{GLO,eq}}; b_r; b_{ICB,code}\right)$$

The full GNSS state vector is thus containing:

1. $\boldsymbol{X_{PVA}}$: The position $\boldsymbol{X_u}$, the velocity $\boldsymbol{V_u}$, and the acceleration $\boldsymbol{A_u}$ (PVA) of the rover.

Sometimes, especially in a low-dynamic application, the consideration of the acceleration is omitted for simplicity. However, this is not the case in the application of interest of this PhD, which includes ground

vehicle. Along with the position and the velocity, it entails appropriate modeling of the rover's acceleration. The Constant-Acceleration Model [37], assuming a random walk to account for the acceleration, is applied to describe the relations among PVA states. The corresponding PVA state transition matrix $\boldsymbol{\Phi_{PVA}}$ and their process noise VC-matrix $\mathbf{Q_{PVA}}$ in one spatial dimension (e.g., *e*-axis of *n*-frame) are:

$$\boldsymbol{\Phi_{PVA}} = \begin{bmatrix} 1 & t_s & \frac{1}{2}t_s^2 \\ 0 & 1 & t_s \\ 0 & 0 & 1 \end{bmatrix}, \mathbf{Q_{PVA}} = \begin{bmatrix} \frac{1}{20}t_s^5 & \frac{1}{8}t_s^4 & \frac{1}{6}t_s^3 \\ \frac{1}{8}t_s^4 & \frac{1}{3}t_s^3 & \frac{1}{2}t_s^2 \\ \frac{1}{6}t_s^3 & \frac{1}{2}t_s^2 & t_s \end{bmatrix} \sigma_e^2$$

where

- t_s is the system update step, i.e. 1 second,
- σ_e^2 is the vehicle acceleration variance in *e*-axis.

There is no exact way to fit the accelerations into a best optimal random process for the Kalman filter, except for taking other external measurements. However, an improved performance is expected compared to the simpler PV modeling.

The case of interest of this thesis is ground car navigation whose vertical motion is constrained. Hence, the process noise level associated to the up direction has been chosen lower compared to the east and north directions. Recommendations of the acceleration variance values in ENU *n*-frame are herein adopted, but with slight modifications $[\sigma_e^2, \sigma_n^2, \sigma_u^2] = [0.7, 0.7, 0.2]((\mathrm{m/s^2})^2)$ [7]. The original vertical acceleration variance of 0.1 $((\mathrm{m/s^2})^2)$ turns out to be a little optimistic by studying the reference trajectory. The VC-matrix of the acceleration process noise applied in the *e*-frame is then determined by a transformation following noise propagation laws:

$$\mathbf{Q_{A-XYZ}} = (\boldsymbol{C_e^n})' \begin{bmatrix} \sigma_e^2 & 0 & 0 \\ 0 & \sigma_n^2 & 0 \\ 0 & 0 & \sigma_u^2 \end{bmatrix} \boldsymbol{C_e^n}$$

where the coordinate frame transformation matrix from *e*-frame to *n*-frame is described by the matrix

$$\boldsymbol{C_e^n} = \begin{bmatrix} -\sin\lambda & cos\lambda & 0 \\ -sin\varphi cos\lambda & -sin\varphi sin\lambda & cos\varphi \\ cos\varphi cos\lambda & cos\varphi sin\lambda & sin\varphi \end{bmatrix}$$

Which depends on the vehicle geodetic coordinates (latitude φ, longitude λ and height h).

2. $[\Delta dt_{ru};\ \Delta \dot{dt}_{ru}]$: <u>The SD clock delay between the receivers and its drift over time.</u>

Since the GPS pseudorange measurements, the GLONASS pseudorange and carrier phase measurements are all single differenced, a SD clock delay term emerges and, together with its drift, needs to be estimated. Generally, a two-parameter model of clock delay and clock drift is used to describe the receiver's clock and the satellite's clock [37], [70]. The state transition matrix and the VC-matrix of the process noise are depicted by

$$\boldsymbol{\Phi_{clk}} = \begin{bmatrix} 1 & t_s \\ 0 & 1 \end{bmatrix}, \boldsymbol{Q_{clk}} = \begin{bmatrix} \frac{h_0}{2}t_s + 2h_{-1}t_s^2 + \frac{2}{3}\pi^2 h_{-2}t_s^3 & h_{-1}t_s + \pi^2 h_{-2}{t_s}^2 \\ h_{-1}t_s + \pi^2 h_{-2}{t_s}^2 & \frac{h_0}{2t_s} + 4h_{-1} + \frac{8}{3}\pi^2 h_{-2}t_s \end{bmatrix}$$

with h_0, h_{-1}, h_{-2} are parameters related to the clock quality performance.

In the following table are the typical values for various types of receiver clock [37]. For example, a temperature compensated crystal oscillator (TCXO)-type oscillator is incorporated in the Ublox receiver that will be used for testing later one, while a more stable ovenized crystal oscillator (OCXO)-type oscillator is used by the TLSE Trimble NetR9 receiver, an IGS reference station.

Table 4-1. Parameters for Clock Modeling

Types / Parameters	TCXO*	OCXO*
$h_0(s)$	2e-19	2e-25
$h_{-1}(rad)$	7e-21	7e-25
$h_{-2}(s^{-1})$	2e-20	6e-25

For the SD clock delay, the state transition matrix stays the same while the VC-matrix is calculated by the following matrix products:

$$\boldsymbol{Q_{SD_{clk}}} = \begin{bmatrix} 1 & 0 & -1 & 0 \\ 0 & 1 & 0 & -1 \end{bmatrix} \begin{bmatrix} Q_{clk_u} & 0 \\ 0 & Q_{clk_r} \end{bmatrix} \begin{bmatrix} 1 & 0 \\ 0 & 1 \\ -1 & 0 \\ 0 & -1 \end{bmatrix} = \boldsymbol{Q_{clk_u}} + \boldsymbol{Q_{clk_r}}$$

3. $\dot{dt_r}$: The Doppler clock drift of the rover's receiver.

Different from the SD clock drift, the Doppler clock drift is only dependent on the rover's clock. Therefore, a third clock-related term is required, with proper covariance value determined by the clock modeling parameters in Table 4-1. Confronting the potential computational singularity, all clock-related states are transformed into range delays by multiplying the speed of light in vacuum c(m/s).

4. $[\boldsymbol{\nabla\Delta N_{GPS}}; \boldsymbol{\Delta N_{GLO,eq}}]$: The integer GPS DD ambiguities and the non-integer GLONASS SD ambiguities.

According to the state property, ambiguities are estimated as constant values on condition that cycle slips are absent. Otherwise the monitoring and resolution process is implemented separately beyond the main navigation KF.

5. $[b_r; b_{ICB,code}]$: The two parameters used to model GLONASS code ICB biases: the slope and the offset.

Similarly, the slope and offset of GLONASS ICB biases are estimated as constant values. The VC-matrix describing their stability are provided in Section 4.3.3.

To conclude, the design matrix $\boldsymbol{H_{GNSS}}$, describing the relation between the GNSS measurements model $\boldsymbol{Y_{GNSS}}$ and the whole state vector $\boldsymbol{X_{GNSS}}$, is thus summarized as:

$$\mathbf{H_{GNSS}} = \begin{bmatrix} \boldsymbol{G}^{PVA}_{\Delta \mathrm{P_{GPS}}} & \boldsymbol{E}_{n_1\times 3} & 0_{n_1\times n_3} & 0_{n_1\times n_4} & 0_{n_1\times 2} \\ \boldsymbol{G}^{PVA}_{\Delta \mathrm{P_{GLO}}} & \boldsymbol{E}_{n_2\times 3} & 0_{n_2\times n_3} & 0_{n_2\times n_4} & \boldsymbol{G}^{ICB}_{\Delta \mathrm{P_{GLO}}} \\ \boldsymbol{G}^{PVA}_{\nabla\Delta\Phi_{\mathrm{GPS}}} & 0_{n_3\times 3} & \boldsymbol{\lambda_{n_3\times n_3}} & 0_{n_3\times n_4} & 0_{n_3\times 2} \\ \boldsymbol{G}^{PVA}_{\Delta\Phi_{\mathrm{GLO}}} & \boldsymbol{E}_{n_4\times 3} & 0_{n_4\times n_3} & \boldsymbol{\lambda'_{n_4\times n_4}} & 0_{n_4\times 2} \\ \boldsymbol{G}^{PVA}_{D_{\mathrm{GPS}}} & \boldsymbol{E}'_{n_5\times 3} & 0_{n_5\times n_3} & 0_{n_5\times n_4} & 0_{n_5\times 2} \\ \boldsymbol{G}^{PVA}_{\mathrm{D_{GLO}}} & \boldsymbol{E}'_{n_6\times 3} & 0_{n_6\times n_3} & 0_{n_6\times n_4} & 0_{n_6\times 2} \end{bmatrix}$$

Where

- $\boldsymbol{Y_{GNSS}} = [\boldsymbol{\Delta P_{GPS}}; \boldsymbol{\Delta P_{GLO}}; \boldsymbol{\nabla\Delta\Phi_{GPS}}; \Delta\boldsymbol{\Phi_{GLO}};\ \boldsymbol{D_{GPS}}; \boldsymbol{D_{GLO}}]$ is the whole GNSS measurements vector, with n_1 the length of SD GPS pseudoranges $\boldsymbol{\Delta P_{GPS}}$, n_2 the length of SD GLONASS pseudoranges $\boldsymbol{\Delta P_{GLO}}$, n_3 the length of DD GPS carrier phases $\boldsymbol{\nabla\Delta\Phi_{GPS}}$, n_4 the length of SD GLONASS carrier phases $\Delta\boldsymbol{\Phi_{GLO}}$, n_5 the length of GPS Doppler observables $\boldsymbol{D_{GPS}}$, and n_6 the length of GLONASS Doppler observables $\boldsymbol{D_{GLO}}$;
- $\boldsymbol{G}^{PVA}_{\Delta \mathrm{P_{GPS}}} = \begin{bmatrix} -\boldsymbol{e_1} & 0_{1\times 3} & 0_{1\times 3} \\ \vdots & \vdots & \vdots \\ -\boldsymbol{e_{n_1}} & 0_{1\times 3} & 0_{1\times 3} \end{bmatrix}$ is a design matrix between $\boldsymbol{\Delta P_{GPS}}$ and $\boldsymbol{X_{PVA}}$ with $\boldsymbol{e_{i\in[1,n_1]}}$ the LOS unit vector between the rover and the GPS satellite i, $0_{1\times 3} = [0\ 0\ 0]$;
- $\boldsymbol{G}^{PVA}_{\Delta \mathrm{P_{GLO}}} = \begin{bmatrix} -\boldsymbol{e_1} & 0_{1\times 3} & 0_{1\times 3} \\ \vdots & \vdots & \vdots \\ -\boldsymbol{e_{n_2}} & 0_{1\times 3} & 0_{1\times 3} \end{bmatrix}$, is a design matrix between $\boldsymbol{\Delta P_{GLO}}$ and $\boldsymbol{X_{PVA}}$ with $\boldsymbol{e_{i\in[1,n_2]}}$ the LOS unit vector between the rover and the GLONASS satellite i;
- $\boldsymbol{G}^{ICB}_{\Delta \mathrm{P_{GLO}}} = \begin{bmatrix} 1 & k_1 \\ \vdots & \vdots \\ 1 & k_{n_2} \end{bmatrix}$ is a design matrix between $\boldsymbol{\Delta P_{GLO}}$ and $[b_r; b_{ICB,code}]$;
- $\boldsymbol{G}^{PVA}_{\nabla\Delta\Phi_{\mathrm{GPS}}} = \begin{bmatrix} -\Delta\boldsymbol{e_1} & 0_{1\times 3} & 0_{1\times 3} \\ \vdots & \vdots & \vdots \\ -\Delta\boldsymbol{e_{n_3}} & 0_{1\times 3} & 0_{1\times 3} \end{bmatrix}$, is a design matrix between $\boldsymbol{\nabla\Delta\Phi_{GPS}}$ and $\boldsymbol{X_{PVA}}$ with $\Delta\boldsymbol{e_{i\in[1,n_3]}} = \mathbf{e^i} - \mathbf{e^p}$ the LOS unit vector difference between GPS satellite i and the carrier phase pivot satellite p, $\boldsymbol{\lambda_{n_3\times n_3}} = \lambda_{GPS}\boldsymbol{I_{n_3\times n_3}}$; ($\boldsymbol{I_{n_3\times n_3}}$ is an identity matrix)
- $\boldsymbol{G}^{\boldsymbol{PVA}}_{\Delta\boldsymbol{\Phi}_{\mathbf{GLO}}} = \begin{bmatrix} -\boldsymbol{e_1} & 0_{1\times 3} & 0_{1\times 3} \\ \vdots & \vdots & \vdots \\ -\boldsymbol{e_{n_4}} & 0_{1\times 3} & 0_{1\times 3} \end{bmatrix}$,is a design matrix between $\boldsymbol{\Delta\Phi_{GLO}}$ and $\boldsymbol{X_{PVA}}$ with $\boldsymbol{e_{i\in[1,n_4]}}$, $\boldsymbol{\lambda'_{n_4\times n_4}} = diag([\lambda_1 \quad \cdots \quad \lambda_{n_4}])$ is a diagonal matrix with diagonal elements in vector $[\lambda_1 \quad \cdots \quad \lambda_{n_4}]$;
- $\boldsymbol{G}^{PVA}_{D_{\mathrm{GPS}}} = \begin{bmatrix} 0_{1\times 3} & -\boldsymbol{e_1} & 0_{1\times 3} \\ \vdots & \vdots & \vdots \\ 0_{1\times 3} & -\boldsymbol{e_{n_5}} & 0_{1\times 3} \end{bmatrix}$ is a design matrix between $\boldsymbol{D_{GPS}}$ and $\boldsymbol{X_{PVA}}$ with $\boldsymbol{e_{i\in[1,n_5]}}$ the LOS unit vector between the rover and the GPS Doppler satellite i;
- $\boldsymbol{G}^{PVA}_{\mathrm{D_{GLO}}} = \begin{bmatrix} 0_{1\times 3} & -\boldsymbol{e_1} & 0_{1\times 3} \\ \vdots & \vdots & \vdots \\ 0_{1\times 3} & -\boldsymbol{e_{n_6}} & 0_{1\times 3} \end{bmatrix}$ is a design matrix between $\boldsymbol{D_{GLO}}$ and $\boldsymbol{X_{PVA}}$ with $\boldsymbol{e_{i\in[1,n_6]}}$ the LOS unit vector between the rover and the GLONASS Doppler satellite i;
- $\boldsymbol{E}_{\blacksquare\times 3} = \begin{bmatrix} 1 & 0 & 0 \\ \vdots & \vdots & \vdots \\ 1 & 0 & 0 \end{bmatrix}$, $\boldsymbol{E'}_{\blacksquare\times 3} = \begin{bmatrix} 0 & 0 & 1 \\ \vdots & \vdots & \vdots \\ 0 & 0 & 1 \end{bmatrix}$

4.2.4 Motion Constraint

With a view to strengthen the performance, any constraint based on the basic knowledge of the vehicle motion can be applied in KF. The Non-Holonomic Constraint (NHC) describes the fact that generally the lateral and vertical velocities are negligible compared to the along-track velocity. This hypothesis, however, does not hold if the vehicle is sliding laterally or jumping. In the case of a GNSS-only system, the NHC provides a virtual velocity observation that the vertical velocity of the vehicle is null. The standard deviation of this constraint is set empirically to [7], [23]:

$$\sigma_{NHC} = max(1e-2, 0.04 * speed) \tag{4-20}$$

4.3 Processing of Signals

As mentioned earlier, the positioning performance of a satellite system highly depends on the DOP and the UERE. The vulnerability of the GNSS receiver signal processing with respect to several error sources, particularly in an urban environment makes the pre-processing of measurements necessary. For instance, outliers need be eliminated via the pre-processing steps. In this section, three schemes to restrain or eliminate the measurement outliers are hence introduced.

4.3.1 Elevation and C/N$_0$ Masks

It is first essential to ensure sufficient GNSS measurements quality is kept. To remove the measurements that are most likely severely degraded by multipath or NLOS effects, an a-priori elevation mask and C/N$_0$ mask can be applied for all GNSS measurements. This step is necessary because the models for the corresponding measurements might be quite erroneous and might lead to large estimation errors or large under- or over-assessment of the position quality.

It is widely agreed that the higher the satellite elevation and received C/N$_0$, the less noisy the measurements. The choice of the masks values is a compromise between a strong geometry and high-quality measurements. Different value pairs have been tested (i.e., elevation mask varying from 5 degrees to 20 degrees with an interval of 5 degrees, C/N$_0$ mask taking values between 25 dB.Hz. and 40 dB.Hz. with an increasing step of 3) and an interesting compromise seems to be an elevation mask of 10 degrees and a C/N$_0$ mask of 35 dB.Hz.

4.3.2 Measurement Weighting Scheme

To reflect the differences in accuracy among the code measurements, the carrier phase measurements and the Doppler measurements, different C/N$_0$-related weighting algorithms based on practical data study have been proposed in [71].

Code Measurements

An empirical model for the code measurements is expressed as:

$$\sigma_P^2 = a + b * 10^{\frac{\left(-\frac{C}{N_0}\right)}{10}} \tag{4-21}$$

with

- $\frac{C}{N_0}$ the signal to noise density value in unit dB.Hz,
- σ_P^2 the variance of code measurements, and
- a, b empirical parameters.

The following values are extracted from [7]:

- GPS code measurements:
  - $a = 1$ and $b = 281^2$ are chosen for rural and sub-urban environments, and
  - $a = -1.5$ and $b = 731^2$ are selected for urban environments.
- GLONASS code measurements are down-weighted by a scale of 1.3 (multiplying 1.69 for variance) compared to GPS code measurement.

An illustration of the relationship between the GPS SD code residuals and the signal strength in a dynamic mode is provided in Figure 4-1. The red curve represents the theoretical standard-deviation values. The collection of data is done with the same equipment used later on for the tests in real conditions.

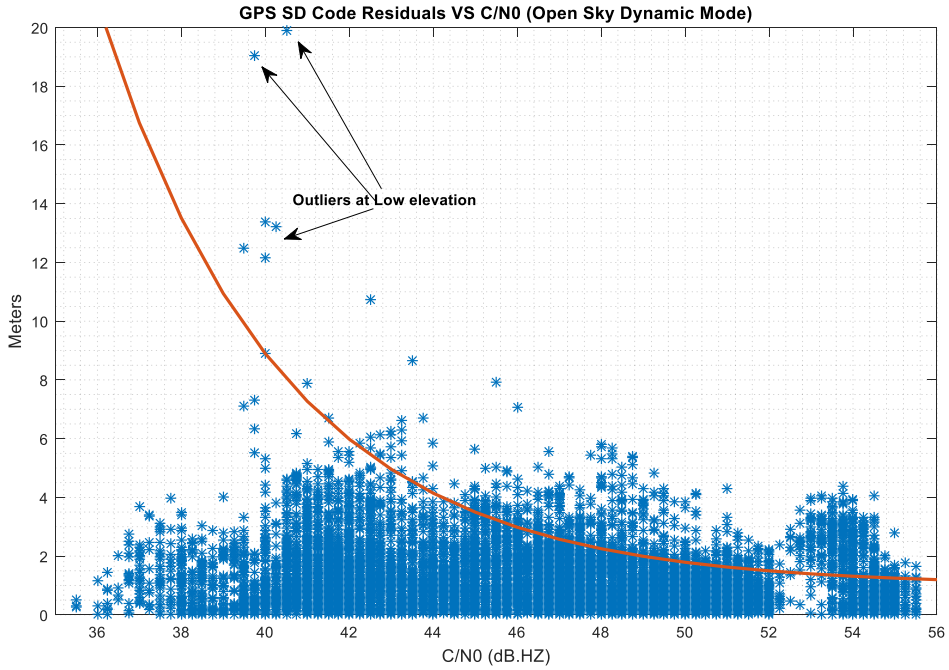

Figure 4-1. The Relation between GPS SD Code Residuals Level and C/N0 in a Dynamic Open-sky Environment

Doppler Measurements

As for the Doppler measurements, the standard deviations seem to be influenced by both vehicle speed and signal strength $\frac{C}{N_0}$. An empirical look-up table was derived in [7] and is used in the frame of this PhD:

σ_D (m/s)	$\frac{C}{N_0}$ (dB.Hz)						
Speed (m/s)	[30, 33]	[33, 36[	[36, 39[	[39, 42[	[42, 45[	[45, 48[	[48, 51]
[0, 3]	0.53	0.43	0.28	0.21	0.13	0.09	0.07
]3, 6]	2.04	1.61	1.08	0.71	0.55	0.32	0.24
]6, 9]	2.37	2.00	1.43	0.86	0.53	0.29	0.18
]9, 12]	3.08	2.33	1.60	1.06	0.99	0.28	0.22
]12, 15]	2.54	1.87	1.25	0.83	0.54	0.27	0.17
]15, 18]	1.26	1.36	1.48	0.80	0.53	0.27	0.15
]18, 21]	1.37	1.29	0.87	0.55	0.44	0.25	0.16
]21, 24]	1.44	1.25	1.09	0.73	0.37	0.26	0.16
]24, 27]	1.33	0.90	0.58	0.47	0.31	0.26	0.11
]27, 30]	1.01	0.92	0.61	0.53	0.31	0.31	0.14

Figure 4-2. Weighting scheme of Doppler measurements

Carrier Phase Measurement

A weighting scheme based on $\frac{C}{N_0}$ is proposed in [72]:

$$\sigma_\Phi^2 = 10^{\frac{\frac{C}{N_{zenith}} - \frac{C}{N_0}}{10}} \sigma^2 \tag{4-22}$$

where

- $\frac{C}{N_{zenith}}$ equals 52 dB.Hz,
- $\sigma^2 = 1e^{-4}[m^2]$ is the variance of the observation at the zenith.

4.3.3 GLONASS Inter-channel Biases

In the case of the GPS signals based on CDMA, the SD carrier phase hardware delays is common for GPS satellites and can be mitigated using DD carrier phase measurements. This makes it easier to resolve the GPS DD ambiguities as integers and thus to access precise positioning.

However, the dependence of GLONASS SD carrier phase hardware delays on the signal frequency makes the resolution of GLONASS SD ambiguities as integers directly from the float KF estimation impossible unless a fine calibration of these biases is done. The notion of Inter-channel biases (ICBs) is brought up to describe the SD hardware delays.

Practical studies have shown certain characteristics of the ICBs such as [73], [74]:

- no obvious pattern of the pseudorange ICBs magnitude as a function of the frequency number is observed, however, there is one on carrier phase ICBs;
- the biases are quite independent of receivers pair to pair;
- the pseudo-range and phase ICBs are all quite stable in time (at least on a monthly scale), which leaves a possibility of pre-calibration.

However, all these previous studies are using high-quality receivers [19], [75]. Among them, some are directly based on IGN stations [21], [22], [76], [77]. In this section, static data collected with a low-cost Ublox M8T receiver (the one used later on for testing) is used for the study of ICBs and show the possibility of calibration. Besides, there is no easy way to separate the GPS SD code hardware delays $\Delta b_{ru,P_{GPS}}$ from the true clock bias $c\Delta dt$ and an equivalent term $c\Delta dt_{eq}$ is thus preferably used instead. To conduct the analysis of ICBs, the GPS and GLONASS measurements can be re-modeled as following:

$$\begin{cases} \Delta P_i^{GPS} = \Delta\rho_i + c\Delta dt_{eq} + \varepsilon_{\Delta P_i} \\ \nabla\Delta\Phi_{ij}^{GPS} = \nabla\Delta\rho_{ij} + \lambda_{GPS}\nabla\Delta N_{ij} + \varepsilon_{\nabla\Delta\Phi_{ij}} \end{cases} \quad (4\text{-}23)$$

$$\begin{cases} \Delta P_m^{GLO} = \Delta\rho_m + c\Delta dt_{eq} + (\Delta_{ru,P_{m,GLO}} - \Delta b_{ru,P_{GPS}}) + \varepsilon_{\Delta P_m} \\ \Delta\Phi_m^{GLO} = \Delta\rho_m + c\Delta dt_{eq} + \lambda_m\Delta N_m + (\Delta b_{ru,\Phi_{m,GLO}} - \Delta b_{ru,P_{GPS}}) + \varepsilon_{\Delta\Phi_m} \end{cases} \quad (4\text{-}24)$$

with

- $\Delta b_{ru,P_{GPS}}$, the GPS SD code hardware delays, common between all GPS satellites;
- $\Delta \mathrm{b}_{\mathrm{ru,P_{m,GLO}}}$, the GLONASS SD code hardware delays;
- $\Delta \mathrm{N_m}$, the true integer GLONASS SD ambiguity,
- $\Delta b_{ru,\Phi_{m,GLO}}$, the GLONASS SD carrier phase hardware delays.

With the described modeling, all single-differential measurements are sharing the common clock bias term Δdt_{eq}.

Code ICBs

Two static data collections of 3 days have been performed using the low-cost Ublox M8T receiver for the calibration of $b_{P_m} = (\Delta b_{ru,P_{m,GLO}} - \Delta b_{ru,P_{GPS}})$, using the previous measurement model. b_{P_m} is representing the over-all effect of code hardware delays and ICBs. The station TLSE equipped with TRIMBLE NetR9 receiver and TRIMBLE TRM59800 antenna, maintained by the Centre National d'Etudes Spatiales (CNES), is chosen as the reference station. The position of the Ublox receiver is previously determined by applying GPS-only static-mode RTK.

Stability over meters of $b_{P_m} = (\Delta b_{ru,P_{m,GLO}} - \Delta b_{ru,P_{GPS}})$ over days is observed. The calibration result is presented in Figure 4-3. As expected, there is no clear relationship between the frequency numbers and the bias magnitudes. The peak-to-peak bias can actually reach up to 9 meters. Based on the current literature, even though the proposed algorithm uses pre-calibration, a two-state model $(b_r, b_{ICB,code})$ (modeling the residual code ICBs as a linear function of the GLONASS frequency index) has been implemented, as previously presented in Eq(4-14). These terms are expected to absorb the residual ICBs after the pre-calibration.

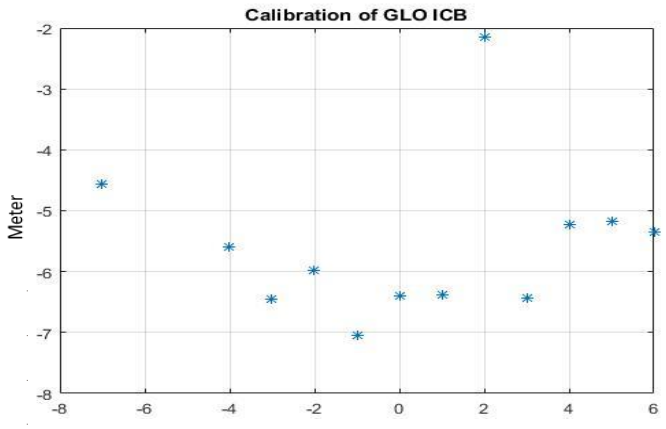

Figure 4-3. Estimated GLONASS Pseudorange ICBs Depending on Frequency Numbers for a Baseline between TLSE and the Ublox M8T Receiver

Carrier phase ICBs

According to present studies, the overall differential hardware bias $\Delta b_{ru,\Phi_{m,GLO}}$ can be further expressed as a summation of a common differential hardware delay $\Delta b_{ru,\Delta\Phi_{0,GLO}}$, which is also the bias at frequency number zero, and an inter-frequency carrier phase bias $b_{m,\Delta\Phi} = k_m b_{slope,\Phi}$ [21], [78]:

$$\Delta b_{ru,\Phi_{m,GLO}} = \Delta b_{ru,\Phi_{0,GLO}} + b_{m,\Delta\Phi} = \Delta b_{ru,\Phi_{0,GLO}} + k_m b_{slope,\Phi}$$

with $b_{slope,\Phi}$ the GLONASS carrier phase ICB slope, stable in terms of months.

The linear relationship between the GLONASS carrier phase ICB $b_{m,\Delta\Phi}$ and the frequency number k_m suggests two calibration algorithms of the carrier phase bias slope $b_{slope,\Delta\Phi}$. The first one is to absorb hardware delays in float GLONASS SD ambiguity estimates, and the second one is to isolate the slope by double-differencing GLONASS ambiguity estimates. Via the Kalman filter, unlike the integer GPS DD ambiguities, estimates of GLONASS SD ambiguities include a secondary float term:

$$\Delta\widehat{N}_m = \Delta N_m + \frac{\Delta b_{ru,\Phi_{m,GLO}} - \Delta b_{ru,P_{GPS}}}{\lambda_m} + \epsilon_{\Delta\widehat{N}_m} \tag{4-25}$$

A common equivalent clock bias term is herein used among GPS and GLONASS SD observables. Therefore, the presence of the second term in the right hand of the Eq(4-25) stops the integer resolution of GLONASS SD ambiguities.

To achieve the integer resolution of GLONASS ambiguities and isolate the slope $b_{slope,\Phi}$, DD ambiguities are formed as below with q the index of the reference satellite:

$$\begin{aligned}
\Delta\widehat{N}_m - \Delta\widehat{N}_q &= \nabla\Delta N_{mq} + \frac{(\Delta b_{ru,\Phi_{m,GLO}} - \Delta b_{ru,P_{GPS}})}{\lambda_m} - \frac{(\Delta b_{ru,\Phi_{q,GLO}} - \Delta b_{ru,P_{GPS}})}{\lambda_q} + \epsilon_{\nabla\Delta\widehat{N}_m} \\
&= \nabla\Delta N_{mq} - \frac{(\lambda_m - \lambda_q)}{\lambda_m\lambda_q}\left(\Delta b_{ru,P_{GPS}} - \Delta b_{ru,\Phi_{GLO}}\right) + \frac{b_{m,\Delta\Phi}}{\lambda_m} - \frac{b_{q,\Delta\Phi}}{\lambda_q} + \epsilon_{\nabla\Delta\widehat{N}_m} \\
&= \nabla\Delta N_{mq} + (k_m - k_q)\frac{(\Delta b_{ru,P_{GPS}} - \Delta b_{ru,\Phi_{GLO}} + b_{m,\Delta\Phi})}{\Delta\lambda_{G1}} + (k_m - k_q)\frac{b_{slope,\Phi}}{\lambda_q} + \epsilon_{\nabla\Delta\widehat{N}_m} \\
&\approx \nabla\Delta N_{mq} + (k_m - k_q)\frac{b_{slope,\Phi}}{\lambda_q} + \epsilon_{\nabla\Delta\widehat{N}_m}
\end{aligned} \tag{4-26}$$

with $\Delta\lambda_{G1} = \frac{c}{\Delta f_{G1}} = 532.9644\ m$, the wavelength corresponding to the GLONASS G1 slot frequency. The approximation is accurate to a tenth-of-millimeter level.

Practically, static data between the Ublox receiver and the TLSE station was previously collected for the calibration. In order to increase the accuracy, float SD GLONASS ambiguities are estimated with the position of the user receiver known. Closest integers are finally removed from GLONASS DD ambiguity estimates $(\Delta\widehat{N}_m - \Delta\widehat{N}_q)$. According to the Eq(4-26) what's remained is the $(k_m - k_q)\frac{b_{slope,\Phi}}{\lambda_q}$ modulo one cycle. The relationship between the remaining residual cycles and their associated GLONASS DD frequency number would tell the value of $b_{slope,\Phi}$. This methodology has been validated considering only IGN stations as in [7]. Nevertheless, it is only recommended for the calibration of the carrier phase ICB among high-quality receivers. The reason is that besides hardware delays, all residual carrier phase observable noises have been absorbed in float SD ambiguity estimates.

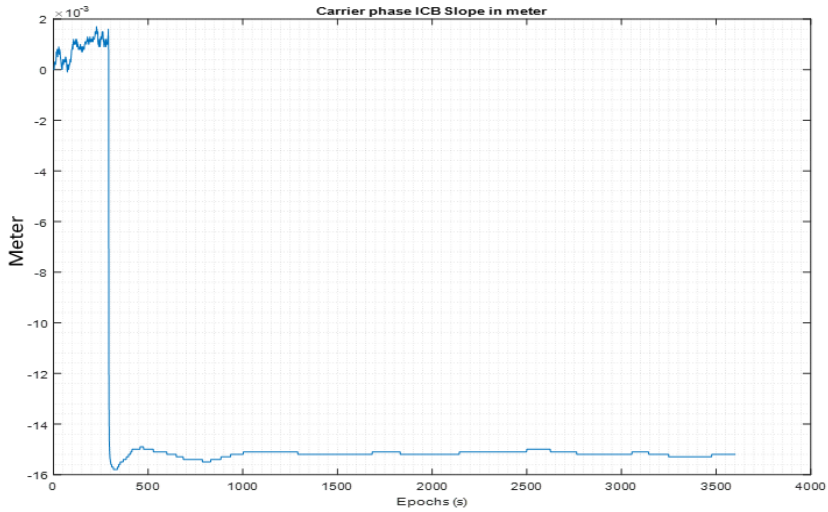

Figure 4-4. Calibration of GLONASS Carrier Phase ICBs Slope [in meter] for a Baseline between TLSE and the Ublox M8T Receiver

Regarding the higher observable noise level of the Ublox receiver, the second calibration method is preferable that a continuous estimation of the slope $b_{slope,\Delta\Phi}$ is performed. DD ambiguities are fixed through the fundamental IAR combination (LAMBDA+FT-RT). The final calibration value of $b_{slope,\Delta\Phi} = -0.0155$ [m] is obtained as illustrated in Figure 4-4. At the beginning, the ICBs slope is initialized and estimated as a float along with other ambiguity states. Attempts to achieve IAR is continuously done and the value of $b_{slope,\Delta\Phi}$ is adjusted and fixed after the IAR succeeds.

4.4 Implementation of Innovation Test

In a constrained environment, GNSS measurements are more affected by non-Gaussian error sources (e.g., NLOS, multipath) [71]. The detection of blunders is thus particularly necessary to ensure a robust PVT solution [67]. Besides the a priori GNSS measurement selection algorithms in Section 4.3.1, another fault detection and exclusion scheme is herein applied based on the KF innovations to handle potential outliers: the innovation test. This detection scheme takes advantage of the system consistency and redundancy considering a priori knowledge of the statistical distribution that the KF innovations in the fault-free case should follow. The basic implementation steps of the innovation test: Detection and Identification, are detailed in this section.

1. Detection

For the current epoch $(k+1)$, the KF innovation vector with p entries $\widetilde{\boldsymbol{Y}}_{\boldsymbol{k+1}} \epsilon \mathbb{R}^p$ is defined as

$$\widetilde{\boldsymbol{Y}}_{\boldsymbol{k+1}} = \boldsymbol{Y}_{\boldsymbol{k+1}} - \widehat{\boldsymbol{Y}}_{\boldsymbol{k+1}} = \boldsymbol{Y}_{\boldsymbol{k+1}} - \boldsymbol{H}_{\boldsymbol{k+1}} \widehat{\boldsymbol{X}}_{\boldsymbol{k+1|k}}$$

and its VC-matrix is

$$\boldsymbol{C}_{\boldsymbol{k+1}} = \boldsymbol{H}_{\boldsymbol{k+1}} \boldsymbol{P}_{\boldsymbol{k+1|k}} \boldsymbol{H}_{\boldsymbol{k+1}}^{\boldsymbol{T}} + \boldsymbol{R}_{\boldsymbol{k+1}}.$$

With state estimates $\hat{X}_{k+1|k}$ from the previous epoch, the measurement innovations $\widetilde{\boldsymbol{Y}}_{\boldsymbol{k+1}}$ provide an indication of whether the current epoch measurements and state estimates are consistent via a global test [2], [79]. The null hypothesis H_0 assumes that no measurement blunder exists, while the alternative hypothesis H_a considers that the innovation vector is biased by $\boldsymbol{M}_{\boldsymbol{k}} \boldsymbol{\nabla}_{\boldsymbol{k}}$. $\boldsymbol{M}_{\boldsymbol{k}}$ is the mapping matrix

describing the way how the bias vector $\boldsymbol{\nabla_k}$ interferes with the observations. The distribution of the innovation vector under those hypotheses are respectively

$$\tilde{Y}_{k+1|\mathrm{H}_0} \sim N(0, \boldsymbol{C_{k+1}})$$

$$\tilde{Y}_{k+1|\mathrm{H}_a} \sim N(\boldsymbol{M_k \nabla_k}, \boldsymbol{C_{k+1}})$$

Under the null hypothesis, these innovation components should follow zero-mean Gaussian distributions and the test statistic, the Summation of the Squared Errors (SSE), follows a Chi-square distribution, with the degree of freedom equal to the size of the innovation vector, p, as no restrictions are imposed on the mean value of $\widetilde{\boldsymbol{Y}}_{\boldsymbol{k+1}}$:

$$SSE = \widetilde{\boldsymbol{Y}}_{\boldsymbol{k+1}}^{\boldsymbol{T}} * (\boldsymbol{C_{k+1}})^{-1} * \widetilde{\boldsymbol{Y}}_{\boldsymbol{k+1}}$$

The overall validity of the null hypothesis is tested herein by comparing the test statistic SSE with a critical threshold T_{α_1}. The threshold value depends on a pre-defined significance level (i.e., the probability of false alarm) α_1.

The presence of unspecified outliers is pronounced whenever the test statistic SSE oversteps the threshold T_{α_1} and the whole procedure passes to the next identification step.

2. Identification

When the null hypothesis is rejected in the previous global test, local tests are performed to identify the outliers. The local test is performed on each innovation term $\widetilde{\boldsymbol{Y}}_{\boldsymbol{k+1,i}}$ with $i \in [1, 2, \dots, p]$. Besides, alternative hypotheses need be specified. To restrict our attention to the single-blunder case, the mapping matrix $\boldsymbol{M_k}$ reduces to a column vector, denoted as $\boldsymbol{M_{k,i}} = [\boldsymbol{0}, \dots, \boldsymbol{1}, \dots, \boldsymbol{0}]^{\boldsymbol{T}}$. Only the i^{th} entry is 1. The test statistic to test H_0 against H_a is constructed as

$$|\boldsymbol{t_{k+1,i}}| = \left| \frac{\boldsymbol{M_{k,i}^T (C_{k+1})^{-1} \widetilde{Y}_{k+1}}}{\sqrt{\boldsymbol{M_{k,i}^T (C_{k+1})^{-1} M_{k,i}}}} \right| \geq \boldsymbol{N_{1-\left(\frac{\alpha_2}{2}\right)}}$$

where

- $\boldsymbol{N_{1-\left(\frac{\alpha_2}{2}\right)}}$ is the decision threshold as the test statistic hold a standard normal distribution under H_0, and
- $\boldsymbol{\alpha_2}$ (e.g., 0.03) is the acceptable probability of false alarm.

However, the assumption of having the single-blunder case is not always the reality. Besides, the presence of one severely deteriorated measurement could mislead other measurements failing the local test. Hence, a modified version of the adaptation step is required, other than simply eliminating all the detections. Theoretical validation is provided in [67]. What's more, whenever the global test fails, some procedures need be implemented even if no outlier has been identified, as the over-all reliability of the system is broken.

The modified identification test is thus as follows: each time the global test fails, the local test is performed on each innovation component:

- When multiple outliers are identified by the local tests, only the one with the maximum $|\boldsymbol{t_{k+1,i}}|$ is rejected to avoid the case where a blunder is large enough to cause multiple local failures.
- When there is no outlier identified, still the innovation with the maximum $|\boldsymbol{t_{k+1,i}}|$ is rejected.

The global test is always re-run until it succeeds in ensuring the integrity among the innovation sequence. Beside the code pseudorange and Doppler observables, carrier phase measurements can also be taken into account in the measurement selection to detect large CS on the rover side and especially on reference station side. Based on Doppler observables, the proposed cycle slip detection and repair scheme in next section holds limitations when the reference station does not provide Doppler observables.

4.5 Cycle Slip Detection and Repair

The occurrence of a cycle slip describes the fact that the value of a carrier phase ambiguity term does not hold constant between two consecutive epochs. If the corresponding ambiguity state in the KF is not re-initialized, the value of the CS should be estimated and added to the ambiguity state. Otherwise, the estimation of the ambiguity will become erroneous.

Frequent re-initializations of ambiguities will however undermine the profits that high-accuracy carrier phase measurements bring to the system. The objective of the proposed CS detection and repair is thus to try to maintain as much as possible the same ambiguity states without re-initialization. Indeed, assuming that a CS occurs at each epoch is detrimental to the PVT algorithm accuracy performance since it implies a constant re-estimation of the float ambiguity states without benefiting from their potential continuity. Frequent re-initializations will thus undermine the profits that high-accuracy carrier phase measurements bring to the system. It is, on the other hand, the least risky in terms of PVT reliability.

Still, it might be important to closely monitor the occurrence of data outage or CS continuously to follow the continuous-phase ambiguity model with confidence. According to [7], the causes of CS are signal obstruction, low C/N_0, failure in the receiver software and the receiver dynamic which may cause a phase error exceeding the PLL discrimination linear domain [80]. Even though the frequency of a high-quality receiver suffering CS in an open-sky is considerably low, the CS condition that a low-cost receiver mounted on the top of a vehicle driven in an urban area may confront is relatively much more severe.

The aim of a CS-DR scheme is thus to detect the occurrence of CS and to enable the continuous use of constant carrier phase ambiguity when no CS is detected (either to be able to fix it or to be able to use its accurately-estimated value). Besides the proposed CS-DR scheme, loss of lock indicators (LLI) provided by receivers can also be taken into account.

In this section, the important CS detection and repair (CS-DR) scheme is presented.

4.5.1 Loss of Lock Indicator

Indicators of CS detection should first be constructed. In this subsection, the receiver-provided CS indicators are presented.

The loss of lock indicators (LLI) for the carrier phase observations provided by the receivers reflect the CS condition [36]. There is no reason to neglect this indicator. According to the RINEX format, 2 bits are allocated to provide this indicator, thus the LLI may take a value among $[0, 1, 2, 3]$. The occurrence of CS is detected when the bit 0 of LLI is set (i.e., $LLI \in [1, 3]$) or when there is a transition of the parity unknown flag bit 1 compared to the previous epoch. Besides, the presence of a half-cycle slip is suspected when the bit 1 is set and the associated satellite will be disregarded during the following IAR process. What's more, the selection of the reference satellite should also avoid those half-cycle slip valid satellites.

4.5.2 Cycle Slip Detection and Doppler Aiding

The Doppler measurements, with good accuracy in good signal condition, are always worthy consideration in GNSS applications. For example, they can be used to smooth the PVT solution [81]–[83]. In this PhD thesis, a Doppler-aiding CS-DR is implemented to maximize the system's capability of handling CS .

The proposed CS-DR scheme is based on the following system [7]:

$$\begin{cases} \delta P^i{}_{cs} = \dfrac{D^i(k) + D^i(k-1)}{2}.t_s = \delta\rho_i + \delta dt + \varepsilon_{\delta P^i{}_{cs}} \\ \delta\Phi^i{}_{cs} = \Phi^i(k) - \Phi^i(k-1) = \delta\rho_i + \delta dt + CS_i.\lambda_i + \varepsilon_{\delta\Phi^i{}_{cs}} \end{cases} \quad (4\text{-}27)$$

where

- $\delta P^i_{CS}\,[m]$ is the pseudorange variation between two consecutive epochs k and $(k-1)$, determined by the product of the average Doppler observable and the time interval t_s;
- $\delta\Phi^i{}_{cs}\,[m]$ is the difference between two consecutive carrier-phase observables;
- δdt is the difference between rover clock delays of two successive epochs, the unit is in meter;
- $CS_i\,[cycle]$ is the integer CS value.

Considering a high rate system (t_s is lower than 1s), the difference between measurements δP^i_{CS} and $\delta\Phi^{\mathrm{i}}{}_{\mathrm{cs}}$ will be the CS if it occurs.

The geometry matrix comes from the linearization of the system measurements:

$$\delta\rho = \rho^i(k) - \rho^i(k-1) = e^i(k)\left[POS^i_{sat}(k) - POS(k)\right] - e^i(k-1).\left[POS^i_{sat}(k-1) - POS(k-1)\right]$$

$$\delta\rho + e^i(k-1).\left[POS^i_{sat}(k-1) - POS(k-1)\right] = e^i(k).\left[POS^i_{sat}(k) - POS(k-1)\right] - e^i(k).\delta X(k)$$

where

- $POS^i_{sat}(\blacksquare)$ the position of satellite i at transmitting time before nominal epoch ■,
- $POS(\blacksquare)$ the rover's position at epoch ■,
- $\delta X(\blacksquare)$ the between-epochs variation of the rover's position and
- $e^i(\blacksquare)$ the unit vector directing from the rover to the satellite at epoch■

Therefore, with measurements corrected by $\delta\rho_{corr} = e^i(k)\left[POS^i_{sat}(k) - POS(k-1)\right] - e^i(k-1).\left[POS^i_{sat}(k-1) - POS(k-1)\right]$, the relation between the measurements and the states becomes:

$$Y(k) = \begin{bmatrix} \delta P^i{}_{cs,corr} \\ \delta\Phi^i{}_{cs,corr} \end{bmatrix} = H.\begin{bmatrix} \delta X(k) \\ \delta dt \\ CS \end{bmatrix} + \varepsilon \quad (4\text{-}28)$$

$$H = \begin{bmatrix} -e^1(k) & 1 & 0 & \dots & 0 \\ \vdots & \vdots & \vdots & \ddots & \vdots \\ -e^n(k) & 1 & 0 & \dots & 0 \\ -e^1(k) & 1 & \lambda_1 & \dots & 0 \\ \vdots & \vdots & \vdots & \ddots & \vdots \\ -e^m(k) & 1 & 0 & \dots & \lambda_m \end{bmatrix}$$

With the assumption that CS does not generally occur on all satellites at a given epoch, it is important to be able to separate the carrier phase measurements suffering CS from those free from CS. To do so, a separation based on a phase prediction test and Chi-square test (referred later to Step 1 and Step 2)

between highly probable and unlikely CS-contaminated satellites will strengthen the system [84]. The whole CS-DR process follows 4 steps:

Step 1. Raw CS detection test

δP_{CS}^{i} can also be considered as the prediction of $\delta \Phi^{i}{}_{cs}$ when no CS occurs. A phase prediction test as follows will detect large CS occurrences:

$$H_0:\ t_{CS}^{i} = \left|\delta\Phi_{cs}^{i} - \delta P_{cs}^{i}\right| \leq \mathrm{T} * \sigma_{t_{CS}}^{\mathrm{i}} \tag{4-29}$$

The capability of the test depends on the measurement accuracy $\sigma_{t_{CS}}$ and the threshold T defined by a tolerable false alarm rate α_1. As the fact that the high-uncertainty of δP_{cs}^{i} may corrupt the test H_0, an absolute cycle number constraint $\mathrm{N_{cs}}$ (in cycle) is also required. For those satellites having $t_{CS}^{i} > \lambda_i \mathrm{N_{cs}}$, they are concluded CS-corrupted.

Step 2. CS-free measurements confirmation test

Following Step 1, a separation of satellites into two sub-groups ***F*** and ***S*** is done. The letter '***F***' signifies fail-passing the test H_0 and reversely, the letter '***S***' is for success.

If Group ***S*** is populated by less than 5 measurements, it is augmented by the measurements that led to up to the 5 smallest value of $\left|\delta \Phi^{i}{}_{cs} - \delta P^{i}{}_{cs}\right|$.

A Chi-square test is conducted on Group ***S*** to confirm that the measurements of group S are CS-free. This Chi-square test is based on the assumption that $\delta \Phi^{i}{}_{cs}$ has no CS. As a consequence, the following system using only measurements of Group ***S*** is solved based on weighted LS:

$$Y_S = [\delta\Phi_{cs}^{i}] = H.\begin{bmatrix}\delta X(k)\\ \delta dt\end{bmatrix} + \varepsilon, i \in \boldsymbol{S} \tag{4-30}$$

The sum of the squared phase measurements residuals should follow a Chi-square distribution. Thus a comparison of the test statistics to a threshold defined by the significance level α_2 will conclude whether the null-CS is true or not. If the test is passed, all members of Group ***S*** are assumed CS-free.

Step 3. Converging with Group ***F***

Following the test result in Step 2, two cases can occur:

a. Satellites in Group ***S*** are CS-free.
   In this case, $\delta \Phi^{i}{}_{cs,i\in \boldsymbol{S}}$ will serve as precise measurements to strengthen the model. Only satellites in Group ***F*** are assumed to be potentially CS-contaminated. Thus, the measurement model is

$$Y = \begin{bmatrix}\delta \Phi^{i}{}_{cs,i\in S}\\ \delta P^{i}{}_{cs,i\in F}\\ \delta \Phi^{i}{}_{cs,i\in F}\end{bmatrix} = H.\begin{bmatrix}\delta X(k)\\ \delta dt\\ CS_F\end{bmatrix} + \varepsilon \tag{4-31}$$

b. Satellites in Group ***S*** and ***F*** are all potentially CS-contaminated.
   This time, these two groups are gathered. Instead of the state vector $\boldsymbol{CS_F}$ only for group ***F***, a state vector including all CS needs to be resolved. The new measurement model including the CS state is:

$$Y = \begin{bmatrix}\delta P_{cs}^{i}\\ \delta \Phi_{cs}^{i}\end{bmatrix} = H.\begin{bmatrix}\delta X(k)\\ \delta dt\\ CS_i\end{bmatrix} + \varepsilon, i \in \boldsymbol{F} \cup \boldsymbol{S} \tag{4-32}$$

In cases a and b, the estimates of the *CS* are calculated via a WLS filter, noted as

$$\widehat{CS} = \begin{bmatrix}\widehat{CS}_1\\ \widehat{CS}_2\\ \vdots\\ \widehat{CS}_n\end{bmatrix}$$

Step 4. Information passed to the main GNSS positioning KF

There are thus 2 possible results of CS-DR:

- No CS for Group $\boldsymbol{S}$, and only a float estimation of the CS for Group $\boldsymbol{F}$;
- Only a float estimation of the CS for all satellites.

In all cases, the ambiguity estimates in the KF are corrected accordingly. For the ambiguity states of the satellites without CS, a very small process noise level (e.g, 1e-6 [cycle²]) is applied. On the other hand, the covariance of ambiguity states associated to only an estimated float CS is largely inflated to represent the uncertainty of the CS estimation (a typical value of e.g. 10^2 [cycle²] is used). Of course, instead of big covariance inflation, an alternative is to fuse the corresponding covariance of the estimates $\widehat{CS}$ into ambiguity estimation if a big trust is put on rover states.

In case when Doppler observables are also provided on the station side, a CS-DR scheme will also be conducted on the station. Combined information of float CS on both the rover and station sides will passed through.

4.6 Modified Partial Integer Ambiguity Resolution

Taken the intention of controlling the probability of false fixing P_f and the performance obtained from the FT-RT, a modified version of partial integer ambiguity resolution (Partial-IAR) methodology is proposed in this section.

The optimal ILS estimator, the LAMBDA method, is always utilized along with the validation methodology FT-RT. As there is no specific formula to calculate the P_f, the envelope of P_f is practically approximated by an upper bound related to the Integer Bootstrapping Estimator. Combining the Eq(3-16) with the Table 3-1, the following relationship is derived

$$P_f \leq P_{f,ILS} = 1 - P_{s,ILS} \leq 1 - P_{s,IB} \leq 1 - P_{s,0} \tag{4-33}$$

where $P_{S,0}$ is the pre-defined limit value which defines the lowest performance expected.

It is also important to consider that the resolution of the whole integer ambiguity set is often not possible, and the distinction of quality among the ambiguities should be considered by virtue of their model strength [84], [85]. Thus, the Partial-IAR is brought up so that instead of the whole set, a subset of the ambiguities which may be more easily and correctly fixed should be extracted.

The de-correlated ambiguities can be listed with their uncertainties $\sigma_{\hat{z}_i}$ in an ascendant order. Under the criterion that the probability of success fixing P_S is higher than the value $P_{S,0}$, the first m ambiguities can thus be chosen to pass the whole IAR process. The whole operating scheme of the proposed Partial-IAR is illustrated in Figure 4-5.

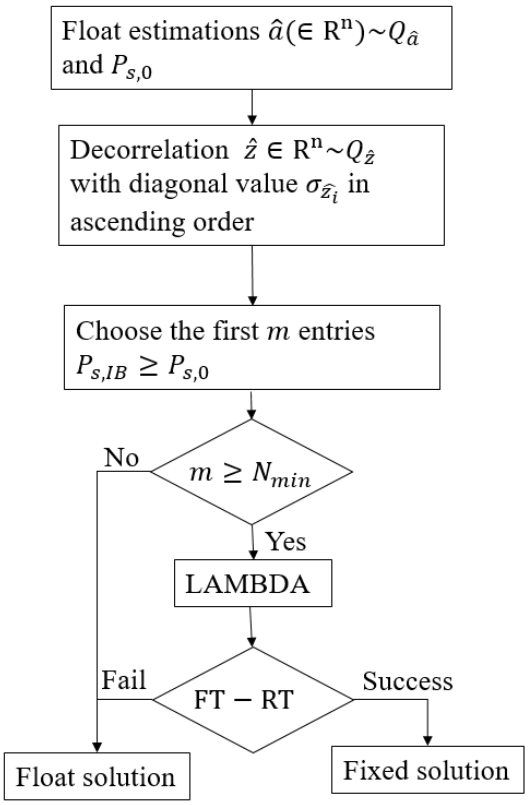

Figure 4-5. Scheme of the Partial-Integer Ambiguity Resolution

4.7 Conclusion

In this chapter, major modules of the proposed precise positioning algorithm have all been presented. A detailed scheme of the implemented GNSS positioning filter can be found on Figure 4-6. After the selection of GNSS measurements by basic C/N0 and elevation masks, a further check on code and Doppler observables based on an Innovation test followed. As the proposed CS-DR highly depends on Doppler observables, satellites associated to potentially corrupted Doppler measurements will be treated as CS-deteriorated ones. Considering the importance of ambiguity states, any potential state change , i.e. CS, should be noticed and properly handled. After the CS-DR, a second Innovation test only on carrier phase innovations is conducted to provide a double-check on ambiguities. Finally, attempts to fix float ambiguities are made. When they succeed, fixed PVA solution after the LAMBDA adjustment will be used in next positioning epoch.

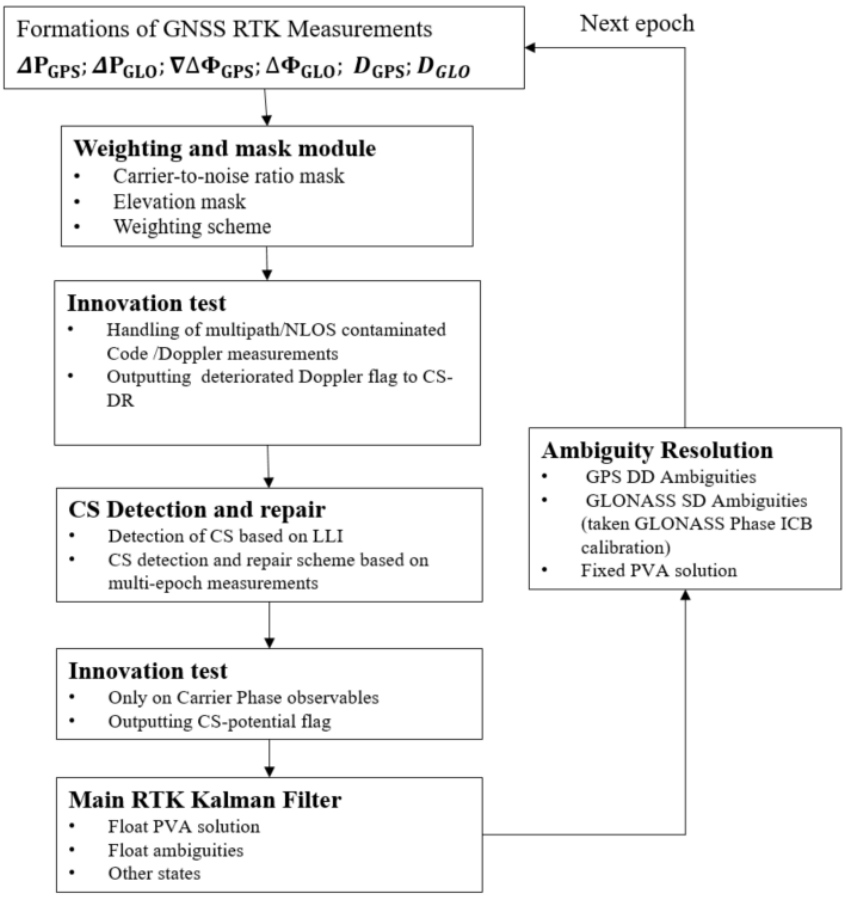

Figure 4-6. Scheme of the Implemented GNSS Positioning Filter

5 GNSS Tests and Results

In the previous chapters, the proposed algorithm for RTK positioning in constrained environment with the low-cost single frequency GNSS receiver has been introduced and described. In the current chapter, this algorithm will be tested using real data. Two data campaigns have been collected in Toulouse, France. First of all, the set-up and the environment conditions where the data was collected will be reviewed. The RTKLIB software is then briefly introduced. As a popular precise positioning program, it will provide representative reference positioning results. Then, the positioning performance of our proposed algorithm will be studied. Different processing methods are progressively added to illustrate their influence on the position performance, which are in particular:

- the use of the environment-dependent code/Doppler measurement weighting scheme;
- the consideration of the GLONASS constellation and the GLONASS code ICB calibration;
- the operation of the proposed CS-DR (Cycle Slip Detection and Repair) mechanism;
- the correction of GLONASS carrier phase ICB, and the inclusion of GLONASS ambiguities into IAR (Integer Ambiguity Resolution) scheme.

5.1 Test Description

In order to evaluate the performance of the proposed RTK and RTK/INS algorithms, two data campaigns have been collected. In this section, the equipment embedded in the test vehicle will be firstly presented, followed by descriptions of the data collections. Information about the precise positioning software, RTKLIB, is provided in the last sub-section.

5.1.1 Equipment Description

The GNSS data used for this study was collected in Toulouse area by a Ublox M8T evaluation kit [86] connected to its magnetic patch antenna showed in the picture below. The compact receiver was providing raw measurements at 1 Hz. The antenna was magnetic mounted and fixed on the roof of the vehicle allowing GPS/GLONASS tracking on L1. GNSS data was stored in a computer connected to the receiver via a USB link and monitored by the u-center software. A picture of the Ublox M8T EVK kit is provided in Figure 5-1. At the same time, the Xsens Mti IMU [87] set at 100 Hz was embedded inside the driving vehicle. The temporal synchronization between the GNSS unit and inertial unit has been perfectly guaranteed by using PPS triggering of the IMU from the Ublox.

Figure 5-1. Ublox M8T Evaluation Kits

In order to provide the reference trajectories, the Novatel SPAN equipment, which is composed of a Novatel L1/L2 receiver, a Novatel ANT-532-C antenna and a tactical grade IMU, a FSAS inertial module with fiber optical gyrometers, is also placed inside the vehicle. A multi-baseline post-processing RTK mode is used to calculate the reference trajectory. A picture of the vehicle roof, the SPAN receiver and inertial unit is presented in Figure 5-2.

Figure 5-2. Top of the vehicle roof (left) with the Novatel antenna in white and the Ublox antenna in black; Inside the vehicle (right) the Novatel receiver and the inertial unit side-by-side.

5.1.2 Data Collections

The first data set was collected when the vehicle was driven from ENAC (Ecole Nationale de l'Aviation Civile) to the city center along the Canal de Midi. The whole trajectory in Google Earth is represented in Figure 5-3. Two representative pictures of the driving environment are provided in Figure 5-4.

The second data set was stored when the vehicle was driven around the city center. Most part of the trajectory was either along narrow roads with high buildings on both sides or on avenues covered by trees. The whole trajectory of the data set 2 is depicted in Google Earth in Figure 5-5. Some typical street-view pictures are presented in Figure 5-6.

Figure 5-3. Trajectory in red of Data set 1 in Google Earth

Figure 5-4. Example of Urban (left)and semi-urban (right)environment along the canal during the first data collection. The street view and the yellow driving strip are provided by Google Earth.

Figure 5-5. Trajectory in red of Data set 2 in Google Earth

Figure 5-6. Example of Urban environment during the Second Data collection. The street view is provided by Google Earth.

Reference Trajectory Generation

As aforementioned, the referential trajectory was provided by the Novatel Span module using Inertial Explorer version 8.70, in a post-processing mode. The inertial unit was tightly integrated with the Novatel L1/L2 receiver on a multi-station forward-backward smoothed RTK mode. Three available GNSS reference stations around Toulouse are involved which are TLSE, TLMF, and TLSG, from the

Reseau GNSS Permanent (RGP) network. Inertial Explorer is set to use the L1/L2 GPS/GLONASS measurements along with the tactical grade IMU measurements to derive the reference trajectory. The estimated standard deviations in local frame of the reference trajectory are plotted in Figure 5-7 and Figure 5-9. Unfortunately, the states of whether ambiguities are fixed or not are not indicated on the plots. But, centimeter-level positioning accuracy is expected when ambiguities are fixed. With Data set 1, a centimeter-level accuracy is globally guaranteed while a few increases of the standard deviation exist due to occasional signal blockages by the bridges. The number of tracked GPS/GLONASS satellites seen by the Novatel set during the data collection is provided in Figure 5-8.

Compared to the Data set 1, a much denser urban environment was experienced during the Data set 2, and severer signal masking was expected. The bad GNSS condition is also reflected in the number of available satellites tracked by the Novatel set, referring to Figure 5-10. Deduced from the Figure 5-9, ambiguities are even rarely fixed during the whole data campaign with the dual-frequency Novatel Span module in a post-processing mode.

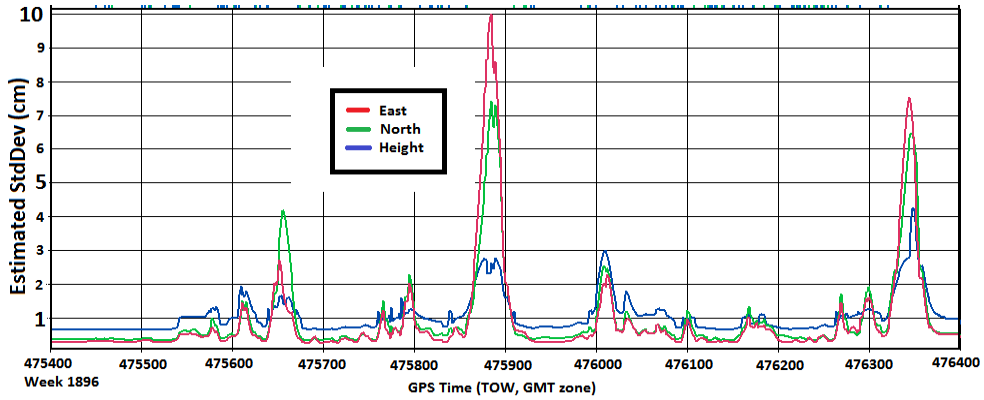

Figure 5-7. Estimated position standard deviation in ENU frame of the referential trajectory (Data set 1)

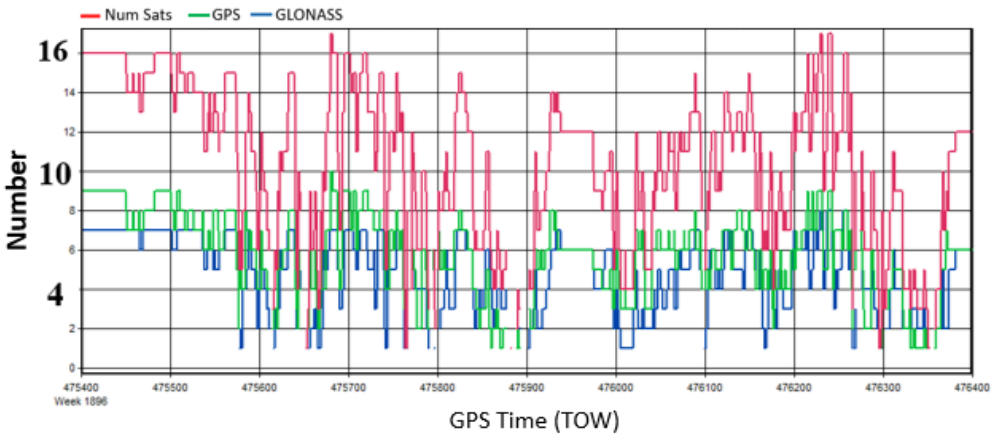

Figure 5-8. Number of tracked satellites during the trajectory (Data set 1)

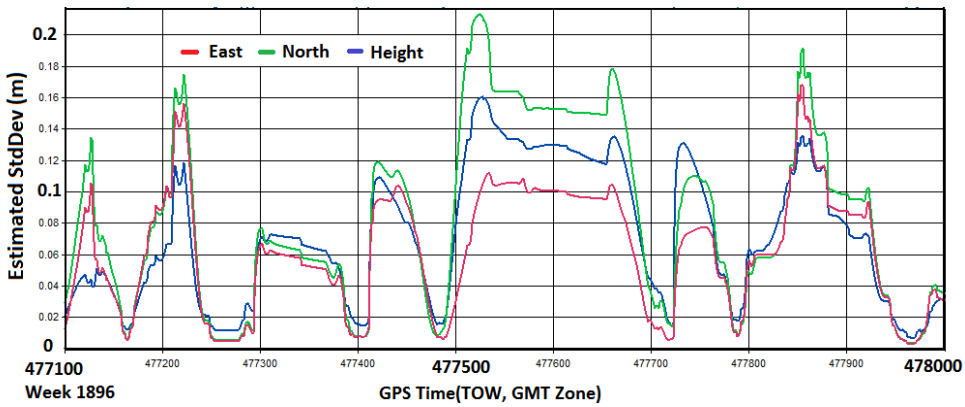

Figure 5-9. Estimated position standard deviation in ENU frame of the referential trajectory (Data set 2)

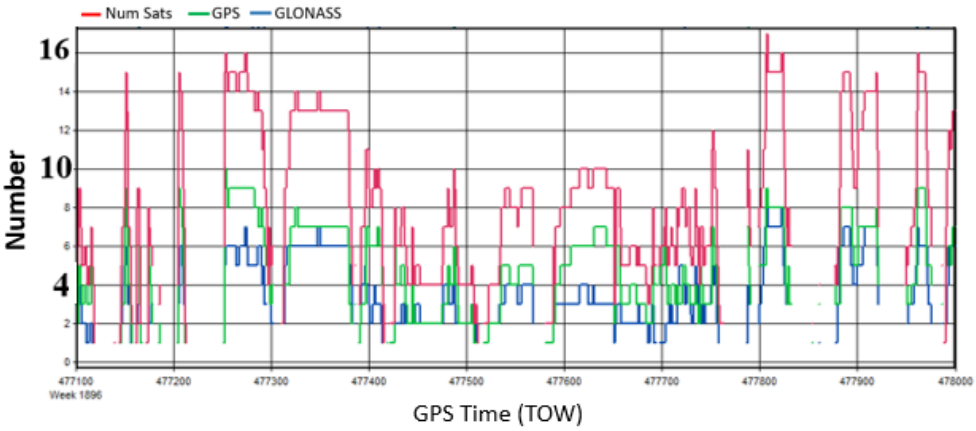

Figure 5-10. Number of tracked satellites during the trajectory (Data set 2)

The estimated reference velocities of the driven vehicle during the data collections are provided in Figure 5-11. A general lower velocity and more frequent stops were experienced during Data set 2, a denser urban environment.

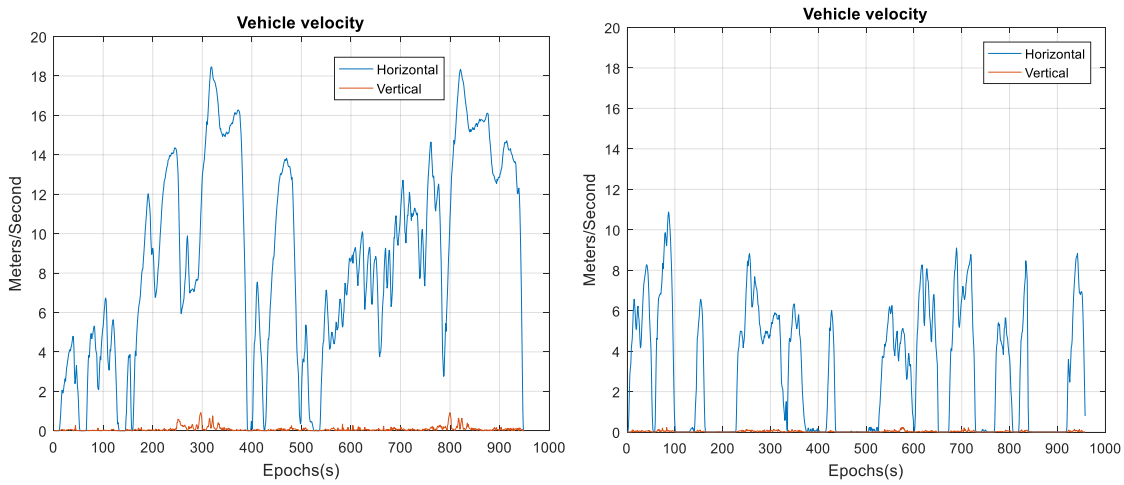

Figure 5-11. Horizontal and vertical reference velocity. Data set 1 on the left and Data set 2 on the right.

Availability of GNSS Measurements on Rover Side

In this part, the availability of the tracked GNSS measurements viewed by the Rover receiver is also analyzed in both data campaigns. The number of tracked GPS/GLONASS satellites is plotted in Figure 5-12 and Figure 5-13. Neither an elevation mask nor a C/N0 mask is applied. Compared to the number of tracked satellites in the Novatel receiver's view, the high-sensitivity of the Ublox rover receiver always provides a higher number of available satellite measurements. Definitely, some measurements should be disregarded for their low quality.

In order to provide a clearer impression of different GNSS measurements' availability, percentages of each measurement's availability during the whole trajectory are provided in Table 5-1.

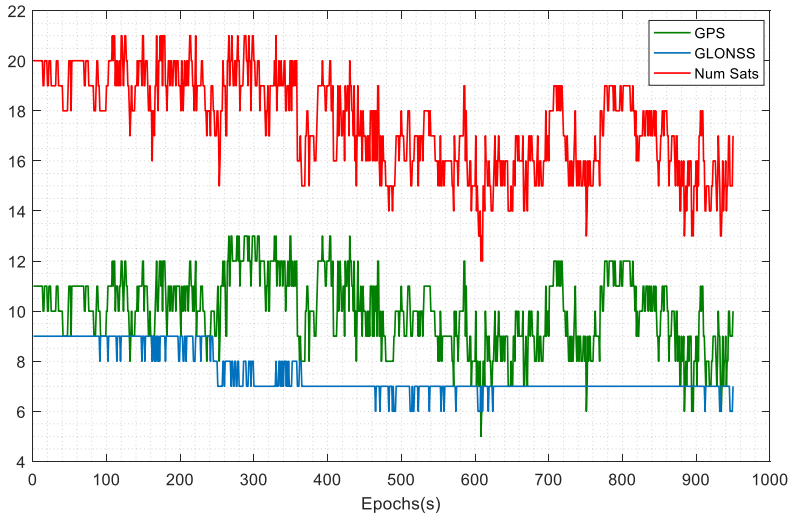

Figure 5-12. Number of tracked satellites during Data set 1. No elevation or C/N0 value mask is applied.

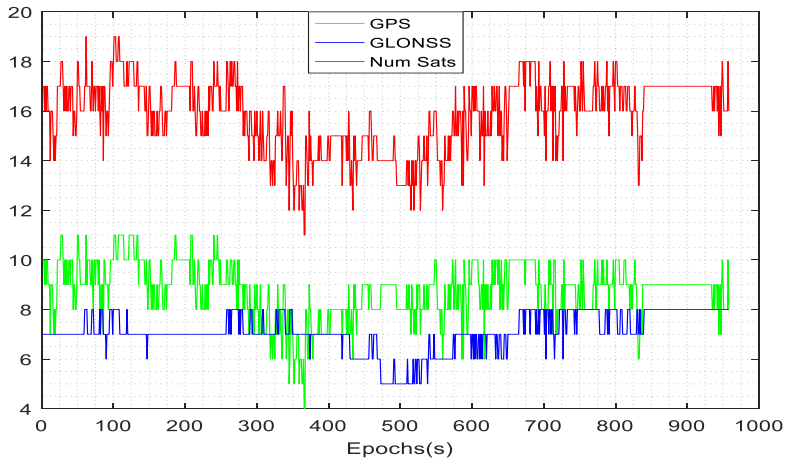

Figure 5-13. Number of tracked satellites during Data set 2. No elevation or C/N0 value mask is applied.

Table 5-1. Availability statistics of GNSS measurements during data collections. No masks applied.

		Data set 1			Data set 2		
Available observables		**C1**	**D1**	**L1**	**C1**	**D1**	**L1**
GPS-only	**At least 4**	100%	100%	98.6%	100%	100%	90.8%
	At least 5	100%	100%	94.7%	99.8%	99.8%	79.4%
	At least 6	99.9%	99.9%	87.1%	99.2 %	99.2%	66.2%
	At least 7	99.1%	99.1%	74.2%	96.7%	96.7%	49.2%
	At least 8	95.6%	95.6%	57.9%	88.6%	88.6%	31.0%
GPS +GLONASS	**At least 4**	100%	100%	100%	100%	100%	99.6%
	At least 5	100%	100%	99.6%	100%	100%	98.2%
	At least 6	100%	100%	99.5%	100%	100%	93.9%
	At least 7	100%	100%	98.5%	100%	100%	87.7%
	At least 8	100%	100%	96.6%	100%	100%	81.6%

As observed from the Table 5-1, as a GNSS receiver, the Ublox rover receiver has a good capability to provide code tracking measurements. Also, the observability of code measurements is always higher than that of carrier phase measurements. When only GPS is considered, the percentage of having at least 5, or 6 carrier phase observables is on a severe decrease especially during a more challenging environment in Data set 2. This fact sets an upper operating bound of those IAR methodologies or CS-DR schemes which predefined a minimum number of involved ambiguities. As indicated in Section 4.5.2, a minimum of 5 CS-free satellites is required to pronounce a CS-free situation. Besides, the consideration of the GLONASS constellation improves significantly the measurements availability.

Among aforementioned RGP network reference stations, the station TLSE equipped with TRIMBLE NetR9 receiver and TRIMBLE TRM59800 antenna is chosen as the reference station in our single-station RTK algorithm. The baseline between our rover vehicle and the station TLSE is comparably shorter than with the other two stations. Along the 2 data collections, the lengths of the baselines are reflected in next Figure 5-14. The longest distance is less than 5 km. The situation of short-baseline is therefore agreeably confirmed.

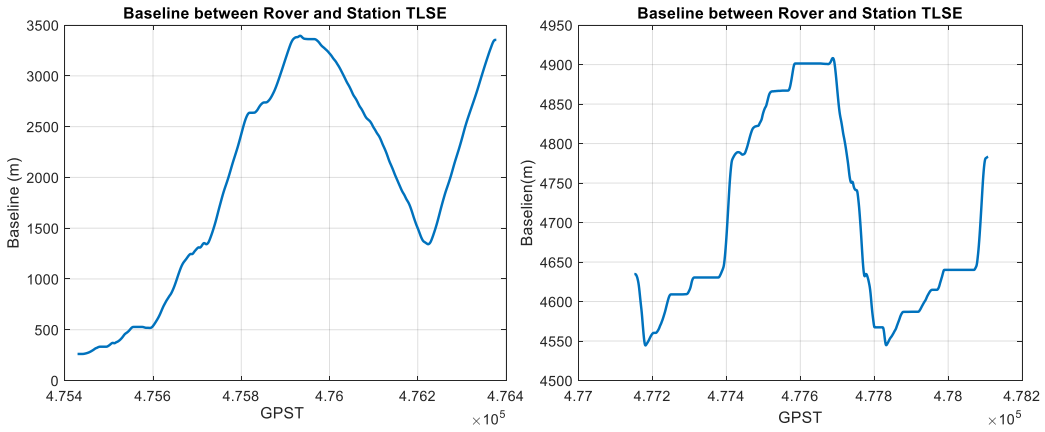

Figure 5-14. Baseline length between rover and station TLSE during Data set 1 (left) and Data set 2 (right)

5.1.3 Introduction of RTKLIB

RTKLIB is an open-source program package for standard and precise GNSS positioning (RTK and PPP) developed by Akio Yasuda and Tomoji Takasu of the Laboratory of Satellite Navigation, Tokyo University of Marine Science and Technology [88], [89]. Since the first release in 2006, constant refinements have been added and it has been widely implemented to provide signal statistics or positioning results [88], [90]–[94]. The latest version 2.4.3, released in 2015, supports various real-time or post-processing positioning modes, i.e., the single point positioning, the code-based DGNSS positioning, the post-processing RTKPOST, etc. Support for system integration between GNSS and INS is not provided and always on the to-do-list.

This RTKLIB program package, considering its good performance in good signal condition (i.e. open sky, static mode), will be used in this chapter to provide reference positioning results. An example of the RTKPOST module configuration details is depicted in Figure 5-15. Without specific clarification, these configuration parameters are selected for performance analysis sections, i.e. Section 5.2.1. A default elevation mask of 10 degrees and a signal strength mask of 35 dB.Hz are implemented. With the presence of a technical issue that the RTKPOST module can not load two navigation files (i.e., one for only GPS, another for GLONASS) at the same time, only GPS satellites are taken into account. As for the resolution of GPS ambiguities, a continuous ambiguity resolution mode is chosen so that ambiguities are considered constant when no cycle slip is detected. It matches the common knowledge on ambiguities. The embedded default algorithms for the integer ambiguity estimation is LAMBDA and for the validation test is the classic FT-RT. A default ratio threshold of 3 is set. The default RTKLIB measurements weighting scheme stays unmodified. Finally, a reasonable acceleration process noise model, consistent with the one mentioned in Section 4.2.3, is applied.

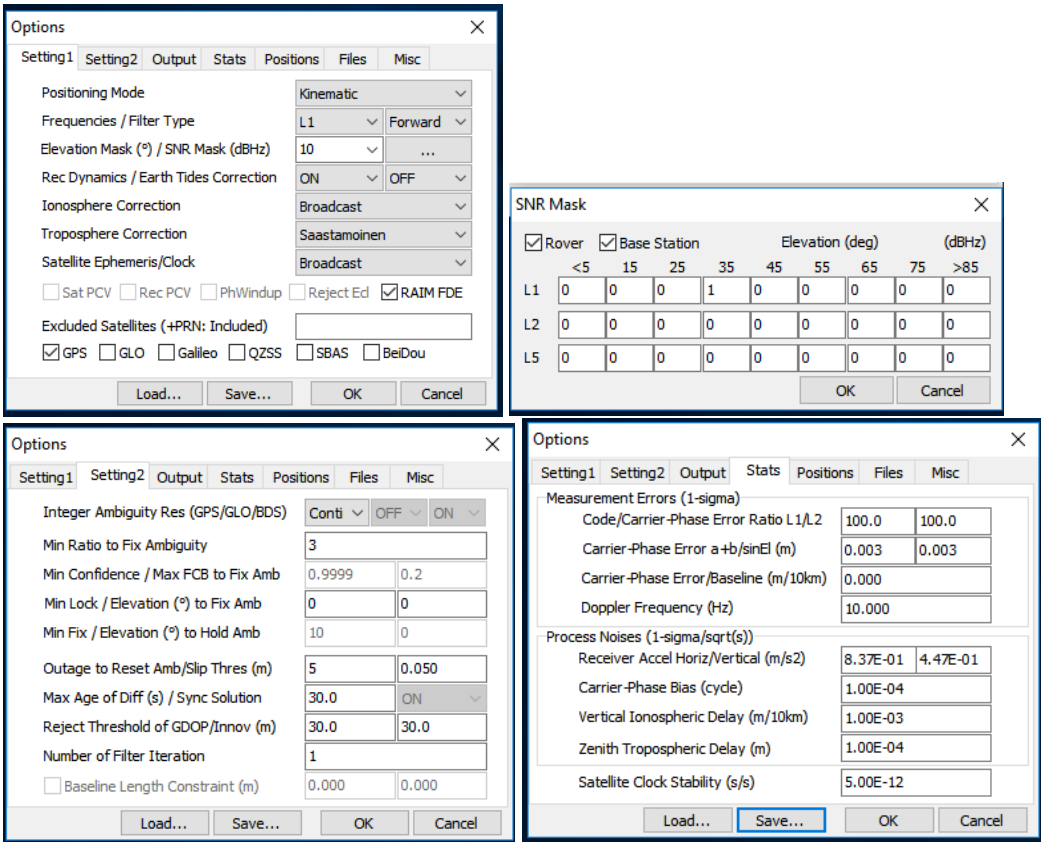

Figure 5-15. Configuration tabs of RTKLIB Continuous GPS AR Mode

Not only the positioning results of GPS continuous AR mode will be studied, but also the results of the DGPS mode will also be presented. The comparison between these two modes will depict the differences brought by the carrier phase measurements.

5.2 Analysis of Positioning Performances

In this section, the analysis of positioning performance with Data set 1 will be conducted, followed by the results on Data set 2. First of all, the RTKLIB solutions are presented, showing a basic positioning performance that a popular program can provide. Then, different propositions to progressively improve our RTK methodology are discussed.

As our goal is to provide reliable solutions for ground vehicles, the horizontal positioning performance is emphatically exploited in solution comparisons. The 68th, 95th and 99th percentiles of the horizontal positioning error will be presented and compared.

Another performance indicator is the wrong fix rate, when attempts are made to have integer ambiguities resolved and fixed ambiguities are obtained. Compared to the precision brought by correct fix solution, the unexpected severe bias brought by wrong fixing is more fatal. The theoretical definition of the wrong fix rate is the percentage of epochs having ambiguities fixed to a wrong integer among the total number of epochs when ambiguities are declared fixed. With the difficulty of knowing the true value of ambiguities, the optimistic definition of the wrong fixing brought up by [7] is herein adopted. Only moments when the horizontal bias between the resolved position solution and the reference trajectory solution exceeds 50 centimeters are taken into account during the calculation of the wrong fix rate.

5.2.1 RTKLIB Solution

The horizontal performance of the RTKLIB DGPS mode and of the continuous AR mode using the Data set 1 are provided in Figure 5-16 and Figure 5-17 respectively. Configuration parameters mentioned in 5.1.3 are used. The position differences in horizontal plane are plotted in blue. The inclusion of high-precision carrier phase measurements smoothed the position plots. However, contrarily to the DGPS mode in Figure 5-16, position errors are rarely wrapped by the 3-sigma curve in Figure 5-17. An over-optimistic modeling of the whole positioning system can then be suspected for AR mode. Numerical performance summary is provided in Table 5-2. Due to the poor geometry, the 95th percentile of the DGPS mode can easily reach 5 meters. For both the DGPS mode and the continuous AR mode, we've tried to loosen the measurements selection criteria by setting the C/N0 mask at 25 dB.Hz to increase the number of measurements. Nevertheless, by comparing the final position performance, the inclusion of low-quality measurements clearly brings no noteworthy difference.

A closer view of the continuous AR mode position error is presented in Figure 5-18. Epochs when fix solution is obtained are marked with black asterisks. Contrary to anticipation, big position biases are observed when ambiguities are fixed. Thus, the ambiguity resolution is very unreliable as 86.8% epochs among all the fixes are wrongly fixed.

Table 5-2. Performance summary of the RTKLIB in DGPS mode and Continuous GPS AR mode processing the Data set 1

	Horizontal Positioning Error (in meter)				
Data Set 1	**68th Percentile**	**95th Percentile**	**98th Percentile**	**Fix Rate**	**Wrong Fix Rate**
DGPS-Mode	1.46	5.37	10.72	--	--
Continuous AR- Mode	2.76	13.08	88.45	8.0%	86.8%

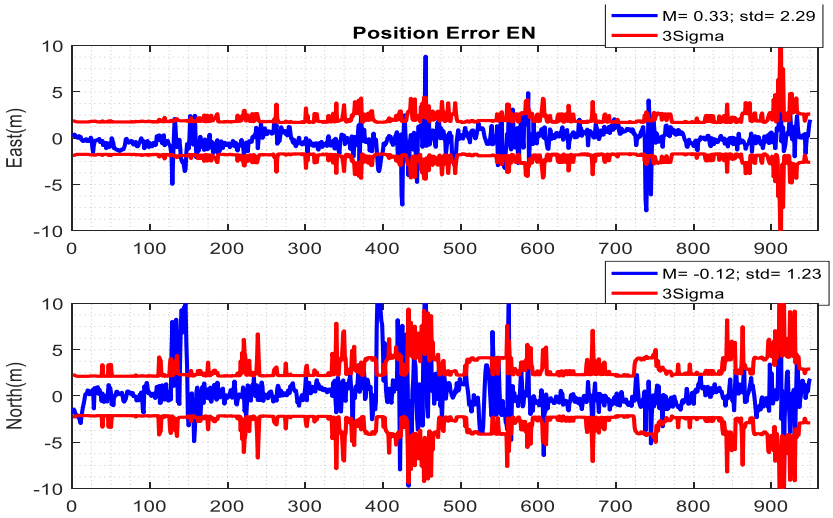

Figure 5-16. Horizontal performance of the RTKLIB DGPS mode (Data set 1)

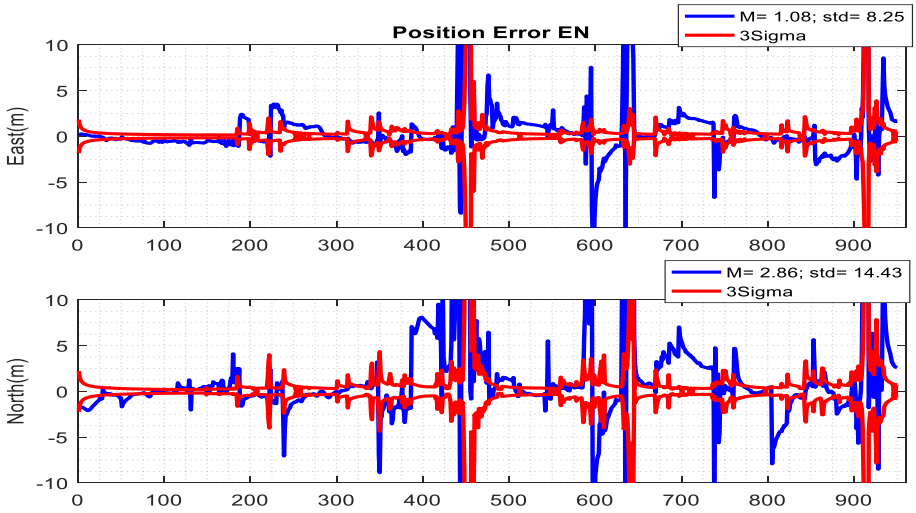

Figure 5-17. Horizontal performance of the RTKLIB continuous AR mode (Data set 1)

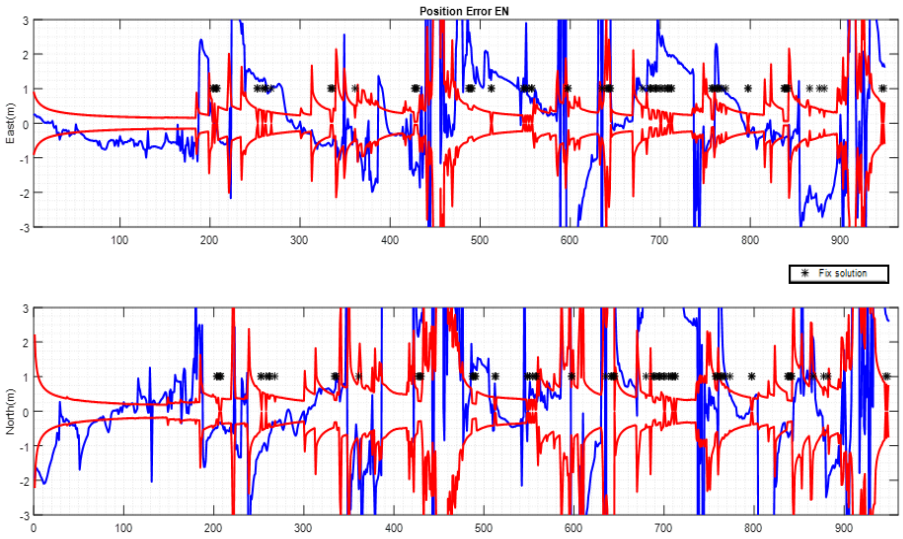

Figure 5-18. Horizontal performance of the RTKLIB continuous AR mode (Data set 1), and moments obtaining fix solution marked in black

Compared to the Data set 1, a more constrained environment is associated with the Data set 2. In Table 5-3 is illustrated the performance summary of RTKLIB in DGPS mode and continuous GPS AR mode. Detailed positioning errors and their relevant 3-sigma curves are presented in Figure 5-19 and Figure 5-20. A first remark by observing the DGPS position results is the lack of RTKLIB's ability to exclude multipath/NLOS deteriorated measurements. An over-optimistic bounding model of the measurement vector results in a non-coverage of the error by the 3-sigma bounds. The position performance is much degraded when attempting to fix GPS ambiguities. The IAR in a constrained condition was always an intractability that is worthy exploitations.

Table 5-3. Performance summary of the RTKLIB in DGPS mode and Continuous GPS AR mode processing the Data set 2

	Horizontal Positioning Error (in meter)				
Data Set 2	**68th Percentile**	**95th Percentile**	**98th Percentile**	**Fix Rate**	**Wrong Fix Rate**
DGPS-Mode	6.16	28.02	115.25	--	--
Continuous AR- Mode	7.58	81.68	478.05	8.5%	93.8%

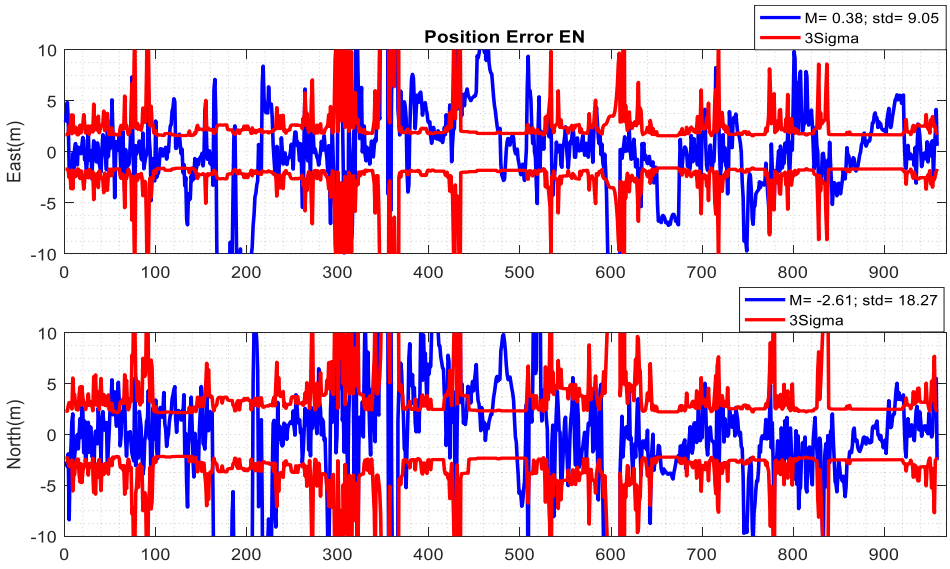

Figure 5-19. Horizontal performance of the RTKLIB DGPS mode (Data set 1)

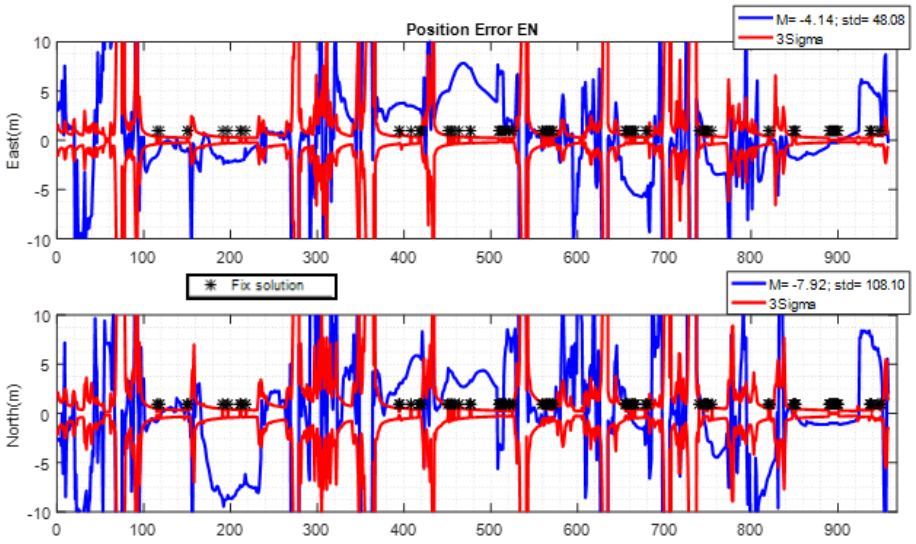

Figure 5-20. Horizontal performance of the RTKLIB continuous AR mode, and moments obtaining fix solution marked in black (Data set 2)

5.2.2 GNSS-only DGPS and DGNSS Solutions

Starting from this section, the positioning performance with only GNSS observables processed by our proposed methodologies will be presented. In this section, the DGPS results will first be presented to show the impact on position performance of the code/Doppler measurement weighting scheme mentioned in Section 4.3.2. Then, the benefits that a second constellation such as GLONASS can bring are depicted. The positioning filter used are the following:

- Only the code and Doppler measurements are for this moment considered during the construction of the main positioning KF;
- An elevation mask of 10 degrees is applied;
- A C/N0 mask of 30 dB.Hz is generally used;
- The parameter pair (α_1, α_2) defining the Innovation test is empirically set as $(0.2, 0.03)$;
- A down-weighting factor of 1.69 is applied when considering GLONASS code measurements.

In the first place, to show the impact of the measurement scheme, with the Data campaign 1 two position results which use only GPS code/Doppler measurements and common Innovation test parameters, but one with environment type 'Rural' and another choosing 'Urban', are depicted in Figure 5-22 and Figure 5-23. The number of tracked satellites under the elevation and C/N0 masks (10 degrees and 30 dB/Hz) are depicted in Figure 5-21. Compared to Figure 5-12 where no masks has been planted, a general decrease of 2 satellites for each constellation (GPS and GLONASS) is observed.

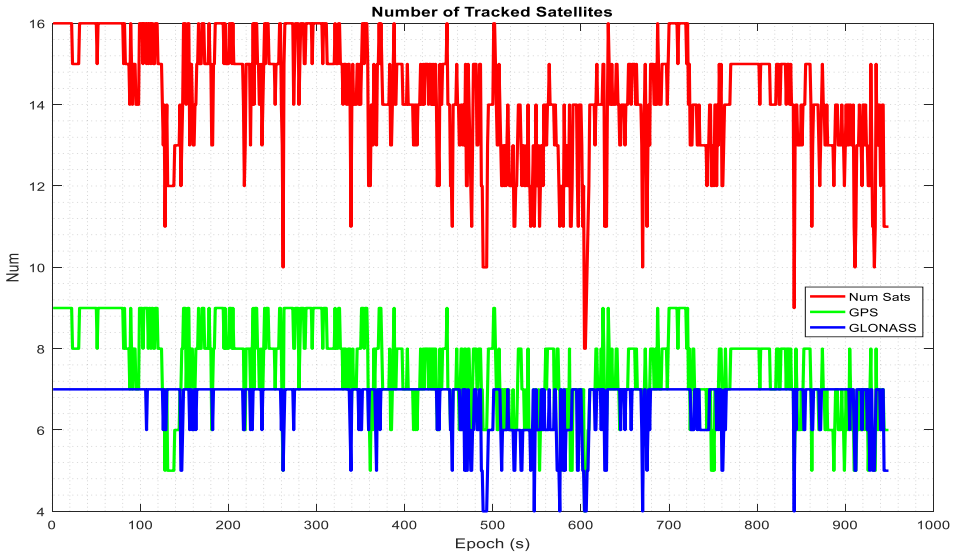

Figure 5-21. Number of tracked satellites during Data set 1. Elevation and C/N0 masks (10 degrees and 30 dB/Hz) are applied.

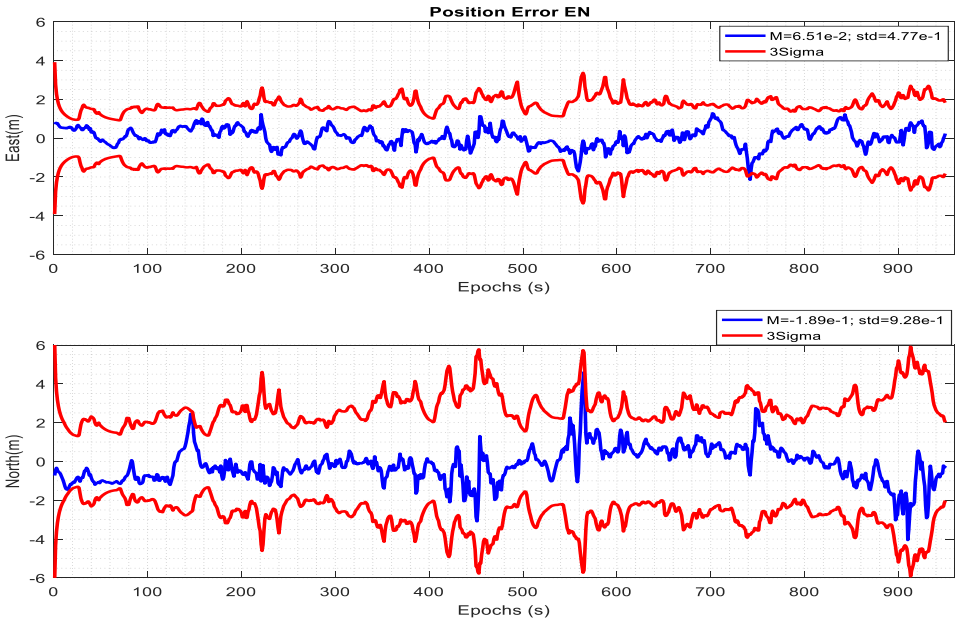

Figure 5-22. Horizontal DGPS position difference between estimated trajectory and the reference trajectory (Data set 1) with associated environment type chosen as 'Rural'.

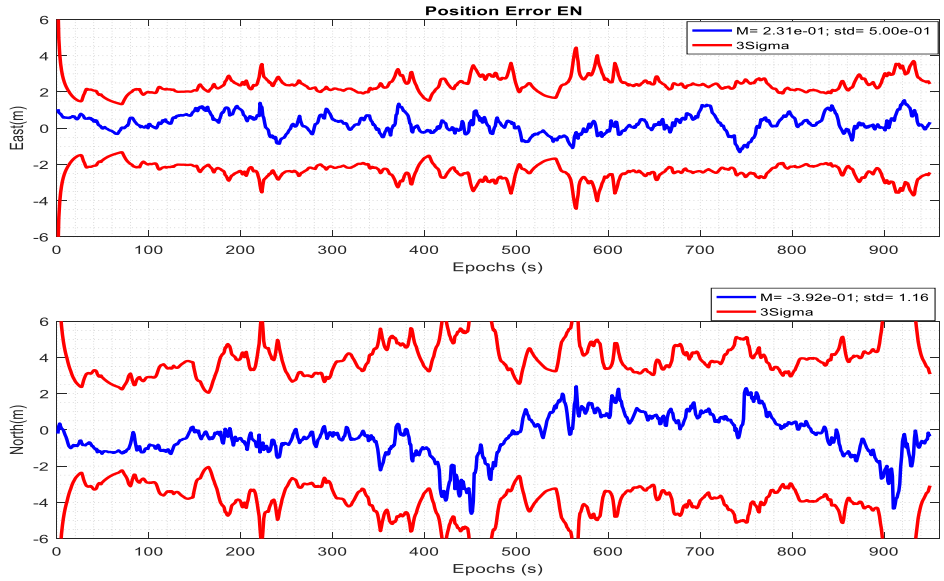

Figure 5-23. Horizontal DGPS position difference between estimated trajectory and the reference trajectory (Data set 1) with associated environment type chosen as 'Urban'.

Observing the driving trajectory of the Data set 1, it was truly not as a dense urban area as the are that the Data set 2 is associated to. As indicated in Figure 5-23, the general down-weighting of code measurements while choosing the urban type environment gives a better but pessimistic coverage of horizontal position errors by 3 sigma plots and worse positioning statistics. The mean horizontal (east and north directions) positioning biases are **[0.065, -0.189]** meters with standard deviations **[0.477, 0.928]** in Figure 5-22, while in Figure 5-23 the corresponding statistics are **[0.231, -0.392]** meters with standard deviations **[0.5, 1.16]**. The 95 percentile horizontal error value is **2.57** meters in Figure 5-23 whereas the value is **1.98** meters in Figure 5-22. Appropriately weighting code/Doppler measurements

brings a remarkable improvement. The tuning of observation variance-covariance matrix is proven to be important for a KF.

The code ICB calibration values mentioned in Section 4.3.3 have shown their ruleless relevance to GLONASS signal frequency and a magnitude level of meters. Therefore, the impossibility of being ignored requires the code ICB bias being corrected for the inclusion of GLONASS code/Doppler in positioning. The horizontal DGNSS positioning errors of the Data set 1 are plotted in Figure 5-24. The summary of positioning performances is presented in Table 5-4.

Comparing the Figure 5-22 and Figure 5-24, the improvement brought by the consideration of GLONASS code/Doppler measurements in positioning statistics is modest. However, the decrease of 3-sigma bounds is remarkable. The confidence in position solution has augmented. The values of HDOP are provided in Figure 5-25, with the red curve corresponding to the previous DGPS case and the blue line describing the DGNSS case. Compared to the case of DGPS, the value of DGNSS HDOP is always much smaller and the mean value is now 0.76 instead of 1.07. Therefore, in the case of Data set 1, when the only-GPS situation already shows a good geometry condition, the impact of refining the geometry by including GLONASS on the final positioning performance is limited.

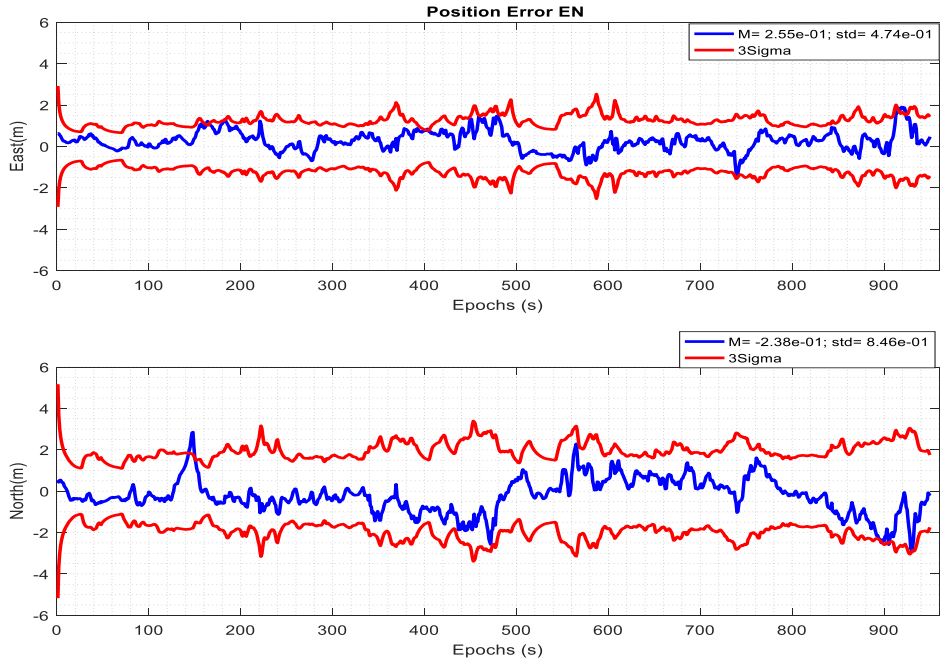

Figure 5-24. Horizontal DGNSS (GPS+GLONASS) position difference between estimated trajectory and the reference trajectory (Data set 1) with associated environment type chosen as 'Rural'

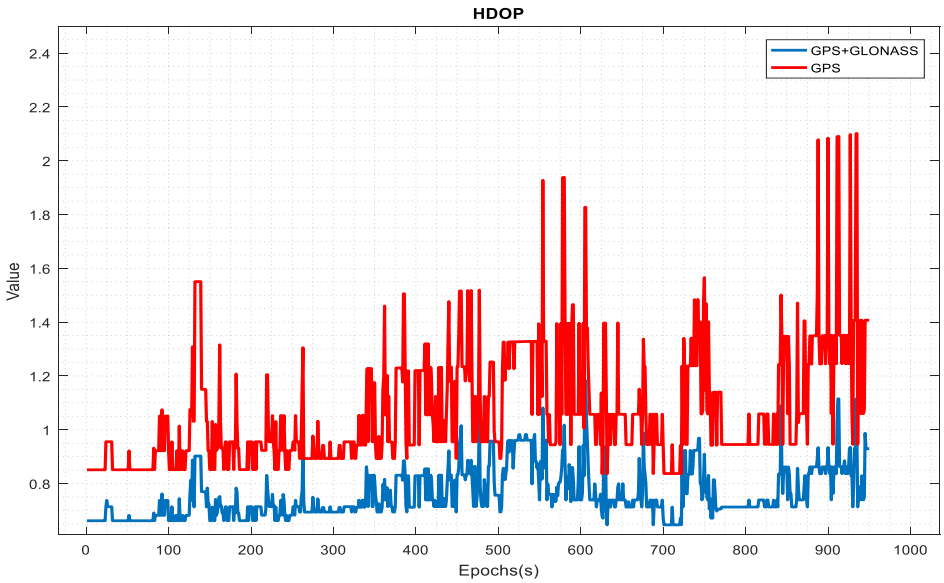

Figure 5-25. HDOP values of the DGPS case (in red) and the DGNSS case (in blue) (Data set 1)

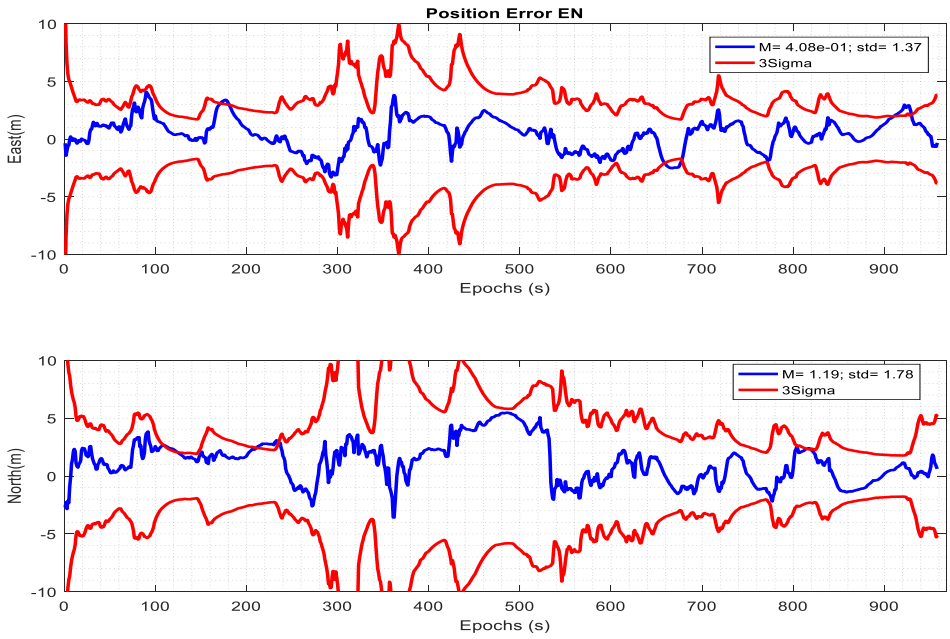

Figure 5-26. Horizontal DGPS position difference between estimated trajectory and the reference trajectory (Data set 2) with associated environment type chosen as 'Urban'. Masks are (30 dB/Hz, 10°).

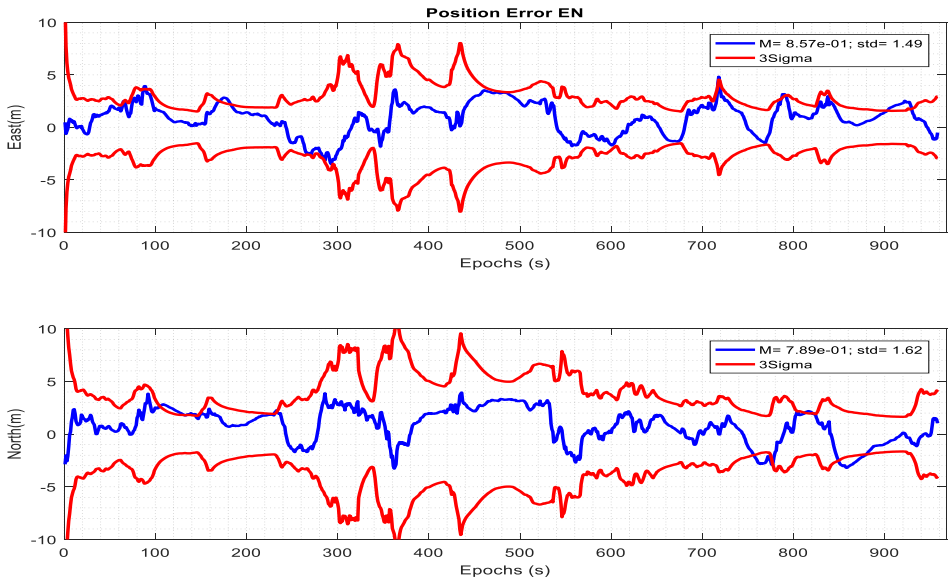

Figure 5-27. Horizontal DGNSS (GPS+GLONASS) position difference between estimated trajectory and the reference trajectory (Data set 2) with associated environment type chosen as 'Urban'. Masks are (30 dB/Hz, 10°).

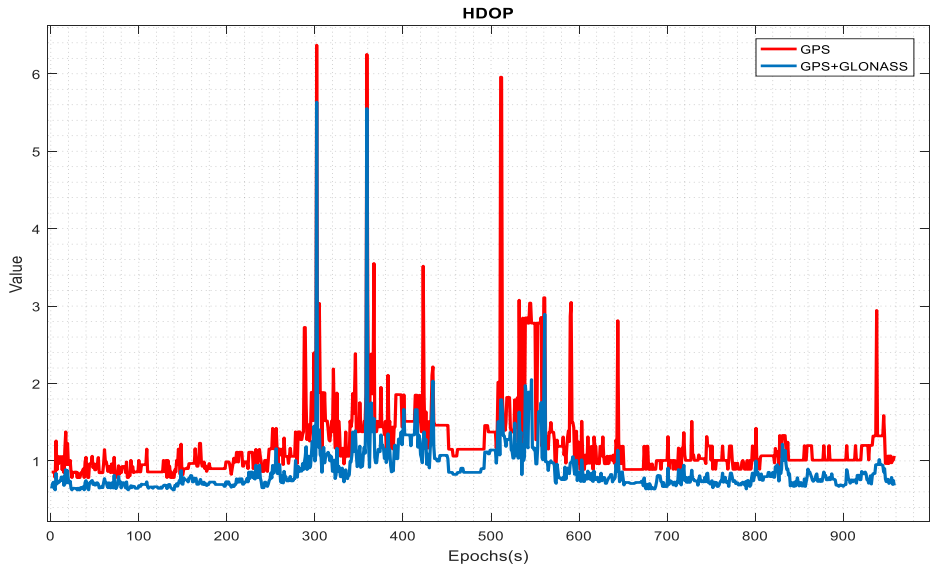

Figure 5-28. HDOP values of the DGPS case (in red) and the DGNSS case (in blue) (Data set 2)

As for the Data set 2, the DGPS and DGNSS horizontal position errors are provided in Figure 5-26 and Figure 5-27 respectively. The HDOP values of both cases are plotted in Figure 5-30. The positioning fluctuant zones, i.e. the interval between 300 and 400 epochs, and the interval after 500 epochs, are also reflected in HDOP plot. Unexpectedly, even though the mean value of HDOP has decreased from 1.21 in the DGPS case to 0.88 in the DGNSS case, a little worse performance is reflected by the horizontal performance percentiles listed in Table 5-4.

Clearly, a much more constrained environment is associated to the Data set 2 and GNSS measurements are more vulnerable to great multipath/NLOS errors. Indeed, the detection and exclusion of deteriorated observables are essential for an accurate solution. The original intention of the Innovation test is to allow using lower elevation and lower C/N0 masks while providing a double-check on measurement consistency, and eventually improve the satellite geometry. Nevertheless, herein with the Data set 2, the combination of the aforementioned masks values (30 dB.Hz, 10°) and the current Innovation test seems to be insufficient, as very few GNSS measurements have been detected even though their corresponding innovation values could reach to a level of 10 meter. Increasing the C/N0 mask to 35 dB.Hz while all other parameters are kept the same, new DGNSS positioning performances are summarized in the Table 5-4. Tracked number of satellites are provided in Figure 5-30. The temporal positioning errors of the Data set 2 with the higher signal strength are presented in Figure 5-29. With the original good GNSS geometry and good exclusion of outliers, the percentile values related to the Data set 1 have not deteriorated at all. However, an obvious performance improvement is present with the Data set 2 during the fluctuant zones (i.e., i.e. the interval between 300 and 400 epochs, and the interval after 500 epochs). Through those fluctuant sections, the positioning error has decreased and the curve is better bounded by 3-sigma plots. The intentional compromise towards the satellite geometry by keeping outliers but low-weighted may not a clever choice. Besides, concerning erroneous measurements elimination, the C/N0 mask is always an efficient scheme.

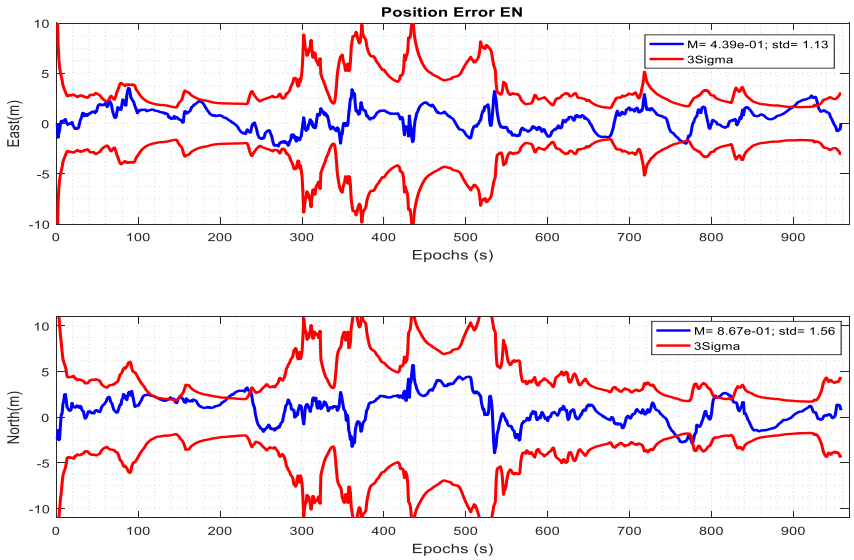

Figure 5-29. Horizontal DGNSS (GPS+GLONASS) position difference between estimated trajectory and the reference trajectory (Data set 2) with associated environment type chosen as 'Urban'. Masks are (35 dB/Hz, 10°).

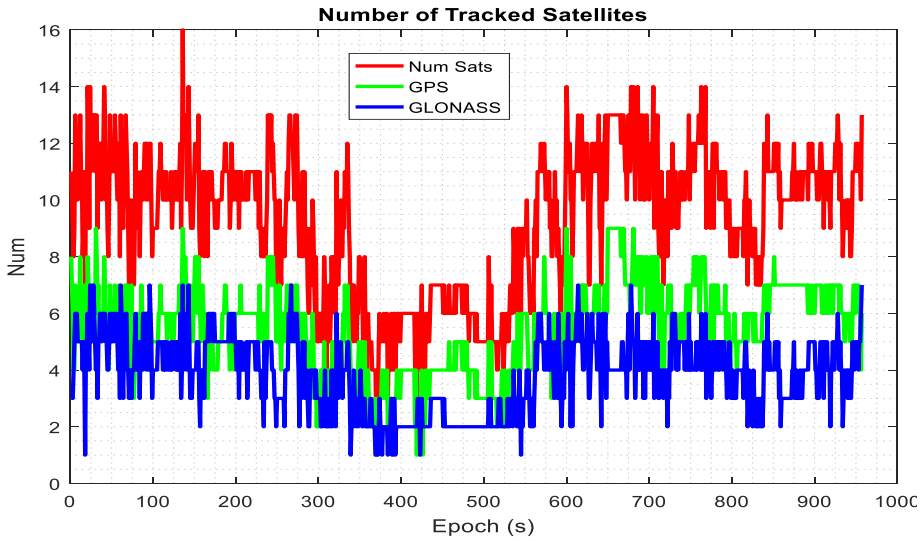

Figure 5-30. Number of tracked satellites during Data set 2. Elevation and C/N0 masks (10 degrees and 35 dB/Hz) are applied.

Table 5-4. Performance summary of the DGPS and DGNSS results

		Horizontal Positioning Error (in meter)		
		68th Percentile	**95th Percentile**	**98th Percentile**
Data Set 1	**DGPS** (30 dB.HZ)	**1.01**	**1.98**	**2.92**
	DGNSS (30 dB.HZ)	1.03	2.01	2.51
	DGNSS (35 dB.HZ)	0.98	2.12	2.40
Data Set 2	**DGPS** (30 dB.HZ)	**2.55**	**4.99**	**5.58**
	DGNSS (30 dB.HZ)	**2.59**	**5.74**	**6.31**
	DGNSS (35 dB.HZ)	**2.32**	**3.81**	**4.57**

5.2.3 GNSS-only Float RTK Solutions

In this section, the impact of the CS-DR scheme proposed in Section 4.5 is introduced. The word 'float' indicates that the ambiguities are kept float. Differential ambiguities are regarded as constant floats during the construction of the positioning KF whenever there was no CS detected.

The first attempt herein is to rely only on carrier phase LLI information, the status indicators of the tracking channel, to predict the presence of CS. The same configuration, related to the combination of elevation/signal-strength masks and the Innovation test applied on code/Doppler measurements in previous section is kept, i.e. (30 dB.Hz, 10°) for the Data 1 and (35 dB.Hz, 10°) for the Data 2. Results for the Data set 1 and the Data set 2 are illustrated respectively in Figure 5-31 and Figure 5-32.

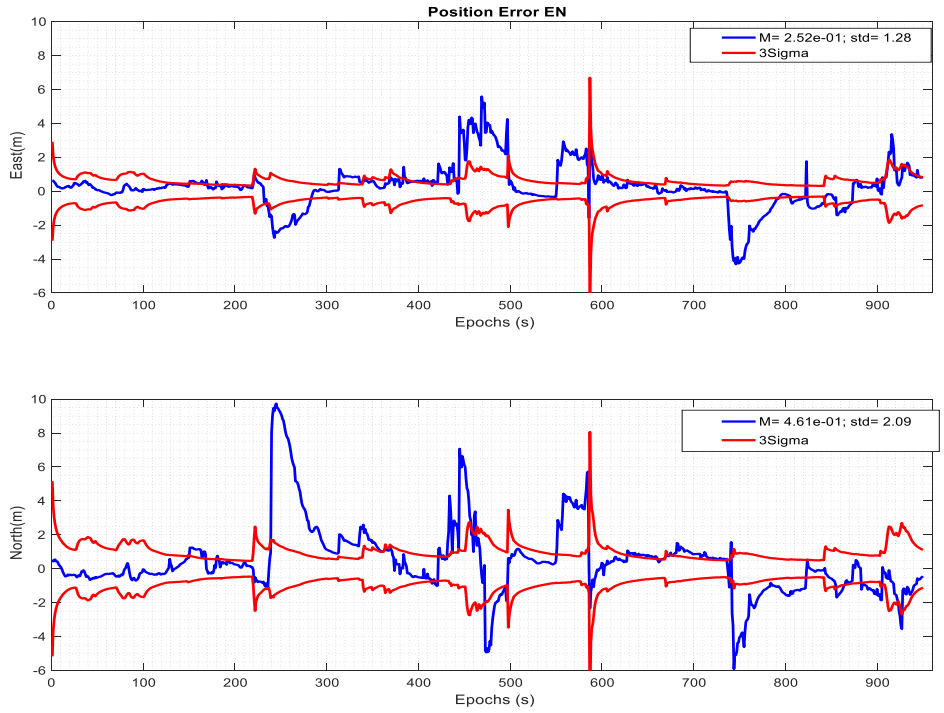

Figure 5-31. Horizontal Float GNSS (GPS+GLONASS) position difference between estimated trajectory and the reference trajectory (Data set 1) with associated environment type chosen as 'Rural'. CS Detection relies only on LLI.

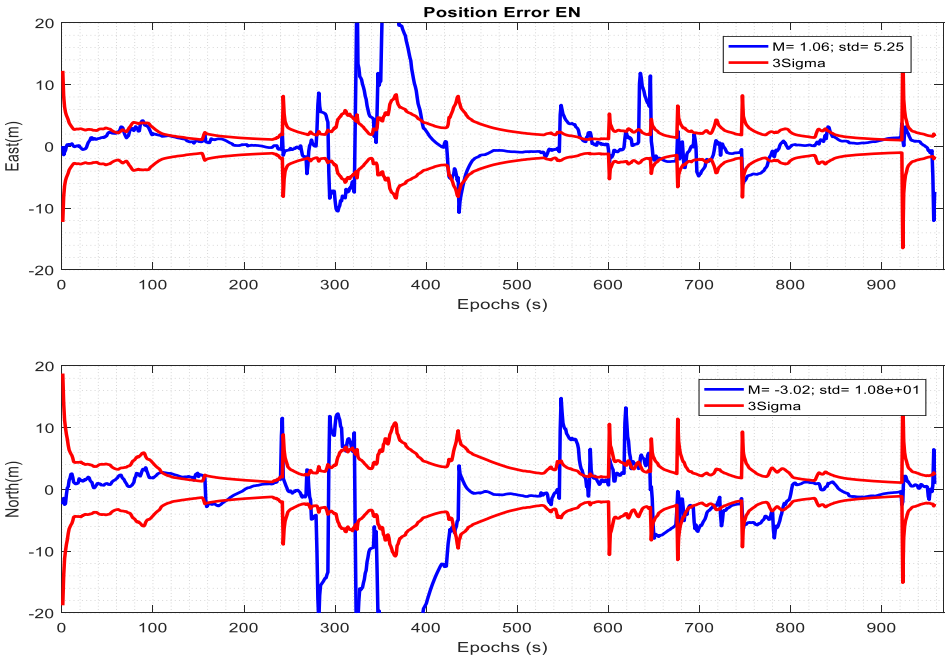

Figure 5-32. Horizontal Float GNSS (GPS+GLONASS) position difference between estimated trajectory and the reference trajectory (Data set 2) with associated environment type chosen as 'Urban'. CS Detection relies only on LLI.

Clearly a mass miss-detection of CS is observed. Position errors can easily exceed 10 meters and immensely break the 3-sigma envelopes. In order to determine the operation of the proposed CS-DR, 3

parameters $(\alpha_1, \alpha_2, \mathrm{N_{cs}})$ need first to be specified: α_1 the tolerable false alarm rate controlling the raw CS detection test; the absolute cycle number constraint $\mathrm{N_{cs}}$; α_2 the significance level defining the CS-free confirmation test. Different combinations of the triplet $(\alpha_1, \alpha_2, \mathrm{N_{cs}})$ are applied and solutions are compared based on the 95th percentile horizontal position error. As an extra check on carrier phase observables, another Innovation test working only on carrier phase innovations is implemented. All results regarding the Data set 1 are displayed in Table 5-5.

Table 5-5. 95th Percentile value of the horizontal position error for different CS-DR values $(\alpha_1, \alpha_2, N_{cs})$ (Data set 1)

		α_1					
		0.03			0.003		
	$\mathrm{N_{cs}}$	1	3	10	1	3	10
α_2	0	1.51	1.51	1.41	1.51	1.42	**1.39**
	0.5	1.54	1.48	1.77	1.54	1.48	**1.78**
	0.2	1.51	1.50	1.71	1.51	1.52	1.71

The CS-DR scheme was designed not only to be able to detect all underlying CS but also to leave alone those CS-free satellites, as the key to successful IAR is the continuous converging of differential ambiguities. Gladly, a first remark from the Table 5-5 is that there is no clue of miss-detecting vital CS for all triplet combinations. Nevertheless, there are still two values underlined respectively in red, the maximum 95th percentile error corresponding to the triplet $(\alpha_1, \alpha_2, \mathrm{N_{cs}}) = (0.003, 0.5, 10)$, and in green the minimum 95th percentile error corresponding to the triplet $(\alpha_1, \alpha_2, \mathrm{N_{cs}}) = (0.003, 0, 10)$, which deserve more attention. It seems that on the basis of all potential vital cycle slips being detected, the less sensitive CS-DR scheme presents better positioning results. Take the instance of the triplet $(\alpha_1, \alpha_2, \mathrm{N_{cs}}) = (0.003, 0, 10)$, the detection of potential CS on each tracked satellite on each temporal epoch is depicted in red cross in Figure 5-33. For each epoch, the number of satellites declared CS-free and the number of satellites detected with CS are depicted in Figure 5-34. The total number of epochs holding (more than 5) CS-free satellites is **862** and there are **734** epochs in which CS-deteriorated satellites are detected.

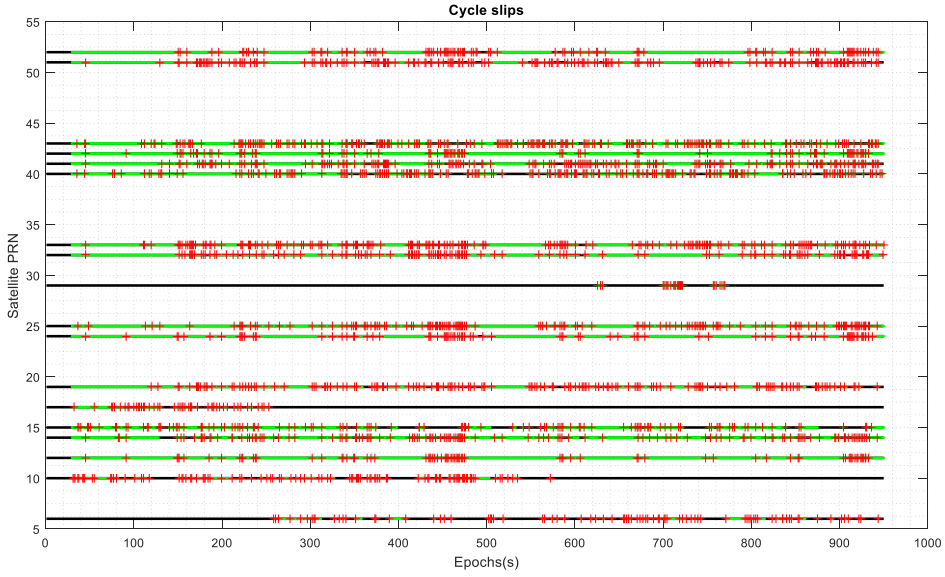

Figure 5-33. Detected presence of potential CS marked in red cross, with CS-DR scheme taking the values $(\alpha_1, \alpha_2, N_{cs}) = (0.003, 0, 10)(Data\ set\ 1)$.

An indicator, CS-free rate, which is the ratio in percentage between the number of epochs having CS detected and the number of epochs having the corresponding satellite tracked, is used here to provide a general vision of CS on carrier phase observables. To provide a comparison of CS detection rates between the triplets $(0.003, 0, 10)$ and $(0.003, 0.5, 10)$, the detailed CS-free rates for each satellite are listed in Table 5-6. A general decline of the CS-free rate between **4.6%** and **13%** on each satellite when a more sensitive CS-DR triplet $(0.003, 0.5, 10)$ is observed.

Table 5-6. CS-free rates for each tracked satellite for two CS-DR triplet values $(\alpha_1, \alpha_2, N_{cs})$ (Data set 1)

	CS-free rate (CS presence/Satellite visibility)								
PRN	**6**	**10**	**12**	**14**	**15**	**17**	**19**	**24**	**25**
$(0.003, 0, 10)$	62.9%	62.5%	91.4%	82.7%	81.1%	63.4%	78.6%	90.4%	83.0%
$(0.003, 0.5, 10)$	58.1%	55.4%	78.4%	72.8%	71.7%	59.5%	70.6%	77.9%	72.8%
PRN	**29**	**32**	**33**	**40**	**41**	**42**	**43**	**51**	**52**
$(0.003, 0, 10)$	30.6%	85.4%	78.4%	68.1%	78.4%	89.8%	70.5%	77.8%	88.0%
$(0.003, 0.5, 10)$	25.0%	74.5%	69.8%	60.3%	69.5%	77.7%	62.6%	69.8%	76.7%

What's more, in order to hold the continuity of ambiguity estimation, the number of epochs having more than 5 satellites identified as CS-free is checked. In the case corresponding to the triplet $(\alpha_1, \alpha_2, \mathrm{N_{cs}}) = (0.003, 0, 10)$, where we obtain the minimum 95th percentile error, **862** epochs are declared holding more than 5 CS-free satellites. However, the number of 5 CS-free satellites epochs decreases to **737** in the case $(\alpha_1, \alpha_2, \mathrm{N_{cs}}) = (0.003, 0.5, 10)$ where we obtain the largest 95th percentile error, which means in other words that in total **125** epochs there are CS-free satellites contaminated. The number of epochs having satellites detected with CS arises from **734** to **740**. The temporal conditions are reflected in Figure 5-34 and Figure 5-35. The triplet value $(\alpha_1, \alpha_2, \mathrm{N_{cs}}) = (0.003, 0, 10)$ will be kept in following test on Data set 1 if there is no specific statement made. The horizontal position results are presented in Figure 5-36. A general good coverage of the 3-sigma bounds over the positioning errors is observed. Besides, the good handling of carrier phase measurements provides a smoother and a more accurate position solution compared to Figure 5-24.

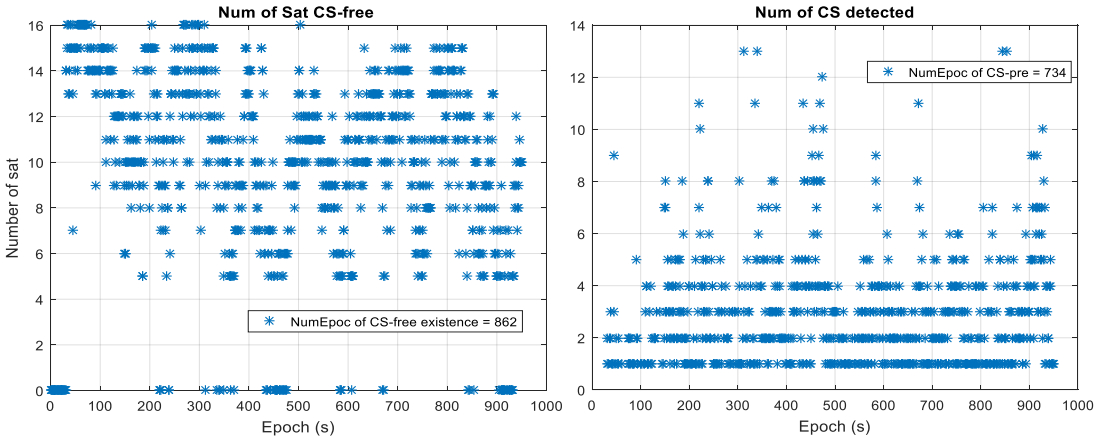

Figure 5-34. Data set 1. Number of epochs holding satellites declared CS-free(on the left), and Number of epochs holding satellites declared CS- deteriorated (on the right). CS-DR scheme takes the values $(\alpha_1, \alpha_2, N_{cs}) = (0.003, 0, 10)$.

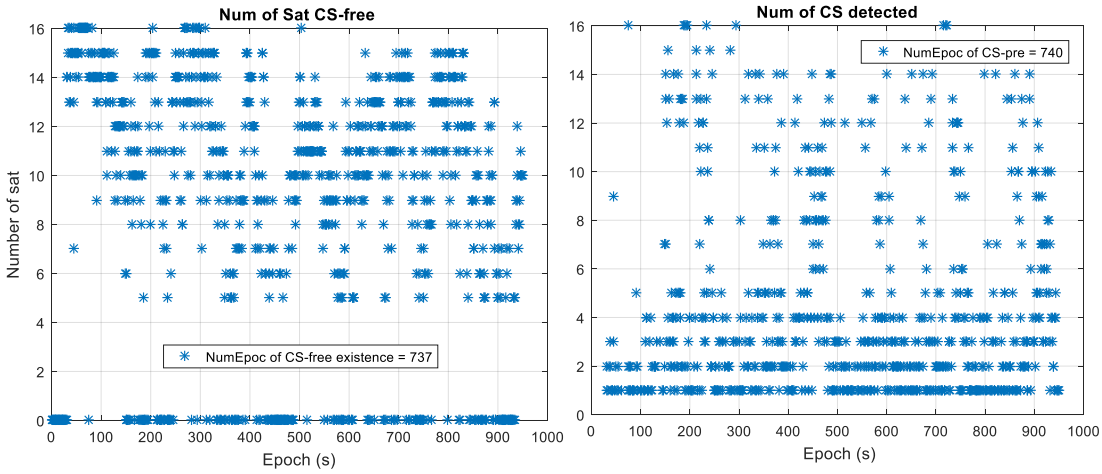

Figure 5-35. Data set 1. Number of epochs holding satellites declared CS-free(on the left), and Number of epochs holding satellites declared CS- deteriorated (on the right). CS-DR scheme takes the values $(\alpha_1, \alpha_2, N_{cs}) = (0.003, 0.5, 10)$.

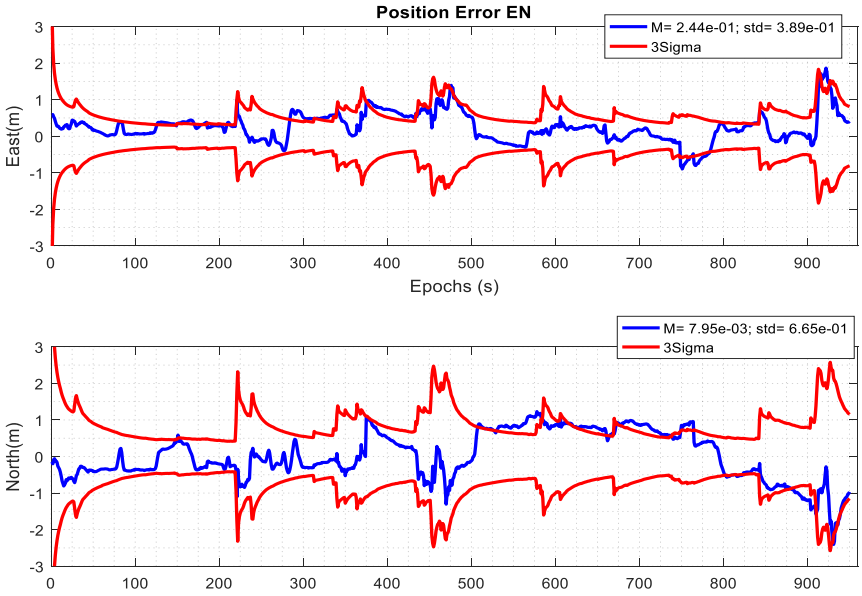

Figure 5-36. Horizontal Float GNSS (GPS+GLONASS) position difference between estimated trajectory and the reference trajectory (Data set 1) with associated environment type chosen as 'Rural'. CS-DR scheme takes the values $(\alpha_1, \alpha_2, N_{cs}) = (0.003, 0, 10)$.

In Table 5-7 are displayed performance summary values related to the Data set 2. The triplet value $(\alpha_1, \alpha_2, \mathrm{N_{cs}}) = (0.003, 0, 10)$, which works the best in the case of Data set 1, provides a relative large 95$^{\text{th}}$ percentile error. According to the Table 5-7, the consideration of an extra CS-free confirmation test with $\alpha_2 = 0.5$ would be more appropriate. As indicated in Figure 5-37 and Figure 5-38, the number of epochs having more than 5 CS-free satellites drops from **611** of the case $(\alpha_1, \alpha_2, \mathrm{N_{cs}}) = (0.003, 0, 10)$ to **586** $(\alpha_1, \alpha_2, \mathrm{N_{cs}}) = (0.003, 0.5, 10)$. The temporal horizontal positioning errors of the two triplet values: $(\alpha_1, \alpha_2, \mathrm{N_{cs}}) = (0.003, 0, 10)$ and $(\alpha_1, \alpha_2, \mathrm{N_{cs}}) = (0.003, 0.5, 10)$, are plotted separately in Figure 5-39 and Figure 5-40. A general good coverage of the 3-sigma bounds over the positioning errors

is observed on both figures. Compared to the Figure 5-39, an obvious improvement is remarked around the epoch 300 as a more stable solution encompassed by the 3-sigma bounds is observed in Figure 5-40. Similarly, the triplet value $(\alpha_1, \alpha_2, \mathrm{N_{cs}}) = (0.003, 0.5, 10)$ will be kept in following test on Data set 2 if there is no specific statement made.

Table 5-7. 95th Percentile value of the horizontal position error for different CS-DR values $(\alpha_1, \alpha_2, N_{cs})$ (Data set 2)

		α_1					
		0.03			0.003		
	$\mathrm{N_{cs}}$	1	3	10	1	3	10
α_2	0	3.29	3.628	**4.634**	3.296	3.628	**4.611**
	0.5	3.30	3.343	**3.174**	3.30	3.344	**3.175**
	0.2	3.294	3.37	3.474	3.295	3.373	3.455

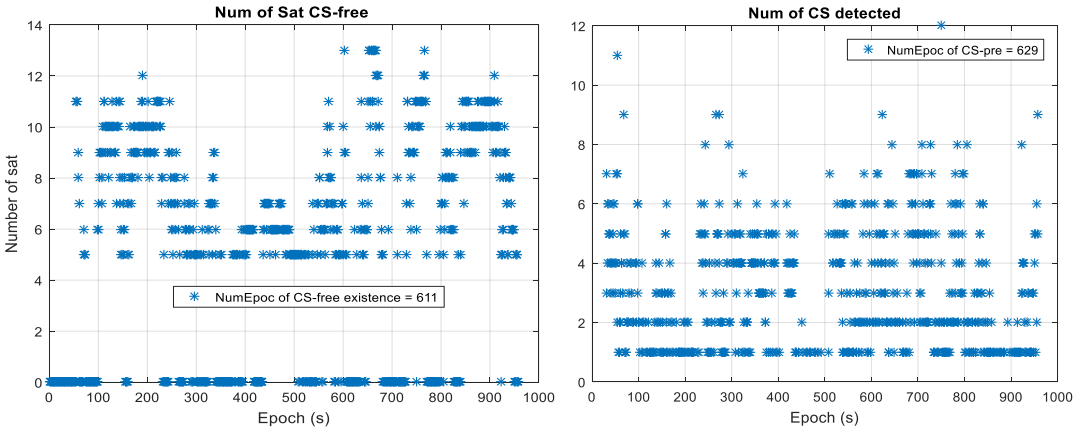

Figure 5-37. Data set 2. Number of epochs holding satellites declared CS-free(on the left), and Number of epochs holding satellites declared CS- deteriorated (on the right). CS-DR scheme takes the values $(\alpha_1, \alpha_2, N_{cs}) = (0.003, 0, 10)$.

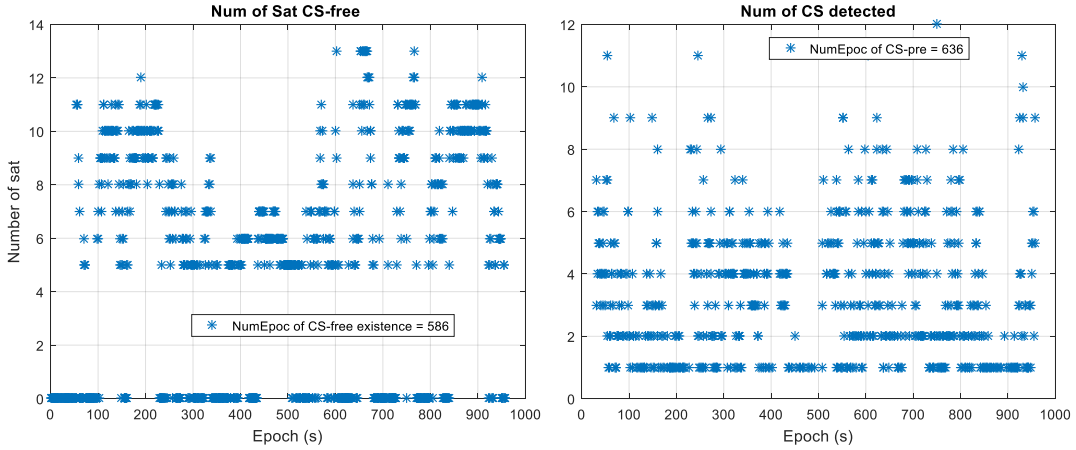

Figure 5-38. Data set 2. Number of epochs holding satellites declared CS-free(on the left), and Number of epochs holding satellites declared CS- deteriorated (on the right). CS-DR scheme takes the values $(\alpha_1, \alpha_2, N_{cs}) = (0.003, 0.5, 10)$.

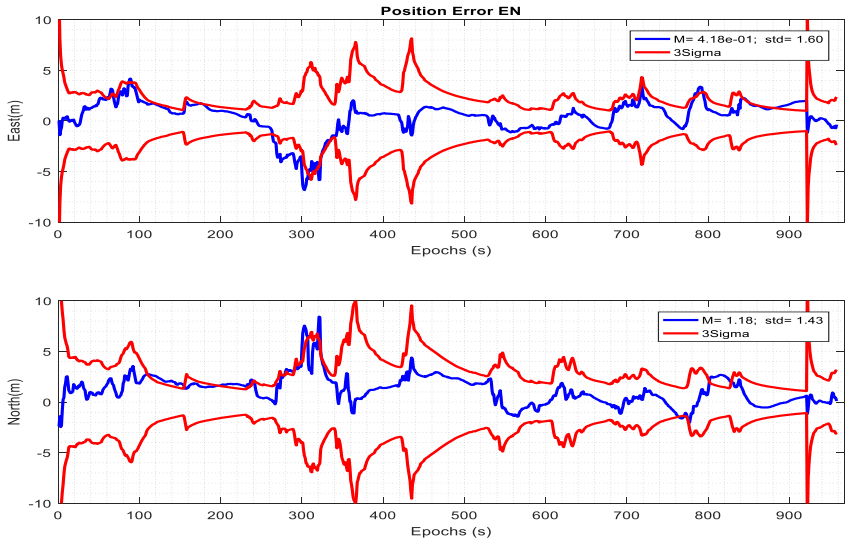

Figure 5-39. Horizontal Float GNSS (GPS+GLONASS) position difference between estimated trajectory and the reference trajectory (Data set 2) with associated environment type chosen as 'Rural'. CS-DR scheme takes the values $(\alpha_1, \alpha_2, N_{cs}) = (0.003, 0, 10)$.

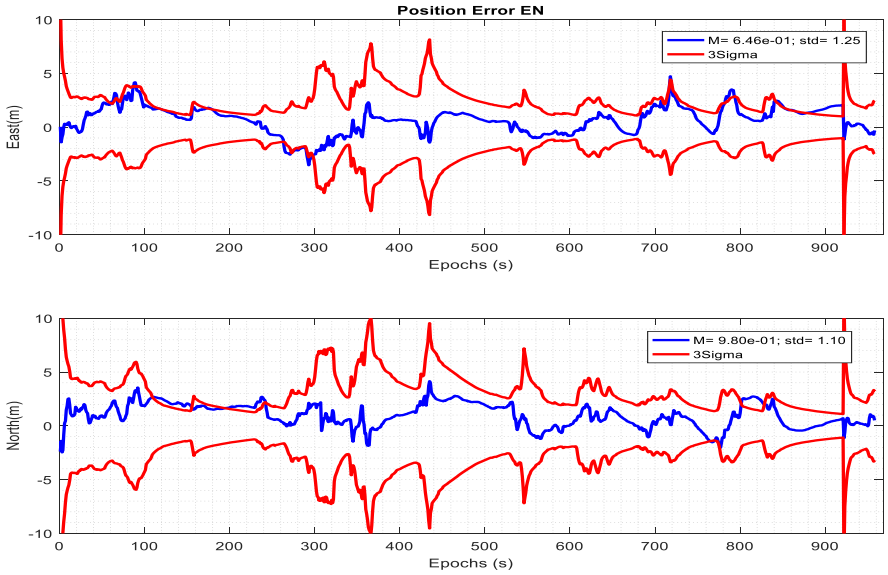

Figure 5-40. Horizontal Float GNSS (GPS+GLONASS) position difference between estimated trajectory and the reference trajectory (Data set 2) with associated environment type chosen as 'Rural'. CS-DR scheme takes the values $(\alpha_1, \alpha_2, N_{cs}) = (0.003, 0.5, 10)$.

5.2.4 GNSS-only AR Solution

In this section, the principle of the proposed Partial-IAR (Partial-Integer Ambiguity Resolution) scheme proposed will be discussed. Estimated float DD GPS ambiguities are directly processed, while calibrated carrier phase ICBs first need to be isolated from GLONASS ambiguities before entering the IAR (Integer Ambiguity Resolution) scheme.

First of all, in order to provide a baseline IAR solution of the Data set 1, the classic FT-RT (Fixed Threshold-Ratio Test)is applied. A minimum number of 5 DD ambiguities to enter IAR is generally required [7] and an empirical ratio threshold of 2 is taken. Horizontal position errors are presented in Figure 5-41. Obvious positioning errors have been remarked due to false ambiguity resolutions.

In order to provide a comparable solution, the same ratio threshold of 2 and a minimum number of 5 ambiguities are both adopted in the utilization of the modified Partial-IAR scheme. In addition, a minimum threshold for the probability of success fixing $P_{S,0} = 99.5\%$ (default value) is set.

For Data set 1, in Figure 5-42 are displayed the horizontal position errors as a function of time. The performance summary is listed in Table 5-8. Better horizontal percentile values are obtained with the modified Partial-IAR scheme. Then, even though with similar fix rate **5.6%,** a much lower wrong fixing rate of **16.7%** is achieved in the Partial-IAR case. Nevertheless, facing a biased fixed solution, it is always better to keep solutions float. However, the overall performance is not at all satisfying. Indeed, the fact that float solution is not accurate enough (providing a low P_S value) leads to a rather frequent fail of the ambiguity validation test. Despite the ratio test between the two best integer candidates, the number of epochs having more than 5 ambiguities passing through the Partial-IAR scheme, while holding a P_S greater than $P_{S,0}$ is only **12.8%.** The fixing rate is highly limited in the beginning. The value of P_S calculated based on the best 5 satellites having the lowest uncertainty is plotted in Figure 5-43.

The additional information provided by other equipment, for example, the inertial units can be very interesting. First of all, the better confidence on rover's attitude gives the choice of trusting the covariance associated to estimated CSs, other than applying a general big covariance inflation of all detected CS-contaminated ambiguities. Besides, float estimates of ambiguities are expected to be more accurate due to the incorporation of IMU measurements.

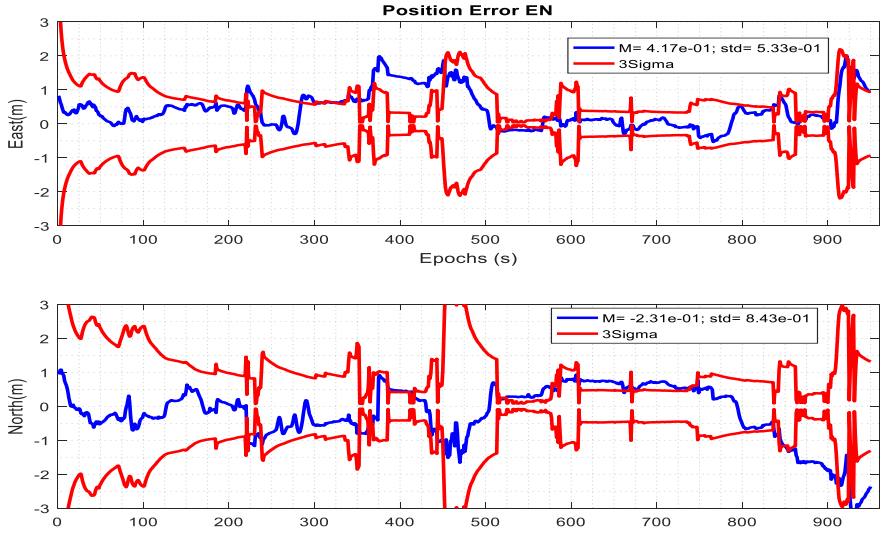

Figure 5-41. Horizontal performance of the IAR solution using FT-RT as the ambiguity validation method. (Data set 1)

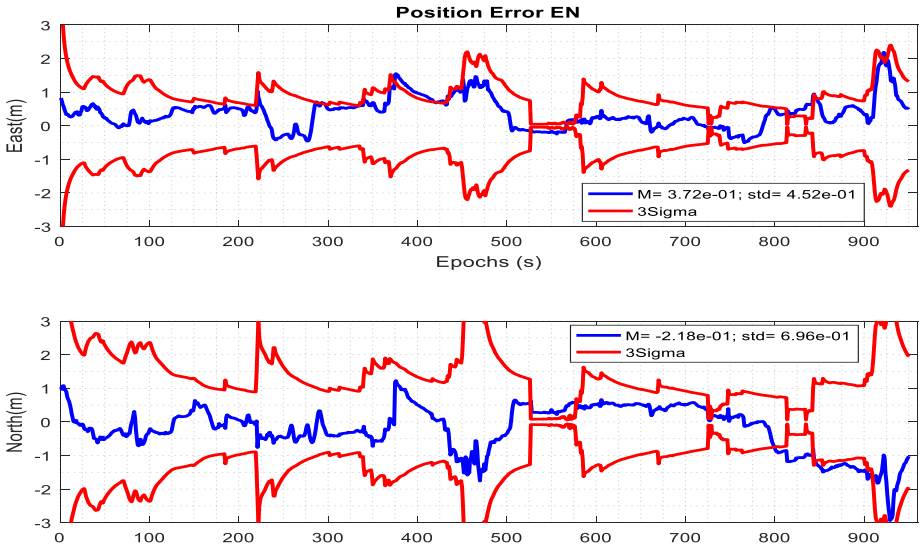

Figure 5-42. Horizontal performance of the IAR solution using the proposed Partial-IAR as the ambiguity validation method. (Data set 1)

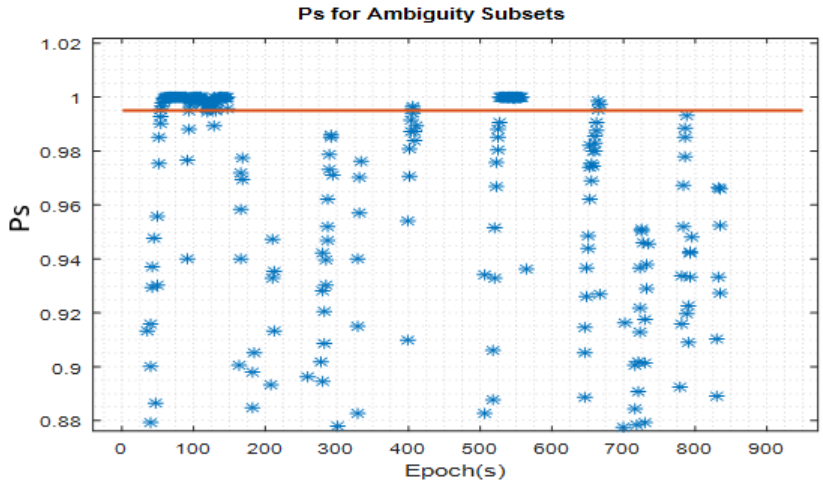

Figure 5-43. The probability of success Ps calculated based on the 5 ambiguities having the lowest uncertainty (Data set 1)

Table 5-8. Performance summary of the IAR results processing the Data set 1 using FT-RT and a modified Partial-IAR validation schemes.

	Horizontal Positioning Error (in meter)				
Data Set 1	**68th Percentile**	**95th Percentile**	**98th Percentile**	**Fix Rate**	**Wrong Fix Rate**
FT-RT	0.84	2.12	3.25	5.4%	63%
Partial-IAR	0.74	1.80	2.52	5.6%	16.7%

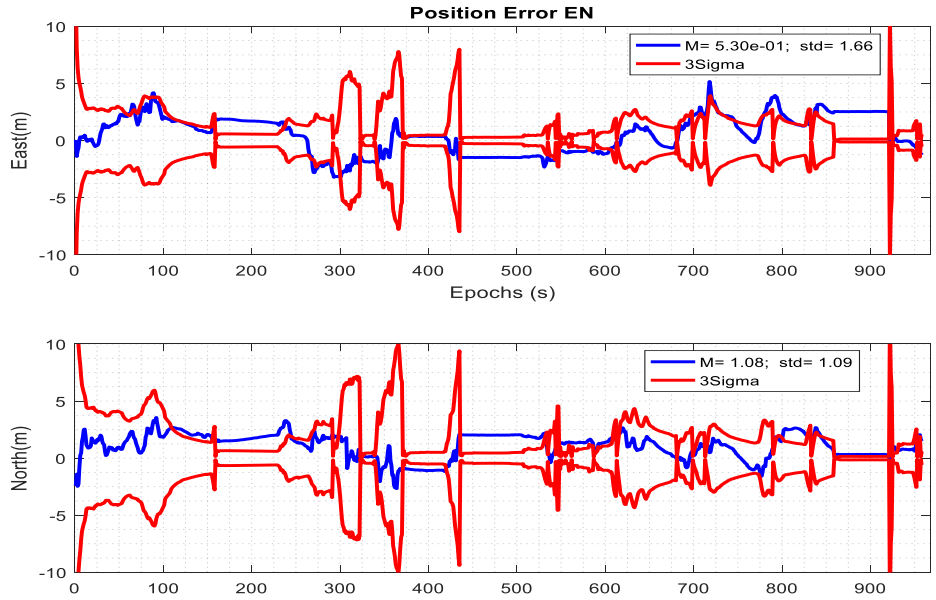

Figure 5-44. Horizontal performance of the IAR solution using FT-RT as the ambiguity validation method. (Data set 2)

Data set 2 measurements were collected in a much denser environment than data set 1 measurements. The classical IAR (FT-RT) scheme with the ratio threshold of 2 and minimum 5 satellites being fixed provides a positioning error plotted in Figure 5-44. The fixing rate is still low at **4%**, while the wrong fixing rate is relatively high at **97.1%.**

As for the case with modified Partial-IAR scheme, there is no fixing success declared. Same results as for the previous float RTK are obtained. Too frequent appearances of cycle slips clearly interrupt the resolution of float ambiguities. The minimum threshold selected for the success rate is never exceeded when a minimum number of 5 satellites is required. The temporal success rate is provided in Figure 5-45.

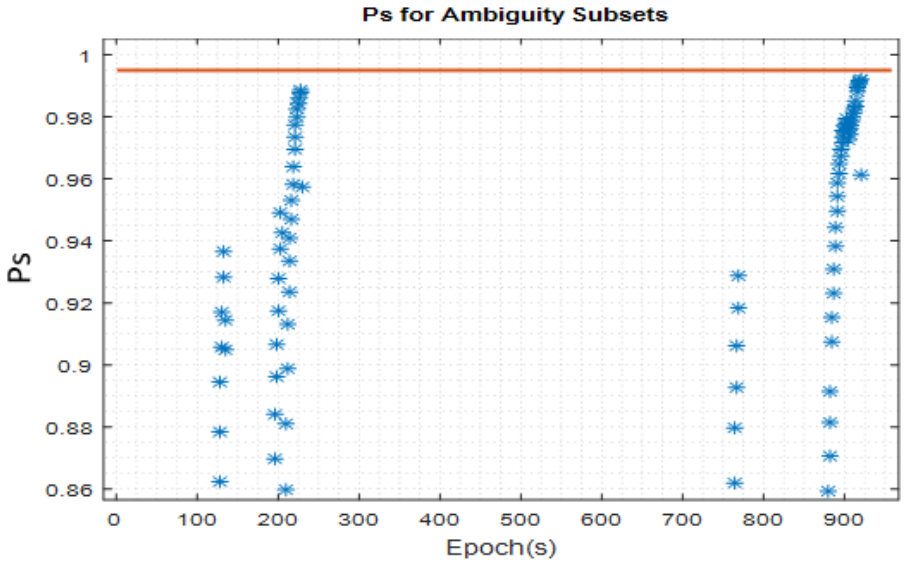

Figure 5-45. The probability of success Ps calculated based on the 5 ambiguities having the lowest uncertainty (Data set 2)

6 Improving the Navigation with GNSS/INS Integration

An Inertial Navigation System (INS) is an autonomous system that provides the position, velocity and attitude information of the rover with the help of a set of inertial sensors (also known as inertial measurement unit (IMU)), and a navigation processor [1], [2]. The INS is less vulnerable to outliers than the GNSS especially in a constrained environment. However, the navigation quality of a low-cost INS degrades quickly in a stand-alone mode mainly because of measurement biases. Therefore, to improve the over-all navigation performance, a low-cost INS will be integrated with GNSS.

In this chapter, there will be firstly some introductory sections on the INS. Then the GNSS/INS integration techniques are interpreted in the end.

6.1 Overview of INS

An IMU nominally consists of three accelerometers to measure the vehicle accelerations in three mutually orthogonal directions, and three gyroscopes to scale the rotation in three mutually orthogonal directions. Usually, these two triads are parallel, sharing the same origin. A strapdown architecture is typically applied, meaning that the sensor axes are fixed in the body of the IMU.

IMUs are classified into different grades according to their performance: the marine-grade, the aviation grade, the tactical grade and the automotive grade [2], [67]. Generally the higher the grade is, the more it costs. A marine-grade INS, used in ships, submarines or some spacecraft, can cost over 1 million dollars while a navigation drift of less than 1.8 km over a whole daytime is guaranteed. Aviation-grade INSs, designed especially for military and commercial airlines, can cost around 100, 000 dollars while a horizontal navigation drift in the first hour of operation should be less than 1.5 km. A tactical-grade INS, at a price between 5000 dollars to 20000 dollars, is expected to provide reliable navigation performance for a few minutes.

The miniaturization, low cost, low power consumption and mass-production capacity have made the micro-electro-mechanical system (MEMS) sensors more and more attractive for automotive applications [2], [24]. However, compared to higher grade sensors, MEMS sensors still exhibit larger errors which demand careful handling.

A dead reckoning principle is usually applied in INS to determine the vehicle's current position and attitudes information, with previous knowledge of the vehicle and the measured accelerations and angular rates at the output of inertial sensors, together with a gravity field model or baro-altimeter information [2], [28]. Integrations over time of accelerations and angular rates are used to update the information.

In this section, the modeling of IMU measurements will be first given, followed by the relationships between several involved frames.

To avoid confusion, the notation $\boldsymbol{x}_{\boldsymbol{\beta\alpha}}^{\boldsymbol{\gamma}}$ is used to describe the kinematic quantities $\boldsymbol{x}$, such as the position, the velocity, the accelerations, or the angular rate, of the object frame $\boldsymbol{\alpha}$ with respect to the reference frame $\boldsymbol{\beta}$ resolved in the frame $\boldsymbol{\gamma}$ axes.

6.1.1 Attitudes of Vehicle

Euler angles are terms used to describe the attitudes of the vehicle with respect to the local *n-frame*. Before introducing the attitudes, the body frame, normally aligned with the vehicle frame, should be specified.

Body frame (right, forward, up, b-frame): the body frame, is defined as

- the origin coinciding with the center of IMU
- x^b-axis pointing towards the right of the vehicle, the rotating-axis of the pitch angle,
- y^b-axis pointing towards the front of the vehicle, the rotating-axis of the roll angle, and
- z^b-axis pointing towards the vertical up direction of the vehicle, along which is rotating the yaw angle.

Euler angles (Roll, Pitch, Heading(Yaw)): attitudes of *b*-frame with reference to local *n*-frame, see following Figure 6-1.

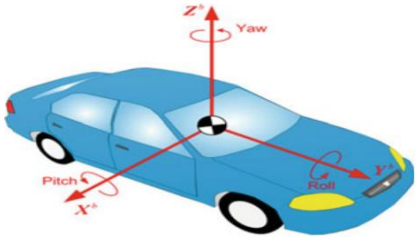

Figure 6-1. The b-frame and attitudes of a vehicle, extracted from [28]

6.1.2 Modeling of IMU Measurements

An accelerometer can be typically modelled as consisting of a known proof mass, which is restrained by a pair of springs and free to move along the sensitive axis. The displacement from the equilibrium position is measured to output finally the specific force on the mass. With the presence of the gravitational field, the relation between the specific force and the acceleration is given by:

$$\boldsymbol{f_{ib}^b} = \boldsymbol{a_{ib}^b} - \boldsymbol{\gamma_{ib}^b} \tag{6-1}$$

where

- $\boldsymbol{f_{ib}^b}$ is the three-dimensional specific force,
- $\boldsymbol{\gamma_{ib}^b}$ is the gravitational acceleration, and
- $\boldsymbol{a_{ib}^b}$ is the vehicle acceleration with respect to (w.r.t) the *i-frame*.

A gyroscope is a sensor used to provide angular rates of the vehicle with respect to the inertial frame. The three main types of gyros are spinning mass, optical, and vibratory. Each has its own physical principle. For more details, refer to [24], [95].

The IMU measurements are typically corrupted by errors like biases, scale factors and misalignment errors, etc. At the outputs of IMU sensors, collected raw measurements are modelled as following [2], [23]:

$$\begin{aligned} \tilde{\boldsymbol{f}}_{\boldsymbol{ib}}^{\boldsymbol{b}} &= \boldsymbol{b_a} + (\boldsymbol{I_3} + \boldsymbol{S_a})\boldsymbol{f_{ib}^b} + \boldsymbol{\eta_a} \\ \tilde{\boldsymbol{\omega}}_{\boldsymbol{ib}}^{\boldsymbol{b}} &= \boldsymbol{b_g} + (\boldsymbol{I_3} + \boldsymbol{S_g})\boldsymbol{\omega_{ib}^b} + \boldsymbol{\eta_g} \end{aligned} \tag{6-2}$$

Biases in gyroscope and accelerometer are typically composed of two parts [2], [67], [87]:

- **static** (known as turn on bias, constant throughout an IMU operating period, but varies from run to run) and

- **dynamic** (in run bias/bias instability, varies over periods of order a minute)

$$\boldsymbol{b_a} = \boldsymbol{b_{as}} + \boldsymbol{b_{ad}}$$
$$\boldsymbol{b_g} = \boldsymbol{b_{gs}} + \boldsymbol{b_{gd}} \tag{6-3}$$

Generally, the static parts are modelled as random constant processes (or calibrated) and the dynamic parts are represented with a first-order Gauss-Markov process.

The scale factor error is the departure of the input-output gradient of the instrument from unity. The scale factor errors of the gyro and accelerometer are denoted as $\boldsymbol{s_a} = [s_{a,x}, s_{a,y}, s_{a,z}]$ and $\boldsymbol{s_g} = [s_{g,x}, s_{g,y}, s_{g,z}]$. Cross-coupling errors arise from the misalignment of the sensitive axes of the inertial sensors with respect to the orthogonal axes of the body frame, due to manufacturing limitations. In vibratory sensors, cross-coupling errors can also arise due to the cross-talk between individual sensors. The notation $m_{*,\alpha\beta}$ denotes the cross-coupling coefficient sensed by the α-axis of the sensor * due to the β -axis. Finally, the scale factor and the cross-coupling errors for a nominally orthogonal accelerometer and gyro triad:

$$\boldsymbol{S_a} = \begin{bmatrix} s_{a,x} & m_{a,xy} & m_{a,xz} \\ m_{a,yx} & s_{a,y} & m_{a,xz} \\ m_{a,zx} & m_{a,zy} & s_{a,z} \end{bmatrix}, \boldsymbol{S_g} = \begin{bmatrix} s_{g,x} & m_{g,xy} & m_{g,xz} \\ m_{g,yx} & s_{g,y} & m_{g,xz} \\ m_{g,zx} & m_{g,zy} & s_{g,z} \end{bmatrix}$$

The scale factor and the cross-coupling errors are unit-less and typically expressed in parts per million (ppm).

Strictly, all above states need be modeled to fully represent an INS navigation, which is however only theoretically possible. In practical applications, limited to vehicle dynamics, data collection campaigns, and the fact that adding more states will weaken the system, the relatively small cross-coupling coefficients are omitted [67]. In this PhD, considering the computation efficiency, only the diagonal parameters of the matrix $\boldsymbol{S_{\blacksquare}}$ are thus considered. In fact, along with the technology development in MEMS, the scale factor error even for very low-cost MEMS sensors is over-bounded by a very low percentage (e.g., 3%)[24]. According to the data sheet of the XSENS MTi, the one used in this study, a scale factor error less than 0.5% is guaranteed [96]. Therefore, a simplified modeling of INS measurements only with biases parameters is also acceptable.

6.1.3 Coordinate Transformation Matrix between Reference Frames

For different conveniences or objectives, a specific reference frame is sometimes preferred than others to better describe a quantity. Thus, the notion of a coordinate transformation matrix $\boldsymbol{C_{\alpha}^{\beta}}$, also known as the direction cosine matrix (DCM), need be brought up, which transforms a quantity vector expressed in $\boldsymbol{\alpha}$ frame axes to $\boldsymbol{\beta}$ frame axes [2]. In this section, the coordinate transformation matrices between frame pairs (*b*-frame, *n*-frame), (*e*-frame, *i*-frame), and (*e*-frame, *n*-frame) are interpreted.

6.1.3.1 *b*-frame and *n*-frame

Euler angles $\boldsymbol{\psi_{nb}} = [\phi_{nb}, \theta_{nb}, \psi_{nb}]$, respectively (roll, pitch, heading), are used to describe attitudes of the *b*-frame w.r.t the local *n*-frame. The transformation matrix from *b*-frame to *n*-frame is broken into 3 successive rotations around axes in order z^b, x^b and y^b, represented by $\boldsymbol{C_b^n}$ [23]:

$$\boldsymbol{C_b^n} = \left(\boldsymbol{C_n^b}\right)^{\boldsymbol{T}} = \boldsymbol{R_z}(\psi_{nb})\boldsymbol{R_x}(-\theta_{nb})\boldsymbol{R_y}(-\phi_{nb}) \tag{6-4}$$

where

$$\boldsymbol{R_z}(\psi_{nb}) = \begin{bmatrix} cos(\psi_{nb}) & sin(\psi_{nb}) & 0 \\ -sin(\psi_{nb}) & cos(\psi_{nb}) & 0 \\ 0 & 0 & 1 \end{bmatrix},\ \boldsymbol{R_x}(-\theta_{nb}) = \begin{bmatrix} 1 & 0 & 0 \\ 0 & cos\theta_{nb} & -sin\theta_{nb} \\ 0 & sin\theta_{nb} & cos\theta_{nb} \end{bmatrix},$$

$$\boldsymbol{R_y}(-\phi_{nb}) = \begin{bmatrix} cos\phi_{nb} & 0 & sin\phi_{nb} \\ 0 & 1 & 0 \\ -sin\phi_{nb} & 0 & cos\phi_{nb} \end{bmatrix}.$$

- **$\boldsymbol{C_b^n}$ and Euler angles**

The detailed representation of $\boldsymbol{C_b^n}$ depending on Euler angles is thus by expanding Eq(6-4):

$$\boldsymbol{C}_b^n\ (1,1) = cos\phi_{nb}cos\psi_{nb} + sin\phi_{nb}sin\theta_{nb}sin\psi_{nb} \qquad \boldsymbol{C}_b^n\ (1,2) = cos\theta_{nb}sin\psi_{nb}$$

$$\boldsymbol{C}_b^n\ (2,1) = -cos\phi_{nb}sin\psi_{nb} + sin\phi_{nb}sin\theta_{nb}cos\psi_{nb} \qquad \boldsymbol{C}_b^n\ (2,2) = cos\theta_{nb}cos\psi_{nb}$$

$$\boldsymbol{C}_b^n\ (1,3) = sin\phi_{nb}cos\psi_{nb} - cos\phi_{nb}sin\theta_{nb}sin\psi_{nb} \qquad \boldsymbol{C}_b^n\ (3,1) = -sin\phi_{nb}cos\theta_{nb}$$

$$\boldsymbol{C}_b^n\ (2,3) = -sin\phi_{nb}sin\psi_{nb} - cos\phi_{nb}sin\theta_{nb}cos\psi_{nb} \qquad \boldsymbol{C}_b^n\ (3,2) = sin\theta_{nb}$$

$$\boldsymbol{C}_b^n\ (3,3) = cos\phi_{nb}cos\theta_{nb}$$

Conversely, attitude angles can also be determined from the transformation matrix $\boldsymbol{C_b^n}$ as following:

$$\begin{cases} \phi_{\mathrm{nb}} = -arctan\left(\dfrac{\mathbf{C}_{\mathrm{b}}^{\mathrm{n}}\ (3,1)}{\mathbf{C}_{\mathrm{b}}^{\mathrm{n}}\ (3,3)}\right) \\ \theta_{\mathrm{nb}} = arcsin\left(\mathbf{C}_{\mathrm{b}}^{\mathrm{n}}\ (3,2)\right) \\ \psi_{\mathrm{nb}} = arctan\left(\dfrac{\mathbf{C}_{\mathrm{b}}^{\mathrm{n}}\ (1,2)}{\mathbf{C}_{\mathrm{b}}^{\mathrm{n}}\ (2,2)}\right) \end{cases} \tag{6-5}$$

When Euler angles represent small angles, the DCM can be approximated as a function of the **skew-symmetric** matrix, noted $[\bar{\boldsymbol{\psi}}_{\boldsymbol{nb}} \times]$, of the re-ordered version of attitudes $\bar{\boldsymbol{\psi}}_{\boldsymbol{nb}} = [\,-\theta_{nb}, -\phi_{nb}, \psi_{nb}]$:

$$\boldsymbol{C}_b^n = C(\boldsymbol{\psi_{nb}}) = \begin{bmatrix} 1 & \psi_{nb} & \phi_{nb} \\ -\psi_{nb} & 1 & -\theta_{nb} \\ -\phi_{nb} & \theta_{nb} & 1 \end{bmatrix} = I_3 - [\bar{\boldsymbol{\psi}}_{\boldsymbol{nb}} \times] \tag{6-6}$$

- **Quaternion**

Other than a DCM, the series of rotations between *b*-frame and the local *n*-frame can be summarized into a rotation of angle θ around the rotation axis (q_1, q_2, q_3), and the transformation matrix is represented by a quaternion $\boldsymbol{q}$, a four-dimensional vector:

$$\boldsymbol{q} = \begin{bmatrix} q_1 \\ q_2 \\ q_3 \\ q_4 \end{bmatrix} = \begin{bmatrix} \dfrac{\theta_x}{\theta} sin0.5\theta \\ \dfrac{\theta_y}{\theta} sin0.5\theta \\ \dfrac{\theta_z}{\theta} sin0.5\theta \\ cos0.5\theta \end{bmatrix} \tag{6-7}$$

where

- $\theta = \|\boldsymbol{\theta}\| = \sqrt{\theta_x^2 + \theta_y^2 + \theta_z^2}$ is the magnitude of the rotation,
- (q_1, q_2, q_3) represent the axis around which the rotation is implemented.

The components of a quaternion always respect the constraint that

$$q_1^2 + q_2^2 + q_3^2 + q_4^2 = 1.$$

Compared to a rotation matrix, a quaternion representation is more stable, and mathematically more efficient as only four components are involved [1], [67].

Not being an intuitive way to represent rotations, the utilization of the quaternion requires more attention to avoid mistakes. For a rotating frame, the expression of the time-dependent quaternion is not direct and differential quality of the quaternion need firstly be established.

While the quaternion parameters are functions of time, the associated differential equation is

$$\dot{\boldsymbol{q}} = \frac{1}{2}\bar{\boldsymbol{\Omega}}(\boldsymbol{w})\boldsymbol{q} \tag{6-8}$$

where $\bar{\boldsymbol{\Omega}}(\boldsymbol{w})$ is of the following particular form

$$\bar{\boldsymbol{\Omega}}(\boldsymbol{w}) = \begin{bmatrix} 0 & w_z & -w_y & w_x \\ -w_z & 0 & w_x & w_y \\ w_y & -w_x & 0 & w_z \\ -w_x & -w_y & -w_z & 0 \end{bmatrix} = \begin{bmatrix} -[\boldsymbol{w}\times] & \boldsymbol{w} \\ -\boldsymbol{w}^{\boldsymbol{T}} & 0 \end{bmatrix} \tag{6-9}$$

and $[\boldsymbol{w}\times]$ is the skew-symmetric matrix of the angular velocity vector $\boldsymbol{w}$ of the body rotation, $\boldsymbol{w} = [w_x, w_y, w_z]^T$.

To obtain the discrete closed form solution of the previous equation, a short time interval is assumed between epoch k and epoch $(k+1)$ [28]:

$$\boldsymbol{q_{k+1}} = \left(\sum_{n=0}^{\infty} \frac{1}{2^n}\bar{S}^n\right)\boldsymbol{q_k} \cong \boldsymbol{q_k} + \frac{1}{2}[2\left(cos\left(\frac{\theta}{2}\right) - 1\right)\cdot I_4 + \frac{sin\left(\frac{\theta}{2}\right)}{\theta/2}\bar{S}(\boldsymbol{w})]\boldsymbol{q_k} \tag{6-10}$$

where $\bar{S}(\boldsymbol{w}) = \bar{\boldsymbol{\Omega}}(\boldsymbol{w})\Delta t = \begin{bmatrix} -[\boldsymbol{\theta}\times] & \boldsymbol{\theta} \\ -\boldsymbol{\theta}^{\boldsymbol{T}} & 0 \end{bmatrix}$.

- **$\boldsymbol{C_b^n}$ and Quaternion**

In the case of the frame pair (b-frame, n-frame), the conversion of a quaternion into a coordinate transformation matrix DCM is reflected by:

$$\boldsymbol{C_b^n} = \boldsymbol{C}(\boldsymbol{q_b^n})$$

$$= \begin{bmatrix} q_4^2 + q_1^2 - q_2^2 - q_3^2 & 2(q_1q_2 - q_3q_4) & 2(q_1q_3 + q_2q_4) \\ 2(q_1q_2 + q_3q_4) & q_4^2 - q_1^2 + q_2^2 - q_3^2 & 2(q_2q_3 - q_1q_4) \\ 2(q_1q_3 - q_2q_4) & 2(q_2q_3 + q_1q_4) & q_4^2 - q_1^2 - q_2^2 + q_3^2 \end{bmatrix} \tag{6-11}$$

$$\boldsymbol{q_b^n} = \begin{bmatrix} q_1 \\ q_2 \\ q_3 \\ q_4 \end{bmatrix} = \begin{bmatrix} \dfrac{\boldsymbol{C_b^n}(3,2) - \boldsymbol{C_b^n}(2,3)}{4q_4} \\ \dfrac{\boldsymbol{C_b^n}(1,3) - \boldsymbol{C_b^n}(3,1)}{4q_4} \\ \dfrac{\boldsymbol{C_b^n}(2,1) - \boldsymbol{C_b^n}(1,2)}{4q_4} \\ 0.5\sqrt{1 + \boldsymbol{C_b^n}(1,1) + \boldsymbol{C_b^n}(2,2) + \boldsymbol{C_b^n}(3,3)} \end{bmatrix} \tag{6-12}$$

In terms of attitudes angles, $\boldsymbol{\psi_{nb}} = [\phi_n, \theta_{nb}, \psi_{nb}]$ the quaternion is expressed as:

$$\boldsymbol{q_b^n} = \begin{bmatrix} cos\dfrac{\phi_{nb}}{2} sin\dfrac{\theta_{nb}}{2} cos\dfrac{\psi_{nb}}{2} + sin\dfrac{\phi_{nb}}{2} cos\dfrac{\theta_{nb}}{2} sin\dfrac{\psi_{nb}}{2} \\ -cos\dfrac{\phi_{nb}}{2} sin\dfrac{\theta_{nb}}{2} sin\dfrac{\psi_{nb}}{2} + sin\dfrac{\phi_{nb}}{2} cos\dfrac{\theta_{nb}}{2} cos\dfrac{\psi_{nb}}{2} \\ -cos\dfrac{\phi_{nb}}{2} cos\dfrac{\theta_{nb}}{2} sin\dfrac{\psi_{nb}}{2} + sin\dfrac{\phi_{nb}}{2} sin\dfrac{\theta_{nb}}{2} cos\dfrac{\psi_{nb}}{2} \\ cos\dfrac{\phi_{nb}}{2} cos\dfrac{\theta_{nb}}{2} cos\dfrac{\psi_{nb}}{2} + sin\dfrac{\phi_{nb}}{2} sin\dfrac{\theta_{nb}}{2} sin\dfrac{\psi_{nb}}{2} \end{bmatrix} \tag{6-13}$$

6.1.3.2 *e*-frame and *i*-frame

With w_{ie} the value of the rotation rate, the angular rotation vectors of the *e*-frame w.r.t *i*-frame expressed in *i*-frame and *n*-frame are respectively:

$$\boldsymbol{w_{ie}^i} = \boldsymbol{w_{ie}^e} = \begin{bmatrix} 0 \\ 0 \\ w_{ie} \end{bmatrix}, \qquad \boldsymbol{w_{ie}^n} = \begin{bmatrix} 0 \\ w_{ie} cos\varphi \\ w_{ie} sin\varphi \end{bmatrix} \tag{6-14}$$

where φ is the latitude of the *n*-frame origin.

With the hypothesis that the *e*-frame and the *i*-frame coincide at initial time, the rotation matrix between those two frames at time t is thus defined as:

$$\boldsymbol{C_i^e} = (\boldsymbol{C_e^i})^{-1} = (\boldsymbol{C_e^i})^T = \begin{bmatrix} cos\, w_{ie}t & sin\, w_{ie}t & 0 \\ -sin\, w_{ie}t & cos\, w_{ie}t & 0 \\ 0 & 0 & 1 \end{bmatrix} \tag{6-15}$$

6.1.3.3 *e*-frame and *n*-frame

The DCM between the *e*-frame and the *n*-frame is expressed as:

$$\boldsymbol{C_e^n} = (\boldsymbol{C_n^e})^{-1} = (\boldsymbol{C_n^e})^T = \boldsymbol{R_x}(-\varphi + \pi/2)\boldsymbol{R_z}(\lambda + \pi/2) \tag{6-16}$$

The expanded expression of the $\boldsymbol{C_e^n}$ is thus

$$\boldsymbol{C_e^n} = \begin{bmatrix} -\sin\lambda & cos\lambda & 0 \\ -sin\varphi cos\lambda & -sin\varphi sin\lambda & cos\varphi \\ cos\varphi cos\lambda & cos\varphi sin\lambda & sin\varphi \end{bmatrix}$$

where φ is the latitude and λ is the longitude of the *n*-frame origin.

6.2 INS Navigation with Quaternion

The INS navigation can be summarized as a process to update the system states by getting through a set of equations, named the mechanization equations. The corrected specific force measurements and rotation rate measurements at the output of IMU are used for the update. Detailed process of derivations of equations presented in this section will not be addressed, while only final compact forms are underlined. For more information, refer to [2], [28], [97].

6.2.1 Equations of Motion

The equations of motion describe the motion of the vehicle, e.g. the behavior in time of the position, the velocity and the vehicle attitudes. In this work, the equations are expressed under ENU *n*-frame [1], [23]:

$$\begin{bmatrix} \dot{\boldsymbol{r}}_{\boldsymbol{nb}}^{\boldsymbol{n}} \\ \dot{\boldsymbol{v}}_{\boldsymbol{nb}}^{\boldsymbol{n}} \\ \dot{\boldsymbol{C}}_{\boldsymbol{b}}^{\boldsymbol{n}} \end{bmatrix} = \begin{bmatrix} \boldsymbol{F}_{\boldsymbol{rv}}\boldsymbol{v}_{\boldsymbol{nb}}^{\boldsymbol{n}} \\ \boldsymbol{C}_{\boldsymbol{b}}^{\boldsymbol{n}}\boldsymbol{f}_{\boldsymbol{ib}}^{\boldsymbol{b}} - (2\boldsymbol{\Omega}_{\boldsymbol{ie}}^{\boldsymbol{n}} + \boldsymbol{\Omega}_{\boldsymbol{en}}^{\boldsymbol{n}})\boldsymbol{v}_{\boldsymbol{nb}}^{\boldsymbol{n}} + \boldsymbol{g}^{\boldsymbol{n}} \\ \boldsymbol{C}_{\boldsymbol{b}}^{\boldsymbol{n}}(\boldsymbol{\Omega}_{\boldsymbol{ib}}^{\boldsymbol{b}} - \boldsymbol{\Omega}_{\boldsymbol{in}}^{\boldsymbol{b}}) \end{bmatrix} \tag{6-17}$$

with

- $\boldsymbol{r}_{\boldsymbol{nb}}^{\boldsymbol{n}} = (\varphi, \lambda, h)^T$ the geodetic coordinates of the moving object (herein, the center of IMU);
- $\boldsymbol{v}_{\boldsymbol{nb}}^{\boldsymbol{n}} = (v_e, v_n, v_u)^T$ is the velocity vector in *n*-frame, consisting of three components along east, north, and up directions;
- $\boldsymbol{F}_{\boldsymbol{rv}}$ is the transformation matrix describing the relationship between the derivative of the geodetic coordinates and the velocity:

$$\boldsymbol{F}_{\boldsymbol{rv}} = \begin{bmatrix} 0 & \frac{1}{R_M + h} & 0 \\ \frac{1}{(R_N + h)cos\varphi} & 0 & 0 \\ 0 & 0 & 1 \end{bmatrix} \tag{6-18}$$

  with
  - $R_N = \frac{a}{\sqrt{1-e^2 sin^2\varphi}}$ is the normal radius,
  - $R_M = \frac{a(1-e^2)}{\sqrt{(1-e^2 sin^2\varphi)^3}}$ the meridian radius,
  - a the semi-major axis of the earth, and
  - e the eccentricity of the Earth.
- $\boldsymbol{f}_{\boldsymbol{ib}}^{\boldsymbol{b}}$ is the specific force measurements under *b*-frame;
- $\boldsymbol{\Omega}_{\boldsymbol{ie}}^{\boldsymbol{n}} = [\boldsymbol{w}_{\boldsymbol{ie}}^{\boldsymbol{n}} \times]$, with $\boldsymbol{w}_{\boldsymbol{ie}}^{\boldsymbol{n}}$ the notation of the Earth rotation rate vector under *n*-frame defined in Eq(6-14);
- $\boldsymbol{\Omega}_{\boldsymbol{en}}^{\boldsymbol{n}} = [\boldsymbol{w}_{\boldsymbol{en}}^{\boldsymbol{n}} \times]$, with the angular velocity of the *n*-frame w.r.t the *e*-frame expressed in *n*-frame;

$$\boldsymbol{w}_{\boldsymbol{en}}^{\boldsymbol{n}} = \begin{bmatrix} -\dot{\varphi} \\ \dot{\lambda}cos\varphi \\ \dot{\lambda}sin\varphi \end{bmatrix} = \begin{bmatrix} \frac{-v_n}{R_M + h} \\ \frac{v_e}{R_N + h} \\ \frac{v_e tan\varphi}{R_N + h} \end{bmatrix} \tag{6-19}$$

- $\boldsymbol{g^n} = \begin{bmatrix} 0 \\ 0 \\ -g \end{bmatrix}$ is the Earth's gravity field. Refer to Appendix A for more information of the Earth's gravitational terms.

6.2.2 INS Mechanization Equations

Starting from the present states of the vehicle, the states updates are obtained through a set of mechanization equations with IMU measurements. The main idea is based on the approximation that over a small enough temporal step, e.g. the INS mechanization time pace $\Delta t = 0.01s$, derivatives of certain quantities can be treated as constants. Figure 6-2 provides a block view of the INS mechanization process.

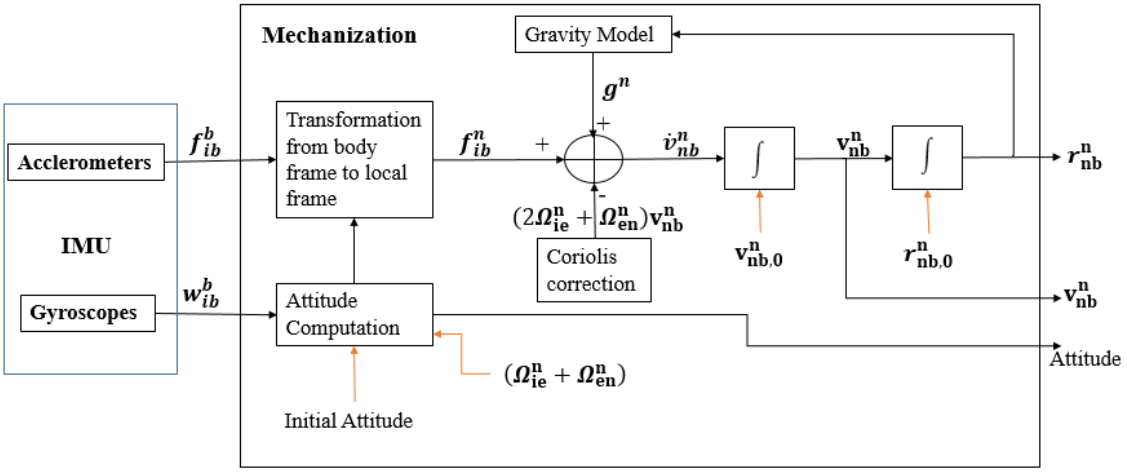

Figure 6-2. A block diagram depicting the mechanization of an INS in the local-level frame

6.2.2.1 Correction of raw IMU measurements

The extraction of the correct specific forces and the rotation rates is based on following equations:

$$\begin{aligned} \boldsymbol{f_{ib}^b} &= \frac{\tilde{\boldsymbol{f}}_{\boldsymbol{ib}}^{\boldsymbol{b}} - \boldsymbol{b_a}}{\boldsymbol{1 + S_a}} \\ \boldsymbol{w_{ib}^b} &= \frac{\tilde{\boldsymbol{w}}_{\boldsymbol{ib}}^{\boldsymbol{b}} - \boldsymbol{b_g}}{\boldsymbol{1 + S_g}} \end{aligned} \tag{6-20}$$

where ■ are collected raw measurements at outputs of IMU sensors.

6.2.2.2 Update of quaternion and attitudes

In order to obtain the update of the quaternion between the *n*-frame and *b*-frame, the angular increment $\boldsymbol{\theta_{nb}^b}$ of the body w.r.t the *n*-frame needs to be determined firstly.

The angular rate vector of the body w.r.t the *n*-frame $\boldsymbol{w_{nb}^b}$ is expressed as

$$\boldsymbol{w_{nb}^b = w_{ib}^b - w_{in}^b = w_{ib}^b - C_n^b w_{in}^n} \tag{6-21}$$

where

- $\boldsymbol{w_{in}^{b}}$ is the angular rate vector of the *n*-frame w.r.t the *i*-frame resolved in *b*-frame,
- $\boldsymbol{w_{in}^{n}}$ is the angular rate vector of the *n*-frame w.r.t the *i*-frame resolved in *n*-frame.

The vector $\boldsymbol{w_{in}^{n}}$ can be expressed as a summation of two parts respectively mentioned in Eq(6-14) and Eq(6-19)

$$\boldsymbol{w_{in}^{n}} = \boldsymbol{w_{ie}^{n}} + \boldsymbol{w_{en}^{n}} \tag{6-22}$$

By subtracting the proper detailed expressions into Eq(6-21), the angular increment $\boldsymbol{\theta_{nb}^{b}}$ is obtained by integrating $\boldsymbol{w_{nb}^{b}}$ over the INS mechanisation interval Δt:

$$\boldsymbol{\theta_{nb}^{b}} = \boldsymbol{\theta_{ib}^{b}} - \boldsymbol{\theta_{in}^{b}} \tag{6-23}$$

Referring to the closed form solution of quaternion in Eq(6-10), the updated quaternion is

$$\begin{bmatrix} q_1 \\ q_2 \\ q_3 \\ q_4 \end{bmatrix}_{k+1} = \begin{bmatrix} q_1 \\ q_2 \\ q_3 \\ q_4 \end{bmatrix}_{k} + \frac{1}{2}\begin{bmatrix} c - s[\boldsymbol{\theta_{nb}^{n}}\times] & s\boldsymbol{\theta_{nb}^{n}} \\ -s(\boldsymbol{\theta_{nb}^{n}})^{T} & c \end{bmatrix}\begin{bmatrix} q_1 \\ q_2 \\ q_3 \\ q_4 \end{bmatrix}_{k} \tag{6-24}$$

where

- $c = 2(\cos\frac{\theta}{2} - 1)$,
- $s = \frac{\sin(\theta/2)}{\theta/2}$
- $\theta = \|\boldsymbol{\theta_{nb}^{n}}\|$

Once the quaternion has been updated, the transformation matrix can be updated using Eq(6-11) and new attitudes are obtained using Eq(6-5).

6.2.2.3 Update of velocity and position

The derivative of the vehicle velocity Eq(6-17) is approximately constant over the update duration Δt and the velocity increment is calculated as

$$\Delta\boldsymbol{v_{nb}^{n}} = \boldsymbol{C_{b}^{n}}\boldsymbol{f_{ib}^{b}}\Delta t - (2\boldsymbol{\Omega_{ie}^{n}} + \boldsymbol{\Omega_{en}^{n}})\boldsymbol{v_{nb}^{n}}\Delta t + \boldsymbol{g^{n}}\Delta t \tag{6-25}$$

where $\boldsymbol{g^{n}} = [0, 0, -g]^{T}$ is the gravity vector expressed in *n*-frame.

The updated velocity of epoch $(k+1)$ is thus obtained by

$$\boldsymbol{v_{nb,k+1}^{n}} = \boldsymbol{v_{nb,k}^{n}} + \frac{1}{2}(\Delta\boldsymbol{v_{nb,k}^{n}} + \Delta\boldsymbol{v_{nb,k+1}^{n}}) \tag{6-26}$$

Similarly, the final updated geodetic coordinates are

$$\boldsymbol{r_{nb,k+1}^{n}} = \boldsymbol{r_{nb,k}^{n}} + \frac{1}{2}\boldsymbol{F_{rv}}(\boldsymbol{v_{nb,k+1}^{n}} + \boldsymbol{v_{nb,k}^{n}}) \tag{6-27}$$

6.2.3 INS Error States Model

The performance of an INS depends on various elements, for instance the knowledge of IMU measurements errors' characteristics, the choice of the estimation method, etc. A KF is usually preferred to a LS, which takes not only the current condition into account, but also the system dynamics. To conduct a linear system, the error states model is herein applied. In this section, we will give for the INS-only system an example of typical parameters related to error states.

6.2.3.1 Notations of Error States

Among the states of interest, and apart from the desired parameters describing the position, velocity and attitudes of the vehicle, the errors affecting the MEMS measurements also need to be considered for a better mitigation, namely the measurement biases and the scale factors. Besides, in terms of the position error, it is preferred to express them in meters than in radians in order to avoid numeric instability [65].

Hence, let $\boldsymbol{p_{nb}^n}$ be the vehicle position expressed in the local frame. Error states are thus defined as differences between states estimates (terms with 'hat') and their true values with the following notations:

$$\begin{cases} \delta \boldsymbol{p_{nb}^n} = \widehat{\boldsymbol{p}}_{\boldsymbol{nb}}^{\boldsymbol{n}} - \boldsymbol{p_{nb}^n} \\ \delta \boldsymbol{v_{nb}^n} = \widehat{\boldsymbol{v}}_{\boldsymbol{nb}}^{\boldsymbol{n}} - \boldsymbol{v_{nb}^n} \\ \delta \bar{\boldsymbol{\psi}}_{\boldsymbol{nb}} = \widehat{\bar{\boldsymbol{\psi}}_{\boldsymbol{nb}}} - \bar{\boldsymbol{\psi}}_{\boldsymbol{nb}} \\ \delta \boldsymbol{b_a} = \boldsymbol{b_a} - \widehat{\boldsymbol{b}}_{\boldsymbol{a}} \\ \delta \boldsymbol{s_a} = \boldsymbol{s_a} - \hat{\boldsymbol{s}}_{\boldsymbol{a}} \\ \delta \boldsymbol{b_g} = \boldsymbol{b_g} - \widehat{\boldsymbol{b}}_{\boldsymbol{g}} \\ \delta \boldsymbol{s_g} = \boldsymbol{s_g} - \hat{\boldsymbol{s}}_{\boldsymbol{g}} \end{cases} \tag{6-28}$$

Remind that the normal order of attitudes is $\boldsymbol{\psi_{nb}} = [\phi_{nb}, \theta_{nb}, \psi_{nb}]$. When we try to figure out the relation between $\delta \boldsymbol{C_b^n} = \widehat{\boldsymbol{C}}_{\boldsymbol{b}}^{\boldsymbol{n}} - \boldsymbol{C_b^n}$ and small attitudes error, the following form is obtained

$$\delta \boldsymbol{C_b^n} = C\left(\widehat{\boldsymbol{\psi}}_{\boldsymbol{nb}}\right) - C\left(\boldsymbol{\psi_{nb}}\right) = -\boldsymbol{E}.\boldsymbol{C_b^n} \tag{6-29}$$

with $\boldsymbol{E} = [\delta \bar{\boldsymbol{\psi}}_{\boldsymbol{nb}} \wedge]$ the skew-symmetric matrix of a modified version of $\delta \boldsymbol{\psi_{nb}}$, noted as $\delta \bar{\boldsymbol{\psi}}_{\boldsymbol{nb}} = [-\delta\theta_{nb}, -\delta\phi_{nb}, \delta\psi_{nb}]^T$ similar to Eq(6-6).

6.2.3.2 Error States Dynamics

The INS error states' dynamics is obtained by doing the perturbation analysis of Eq(6-19). For MEMS IMUs, the turn-on biases are not negligible but they remain constant for a particular run [65]. Thus, the calibration and the correction of the biases are feasible. Generally, the dynamic part of the inertial biases is modeled as a first-order Gauss-Markov process [98]:

$$\begin{aligned} \delta \dot{\boldsymbol{b}}_{\boldsymbol{a}} &= -\boldsymbol{\beta_{ba}} \delta \boldsymbol{b_a} + \boldsymbol{\eta_{ba}} \\ \delta \dot{\boldsymbol{b}}_{\boldsymbol{g}} &= -\boldsymbol{\beta_{bg}} \delta \boldsymbol{b_g} + \boldsymbol{\eta_{bg}} \end{aligned} \tag{6-30}$$

Where

- $\boldsymbol{\beta_{ba}} = \begin{bmatrix} 1/\tau_{bax} & 0 & 0 \\ 0 & 1/\tau_{bay} & 0 \\ 0 & 0 & 1/\tau_{baz} \end{bmatrix}$ and $\boldsymbol{\beta_{bg}} = \begin{bmatrix} 1/\tau_{bgx} & 0 & 0 \\ 0 & 1/\tau_{bgy} & 0 \\ 0 & 0 & 1/\tau_{bgz} \end{bmatrix}$ are the GM process key parameters,

- $\boldsymbol{\tau_{ba}} = \left[\tau_{bax}, \tau_{bay}, \tau_{baz}\right]^T$,
- $\boldsymbol{\tau_{bg}} = \left[\tau_{bgx}, \tau_{bgy}, \tau_{bgz}\right]^T$ are the corresponding correlation times,
- $\boldsymbol{\eta_{ba}}$ and $\boldsymbol{\eta_{bg}}$ are GM process driving noises, zero mean white Gaussian noise, whose spectral densities are denoted respectively as $\boldsymbol{q_{ba}}$ and $\boldsymbol{q_{bg}}$.

Similarly, a first-order GM process is utilized to model the MEMS IMUs scale factors as follows:

$$\begin{aligned} \delta\dot{\boldsymbol{s}}_{\boldsymbol{a}} &= -\boldsymbol{\beta_{sa}}\delta\boldsymbol{s_a} + \boldsymbol{\eta_{sa}} \\ \delta\dot{\boldsymbol{s}}_{\boldsymbol{g}} &= \boldsymbol{\beta_{sg}}\delta\boldsymbol{s_g} + \boldsymbol{\eta_{sg}} \end{aligned} \tag{6-31}$$

where

- $\boldsymbol{\beta_{sa}} = \begin{bmatrix} 1/\tau_{sax} & 0 & 0 \\ 0 & 1/\tau_{say} & 0 \\ 0 & 0 & 1/\tau_{saz} \end{bmatrix}$ and $\boldsymbol{\beta_{sg}} = \begin{bmatrix} 1/\tau_{sgx} & 0 & 0 \\ 0 & 1/\tau_{sgy} & 0 \\ 0 & 0 & 1/\tau_{sgz} \end{bmatrix}$ are the GM process key parameters,
- $\boldsymbol{\tau_{sa}} = \left[\tau_{sax}, \tau_{say}, \tau_{saz}\right]^T$, $\boldsymbol{\tau_{sg}} = \left[\tau_{sgx}, \tau_{sgy}, \tau_{sgz}\right]^T$ are the corresponding correlation times,
- $\boldsymbol{\eta_{sa}}$ and $\boldsymbol{\eta_{sg}}$ are GM process driving noises, zero mean white Gaussian noise, whose spectral densities are denoted respectively as $\boldsymbol{q_{sa}}$ and $\boldsymbol{q_{sg}}$.

Herein, the final compact continuous representation of the states dynamics is provided and the detailed derivation process is provided in Appendix D:

$$\delta\dot{\boldsymbol{x}}_{\boldsymbol{INS}} = \boldsymbol{F_{INS}}\delta\boldsymbol{x_{INS}} + \boldsymbol{G_{INS}}\boldsymbol{u_{INS}} \tag{6-32}$$

with

- $\delta\boldsymbol{x_{INS}} = \left[\delta\boldsymbol{p_{nb}^n} \quad \delta\boldsymbol{v_{nb}^n} \quad \delta\bar{\boldsymbol{\psi}}_{\boldsymbol{nb}} \quad \delta\boldsymbol{b_a} \quad \delta\boldsymbol{b_g} \quad \delta\boldsymbol{s_a} \quad \delta\boldsymbol{s_g}\right]^{\boldsymbol{T}}$ the whole 21 INS error state vector;
- $\boldsymbol{F_{INS}} = \begin{bmatrix} \boldsymbol{F_{pp}} & \boldsymbol{I_3} & 0_{3x3} & 0_{3x3} & 0_{3x3} & 0_{3x3} & 0_{3x3} \\ \boldsymbol{F_{vp}} & \boldsymbol{F_{vv}} & \boldsymbol{F_{ve}} & \boldsymbol{C_b^n} & 0_{3x3} & \boldsymbol{C_b^n F^b} & 0_{3x3} \\ \boldsymbol{F_{ep}} & \boldsymbol{F_{ev}} & \boldsymbol{F_{ee}} & 0_{3x3} & -\boldsymbol{C_b^n} & 0_{3x3} & -\boldsymbol{C_b^n W^b} \\ 0_{3x3} & 0_{3x3} & 0_{3x3} & -\boldsymbol{\beta_{ba}} & 0_{3x3} & 0_{3x3} & 0_{3x3} \\ 0_{3x3} & 0_{3x3} & 0_{3x3} & 0_{3x3} & -\boldsymbol{\beta_{bg}} & 0_{3x3} & 0_{3x3} \\ 0_{3x3} & 0_{3x3} & 0_{3x3} & 0_{3x3} & 0_{3x3} & -\boldsymbol{\beta_{sa}} & 0_{3x3} \\ 0_{3x3} & 0_{3x3} & 0_{3x3} & 0_{3x3} & 0_{3x3} & 0_{3x3} & -\boldsymbol{\beta_{sg}} \end{bmatrix}$ the continuous state transition matrix;
- $\boldsymbol{F_{pp}} = \begin{bmatrix} \frac{v_u}{R_N+h} - \frac{v_n tan\varphi}{R_M+h} & \frac{v_e tan\varphi}{R_M+h} & \frac{-v_e}{R_N+h} \\ 0 & \frac{v_u}{R_M+h} & \frac{-v_n}{R_M+h} \\ 0 & 0 & 0 \end{bmatrix}$ the matrix describing the relationship between the derivative of the position error and itself;
- $\boldsymbol{F_{vp}} = \begin{bmatrix} 0 & \frac{2\omega_{ie}(v_n cos\,\varphi + v_u sin\,\varphi)}{R_M+h} + \frac{v_e v_n}{(R_M+h)(R_N+h)cos^2\varphi} & \frac{v_e v_u}{(R_N+h)^2} - \frac{v_e v_n tan\,\varphi}{(R_N+h)^2} \\ 0 & \frac{-2\omega_{ie} v_e cos\,\varphi}{R_M+h} - \frac{v_e^2}{(R_N+h)(R_M+h)cos^2\varphi} & \frac{v_n v_u}{(R_M+h)^2} + \frac{v_e^2 tan\varphi}{(R_N+h)^2} \\ 0 & -\frac{2\omega_{ie} v_e sin\,\varphi}{R_M+h} & \frac{-v_e^2}{(R_N+h)^2} + \frac{-v_n^2}{(R_M+h)^2} + \frac{2g}{R+h} \end{bmatrix}$ the transformation matrix describing the relationship between the derivative of the velocity error and the position error;

- $\boldsymbol{F_{vv}} = \begin{bmatrix} \frac{v_n tan\varphi - v_u}{R_N+h} & \frac{v_e tan\varphi}{R_N+h} + 2\omega_{ie} sin\varphi & -2\omega_{ie} cos\varphi - \frac{v_e}{R_N+h} \\ \frac{-2v_e tan\varphi}{R_N+h} - 2\omega_{ie} sin\varphi & \frac{-v_u}{R_M+h} & \frac{-v_n}{R_M+h} \\ \frac{2v_e}{R_N+h} + 2\omega_e cos\varphi & \frac{2v_n}{R_M+h} & 0 \end{bmatrix}$ the transformation matrix describing the relation between the derivative of velocity and itself;
- $\boldsymbol{F_{ve}} = \left[\boldsymbol{C_b^n f_{ib}^b} \times\right]$ is a skew symmetric matrix describing the relation between the derivative of velocity and the attitudes, $\boldsymbol{f_{ib}^b}$ is the specific force measurements under *b*-frame;
- $\boldsymbol{F_{ep}} = \begin{bmatrix} 0 & 0 & \frac{v_n}{(R_M+h)^2} \\ 0 & \frac{-\omega_{ie} \sin\varphi}{R_M+h} & \frac{-v_e}{(R_N+h)^2} \\ 0 & \frac{\omega_{ie} \cos\varphi}{R_M+h} + \frac{v_e}{(R_N+h)(R_M+h)cos^2\varphi} & \frac{-v_e tan\varphi}{(R_N+h)^2} \end{bmatrix}$ describing the relation between the derivative of $\delta\bar{\boldsymbol{\psi}}_{\boldsymbol{nb}}$ and $\delta\boldsymbol{p_{nb}^n}$;
- $\boldsymbol{F_{ev}} = \begin{bmatrix} 0 & \frac{-1}{R_M+h} & 0 \\ \frac{1}{R_N+h} & 0 & 0 \\ \frac{tan\varphi}{R_N+h} & 0 & 0 \end{bmatrix}$ the transformation matrix describing the relation between the derivative of $\delta\bar{\boldsymbol{\psi}}_{\boldsymbol{nb}}$ and $\delta\boldsymbol{v_{nb}^n}$;
- $\boldsymbol{F_{ee}} = -[(\boldsymbol{\omega_{ie}^n} + \boldsymbol{\omega_{en}^n}) \wedge]$ the transformation matrix describing the relation between the derivative of $\delta\bar{\boldsymbol{\psi}}_{\boldsymbol{nb}}$ and itself.
- $\boldsymbol{\omega_{ie}}$ the Earth rotation speed; g the nominal component of Earth gravity; R is the mean radius of the Earth, $\boldsymbol{F_b} = diag(\tilde{\boldsymbol{f}}_{\boldsymbol{ib}}^{\boldsymbol{b}})$ and $\boldsymbol{W_b} = diag(\tilde{\boldsymbol{w}}_{\boldsymbol{ib}}^{\boldsymbol{b}})$;
- $\boldsymbol{u_{INS}} = [\boldsymbol{\eta_a} \quad \boldsymbol{\eta_g} \quad \boldsymbol{\eta_{ba}} \quad \boldsymbol{\eta_{bg}} \quad \boldsymbol{\eta_{sa}} \quad \boldsymbol{\eta_{sg}}]^{\boldsymbol{T}}$ the 18-state process noise vector, with $\boldsymbol{\eta_a}$ the accelerometer measurement noise, $\boldsymbol{\eta_g}$ the gyroscope measurement noise, $\boldsymbol{\eta_{ba}}$/$\boldsymbol{\eta_{bg}}$ the accelerometer/gyroscope Gauss-Markov bias driving noises, $\boldsymbol{\eta_{sa}}$/$\boldsymbol{\eta_{sg}}$ the accelerometer/gyroscope Gauss-Markov scale factor driving noises;
- $\boldsymbol{G_{INS}} = \begin{bmatrix} 0_{3x3} & 0_{3x3} & 0_{3x3} & 0_{3x3} & 0_{3x3} & 0_{3x3} \\ \boldsymbol{C_b^n} & 0_{3x3} & 0_{3x3} & 0_{3x3} & 0_{3x3} & 0_{3x3} \\ 0_{3x3} & -\boldsymbol{C_b^n} & 0_{3x3} & 0_{3x3} & 0_{3x3} & 0_{3x3} \\ 0_{3x3} & 0_{3x3} & \boldsymbol{I_{3x3}} & 0_{3x3} & 0_{3x3} & 0_{3x3} \\ 0_{3x3} & 0_{3x3} & 0_{3x3} & \boldsymbol{I_{3x3}} & 0_{3x3} & 0_{3x3} \\ 0_{3x3} & 0_{3x3} & 0_{3x3} & 0_{3x3} & \boldsymbol{I_{3x3}} & 0_{3x3} \\ 0_{3x3} & 0_{3x3} & 0_{3x3} & 0_{3x3} & 0_{3x3} & \boldsymbol{I_{3x3}} \end{bmatrix}$ the process noise design matrix.

However, it's the discrete form of the state propagation utilized in practical INS navigation. According to Eq(4-4) and Eq(4-5), the discrete INS state dynamic model is in form

$$\delta\boldsymbol{x_{INS,k+1}} = \boldsymbol{\Phi_{INS,k}}\delta\boldsymbol{x_{INS,k}} + \boldsymbol{G_{INS}}\boldsymbol{u_{INS,k}} \tag{6-33}$$

with

- Δt the INS update period, i.e., 0.01s;
- $\boldsymbol{\Phi_{INS,k}} = \boldsymbol{I} + \boldsymbol{F_{INS}}\Delta t$.

The noise covariance matrix of $\boldsymbol{u_{INS,k}}$ is denoted as

$$\boldsymbol{Q_{INS}} = \begin{bmatrix} \boldsymbol{Q_a} & 0_{3x3} & 0_{3x3} & 0_{3x3} & 0_{3x3} & 0_{3x3} \\ 0_{3x3} & \boldsymbol{Q_g} & 0_{3x3} & 0_{3x3} & 0_{3x3} & 0_{3x3} \\ 0_{3x3} & 0_{3x3} & \boldsymbol{Q_{ba}} & 0_{3x3} & 0_{3x3} & 0_{3x3} \\ 0_{3x3} & 0_{3x3} & 0_{3x3} & \boldsymbol{Q_{bg}} & 0_{3x3} & 0_{3x3} \\ 0_{3x3} & 0_{3x3} & 0_{3x3} & 0_{3x3} & \boldsymbol{Q_{sa}} & 0_{3x3} \\ 0_{3x3} & 0_{3x3} & 0_{3x3} & 0_{3x3} & 0_{3x3} & \boldsymbol{Q_{sg}} \end{bmatrix}$$

where

- $\boldsymbol{Q_a}$ and $\boldsymbol{Q_g}$ are covariance matrices related to the white noise $\boldsymbol{\eta_a}$ and $\boldsymbol{\eta_g}$, $\boldsymbol{Q_{ba}}$, $\boldsymbol{Q_{bg}}$, $\boldsymbol{Q_{sa}}$ and
- $\boldsymbol{Q_{sg}}$ are covariance matrices used to model the bias-drift and the scale factors of the accelerometers and the gyroscopes (i.e., a first-order GM process).

The numerical application of these terms will be detailed in Section 6.3.2.

6.3 INS Error Dynamics

The performance of an INS navigation is strongly affected by the system model strength and the processing algorithm. The KF estimation generally provides the optimal navigation solution, but under the pre-assumption that only zero-mean Gaussian process noises are involved. Thereby, the proper stochastic modeling of those non-zero-mean IMU measurements errors is necessary for a robust estimation process.

Many approaches have been devised to achieve the noise identification and extraction of IMU sensors. The current popular ones are for example the Power spectral density (PSD) approach, the Autocorrelation, the Allan Variance (AV) technique, the Autoregressive model or the Wavelet de-noising [99]–[103].

The PSD approach provides the frequency-domain information of the random process. As a dual of the PSD method, the Autocorrelation technique establishes an autocorrelation function based on the experimental data. However, an accurate autocorrelation function is not always feasible and a much longer recording time is required to improve its accuracy [103], [104]. The Autoregressive model and the Wavelet de-noising are good alternatives for high quality IMU necessitating higher order stochastic processes modeling, which at the same time increases the computation burden.

In this PhD, the AV method is used (refer to Appendix C for more information) due to its simplicity, efficiency and the grade of our MEMS unit.

6.3.1 Characteristics of MEMS Sensors

The MEMS sensor used in our real tests is a Mti-28A33G35 model of XSENS motion technology [87]. The MTi is a miniature, gyro-enhanced Attitude and Heading Reference System (AHRS). 3-D calibrated linear acceleration (units m/s²), rate of turn (rad/s) and magnetic fields data (arbitrary units) are collected at its output. The orthogonal Cartesian frame fixed to the device is defined as following:

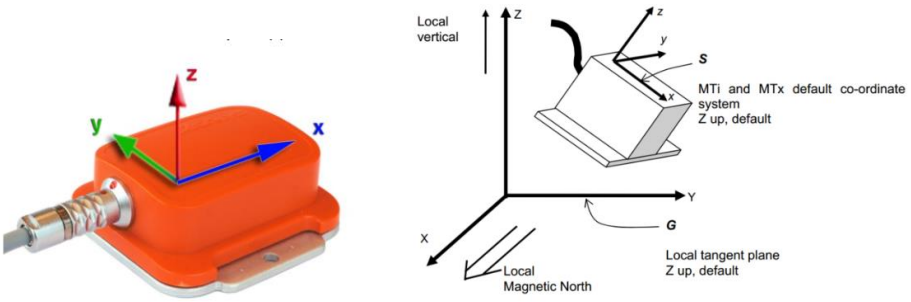

Figure 6-3. Mti sensor-fixed coordinate frame S (Forward, left, up) and Earth-fixed Coordinate frame G(Magnetic North, West, Up)

The measurements of the MEMS sensor provided by the Mti are referred to the sensor-fixed coordinate system $\boldsymbol{S}$. Thus, to have the sensor outputs expressed in b-frame (right-front-up), while having the Mti sensor fixed in the carrying vehicle and the x_S-axis heading the forward direction, a transformation matrix $\boldsymbol{C_s^b}$ need to be used:

$$\boldsymbol{C_s^b} = \begin{bmatrix} 0 & -1 & 0 \\ 1 & 0 & 0 \\ 0 & 0 & 1 \end{bmatrix} \tag{6-34}$$

6.3.2 Modelling of XSENS Errors

Hours-length stationary data have been collected with the XSENS MTi sensor. In this section, theoretical analysis of the data and the practical application in INS navigation are presented.

The stochastic discrete-time model of the gyroscope and the accelerometer of the XSENS Mti is derived on the basis of the measurements made at rest. Inertial sensors outputs are measured with the sampling frequency $f_s = 100Hz$ during a period of 11 000 seconds. The collection of XSENS data expressed in b-frame is showed in Figure 6-4 and Figure 6-5, after removing a constant bias. The basic characteristics of the collected data are illustrated in Table 6-1.

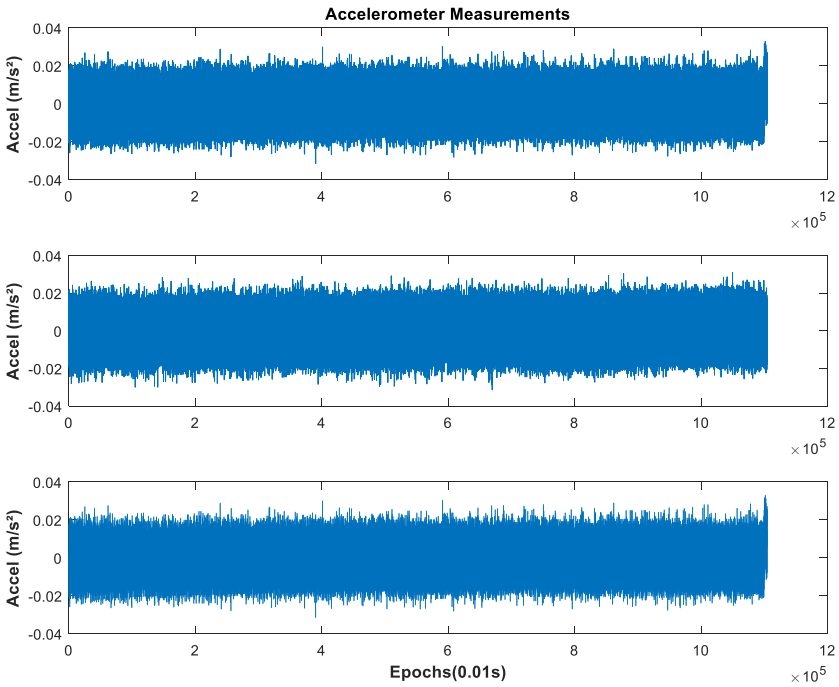

Figure 6-4. Measured Accelerometer data (translated by the mean bias) at outputs of a stationary XSENS MTi expressed in b-frame(x_b, y_b, z_b)

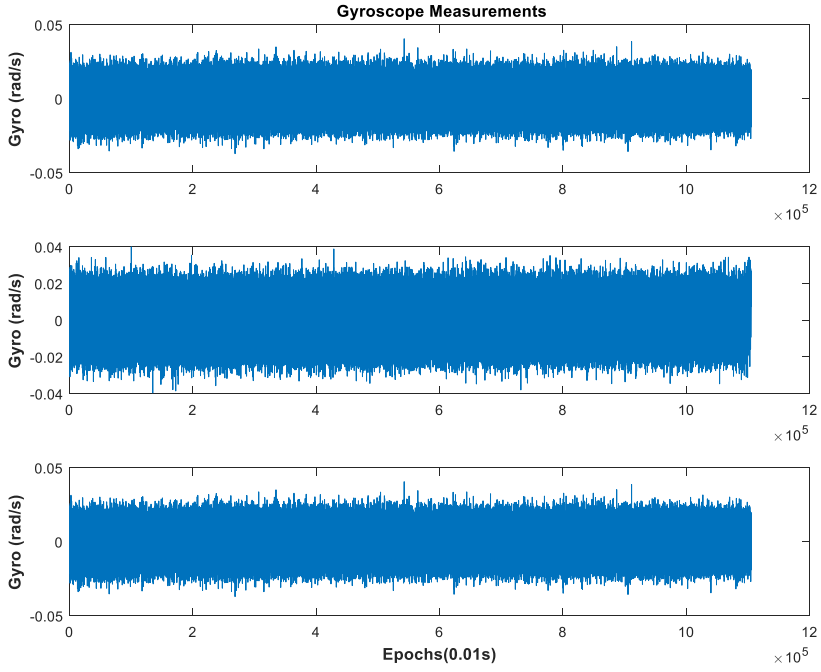

Figure 6-5. Measured Gyroscope data at outputs (translated by the mean bias) of a stationary XSENS MTi expressed in in b-frame(x_b, y_b, z_b)

Table 6-1. Constant Bias and Standard Deviation of MTi measurements in rest

	Accelerometer (m/s²)			Gyroscope (rad/s)		
	X	Y	Z	X	Y	Z
Constant Bias	-0.2577	0.5907	-9.7644	0.01452	0.02608	0.01012
STD	6.698e-3	6.299e-3	8.336e-3	7.94e-3	7.4384e-3	8.309e-3
Over all STD	0.0124			0.0137		

Subsequently, the centered inertial output are analyzed with the AV method to identify the inertial noises. The log-log plot of the Allan variance standard deviation versus cluster times for the accelerometer and the gyroscope are depicted separately in Figure 6-6 and Figure 6-7.

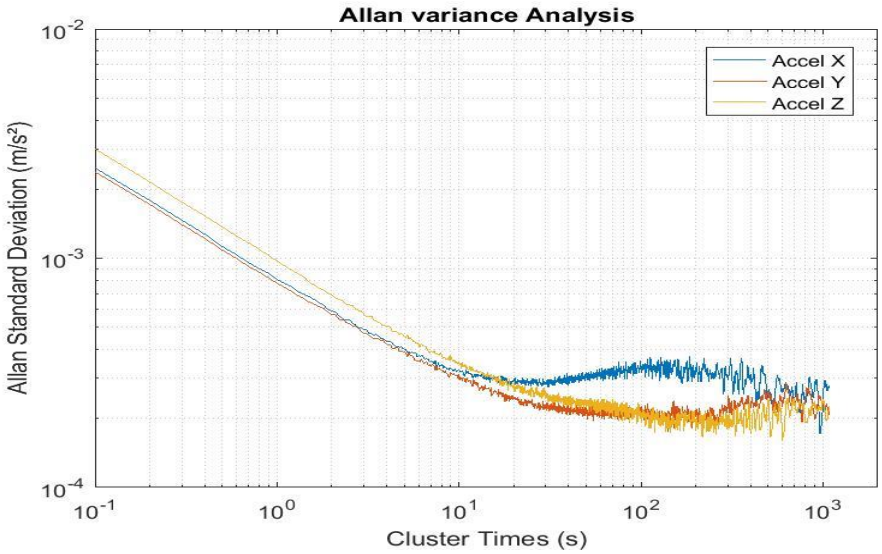

Figure 6-6. Allan Variance for the Accelerometer

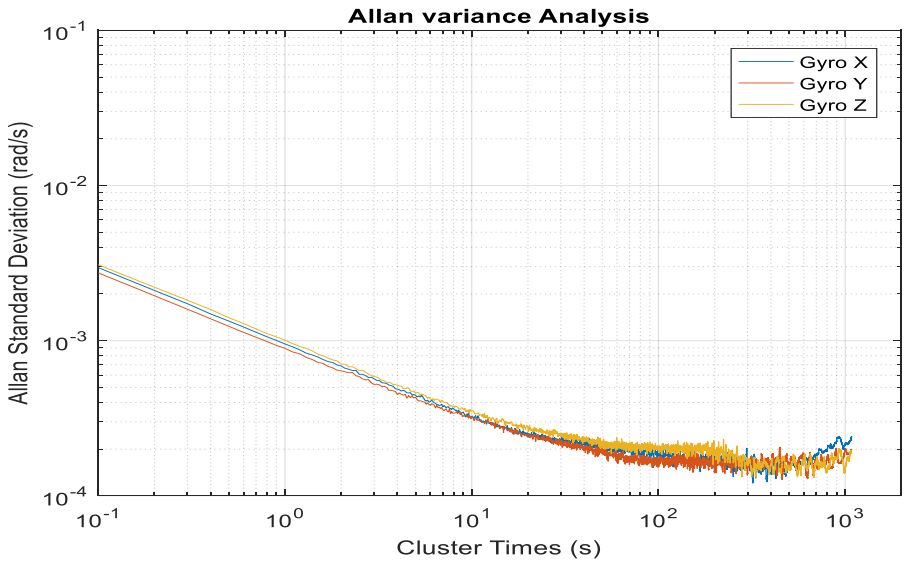

Figure 6-7. Allan Variance for the Gyroscope

Two types of random noises are present according to the plots,

- Random walk from the white noise: the white noise appears on the Allan Deviation plot as a slope with gradient -0.5. The random walk measurement for this noise (ARW for gyroscope and VRW for accelerometer) is obtained by fitting a straight line through the slope and reading its value at t=1s**, $\boldsymbol{N}$;**
- Bias instability appears on the plot as a flat region around the minimum. The numerical value $\boldsymbol{0.664B}$ is the minimum value on the Allan Deviation curve. As a key parameter of a first-order GM process, the correlation times, T_c, is indicated by the lowest flat zone.

In Table 6-2 the corresponding noise parameters are summarized.

Table 6-2. Summary of AV Parameters

		Accelerometer			**Gyroscope**		
		x	y	z	x	y	z
Bias instability	*Tc* (s)	300	300	300	300	300	300
(m/s²) (rad/s)	0.664B	3e-4	2e-4	2e-4	1.5e-4	1.5e-4	2e-4
	B	4.5181e-4	3.012e-4	3.012e-4	2.259e-4	2.259e-4	3.012e-4
VRW $(m/s/\sqrt{s})$ **/ARW** (rad/$\sqrt{s}$)	***N***	8e-4	7.8e-4	1e-3	9.5e-4	9e-4	1e-3

The determination of the terms $\boldsymbol{Q_a}$ and $\boldsymbol{Q_g}$, covariance matrices related to the white noise $\boldsymbol{\eta_a}$ and $\boldsymbol{\eta_g}$ in discrete form are [100]

$$Q_{\blacksquare} = Q_{WN} = \frac{N_{\blacksquare}{}^2}{\Delta t} = \left(\frac{N_{\blacksquare}}{\Delta t}\right)^2 * \Delta t \tag{6-35}$$

with

- $N_{\blacksquare}$ obtained from previous AV study,
- ■ is either $\boldsymbol{a}$ for accelerometers or $\boldsymbol{g}$ for gyroscopes.

Similarly, the covariance value in discrete time of the bias-drift driving noise, $\boldsymbol{Q_{ba}}$ or $\boldsymbol{Q_{bg}}$, is then

$$Q_{\blacksquare} = Q_{GM} = \left(2\frac{{B_{\blacksquare}}^2}{T_c}\right) * \Delta t \tag{6-36}$$

With

- $T_{c,\blacksquare}$ and $B_{\blacksquare}$ obtained from previous AV study,
- ■ is either $\boldsymbol{ba}$ for accelerometers biases or $\boldsymbol{bg}$ for gyroscopes biases.

From the experimental conditions, the parameters related to the scale factors are not readable on the AV plots. However, they are also normally modeled as GM processes with intuitively a much lower process-driving noise level, i.e. 1e-14 and a longer correlation times, i.e. 3 hours [65].

6.4 Implementation of Kalman Filter

6.4.1 Coupling Theory

Varying with the types of information shared between the INS and the GNSS, different coupling approaches are devised: loose coupling and tight coupling [23], [67]. The uncoupled integration and the ultra-tight integration are not interesting for this PhD and is thus not explained.

The loose coupling (LC) takes the INS-only system and GNSS-only system separately. Each system has its own processing block which finally provides updated navigation solutions. The raw GNSS measurements are collected by the receiver and after a GNSS KF, the position and velocity of the rover are calculated. This position and velocity information from GNSS-only filter or other sensors are passed to aid the INS-only filter, and through INS mechanization equations, an updated navigation solution is obtained. Even though being quite simple to implement, LC strategy is not recommended in the context of this PhD for 2 reasons [65], [67]:

- The GNSS-only block is always subject to environmental outliers, especially in an urban area.
- Any failure in either GNSS-only block or in INS-only block will corrupt the whole system performance.

The tight coupling (TC) makes the GNSS and INS fusion at the observables level. A TC KF is implemented to provide an integrated solution. As an integrated system, the TC provides a statistically rigorous sharing of information among states, especially those dedicated to INS-only block and GNSS-only block. Moreover, the process noise is only considered during the INS mechanization process other than in a LC the process noise is applied during both the INS mechanization and the GNSS-only propagation process [67]. The higher confidence on states increases the system ability to eliminate outliers. Finally, the most concerned case, a partial or full outage of GNSS in urban areas, herein does not need a reboot. A re-initialization may take the system tens of minutes to reach the steady-state performance. The implementation details of TC will be presented in the next section.

6.4.2 Tight Coupling Implementation

As an integrated system, the TC state vector needs to combine the INS-only state vector mentioned in Section 6.2.3 and the GNSS-only state vector mentioned in Section 4.2.3. Therefore, besides the part

$\delta \boldsymbol{x}_{\boldsymbol{INS},\boldsymbol{k}}$ inherited from the INS mechanization, extra terms related to the receiver clock, the ambiguities and the GLONASS ICB have to be added

$$\boldsymbol{X^n} = \left(\delta \boldsymbol{p_{nb}^n}; \delta \boldsymbol{v_{nb}^n};\ \delta \bar{\boldsymbol{\psi}}_{\boldsymbol{nb}};\ \delta \boldsymbol{b_a}; \delta \boldsymbol{b_g}; \delta \boldsymbol{s_a}; \delta \boldsymbol{s_g}; \delta \boldsymbol{clk};\ \delta \boldsymbol{Amb}; \delta \boldsymbol{ICB}\right)^T$$

The difference between GNSS measurements and INS-predicted measurements is used as inputs to the main TC KF. The linearization process is similar to Section 4.2.2 while only the linearization point comes from the INS mechanization prediction and the GNSS LOS vectors are expressed in local frame. Through the INS mechanization process, along with each state (position, velocity) estimate of the INS center $\boldsymbol{O_b}$, corresponding state of the GNSS antenna phase center $\boldsymbol{O_B}$ can be calculated considering the lever-arm effect between the 2 systems.

Assuming $\boldsymbol{l^b}$ the lever-arm vector resolved in *b*-frame, representing the vector from the INS center $\boldsymbol{O_b}$ to the GNSS antenna phase center $\boldsymbol{O_B}$, the position and velocity relations between those two origins are:

$$\begin{aligned} \boldsymbol{p_{O_B}^n} &= \boldsymbol{p_{O_b}^n} + \boldsymbol{C_b^n l^b} \\ \boldsymbol{v_{O_B}^n} &= \boldsymbol{v_{O_b}^n} + \boldsymbol{C_b^n}[\boldsymbol{w_{nb}^b} \times]\boldsymbol{l^b} \end{aligned} \tag{6-37}$$

where $\boldsymbol{\Omega_{nb}^b} = [\boldsymbol{w_{nb}^b} \times]$ the skew symmetric matrix of the angular rate vector $\boldsymbol{w_{nb}^b}$.

According to the perturbation analysis, the relation among the error position-velocity states is

$$\begin{aligned} \boldsymbol{\delta p_{O_B}^n} &= \boldsymbol{\delta p_{O_b}^n} + [\boldsymbol{C_b^n l^b} \times]\delta \bar{\boldsymbol{\psi}}_{\boldsymbol{nb}} \\ \boldsymbol{\delta v_{O_B}^n} &= \boldsymbol{\delta v_{O_b}^n} + \{[\boldsymbol{C_b^n \Omega_{ib}^b l^b} \times] - (\boldsymbol{\Omega_{en}^n} + \boldsymbol{\Omega_{ie}^n})[\boldsymbol{C_b^n l^b} \times]\}\delta \bar{\boldsymbol{\psi}}_{\boldsymbol{nb}} \\ &\quad - \boldsymbol{C_b^n}[\boldsymbol{l^b} \times](\boldsymbol{\delta b_g} + diag(\boldsymbol{w_{ib}^b})\delta \boldsymbol{s_g}) \end{aligned} \tag{6-38}$$

Similar to the GNSS case, the design matrix $\boldsymbol{H_{GNSS/INS}}$, the mapping matrix connecting the difference between GNSS measurements and their corresponding INS-predictions, and the whole state vector $\boldsymbol{X^n}$, is thus summarized as:

$$\boldsymbol{H}_{GNSS|INS} = [\boldsymbol{H}_{INS} \quad | \quad \boldsymbol{H}_{GNSS}(:, 10{:}\,end)]$$

$$\boldsymbol{H}_{INS} = \begin{bmatrix} \boldsymbol{G'}^{PVE}_{\Delta P_{GPS}} & 0_{n_1\times 3} & 0_{n_1\times 3} & 0_{n_1\times 3} & 0_{n_1\times 3} \\ \boldsymbol{G'}^{PVE}_{\Delta P_{GLO}} & 0_{n_2\times 3} & 0_{n_2\times 3} & 0_{n_2\times 3} & 0_{n_2\times 3} \\ \boldsymbol{G'}^{PVE}_{\nabla\Delta\Phi_{GPS}} & 0_{n_3\times 3} & 0_{n_3\times 3} & 0_{n_3\times 3} & 0_{n_3\times 3} \\ \boldsymbol{G'}^{PVE}_{\Delta\Phi_{GLO}} & 0_{n_4\times 3} & 0_{n_4\times 3} & 0_{n_4\times 3} & 0_{n_4\times 3} \\ \boldsymbol{G'}^{PVE}_{D_{GPS}} & 0_{n_5\times 3} & \boldsymbol{L}_{D_{GPS},b_g} & 0_{n_5\times 3} & \boldsymbol{L}_{D_{GPS},s_g} \\ \boldsymbol{G'}^{PVE}_{D_{GLO}} & 0_{n_6\times 3} & \boldsymbol{L}_{D_{GLO},b_g} & 0_{n_6\times 3} & \boldsymbol{L}_{D_{GLO},s_g} \end{bmatrix}$$

where

- $\boldsymbol{H}_{GNSS}$ is the GNSS design matrix proposed in Section 4.2.3, $\boldsymbol{H}_{GNSS}(:, 10{:}\,end)$ is the portion describing the relation between GNSS measurements (herein in the GNSS/INS case, the measurements differences) and the rover states except for the first 9 PVA (position-velocity-acceleration) states;
- $\boldsymbol{H}_{INS}$ describes the relation between GNSS/INS measurements and the INS states $\boldsymbol{x_{INS}} = \left[\delta \boldsymbol{p_{nb}^n} \quad \delta \boldsymbol{v_{nb}^n} \quad \delta \bar{\boldsymbol{\psi}}_{\boldsymbol{nb}} \quad \delta \boldsymbol{b_a} \quad \delta \boldsymbol{b_g} \quad \delta \boldsymbol{s_a} \quad \delta \boldsymbol{s_g}\right]^{\boldsymbol{T}}$;

- Same as in Section 4.2.3, n_1 is the length of SD GPS pseudoranges $\boldsymbol{\Delta P_{GPS}}$, n_2 is the length of SD GLONASS pseudoranges $\boldsymbol{\Delta P_{GLO}}$, n_3 is the length of DD GPS carrier phases $\boldsymbol{\nabla\Delta\Phi_{GPS}}$, n_4 is the length of SD GLONASS carrier phases $\boldsymbol{\Delta\Phi_{GLO}}$, n_5 is the length of GPS Doppler observables $\mathbf{D_{GPS}}$, and n_6 is the length of GLONASS Doppler observables $\boldsymbol{D_{GLO}}$;
- $\boldsymbol{G'^{PVE}_{\Delta \mathrm{P_{GPS}}}} = \begin{bmatrix} \boldsymbol{e_{l,1}} & 0_{1\times3} & \boldsymbol{e_{l,1}L_P^E} \\ \vdots & \vdots & \vdots \\ \boldsymbol{e_{l,n_1}} & 0_{1\times3} & \boldsymbol{e_{l,n_1}L_P^E} \end{bmatrix}$ is a design matrix between $\boldsymbol{\Delta P_{GPS}}$ and $\boldsymbol{X_{PVE}} = [\delta\boldsymbol{p_{nb}^n} \quad \delta\boldsymbol{v_{nb}^n} \quad \delta\bar{\boldsymbol{\psi}}_{\boldsymbol{nb}}]^T$ with $\boldsymbol{e_{l,i\in[1,n_1]}}$ the LOS unit vector between the rover and the GPS satellite i expressed in local frame, $\boldsymbol{L_P^E} = [\boldsymbol{C_b^n l^b}\times]$;
- $\boldsymbol{G'^{PVE}_{\Delta \mathrm{P_{GLO}}}} = \begin{bmatrix} \boldsymbol{e_{l,1}} & 0_{1\times3} & \boldsymbol{e_{l,1}L_P^E} \\ \vdots & \vdots & \vdots \\ \boldsymbol{e_{l,n_2}} & 0_{1\times3} & \boldsymbol{e_{l,n_2}L_P^E} \end{bmatrix}$, is a design matrix between $\boldsymbol{\Delta P_{GLO}}$ and $\boldsymbol{X_{PVE}}$ with $\boldsymbol{e_{l,i\in[1,n_2]}}$ the LOS unit vector between the rover and the GLONASS satellite i expressed in local frame;
- $\boldsymbol{G'^{PVE}_{\nabla\Delta\Phi_{\mathrm{GPS}}}} = \begin{bmatrix} \boldsymbol{\Delta e_{l,1}} & 0_{1\times3} & \boldsymbol{\Delta e_{l,1}L_P^E} \\ \vdots & \vdots & \vdots \\ \boldsymbol{\Delta e_{l,n_3}} & 0_{1\times3} & \boldsymbol{\Delta e_{l,n_3}L_P^E} \end{bmatrix}$, is a design matrix between $\boldsymbol{\nabla\Delta\Phi_{GPS}}$ and $\boldsymbol{X_{PVE}}$ with $\boldsymbol{\Delta e_{l,i\in[1,n_3]}} = \boldsymbol{e_{l,i}} - \boldsymbol{e_{l,p}}$ the LOS unit vector difference expressed in local frame between GPS satellite i and the carrier phase pivot satellite p, $\boldsymbol{\lambda_{n_3\times n_3}} = \lambda_{GPS} * \mathbf{I_{n_3\times n_3}}$; ($\mathbf{I_{n_3\times n_3}}$ is an identity matrix);
- $\boldsymbol{G'^{PVE}_{\Delta\Phi_{\mathrm{GLO}}}} = \begin{bmatrix} \boldsymbol{e_{l,1}} & 0_{1\times3} & \boldsymbol{e_{l,1}L_P^E} \\ \vdots & \vdots & \vdots \\ \boldsymbol{e_{l,n_4}} & 0_{1\times3} & \boldsymbol{e_{l,n_4}L_P^E} \end{bmatrix}$ is a design matrix between $\boldsymbol{\Delta\Phi_{GLO}}$ and $\boldsymbol{X_{PVE}}$ with $\boldsymbol{e_{l,i\in[1,n_4]}}$;
- $\boldsymbol{G'^{PVE}_{D_{\mathrm{GPS}}}} = \begin{bmatrix} 0_{1\times3} & \boldsymbol{e_{l,1}} & \boldsymbol{e_{l,1}L_V^E} \\ \vdots & \vdots & \vdots \\ 0_{1\times3} & \boldsymbol{e_{l,n_5}} & \boldsymbol{e_{l,n_5}L_V^E} \end{bmatrix}$ is a design matrix between $\boldsymbol{D_{GPS}}$ and $\boldsymbol{X_{PVE}}$ with $\boldsymbol{e_{l,i\in[1,n_5]}}$ the LOS unit vector between the rover and the GPS Doppler satellite i expressed in local frame, $\boldsymbol{L_V^E} = \left[\boldsymbol{C_b^n\Omega_{ib}^b l^b}\times\right] - (\boldsymbol{\Omega_{en}^n} + \boldsymbol{\Omega_{ie}^n})\left[\boldsymbol{C_b^n l^b}\times\right]$;
- $\boldsymbol{L_{D_{GPS},b_g}} = \begin{bmatrix} -\boldsymbol{e_{l,1}C_b^n}\left[\boldsymbol{l^b}\times\right] \\ \vdots \\ -\boldsymbol{e_{l,n_5}C_b^n}\left[\boldsymbol{l^b}\times\right] \end{bmatrix}$ is a design matrix between $\mathbf{D_{GPS}}$ and $\delta\boldsymbol{b_g}$;
- $\boldsymbol{L_{D_{GPS},s_g}} = \begin{bmatrix} -\boldsymbol{e_{l,1}C_b^n}\left[\boldsymbol{l^b}\times\right]diag\left(\boldsymbol{w_{ib}^b}\right) \\ \vdots \\ -\boldsymbol{e_{l,n_5}C_b^n}\left[\boldsymbol{l^b}\times\right]diag\left(\boldsymbol{w_{ib}^b}\right) \end{bmatrix}$ is a design matrix between $\mathbf{D_{GPS}}$ and $\delta\boldsymbol{s_g}$;
- $\boldsymbol{G'^{PVE}_{\mathrm{D_{GLO}}}} = \begin{bmatrix} 0_{1\times3} & \boldsymbol{e_{l,1}} & \boldsymbol{e_{l,1}L_V^E} \\ \vdots & \vdots & \vdots \\ 0_{1\times3} & \boldsymbol{e_{l,n_6}} & \boldsymbol{e_{l,n_6}L_V^E} \end{bmatrix}$ is a design matrix between $\boldsymbol{D_{GLO}}$ and $\boldsymbol{X_{PVE}}$ with $\boldsymbol{e_{l,i\in[1,n_6]}}$ the LOS unit vector between the rover and the GLONASS Doppler satellite i expressed in local frame;
- $\boldsymbol{L_{D_{GLO},b_g}} = \begin{bmatrix} -\boldsymbol{e_{l,1}C_b^n}\left[\boldsymbol{l^b}\times\right] \\ \vdots \\ -\boldsymbol{e_{l,n_6}C_b^n}\left[\boldsymbol{l^b}\times\right] \end{bmatrix}$ is a design matrix between $\mathbf{D_{GLO}}$ and $\delta\boldsymbol{b_g}$;
- $\boldsymbol{L_{D_{GLO},s_g}} = \begin{bmatrix} -\boldsymbol{e_{l,1}C_b^n}\left[\boldsymbol{l^b}\times\right]diag\left(\boldsymbol{w_{ib}^b}\right) \\ \vdots \\ -\boldsymbol{e_{l,n_6}C_b^n}\left[\boldsymbol{l^b}\times\right]diag\left(\boldsymbol{w_{ib}^b}\right) \end{bmatrix}$ is a design matrix between $\boldsymbol{D_{GLO}}$ and $\delta\boldsymbol{s_g}$.

6.5 Motion Constraints

Various constraints can be applied in TC KF to strengthen the performance. Among those, ZUPT, NHC, and ZARU are used herein.

6.5.1 Zero Velocity Update

Zero velocity update (ZUPT or ZVU) is interesting to limit the drift of the solution when the immobility of the vehicle is detected. An immobility test thus needs to be conducted.

6.5.1.1 Detection of immobility

In [105], the vehicle is assumed to be stationary when the velocity is under a certain threshold. The threshold value needs to be determined by the velocity information during a calibration campaign, where the vehicle is known to be stationary. According to [2], [23], [24], when all velocities are under 0.5 m/s (a threshold tested in various environments), the standard deviation of IMU accelerometer measurements can be used to confirm the motionless of the vehicle. The perturbation level of the accelerometer measurements in stationary mode differs from the kinematic mode. Therefore, the performance (standard deviation) $\sigma_{acc,0}$ of accelerometer measurements in stationary mode need be analyzed in a prior phase. In this PhD, the immobility detection scheme with a confirmation scheme based on inertial raw measurements is applied. The immobility is assumed present during T_{imm} only in case that all velocities during the interval T_{imm} are less than 0.5 m/s, and the StdDev of measured forces is less than $3\sigma_{acc,0}$.

6.5.1.2 Measurement model

When an immobility is confirmed, the ZUPT constraint is modeled as,

$$\mathbf{y_{ZUPT}} = \begin{bmatrix} \hat{v}_x^b - 0 \\ \hat{v}_y^b - 0 \\ \hat{v}_z^b - 0 \end{bmatrix} = \delta \boldsymbol{v_{nb}^b} = \left(\hat{C}_b^n\right)^T \delta \boldsymbol{v_{nb}^n} - \left(\hat{C}_b^n\right)^T [\hat{\boldsymbol{v}}_{\boldsymbol{nb}}^{\boldsymbol{n}} \times] \cdot \delta \boldsymbol{\psi} \tag{6-39}$$

with $\hat{\boldsymbol{v}}_{\boldsymbol{nb}}^{\boldsymbol{n}}$ and $\hat{\boldsymbol{v}}_{\boldsymbol{nb}}^{\boldsymbol{n}} = \left[\hat{v}_x^b, \hat{v}_y^b, \hat{v}_z^b\right]^{\boldsymbol{T}}$ the estimated velocity vector respectively expressed in n-frame and in b-frame.

The corresponding design matrix is

$$\boldsymbol{H_{ZUPT}} = \left[0_3\ , \left(\hat{C}_b^n\right)^T, -\left(\hat{C}_b^n\right)^T [\hat{\boldsymbol{v}}_{\boldsymbol{nb}}^{\boldsymbol{n}} \times], 0_{3\times(N-9)}\right] \tag{6-40}$$

The measurement uncertainty put on forward-direction speed is simply 0.5 m/s .

6.5.2 Non-Holonomic Constraint

The Non-Holonomic constraint (NHC) describes the fact that generally, the lateral and vertical velocities are negligible compared to the straightforward velocity. This hypothesis does not hold if the vehicle is sliding laterally or jumping.

This constraint is always used in this PhD. The NHC is modeled as

$$\mathbf{y_{NHC}} = \begin{bmatrix} \hat{v}_x^b - 0 \\ \hat{v}_z^b - 0 \end{bmatrix} \tag{6-41}$$

Compared to the ZUPT, the design matrix $\boldsymbol{H_{NHC}}$ omits the second line of the matrix H_{ZUPT}:

$$\boldsymbol{H_{NHC}} = \boldsymbol{H_{ZUPT}}([1,3],:) \tag{6-42}$$

The measurement noise covariance is adjusted empirically to account for the velocity uncertainty into the vehicle motion.

The standard deviation of the measurements noise is set empirically to be $[0.04, 0.08] * Speed$.

6.5.3 Zero Angular Rate Update

The Zero Angular Rate Update (ZARU) constraint assumes that the angular rate should also be null when the vehicle is confirmed in stationary mode, the same detection condition as ZUPT.

The constraint measurements are given by

$$\mathbf{y_{ZARU}} = \begin{bmatrix} w_{ib,x}^b - 0 \\ w_{ib,y}^b - 0 \\ w_{ib,z}^b - 0 \end{bmatrix} = \boldsymbol{\delta w_{ib}^b} \tag{6-43}$$

where $\boldsymbol{w_{ib}^b} = \left[w_{ib,x}^b, w_{ib,y}^b, w_{ib,z}^b\right]^{\boldsymbol{T}}$ is the corrected angular rate vector of the *b*-frame w.r.t the *i*-frame resolved in *b*-frame,

The geometry matrix is:

$$\boldsymbol{H_{ZARU}} = \left[0_3, 0_3, 0_3, 0_3, I_3, 0_{3\times(N-15)}\right] \tag{6-44}$$

The measurement noise covariance level depends on the sensor vibration and other disturbances. Besides, higher weight is put on the measurement around the yaw axis as the yaw axis ($\hat{w}_{ib,z}^b$) is less affected by disturbances than the other two directions [2].

6.6 Conclusion

In this chapter, major modules of the proposed INS/GNSS integration algorithm have been all presented. The functioning scheme of the INS/GNSS TC is depicted in Figure 6-8. On the basis of the GNSS RTK positioning scheme, an INS mechanization process is added on the plot. Adopting the error states modeling, predictions of error states from the INS mechanization process are passed to the main INS/GNSS Kalman filter. The differences between GNSS observables and their corresponding predictions based on error states serve as inputs of the main KF. Besides, additional motion constraints are added to the KF when demanding conditions are satisfied.

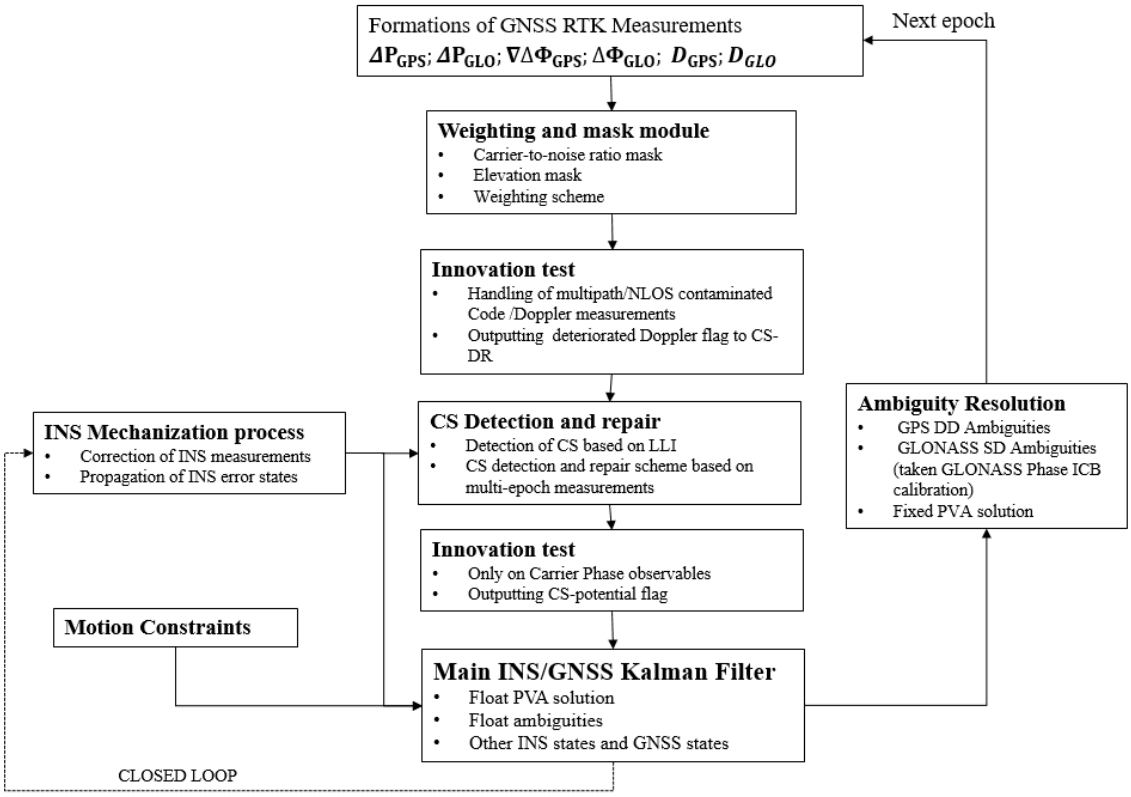

Figure 6-8. Scheme of the Implemented GNSS/INS Positioning Filter

7 Tests and Results

In previous chapters, the proposed algorithm for RTK positioning in constrained environment with the low-cost single frequency GNSS receiver coupled with MEMS INS navigation has been introduced and described. In this chapter, performance of this integration algorithm will be illustrated using previously described GNSS data in Section 5.1.2, i.e. rural Data set 1 and urban Data set 2, and corresponding inertial data collected with the inertial equipment XSENS.

7.1 DGNSS/INS Results

In this section, illustrations of the tight coupling (TC) performance between GNSS code and Doppler measurements, and the low-cost MEMS will firstly be analyzed. This integration without considering GNSS carrier phase measurements, in other words, ignoring the problematics related to ambiguity resolutions, will show in the first place the performance of a low-cost MEMS integrated with meter-level GNSS measurements.

In the first place, the TC tests are conducted with both the Data set 1 and Data set 2. Same relevant parameters are used as in Section 5.2.3. The positioning results are plotted respectively in Figure 7-1 and Figure 7-2.

By comparing Figure 7-1 and Figure 5-24 of the Data set 1, no improvement in positioning statistics is observed. With the integration with INS, the 95 percentile of the horizontal positioning error is now **2.12** meters, compared to the DGNSS only case **2.01** meters. Globally, a very similar temporal positioning error curve to the GNSS only case is provided by the TC of DGNSS and INS.

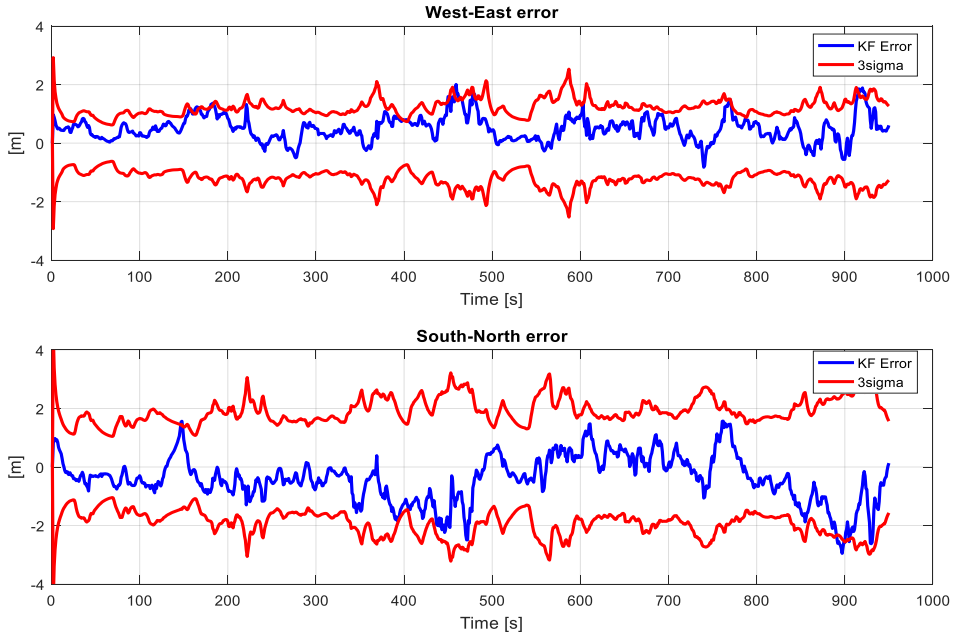

Figure 7-1. Horizontal DGNSS/INS position difference between estimated trajectory and the reference trajectory (Data set 1) with associated environment type chosen as 'Rural'.

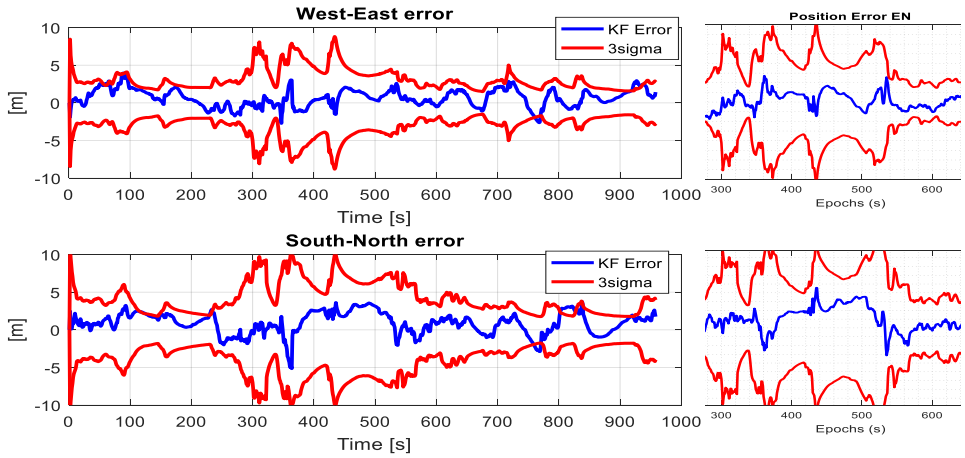

Figure 7-2. At left: Horizontal DGNSS/INS position difference between estimated trajectory and the reference trajectory (Data set 2) with associated environment type chosen as 'Urban'. At right, copy of the Figure 5-29 for DGNSS only, portion between Epochs 200 and 600. .

In the Data set 2 case, as a comparison, the positioning results of the DGNSS scheme is copied herein on the right in Figure 7-2. The 95 percentile of the horizontal positioning error has a small reduction, from **3.8** meters to **3.4** meters. By observing the temporal positioning results, a slightly better and smoother error curve, as well as a slightly lower 3-sigma bounds are present on the interval between 200 and 400 epochs. As indicated in Figure 5-28 and Figure 5-30, this interval corresponds to a comparably lower availability of GNSS satellites. During this interval, the HODP value has increased with several peaks and the total number of available GNSS satellites is around 5.

Looking at the illustrative results obtained from Data set 1 and Data set 2, the visibility of satellites is in good condition, the improvement brought by the consideration of such a low-quality MEMS is very limited as DGNSS outperforms the MEMS. In the case of Data set 1, the horizontal positioning performance, holding a 3-sigma less than 2 meters in GNSS-only condition, has stayed the same while tightly coupling with the MEMS. As for the Data 2, the uncertainty level on positioning errors does not have a remarkable decrease after TC and a very similar positioning curve is observed during most temporal portions. Nevertheless, a small benefit of integrating a MEMS is observed when a lack of available GNSS measurements exists.

7.2 Performance of INS-aided CS-DR

In this section, we first give initial illustrations of performance of float RTK integrated with INS, followed by IAR results.

With the presence of precise INS information, inertial predictions of position states and Doppler-derived clock delay rate are utilized as additional observables inside the CS-DR scheme. Therefore, only the rural Data set 1 will be used herein for tests. With the urban Data set 2, a positioning performance with 3 sigma values at a level of 5 meters is definitely not precise enough to provide extra references to CS repair.

Instead of a big inflation on CS-deteriorated ambiguities' covariance, it will be more of interest if a proper value, for example the corresponding covariance calculated inside the CS LS filter, can be used.

Conserving the same CS-DR parameters as in Section 5.2.3, i.e. the triplet $(\alpha_1, \alpha_2, N_{cs}) = (\mathbf{0.003}, \mathbf{0}, \mathbf{10})$ and a minimum of **5** satellites required for CS-free declaration, the positioning results with ambiguities inflated by calculated covariance values are plotted in Figure 7-3. The 95 percentile of

horizontal positioning errors is **1.89** meters, larger than **1.39** meters of the case when only float RTK-GNSS is involved. The number of epochs having more than 5 CS-free satellites is herein **824** in Figure 7-4, and the number of epochs having CS detected is **648** in Figure 7-5. Remind that in the float RTK-GNSS case (Figure 5-34), the numbers were **862** the number of epochs holding CS-free satellites and **734**, the number of epochs having CS detected. Herein, a cleaner CS condition is reflected and there is no sign of fatal miss-detections of big CSs.

By comparing the positioning errors, quite similar curves are observed in both Figure 7-3 and Figure 5-36, except for the interval from epoch 450 to epoch 480. Only during this temporal section a remarkable deterioration is found. According to the Figure 7-4, the algorithm constantly declares all satellites CS-deteriorated during epochs 450 to 480. Instead of occasionally modifying the positioning results in the case only-GNSS, herein the integration system choses to stick with the biased but tolerable-to-INS solution, until the continuous convergence of GNSS ambiguities reclaims.

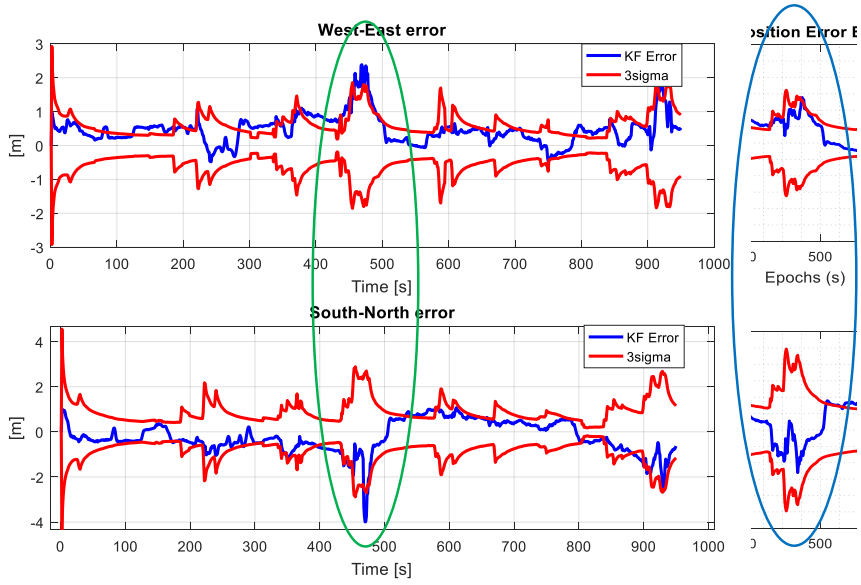

Figure 7-3. On the left: Horizontal Float RTK/INS position difference between estimated trajectory and the reference trajectory (Data set 1) with ambiguity covariance inflation by corresponding CS covariance. On the right: Portion of Figure 5-36, case only –GNSS.

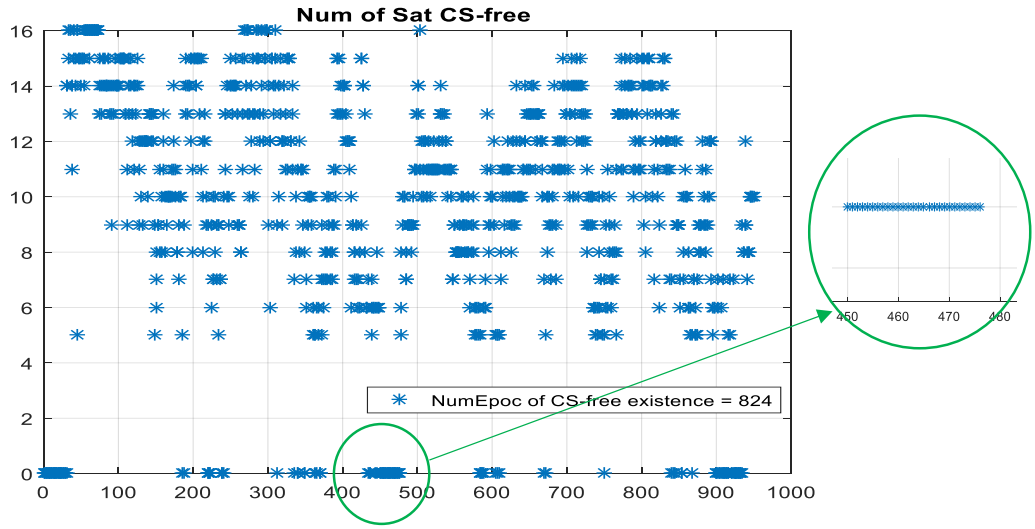

Figure 7-4. Number of satellites declared CS-free in each epoch (Data set 1, minimum number of 5 is required). CS-DR scheme takes the values $(\alpha_1, \alpha_2, N_{cs}) = (0.003, 0, 10)$.

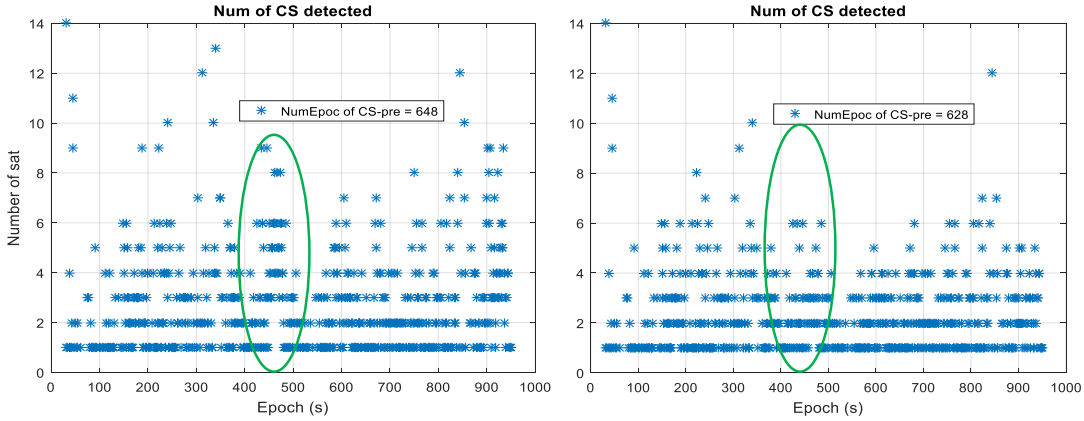

Figure 7-5. Number of satellites declared CS-deteriorated in each epoch (Data set 1). CS-DR scheme takes the values $(\alpha_1, \alpha_2, N_{cs}) = (0.003, 0, 10)$. *On the left: minimum number of 5 satellites is required for CS-free declaration. On the right: no requirement on minimum number of satellites for CS-free declaration.*

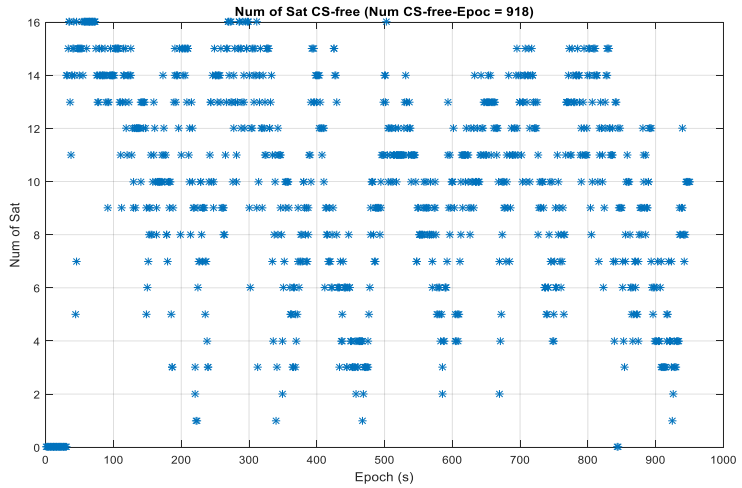

Figure 7-6. Number of satellites declared CS-free in each epoch (Data set 1). CS-DR scheme takes the values $(\alpha_1, \alpha_2, N_{cs}) = (0.003, 0, 10)$.

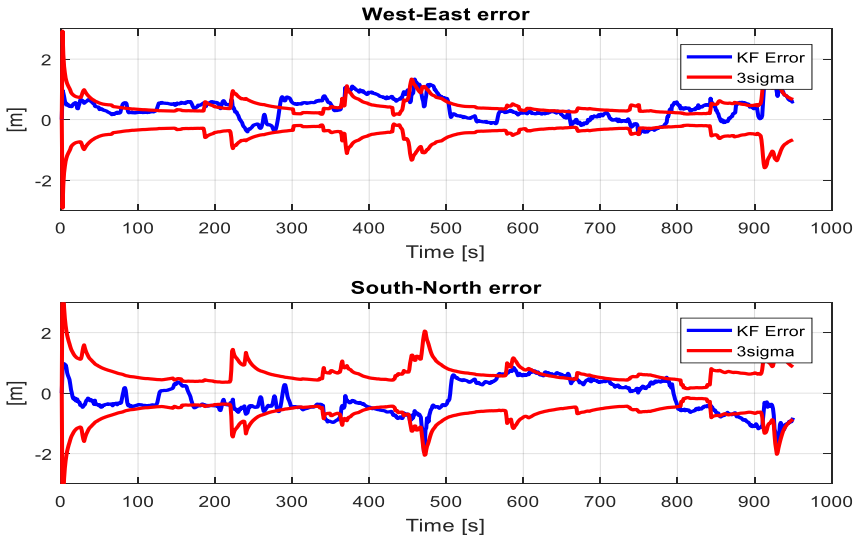

Figure 7-7. Horizontal Float RTK/INS position difference between estimated trajectory and the reference trajectory (Data set 1) with ambiguity covariance inflation by corresponding CS covariance. Minimum number of 5 is not required for CS-free declaration.

With the consideration of the additional 4 (i.e., 3 position states and the clock-delay rate) measurements, the minimum number of 5 satellites for declaring CS-free is no longer required. In this way, the number of epochs holding CS-free satellites arises from **824** to **918**, as indicated in Figure 7-6. By comparing the 2 plots in in Figure 7-5, another 20 CS-affecting epochs (**648-628**) are released. The 95 percentile of horizontal positioning errors is **1.32** meters, a performance comparable to **1.39** meters of the only-GNSS case. The relation between temporal positioning errors and their corresponding 3-sigma plots is showed in Figure 7-7. Compared with the Figure 7-3, along with the increased presence of CS-free satellites, much smoother positioning performance and 3-sigma envelopes are reflected in Figure 7-7. Besides, the positioning bias during epochs 450 and 480 is perfectly controlled.

Same as in previous Section 5.2.4, the performance of the Partial-IAR (Partial-Integer Ambiguity Resolution) methodology with associated parameters such as the threshold for the probability of success fixing $P_{S,0} = 99.5\%$, an empirical ratio threshold of 2 and a minimum number of 5 DD ambiguities to enter IAR, will be presented. First of all, the value of P_S calculated based on the best 5 satellites having the lowest uncertainty is studied in Figure 7-8. The percentage of holding a P_S greater than $P_{S,0}$ is herein **19.05%.** The value was **12.8%** in Section 5.2.4. As expected, continuous estimation of ambiguities provides a better anticipation of success fixing.

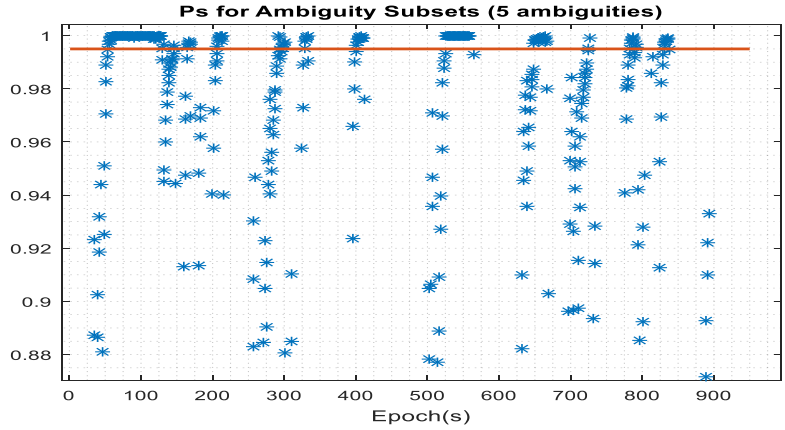

Figure 7-8. The probability of success Ps calculated based on the 5 ambiguities having the lowest uncertainty (Data set 1)

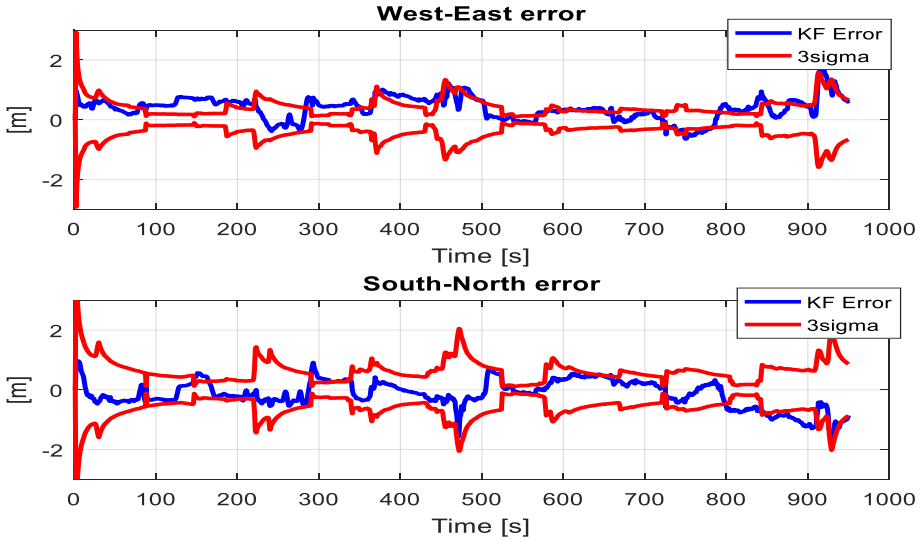

Figure 7-9. Horizontal performance of the IAR solution using the proposed Partial-IAR as the ambiguity validation method (Data set 1)

Table 7-1. Performance summary of the IAR results processing the Data set 1 using a modified Partial-IAR validation scheme.

	Horizontal Positioning Error (in meter)				
Data Set 1	**68th Percentile**	**95th Percentile**	**98th Percentile**	**Fix Rate**	**Wrong Fix Rate**
GNSS IAR	0.74	1.80	2.52	5.6%	16.7%
GNSS/INS IAR	0.74	1.26	1.75	4.8%	9.3%

The horizontal positioning results are provided in Figure 7-9. With the positioning statistics of the GNSS case, new GNSS/INS performance indicators are summarized in Table 7-1. Smaller horizontal positioning error percentiles are obtained in the case GNSS/INS. A 95th percentile of **1.26** meter is comparable with the previous float GNSS/INS case. Still a comparably low fix rate of **4.8%** is obtained. The fixing zone is mainly located between epoch 500 and 600, where a constantly big value of P_S is guaranteed. Nevertheless, the wrong fix rate is much lower **9.3%,** in comparison with **16.7%** of the GNSS case.

8 Conclusions and Proposals on Future Work

8.1 Conclusions

This thesis carried out the analysis of integrated INS/GNSS (GPS+GLONASS) for land vehicle applications, using carrier phase measurement for high accuracy. Illustrations of performance are taken from data collection performed in a light urban environment in Toulouse.

The Float-RTK has been proven to work well with consistent bounds especially during CS-free periods. As results, a performance of holding the 95 percentile horizontal error at a 1-meter level in lightly constrained environment, and at a 3-meter level in an urban area are obtained. The importance of CS-DR (Cycle Slip Detection and Repair) appears obvious. The miss-detection and false-detection of CS both deteriorate the solution in urban situations, by biasing the carrier phase position at a certain period of the data collection. The carrier phase measurements are also not fully used due to the difficulty to detect and repair reliably CSs in difficult conditions.

The reliability of the fixed carrier phase ambiguity solution is not yet satisfactory in urban environments due to the frequent occurrences of CS and the low ambiguity fixing rate. The demanding criteria for a declared ambiguity fixing are rarely satisfied. This could be expected as only L1 measurements are used. This is clearly a field to improve.

The coupling of a low-cost single frequency receiver with low-cost IMU does not boost the positional accuracy when the GNSS signals are received in good conditions, and does not seem to improve the AR. However, the improvement brought by low-cost IMU when operating in a constrained environment is more obvious.

8.2 Proposals for Future Work

The proposed work can be improved in the following aspects:

- **Multi-constellation/Multi-frequency**: For this study, only the GPS and GLONASS constellations are taken into account because the low-cost receiver used did not process Galileo signals and the visibility of Galileo and BeiDou satellites in Toulouse was rare at the time of the thesis. Taken the distinguished developments in constellation construction of Galileo and BeiDou, we believe that the inclusion of Galileo and BeiDou would bring more reliability on PVT solutions, in particular though their pilot signals. With the technology development of GNSS receivers, the possibility of using multi-frequency receivers may arise. Under the concept of RTK, other than improving the positioning performance, a further verification of hypothesis imposed on our algorithms can be done.
- **Measurement correction models**: When centimeter-level precise positioning is envisioned, some measurement correction models which have been previously ignored need be carefully reconsidered, such as the wind-up effect, the phase center calibration, etc [6], [106].
- **Coupling with high-quality sensors**: With the technology development in inertial industry, the price of high-quality inertial units tends to decrease. Under the concept of low-cost, comparable higher-quality units are of more interests.
- **Integrity information**: In addition to the accuracy of the estimated position, a measure of the trust that tells the correctness of the solution should also be provided. The integrity information of navigation solution is for sure a critical and indispensable message for many applications which unfortunately has not been possible to be covered in this dissertation.
- **Refined Cycle slip detection and repair scheme**: For this moment, our proposed CS-DR relies too much on the satellite geometry quality. The CS-free satellite cannot continue to be used when the number of CS-free satellites is less than 5. CS-free satellite should be better identified in the future. The choice of holding the GNSS measurements rate at 1Hz is not to loose the possibility of integrating a

real-time algorithms. With the intention to improve the detection and repair of CS, a higher measurement rate is always an alternative.

- **Integer ambiguity resolution**: In order to limit the influence of low-quality satellites (CS or multipath contaminated ones) that could corrupt the ambiguity resolution of the whole set, Partial-AR has been chosen. The key factor for Partial-IAR relies on the subset selection. More complete criteria should be tested.
- **External aiding**: The contribution of a low-cost MEMS has turned out to show limited effects on RTK performance under semi-urban/urban areas. However, the integration with a higher-grade IMU is still worthy exploring.

References

[1] A. Noureldin, T. B. Karamat, and J. Georgy, *Fundamentals of Inertial Navigation, Satellite-based Positioning and their Integration*. Berlin, Heidelberg: Springer Berlin Heidelberg, 2013.

[2] P. D. Groves, *Principles of GNSS, Inertial, and Multisensor Integrated Navigation Systems*. Artech House, 2013.

[3] Scott Gleason and Demoz Gebre-Eqziabher, *GNSS Applications and Methods*. Artech House, 2009.

[4] H. Kuusniemi, "User-Level Reliability and Quality Monitoring in Satellite-Based Personal Navigation," Thesis for the degree of Doctor of Tchnology, University of Technology, Tampere, 2005.

[5] P. Misra and P. Enge, *Global Positioning System: Signals, Measurements and Performance Second Edition*. 2006.

[6] Peter J.G. Teunissen, *Handbook of Global Navigation Satellite Systems*. Springer, 2017.

[7] S. Carcanague, "Low cost GPS GLONASS Precise Positioning Algorithm in Constrained Environment," Institut National Polytechnique de Toulouse, 2013.

[8] B. Hofmann-Wellenhof, H. Lichtenegger, and E. Wasle, *GNSS-Global Navigation Satellite Systems*. Springer, 2008.

[9] D. Odijk, P. J. G. Teunissen, and A. Khodabandeh, "Single-Frequency PPP-RTK: Theory and Experimental Results," in *Earth on the Edge: Science for a Sustainable Planet*, vol. 139, C. Rizos and P. Willis, Eds. Berlin, Heidelberg: Springer Berlin Heidelberg, 2014, pp. 571–578.

[10] P. J. G. Teunissen, "Towards a unified theory of GNSS ambiguity resolution," *JournPositioning*, vol. Journal of Global Positioning Systems, no. 04, p. 0, 2003.

[11] S. Verhagen, "The GNSS integer ambiguities estimation and validation," Publications on Geodesy, Netherlands Geodetic Commission, Delft, 2005.

[12] P. J. G. Teunissen, "Integer aperture GNSS ambiguity resolution," in *Artificial Satellites*, 2002, vol. 38, No. 3, pp. 79–88.

[13] P. J. Teunissen, "GNSS ambiguity bootstrapping: theory and application," in *Proceedings of international symposium on kinematic systems in Geodesy, geomatics and navigation*, 2001, pp. 246–254.

[14] P. De Jonge, C. Tibernius, and P. Teunissen, "Computational aspects of the LAMBDA method for GPS ambiguity resolution," in *PROCEEDINGS OF ION GPS*, 1996, vol. 9, pp. 935–944.

[15] P. J. G. Teunissen, "An optimality property of the integer least-squares estimator," *Journal of Geodesy*, vol. 73, no. 11, pp. 587–593, Dec. 1999.

[16] P. J. G. Teunissen, P. J. Jonge, and C. Tiberius, "Performance of the LAMBDA method for fast GPS ambiguity resolution," *Navigation*, vol. 44, no. 3, pp. 373–383, 1997.

[17] A. E. Zinoviev, "Using GLONASS in combined GNSS receivers: current status," in *Proceedings of ION GNSS*, 2005, pp. 1046–1057.

[18] Richard Ong, "Reliability of Combined GPS/GLONASS Ambiguity Resolution," Master of Science, UNIVERSITY OF CALGARY, CALGARY, ALBERTA, 2010.

[19] H. Yamada, T. Takasu, N. Kubo, and A. Yasuda, "Evaluation and Calibration of Receiver Inter-channel Biases for RTK-GPS/GLONASS," presented at the Proceedings of the 23rd International Technical Meeting of The Satellite Division of the Institute of Navigation (ION GNSS 2010) September 21 - 24, 2010 Oregon Convention Center, Portland, Oregon Portland, OR, 2010.

[20] J. Wang, C. Rizos, M. P. Stewart, and A. Leick, "GPS and GLONASS integration: modeling and ambiguity resolution issues," *GPS solutions*, vol. 5, no. 1, pp. 55–64, 2001.

[21] L. Wanninger, "Carrier-phase inter-frequency biases of GLONASS receivers," *Journal of Geodesy*, vol. 86, no. 2, pp. 139–148, Feb. 2012.

[22] S. Chuang, Y. Wenting, S. Weiwei, L. Yidong, Y. yibin, and Z. Rui, "GLONASS pseudorange inter-channel biases and their effects on combined GPS/GLONASS precise point positioning," *GPS Solutions*, vol. 17, no. 4, pp. 439–451, Oct. 2013.

[23] A. Angrisano, "GNSS/INS integration methods," 2010.

[24] P. Aggarwal, *MEMS-based integrated navigation*. Artech House, 2010.

[25] "GPS.gov: Space Segment." [Online]. Available: https://www.gps.gov/systems/gps/space/.

[26] IS-GPS-200H, “Navstar GPS Space Segment/Navigation User Interfaces IS-GPS-200H,” Sep. 2013.
[27] GLONASS ICD, “GLONASS Interface Control Document (Edt 5.1).” 2008.
[28] A. Noureldin, T. B. Karamat, and J. Georgy, “Basic Navigational Mathematics, Reference Frames and the Earth’s Geometry,” in *Fundamentals of Inertial Navigation, Satellite-based Positioning and their Integration*, Berlin, Heidelberg: Springer Berlin Heidelberg, 2013, pp. 21–63.
[29] Alain L. Kornhauser, “Global Navigation Satellite System,” Princeton University, 2007.
[30] C. Boucher and Z. Altamimi, “ITRS, PZ-90 and WGS 84: current realizations and the related transformation parameters,” *Journal of Geodesy*, vol. 75, no. 11, pp. 613–619, 2001.
[31] ICD-GPS-200C, “Interface Control Document ICD-GPS-200C.” 2000.
[32] A.N. Zueva, E.V.Novikov, D.I.Pleshakov, and I.V.Gusev, “System of geodetic parameters Zemli 1990 PZ-90.11,” presented at the Proc. 9th Meet . Int . Comm. GNSS (ICG), Work. Group D, Prague (UNOOSA, Vienna 2014), 2014.
[33] Igor Gusev and Olga Sanakina, “Current Status of Global Terrestrial Reference Systems Implemented in GNSS,” Russian Federal Space Agency, 2015.
[34] Stephen Malys, Robert Wong, and Scott A. True, “The WGS84 Terrestrial Reference Frame in 2016,” ICD-11, Sochi Russia, Nov. 2016.
[35] W Lewandowski and E F Arias, “GNSS times and UTC,” *Metrologia*, 2011.
[36] “RINEX The Receiver Independent Exchange Format Version 3.03.” IGS, RINEX Working Group and Radio Technical Commission for Maritime Services Special Committee 104 (RTCM-SC104), 14-Jul-2015.
[37] R. G. Brown and P. Y. C. Hwang, *Introduction to random signals and applied Kalman filtering: with MATLAB exercises*, 4. ed. Hoboken, NJ: Wiley, 2012.
[38] “GNSS signal - Navipedia.” [Online]. Available: http://www.navipedia.net/index.php/GNSS_signal. [Accessed: 24-Apr-2018].
[39] E. D. Kaplan and C. Hegarty, Eds., *Understanding GPS: principles and applications*, 2nd ed. Boston: Artech House, 2006.
[40] Rodrigo Leandro, M. Santos, and R. B. Langley, “UNB Neutral Atmosphere Models Development and Performance,” presented at the Proceedings of ION NTM 2006, Monterey, California, 2006.
[41] L. Wanninger, “Ionospheric Monitoring Using IGS Data,” presented at the IGS Workshop, 1993.
[42] S. Katsougiannopoulos, C. Pikridas, D. Rossikopoulos, I. Ifadis, and A. Fotiou, “Tropospheric refraction estimation using various models, radiosonde measurements and permanent GPS data,” *PS5. 4–GNSS Processing and Applications*, vol. 15, 2006.
[43] “Geometric dilution of precision,” *Wikipédia*. 12-Jan-2018.
[44] D. Laurichesse and F. Mercier, “Real-time PPP with undifferenced integer ambiguity resolution, experimental results,” p. 13, 2010.
[45] D. Laurichesse, F. Mercier, J.-P. Berthias, P. Broca, and L. Cerri, “Integer Ambiguity Resolution on Undifferenced GPS Phase Measurements and Its Application to PPP and Satellite Precise Orbit Determination,” *Navigation*, vol. 56, no. 2, pp. 135–149, juin 2009.
[46] M. Ge, G. Gendt, M. Rothacher, C. Shi, and J. Liu, “Resolution of GPS carrier-phase ambiguities in Precise Point Positioning (PPP) with daily observations,” *Journal of Geodesy*, vol. 82, no. 7, pp. 389–399, Jul. 2008.
[47] A. Rovira-Garcia, J. M. Juan, J. Sanz, G. González-Casado, and E. Bertran, “Fast Precise Point Positioning: A System to Provide Corrections for Single and Multi-frequency Navigation,” *Navigation*, vol. 63, no. 3, pp. 231–247, 2016.
[48] S. Verhagen and P. J. G. Teunissen, “The ratio test for future GNSS ambiguity resolution,” *GPS Solut*, vol. 17, no. 4, pp. 535–548, Nov. 2012.
[49] T. Li and J. Wang, “Analysis of the upper bounds for the integer ambiguity validation statistics,” *GPS Solut*, vol. 18, no. 1, pp. 85–94, Feb. 2013.
[50] P. J. Teunissen, “The least-squares ambiguity decorrelation adjustment: a method for fast GPS integer ambiguity estimation,” *Journal of Geodesy*, vol. 70, no. 1–2, pp. 65–82, 1995.
[51] P. J. G. Teunissen, “Least-squares estimation of the integer GPS ambiguities,” in *Invited lecture, section IV theory and methodology, IAG general meeting, Beijing, China*, 1993.
[52] P. J. G. Teunissen, “Integer aperture bootstrapping: a new GNSS ambiguity estimator with controllable fail-rate,” *Journal of Geodesy*, vol. 79, no. 6–7, pp. 389–397, Aug. 2005.

[53] P. De Jong and C. Tiberius, “The LAMBDA method for integer ambiguity estimation: implementation aspects.” Aug-1996.
[54] D. Kim and R. B. Langley, “GPS ambiguity resolution and validation: methodologies, trends and issues,” in *Proceedings of the 7th GNSS Workshop–International Symposium on GPS/GNSS, Seoul, Korea*, 2000, vol. 30.
[55] X.-W. Chang, X. Yang, and T. Zhou, “MLAMBDA: a modified LAMBDA method for integer least-squares estimation,” *Journal of Geodesy*, vol. 79, no. 9, pp. 552–565, 2005.
[56] S. Verhagen and Bofeng Li, “LAMBDA - Matlab implementation, version 3.0.” 2012.
[57] J. Wang, M. P. Stewart, and M. Tsakiri, “A comparative study of the integer ambiguity validation procedures,” *Earth, planets and space*, vol. 52, no. 10, pp. 813–817, 2000.
[58] S. Verhagen and P. J. Teunissen, “New global navigation satellite system ambiguity resolution method compared to existing approaches,” *Journal of Guidance, Control, and Dynamics*, vol. 29, no. 4, pp. 981–991, 2006.
[59] T. Li and J. Wang, “Some remarks on GNSS integer ambiguity validation methods,” *Survey Review*, vol. 44, no. 326, pp. 230–238, Jul. 2012.
[60] L. Wang and Y. Feng, “Fixed Failure Rate Ambiguity Validation Methods for GPS and Compass,” in *China Satellite Navigation Conference (CSNC) 2013 Proceedings*, vol. 244, J. Sun, W. Jiao, H. Wu, and C. Shi, Eds. Berlin, Heidelberg: Springer Berlin Heidelberg, 2013, pp. 379–397.
[61] S. Verhagen and P. J. G. Teunissen, “On the probability density function of the GNSS ambiguity residuals,” *GPS Solutions*, vol. 10, no. 1, pp. 21–28, Feb. 2006.
[62] P. J. Teunissen and S. Verhagen, “On the foundation of the popular ratio test for GNSS ambiguity resolution,” in *Proc. ION GNSS*, 2004, pp. 2529–2540.
[63] P. J. G. Teunissen and S. Verhagen, “On GNSS ambiguity acceptance tests,” in *Proc. IGNSS Symposium*, 2007.
[64] B. J. Clark and D. M. Bevly, “GPS/INS integration with fault detection and exclusion in shadowed environments,” in *2008 IEEE/ION Position, Location and Navigation Symposium*, 2008, pp. 1–8.
[65] S. Godha, “Performance evaluation of low cost MEMS-based IMU integrated with GPS for land vehicle navigation application,” Library and Archives Canada, 2006.
[66] E.-H. Shin, “Estimation Techniques for Low-Cost Inertial Navigation,” The University of Calgory, 2005.
[67] M. G. Petovello, “Real-time integration of a tactical-grade IMU and GPS for high-accuracy positioning and navigation,” 2004.
[68] P. F. F. N. Ferrao, “Positioning with Combined GPS and GLONASS Observations,” Master of Science Degree in Aerospace Engineering, Instituto Superior Técnico, 2013.
[69] J. Aggrey and S. Bisnath, “Analysis and modelling of pseudorange and carrier-phase biases in GNSS Precise Point Positioning,” in *27th International Technical Meeting of The Satellite Division of the Institute of Navigation*, Tampa, Florida, 2014.
[70] A.-C. Escher, “Study of the Contribution of GNSSINS Hybridization to GNSS Integrity Monitoring for Civil Aviation Applications,” 2003.
[71] Heidi Kuusniemi and G. Lachapelle, “GNSS signal reliability testing in urban and indoor environments,” in *Proceedings of the NTM Conference*, 2004.
[72] S. Carcanague, “Real-time geometry-based cycle slip resolution technique for single-frequency PPP and RTK,” in *ION GNSS 2012, Proceedings of the 25th International Technical Meeting of The Satellite Division of the Institute of Navigation*, 2012, p. pp–1136.
[73] D. Kozlov, M. Tkachenko, and A. Tochilin, “Statistical characterization of hardware biases in GPS+GLONASS receivers,” presented at the Proceedings of the 13th international technical meeting of the Satellite Division of The Institute of Navigation (ION GPS 2000), 2000.
[74] J. Geng, Q. Zhao, C. Shi, and J. Liu, “A review on the inter-frequency biases of GLONASS carrier-phase data,” *Journal of Geodesy*, vol. 91, no. 3, pp. 329–340, Mar. 2017.
[75] L. Wanninger and S. Wallstab-Freitag, “Combined Processing of GPS, GLONASS, and SBAS Code Phase and Carrier Phase Measurements,” presented at the ION GNSS 20th International Technical Meeting of the Satellite Division, Fort Worth, TX, 2007.
[76] J. E. Aggrey, “Multi-GNSS Precise Point Positioning Software Architecture and Analysis of GLONASS Pseudorange Biases,” Master of Science, York University Toronto, 2014.

[77] J. Chen, P. Xiao, Y. Zhang, and B. Wu, "GPS/GLONASS System Bias Estimation and Application in GPS/GLONASS Combined Positioning," in *China Satellite Navigation Conference (CSNC) 2013 Proceedings*, vol. 244, J. Sun, W. Jiao, H. Wu, and C. Shi, Eds. Berlin, Heidelberg: Springer Berlin Heidelberg, 2013, pp. 323–333.
[78] Sleewaegen J., Simsky A., de Wilde W., Boon F., and Willems T., "Demystifying GLONASS Inter-Frequency Carrier Phase Biase," *Inside GNSS*, pp. 57–61, Jun. 2012.
[79] P. J. G. Teunissen, "Quality Control and GPS," in *GPS for Geodesy*, P. J. G. Teunissen and A. Kleusberg, Eds. Berlin, Heidelberg: Springer Berlin Heidelberg, 1998, pp. 271–318.
[80] O. Julien, "Carrier-Phase Tracking of Future Data/Pilot Signals," in *18th International Technical Meeting of The Satellite Division of the Institute of Navigation*, Long Beach, California, 2005.
[81] G. Falco, M. Pini, and G. Marucco, "Loose and Tight GNSS/INS Integrations: Comparison of Performance Assessed in Real Urban Scenarios," *Sensors*, vol. 17, no. 2, p. 255, Jan. 2017.
[82] M. Bahrami and M. Ziebart, "Instantaneous Doppler-aided RTK positioning with single frequency receivers," in *Position Location and Navigation Symposium (PLANS), 2010 IEEE/ION*, 2010, pp. 70–78.
[83] Malek Karaim, Tashfeen B. Karamat, Aboelmagd Noureldin, and Ahmed El-Shafie, "GPS Cycle Slip Detection and Correction at Measurement Level," *British Journal of Applied Science & Technology*, vol. 29, no. 4, pp. 4239–4251, 2014.
[84] S. Verhagen, C. Tiberius, B. Li, and P. J. Teunissen, "Challenges in ambiguity resolution: biases, weak models, and dimensional curse," in *Satellite Navigation Technologies and European Workshop on GNSS Signals and Signal Processing,(NAVITEC), 2012 6th ESA Workshop on*, 2012, pp. 1–8.
[85] P. J. G. Teunissen, P. Joosten, and C. Tiberius, "Geometry-free ambiguity success rates in case of partial fixing," in *Proceedings of ION-NTM*, 1999, pp. 25–27.
[86] Ublox Technology, "EVK-7-8-M8 Ublox GNSS Evaluation Kits."
[87] XSENSTechnologies, "MTi and MTx User Manual and Technical Documentation," Document MT0100P, Version O, Oct. 2010.
[88] T. Takasu and A. Yasuda, "Development of the low-cost RTK-GPS receiver with an open source program package RTKLIB," in *international symposium on GPS/GNSS*, 2009, pp. 4–6.
[89] T. Takasu, "RTKLIB Manuel," 2013.
[90] T. Takasu and A. Yasuda, "Cycle slip detection and fixing by MEMS-IMU/GPS integration for mobile environment RTK-GPS," in *Proceedings of the 21st International Technical Meeting of the Satellite Division of the Institute of Navigation (ION GNSS 2008), Savannah, GA, USA*, 2008, vol. 1619, p. 6471.
[91] H. Sulen, "Civil maritime GNSS combinations in arctic areas," Master of Science in Positioning and Navigational Technology, 2015.
[92] Y. Quan, L. Lau, G. W. Roberts, and X. Meng, "Measurement Signal Quality Assessment on All Available and New Signals of Multi-GNSS (GPS, GLONASS, Galileo, BDS, and QZSS) with Real Data," *Journal of Navigation*, vol. 69, no. 02, pp. 313–334, Mar. 2016.
[93] E. Lie and H. Leithe, "Integrating GNSS/INS/PVT for robust positioning," Master of Science, NTNU, 2016.
[94] V. Elisson and G. Gässler, "Low cost relative gnss positioning with imu integration," Master of Science, Chalmers University of Technology, Göteborg, 2014.
[95] D. H. Titterton and J. L. Weston, *Strapdown inertial navigation technology*, 2. ed., repr. Stevenage: Institution of Electrical Engineers, 2009.
[96] XSENS Technology, "Mti User Manuel," Document MT0605P, Revision B, Dec. 2012.
[97] Mohinder S. Grewal, L. R. Weill, and A. P. Andrews, *Global positioning systems, inertial navigation, and integration*. New York, NY: Wiley, 2001.
[98] I. C. S. L. M. S. Committee, I. O. for Standardization, and I. E. Commission, *IEEE standard specification format guide and test procedure for single-axis interferometric fiber optic gyros*, vol. 802. Institute of Electrical & Electronics Engineers (IEEE), 1998.
[99] N. El-Sheimy, H. Hou, and X. Niu, "Analysis and Modeling of Inertial Sensors Using Allan Variance," *IEEE Transactions on Instrumentation and Measurement*, vol. 57, no. 1, pp. 140–149, Jan. 2008.

[100] A. Quinchia, G. Falco, E. Falletti, F. Dovis, and C. Ferrer, "A Comparison between Different Error Modeling of MEMS Applied to GPS/INS Integrated Systems," *Sensors*, vol. 13, no. 8, pp. 9549–9588, Jul. 2013.
[101] O. J. Woodman, "An introduction to inertial navigation," University of Cambridge, Computer Laboratory, 2007.
[102] X. Zhang, Y. Li, P. Mumford, and C. Rizos, "Allan variance analysis on error characters of MEMS inertial sensors for an FPGA-based GPS/INS system," in *Proceedings of the International Symposium on GPS/GNNS*, 2008, pp. 127–133.
[103] S. Nassar, "Improving the inertial navigation system (INS) error model for INS and INS/DGPS applications," National Library of Canada= Bibliothèque nationale du Canada, 2005.
[104] Y. Zhao, M. Horemuz, and L. E. Sjöberg, "Stochastic modelling and analysis of IMU sensor errors," *Archiwum Fotogrametrii, Kartografii i Teledetekcji*, vol. 22, 2011.
[105] P. Brocard, "Integrity monitoring for mobile users in urban environment," 2016.
[106] M. Hernandez-Pajares *et al.*, "The ESA/UPC GNSS-Lab tool (gLAB): An advanced multipurpose package for GNSS data processing," in *2010 5th ESA Workshop on Satellite Navigation Technologies and European Workshop on GNSS Signals and Signal Processing (NAVITEC)*, Netherlands, 2010, pp. 1–8.
[107] "RINEX The Receiver Independent Exchange Format Version 3.02." IGS, RINEX Working Group and Radio Technical Commission for Maritime Services Special Committee 104 (RTCM-SC104), 03-2013.
[108] B. W. Remondi, "Computing satellite velocity using the broadcast ephemeris," *GPS Solutions*, vol. 8, no. 3, pp. 181–183, Sep. 2004.
[109] IS-GPS-200D, "Navstar GPS Space Segment/Navigation User Interfaces IS-GPS-200D."
[110] P.-Y. Chen, "Experimental Assessment of MEMS INS Stochastic Error Model," PhD Thesis, The Ohio State University, 2015.
[111] H. Hou, "Modeling inertial sensors errors using Allan variance," Library and Archives Canada= Bibliothèque et Archives Canada, 2005.

Appendix
A. Matrix Representations
A.1 Rotation Matrices

For a 3-dimensional coordinate frame, a rotation of an angle θ along its axes $\boldsymbol{x}$, $\boldsymbol{y}$, and $\boldsymbol{z}$ are respectively represented by following matrices:

$$\boldsymbol{R_x}(\theta)=\begin{bmatrix}1 & 0 & 0\\ 0 & cos\theta & sin\theta\\ 0 & -sin\theta & cos\theta\end{bmatrix},\boldsymbol{R_y}(\theta)=\begin{bmatrix}cos\theta & 0 & -sin\theta\\ 0 & 1 & 0\\ sin\theta & 0 & cos\theta\end{bmatrix},\boldsymbol{R_z}(\theta)=\begin{bmatrix}cos\theta & sin\theta & 0\\ -sin\theta & cos\theta & 0\\ 0 & 0 & 1\end{bmatrix}.$$

A.2 Skew Symmetric Matrix

A skew symmetric matrix $\boldsymbol{A}$ of a vector $\boldsymbol{a}=[a_1,a_2,a_3]^{\boldsymbol{T}}$ is defined in form

$$\boldsymbol{A}=[\boldsymbol{a}\times]=\begin{bmatrix}0 & -a_3 & a_2\\ a_3 & 0 & -a_1\\ -a_2 & a_1 & 0\end{bmatrix}$$

The product of a skew matrix $\boldsymbol{A}$ and a vector $\boldsymbol{b}=[b_1,b_2,b_3]^{\boldsymbol{T}}$, whose skew matrix is noted as $\boldsymbol{B}$, can be reformulated as:

$$\boldsymbol{A}\cdot\boldsymbol{b}=-\boldsymbol{B}\cdot\boldsymbol{a}$$

A.3 Gravitation and Gravity

The Earth gravity, different from the gravitation field, incorporates also the centripetal component due to the Earth rotation [1], [2]

$$\boldsymbol{g_b^{\blacksquare}}=\boldsymbol{\gamma_{ib}^{\blacksquare}}-\boldsymbol{\Omega_{ie}^{\blacksquare}\Omega_{ie}^{\blacksquare}r_{eb}^{\blacksquare}}$$

where $\boldsymbol{\gamma_{ib}^{\blacksquare}}$ is the gravitational acceleration vector expressed in ■ frame, $\boldsymbol{\Omega_{ie}^{\blacksquare}}$ is the skew-symmetric representation of the Earth rotation vector $\boldsymbol{w_{ie}^{\blacksquare}}$ and $\mathbf{r}_{\boldsymbol{eb}}^{\blacksquare}$ is the geocentric position.

The detailed formula of the gravitation field in *e*-frame is expressed as

$$\boldsymbol{\gamma_{ib}^{e}}=\frac{-\mu_{\oplus}}{|\mathbf{r}_{\boldsymbol{eb}}^{\boldsymbol{e}}|^3}(\mathbf{r}_{\boldsymbol{eb}}^{\boldsymbol{e}}+\frac{3}{2}J_2\frac{{a_{\oplus}}^2}{|\mathbf{r}_{\boldsymbol{eb}}^{\boldsymbol{e}}|^2}\left[\mathrm{r}_{eb,x}^{e}-5\mathrm{r}_{eb,x}^{e}\left(\frac{\mathrm{r}_{eb,z}^{e}}{|\mathbf{r}_{\boldsymbol{eb}}^{\boldsymbol{e}}|}\right)^2,\mathrm{r}_{eb,y}^{e}-5\mathrm{r}_{eb,y}^{e}\left(\frac{\mathrm{r}_{eb,z}^{e}}{|\mathbf{r}_{\boldsymbol{eb}}^{\boldsymbol{e}}|}\right)^2,3\mathrm{r}_{eb,x}^{e}-5\mathrm{r}_{eb,z}^{e}\left(\frac{\mathrm{r}_{eb,z}^{e}}{|\mathbf{r}_{\boldsymbol{eb}}^{\boldsymbol{e}}|}\right)^2\right]^T)$$

where $\mu_{\oplus}$ is the Earth gravitational constant, J_2 is the 2nd zonal harmonic value, $\mathbf{r}_{\boldsymbol{eb}}^{\boldsymbol{e}}=\left[\mathrm{r}_{eb,x}^{e},\mathrm{r}_{eb,y}^{e},\mathrm{r}_{eb,z}^{e}\right]^{\boldsymbol{T}}$ is the geocentric position vector with its norm denoted by $|\mathbf{r}_{\boldsymbol{eb}}^{\boldsymbol{e}}|$.

Two examples of having the gravity field expressed in *e*-frame and *n*-frame are thus provided:

$$\boldsymbol{g_b^e}=\boldsymbol{\gamma_{ib}^e}+{w_{ie}}^2\begin{bmatrix}1 & 0 & 0\\ 0 & 1 & 0\\ 0 & 0 & 0\end{bmatrix}\mathbf{r}_{\boldsymbol{eb}}^{\boldsymbol{e}}$$

$$\boldsymbol{g_b^n}=\boldsymbol{\gamma_{ib}^n}+{w_{ie}}^2\begin{bmatrix}sin^2\varphi & 0 & sin\varphi cos\varphi\\ 0 & 1 & 0\\ sin\varphi cos\varphi & 0 & cos^2\varphi\end{bmatrix}\boldsymbol{r_{eb}^n}$$

The gravity is often expressed in *n*-frame with its north and east components being zero and only the up component being non-zero:

$$\boldsymbol{g_b^n} = [0, 0, -g]^T$$

The WGS-84 datum provides a simple way for the calculation of the normal gravity, known as the Somigliana model [2]:

$$g_0 = g_e \frac{(1 + 0.001931853 sin^2\varphi)}{\sqrt{1 - e^2 sin^2\varphi}}$$

with $g_e = 9.7803253359 \frac{m}{s^2}, a = 6378137m$ the equatorial radius of the Earth, g_0 the nominal gravity et the ellipsoid.

A4. RINEX File Format

RINEX, the Receiver Independent Exchange Format, was first developed by the Astronomical Institute of the University of Bern for the easy exchange of GNSS data. The original RINEX Version 1 was presented in 1989. The latest version RINEX 3.03 comes out in 2015 with various up-to-date modifications. For further details on RINEX history, refer to [10] and [12].

The RINEX 3.03 format consists of three ASCII file types: 1. Observation data file; 2. Navigation data file; 3. Meteorological data file. Each file has a header section and a data section.

Each observation data file contains the GNSS measurements generated by a given GNSS receiver with the corresponding information on observation types, signal tracking channel, signal strength and the time of reception expressed in the time frame of the receiver.

In order to compute the absolute position of the rover, the position of the observed satellite need to be derived from the navigation data file. Besides all the necessary descriptions of the satellite orbit, corrections of the satellite time to UTC or to other systems and indicators of the satellite status are also contained in the navigation file. For the GPS and GLONASS constellations, different information is contained. While parameters of a Keplerian orbit representation are broadcast for GPS, the Cartesian state vectors of GLONASS are directly provided.

Table A-1. GPS and GLONASS Satellite Parameters in Navigation Data File

GPS Satellite Parameters			
t_{oc}	Time of clock	a_{f0}	Satellite vehicle clock bias
a_{f1}	Satellite vehicle clock drift	a_{f2}	Satellite vehicle clock drift rate
C_{rs}	Amplitude of the sine harmonic correction term to the orbit radius (Orbit 1*)	Δn	Mean motion difference from computed value (Orbit 1)
M_0	Mean anomaly at the reference time (Orbit 1)	C_{uc}	Amplitude of the cosine harmonic correction term to the argument of latitude (Orbit 2)

e	Eccentricity of the orbit (Orbit 2)	C_{us}	Amplitude of the sine harmonic correction term to the argument of latitude (Orbit 2)
$a^{1/2}$	Square root of the semi-major axis of the orbit (Orbit 2)	t_{oe}	IODE, issue of data, ephemeris (Orbit 3)
C_{ic}	Amplitude of the cosine harmonic correction term to the angle of inclination (Orbit 3)	Ω_0	Right ascension of ascending node of orbital plane at the weekly epoch (Orbit 3)
C_s	Amplitude of the sine harmonic correction term to the angle of inclination (Orbit 3)	i_0	Inclination angle at the reference time (Orbit 4)
C_{rc}	Amplitude of the cosine harmonic correction term to the orbit radius (Orbit 4)	w	Argument of perigee (Orbit 4)
$\dot{\Omega}_d$	Rate of change of longitude of the ascending node at the reference time (Orbit 4)	i_{dot}	IDOT, Rate of inclination (Orbit 5)
GLONASS Satellite Parameters			
t_{oc}	Time of clock	t_N	Satellite vehicle clock bias
γ_N	Satellite vehicle relative frequency bias	(x_0, y_0, z_0)	Satellite broadcast position coordinates
(v_{x0}, v_{y0}, v_{z0})	Satellite broadcast velocities	(x''_0, y''_0, z''_0)	Accelerations (lunar and solar perturbation terms)

*The index of 'Orbit' here refers to the broadcast data line number of navigation message recorded in form RINEX 3.03.

B. Satellite Ephemeris

The computation of the satellite orbit is a curve-fit process for a certain time within the 'fit interval' of the ephemeris. As different types of navigation messages are broadcast by GPS and GLONASS satellites, the way their clock correction and position in orbit is also different and will be unfolded in this Appendix.

B.1 GPS Satellite Clock Correction

When a GPS signal is received, the rough transmit time is obtained by

$$t_t = P/c$$

where P[unit m] is the pseudorange observation at the receiver, $c = 299792458\, m/s$ is the speed of light in vacuum [26], [39].

Taken the time t_{rev} when the signal is received by the receiver, the raw transmission time t_{sv} of the signal is given by

$$t_{sv} = t_{rc} - t_t$$

Then the GPS satellite clock delay Δt_{sv} should be subtracted to correct the satellite time,

$$\Delta t_{sv} = a_{f0} + a_{f1} t_{k,oc} + a_{f2} {t_{k,oc}}^2 + \Delta t_r$$

where a_{f0}, a_{f1}, a_{f2} are navigation message in Table A-1, $t_{k,oc}$ is the difference between the true transmission time t and the clock reference t_{oc}, and Δt_r is the clock correction due to the relativistic effects. Herein, a function denoted as $Chk_{(t-t_{oc})}$ is defined to consider a check on the beginning or end of week crossovers,

$$t_{k,oc} = Chk_{(t-t_{oc})} = \begin{cases} t - t_{oc} - 604800, & if\ t - t_{oc} > 302400 \\ t - t_{oc} + 604800, & if\ t - t_{oc} < -302400 \\ t - t_{oc}, & otherwise \end{cases}$$

As the true satellite time t, to be estimated from $(t_{sv} - \Delta t_{sv})$, is unknown, it can be substituted by t_{sv}.

The calculation of the relativistic correction relies on the following equation

$$\Delta t_r = Fea^{1/2} sin E_k$$

where $F = -\frac{2\sqrt{\mu_\oplus}}{c^2} = -4.442807633 \times 10^{-10}$, E_k is the eccentric anomaly of the satellite orbit.

Usually, the value of $E_k \in [0, 2\pi)$ is obtained iteratively given the following relations with mean anomaly M_k

$$M_k = M_0 + \left(\sqrt{\frac{\mu_\oplus}{a^3}} + \Delta n\right) t_{k,oc}$$

$$M_k = E_k + e \sin E_k$$

However, the previously resolved clock correction corresponds to the ionosphere-free combination of dual-frequency (i.e., L1 P(Y) and L2 P(Y)) code combination [6], [7], [109]. The formation of the ionosphere-free code combination P_{IF} is depicted as following:

$$P_1 = \rho + c(dt_r^{GPS} - dT) + I_1 + T + b_{r,P_1} - b_{s,P_1} + \epsilon_{P_1}$$

$$P_2 = \rho + c(dt_r^{GPS} - dT) + I_2 + T + b_{r,P_2} - b_{s,P_2} + \epsilon_{P_2}$$

$$P_{IF} = \frac{f_1^2}{f_1^2 - f_2^2} P_1 - \frac{f_2^2}{f_1^2 - f_2^2} P_2 = \rho + c(dt - dT) + T + b_{r,P_{IF}} - b_{s,P_{IF}}$$

The clock correction includes the true satellite clock and the ionosphere-free combination of satellite hardware:

$$\Delta t_{sv} = dT + \frac{b_{s,P_{IF}}}{c}$$

$$b_{s,P_{IF}} = \frac{f_1^2}{f_1^2 - f_2^2} b_{s,P_1} - \frac{f_2^2}{f_1^2 - f_2^2} b_{s,P_2} = b_{s,P_1} + \frac{f_2^2}{f_1^2 - f_2^2}\left(b_{s,P_1} - b_{s,P_2}\right)$$
$$= b_{s,P_2} + \frac{f_1^2}{f_1^2 - f_2^2}\left(b_{s,P_1} - b_{s,P_2}\right)$$

The frequency-difference between the satellite hardware biases, $\left(b_{s,P_1} - b_{s,P_2}\right)$, is known as differential code bias (DCB). The so-called timing group delay (TGD) broadcast in navigation message is defined as:

$$T_{GD} = \frac{f_2^2}{f_1^2 - f_2^2}\left(b_{s,P_1} - b_{s,P_2}\right)$$

Therefore the clock correction to apply on the P(Y) pseudoranges are expressed as following:

$$P_1 + c(\Delta t_{sv} - T_{GD}) = \rho + cdt_r^{GP} + I_1 + T + b_{r,P_1} + \epsilon_{P_1}$$

$$P_2 + c(\Delta t_{sv} - \frac{f_1^2}{f_2^2}T_{GD}) = \rho + cdt_r^{GPS} + I_2 + T + b_{r,P_2} + \epsilon_{P_2}$$

For GPS L1 C/A users, another correction which accounts for the hardware biases difference between the P1(Y) code and the C/A code should also be considered. However, this correction is not contained in GPS legacy navigation message.

B.2 GPS Satellite Position and Velocity

In order to get the absolute position of the rover, the position and velocity of the satellite need to be computed.

Corrected from Δt_{sv}, the transmission time t of GPS signal is now in hand. To get the satellite position at time t, the first step to get the mean anomaly $M_k$and eccentric anomaly E_k by replacing $t_{k,oc}$ by $t_{k,oe} = Chk_{(t-t_{oe})}$, the time from transmission to ephemeris reference time [28], [108].

Then the true anomaly and argument of latitude come from:

$$\nu_k = tan^{-1}\left\{\frac{\sqrt{1-e^2}\,sin\,E_k\,/(1 - e\,cos\,E_k)}{(cos\,E_k - e)/(1 - e\,cos\,E_k)}\right\}$$

$$\Phi_k = \nu_k + w$$

The derivatives are

$$\dot{M}_k = \sqrt{\frac{\mu_\oplus}{a^3}} + \Delta n$$

$$\dot{E}_k = \frac{\dot{M}_k}{1 - e\,cos\,E_k}$$

$$\dot{\Phi}_k = \dot{\nu}_k = \dot{E}_k\,sin\,E_k\frac{1 + e\,cos\,\nu_k}{sin\,\nu_k\,(1 - e\,cos\,E_k)}$$

Second harmonic orbital perturbations (argument of latitude, radius and inclination):

$$\delta u_k = C_{us}\,sin\,2\Phi_k + C_{uc}\,cos\,2\Phi_k$$

$$\delta r_k = C_{rs}\,sin\,2\Phi_k + C_{rc}\,cos\,2\Phi_k$$

$$\delta i_k = C_{is}\,sin\,2\Phi_k + C_{ic}\,cos\,2\Phi_k$$

Corrected argument of latitude, corrected radius, corrected inclination and corrected longitude of ascending node:

$$u_k = \Phi_k + \delta u_k$$

$$r_k = a(1 - e\,cos\,E_k) + \delta r_k$$

$$i_k = i_0 + \delta i_k + i_{dot} t_{k,oe}$$

$$\Omega_k = \Omega_0 + (\dot{\Omega}_d - w_\oplus) t_{k,oe} - w_\oplus t_{oe}$$

Their derivatives are

$$\dot{u}_k = \dot{\Phi}_k + 2\dot{\Phi}_k (C_{us}\,cos\,2\Phi_k - C_{uc}\,sin\,2\Phi_k)$$

$$\dot{r}_k = ae\dot{E}_k\,in\,E_k + 2\dot{\Phi}_k (C_{rs}\,cos\,2\Phi_k - C_{rc}\,sin\,2\Phi_k)$$

$$i_{k,dot} = i_{dot} + 2\dot{\Phi}_k (C_{is}\,cos\,2\Phi_k - C_{ic}\,sin\,2\Phi_k)$$

$$\dot{\Omega}_k = \dot{\Omega}_d - w_\oplus$$

Satellite position and velocity in orbit plane are thus:

$$x'_k = r_k\,cos\,u_k\,;\; y'_k = r_k\,sin\,u_k$$

$$\dot{x}'_k = \dot{r}_k\,cos\,u_k - y'_k \dot{u}_k;\; \dot{y}'_k = \dot{r}_k\,sin\,u_k + x'_k \dot{u}_k$$

Satellite position $\boldsymbol{X}_{sat}(x_k, y_k, z_k)$ and velocity $\boldsymbol{V}_{sat}(\dot{x}_k, \dot{y}_k, \dot{z}_k)$ expressed in the WGS84 coordinate system are:

$$x_k = x'_k\,cos\,\Omega_k - y'_k\,cos\,i_k\,sin\,\Omega_k$$

$$y_k = y'_k\,sin\,\Omega_k + y'_k\,cos\,i_k\,sin\,\Omega_k$$

$$z_k = y'_k\,sin\,\Omega_k$$

$$\dot{x}_k = \dot{x}'_k\,cos\,\Omega_k - \dot{y}'_k\,cos\,i_k\,sin\,\Omega_k + y'_k i_{k,dot}\,sin\,i_k\,sin\,\Omega_k - y_k\dot{\Omega}_k$$

$$\dot{y}_k = \dot{x}'_k\,sin\,\Omega_k + \dot{y}'_k\,cos\,i_k\,cos\,\Omega_k - y'_k i_{k,dot}\,sin\,i_k\,cos\,\Omega_k + x_k\dot{\Omega}_k$$

$$\dot{z}_k = \dot{y}'_k\,sin\,i_k + y'_k i_{k,dot}\,cos\,i_k$$

B.3 GLONASS Satellite Clock Correction

With the GLONASS navigation message listed in Table A-1, the satellite clock delay Δt_{sv} to be subtracted is derived with following equation [27],

$$\Delta t_{sv} = -t_N + \gamma_N t_{k,oc}$$

The computation of term $t_{k,oc}$ proceeds as the previous GPS case, while the consistency of time references should always be confirmed before doing mathematical operations.

B.4 GLONASS Satellite Position and Velocity

The Fourth-order Runge-Kutta (RK4) is the integration method recommended by GLONASS ICD [27] to determine satellite orbits. The general idea of RK4 is that given the differential function $f(y,t)$ of a continuous variable $y(t)$, the relation between its discrete values of two successive epochs is:

$$y_{n+1}(t_{n+1}) \approx y_n(t_n) + \frac{1}{6}h \cdot (k_1 + 2k_2 + 2k_3 + k_4)$$

where the difference between epochs is the integration step $h = t_{n+1} - t_n$, and terms k_1, k_2, k_3, k_4 are obtained from following equations:

$$k_1 = f(y_n, t_n)$$

$$k_2 = f(y_n + \frac{1}{2}h \cdot k_1, t_n + \frac{1}{2}h)$$

$$k_3 = f(y_n + \frac{1}{2}h \cdot k_2, t_n + \frac{1}{2}h)$$

$$k_4 = f(y_n + h \cdot k_3, t_n + h)$$

In case of the GLONASS satellite orbit calculation, the differentials of the Cartesian states $(\boldsymbol{X}_{sat}, \boldsymbol{V}_{sat})$ are derived from the Newton's Laws of motion where the centrifugal and Coriolis terms are considered

$$\frac{d}{dt}\begin{pmatrix}\boldsymbol{X}_{sat}\\ \boldsymbol{V}_{sat}\end{pmatrix} = \begin{pmatrix}\boldsymbol{V}_{sat}\\ \boldsymbol{a}_{sat}\end{pmatrix}$$

$$\boldsymbol{a}_{sat} = -\mu_{\oplus}\frac{\boldsymbol{X}_{sat}}{r^3} - \frac{3}{2}J_2\mu_{\oplus}\frac{a_{\oplus}^2}{r^5}\begin{pmatrix} x - \frac{5xz^2}{r^5} \\ y - \frac{5yz^2}{r^5} \\ 3z - \frac{5z^3}{r^5}\end{pmatrix} + w_{\oplus}^2\begin{pmatrix}x\\ y\\ 0\end{pmatrix} + 2w_{\oplus}\begin{pmatrix}v_y\\ -v_x\\ 0\end{pmatrix} + \boldsymbol{a}_0$$

where $r = |\boldsymbol{X}_{sat}| = \sqrt{x^2 + y^2 + z^2}$ is the orbital radius, the lunar and solar perturbation term $\boldsymbol{a}_0$ is considered constant during the valid integration interval (typically $\pm$15 min for GLONASS ephemeris propagation).

Regarding the numerical integration step, a constant step of 60 s is applied taking a comprise between the computation burden and the expected precision, certainly when $t_{k,oc} > 60s$.

C. Stochastic Process Modeling

C1. Autocorrelation Function and Power Spectral Density Function

A random signal or a stochastic process should be distinguished from a deterministic signal as it holds certain unpredictability over time [37]. Besides, a random process is considered time stationary or simply stationary if the associated pdf is invariant under a translation of time. The autocorrelation function, an important way to characterize a random process $x(t)$, is defined as [24], [37]

$$R_x(t_1, t_2) = E[x(t_1)x(t_2)] = (stationary\ case)\ \ R_x(t_2 - t_1)$$

where t_1 and t_2 are two arbitrary sampling times.

For a stationary random process, the power spectral density function is defined via the Wiener-Khinchine relation:

$$S_x(jw) = \mathfrak{F}[R_x(\tau)] = \int_{-\infty}^{\infty} R_x(\tau)e^{-jw\tau}dx$$

where $\mathfrak{F}[\blacksquare]$ is the Fourier transform operator and $w = 2\pi f$, f is the frequency in Hz. Compared to $R_x(\tau)$, the $S_x(jw)$ of a process provides information of the frequency content.

C2. Gaussian Random Process

To better modeling the random errors of INS sensors, some common stochastic process need be described in the first place. A Gaussian/normal random variable X always holds the following probability density function (PDF) [24], [37]

$$f_X(x) = \frac{1}{\sqrt{2\pi\sigma}} e^{-\frac{1}{2\sigma^2}(x-m_x)^2}$$

with $m_x = E[X] = \int_{-\infty}^{\infty} x f_X(x)dx$ the mean value and $\sigma^2 = E[(X - E(X))^2]$ the variance.

Thus, an easy way to denote a Gaussian random process is $X \sim N(m_x, \sigma^2)$.

C3. White Noise

White noise is a stationary random process that has a constant power spectral density function:

$$S_{WN}(jw) = A$$

The corresponding autocorrelation function is thus

$$R_{WN}(\tau) = A\delta(\tau)$$

where $\delta(\tau)$ is a Dirac function.

C4. Gauss-Markov Process

A Gauss-Markov (GM) process is a stationary Gaussian process that has an exponential autocorrelation:

$$R_{GM}(\tau) = \sigma^2 e^{-\beta|t|}$$

$$S_{GM}(jw) = \frac{2\sigma^2\beta}{w^2 + \beta^2}$$

where $\beta = {}^1/_{\tau_c}$ is the inverse of the correlation time τ_c.

This GM process $y(t)$ can also be modeled by passing a unit white noise $x(t)$ through a shaping filter as in following figure.

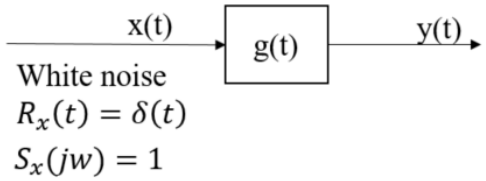

Figure C-1. Shaping Filter

The system model for the shaping filter is in form:

$$G(jw)G(-jw) = \frac{\sqrt{2\beta}}{\beta + jw}\frac{\sqrt{2\beta}}{\beta - jw}$$

And the temporal relation of the continuous system is in form:

$$\dot{y} = -\beta y + \sqrt{2\beta}\, x$$

The discrete form of this system is given as, with T_s the sampling period,

$$Y(k+1) = e^{-\beta T_s} Y(k) + (k)$$

where the variance of the GM process $Y(k)$ is $Q_{GM} = \sigma^2$and the variance of the discrete noise $Q_W = \sigma^2\left(1 - e^{-2\beta T_s}\right)$.

C5. Radom Walk Process

A random walk process can be modeled as the integration of a white noise of power spectral density σ^2, as in Figure C-2

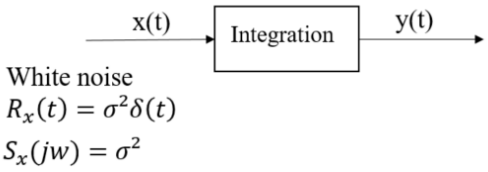

Figure C-2. Random Walk

The continuous and discrete representations of the system are separately

$$\dot{y} = x$$

$$Y(k+1) = Y(k) + X(k)$$

where the noise variance of $X(k)$ is $Q_X = \sigma^2 T_s = Q_{Y,k+1} - Q_{Y,k}$. The random walk process is thus a non-stationary process and its uncertainty increases with time.

C6. Allan Variance Technique

Allan Variance (AV) is a time domain analysis technique originally designed for characterizing noise and stability in clock systems [37], [98]. The technique can be applied to any signal to determine the characters of the underlying noise processes.

The basic idea of the AV technique is that one or more white noise sources of strength ${\sigma_i}^2$ drive the canonical transfer function, resulting in the same statistical and spectral properties as the actual device [99].

The AV of a signal $x(t)$ is a function of averaging time. For an averaging time T, the AV is computed as follows [101]:

1. Take a long sequence of data and divide it into bins of length $T = m * T_s$. There must be enough data for at least 9 bins, otherwise the results obtained begin to lose their significance.
2. Average the data in each bin, $[a(T)_1, a(T)_2, \ldots, a(T)_{n\geq 9}]$, where n the indices of bins.

3. The Allan Variance is then given by

$$\sigma^2(T) = \frac{1}{2(n-1)} * \sum_{i=[1,\dots n-1]} [a(T)_{i+1} - a(T)_i]^2.$$

To determine the characteristics of the underlying noise processes, the Allan Deviation $\sigma(T)$ is plotted as a function of T on a log-log scale. Different types of random process cause slopes with different gradients to appear on the plot. Furthermore, different processes usually appear in different regions of T, allowing their presence to be easily identified. For more information of the theoretical derivations of AV, refer to [98], [99].

A log-log plot of several popular random processes, i.e. the random walk, the bias instability, the quantization noise, the rate random walk, the rate ramp, etc., is provided in Figure C-3.

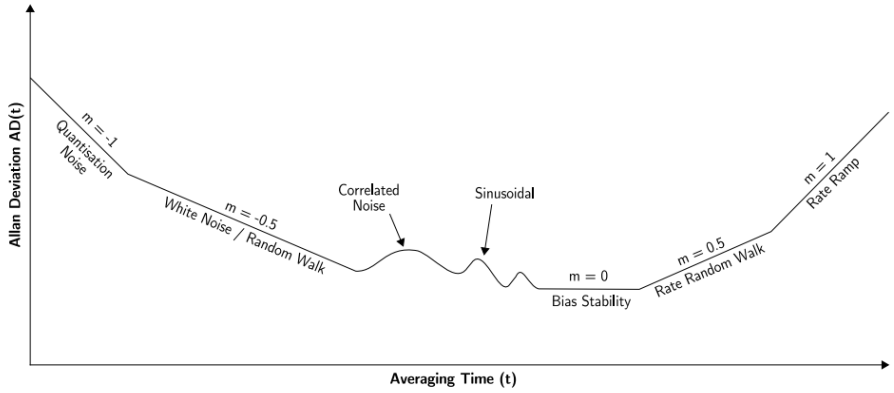

Figure C-3. A possible log-log plot of Allan Deviation, extracted from [98]

The white noise caused by thermos-mechanical events that appears in the output of gyro/accelerometers is known as Angle/Velocity Random Walk (A/VRW) [110]. This high-frequency noise is reflected on the plot with a slop -0.5 whose Allan deviation is in form [111]

$$\sigma_{WN}(T) = N/\sqrt{T}$$

with N ths noise key parameter. The value of N reads at the cluster time $T=1s$ in the Figure C-4.

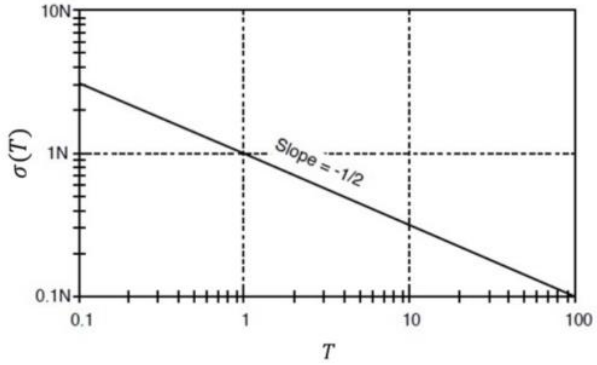

Figure C-4. Plot for Angle/Velocity Random Walk [110]

The flicker noise, also known as bias instability in the INS community, is nominally caused by the random flickering of the electronics or other components. This noise is related to the Allan deviation by

$$\sigma_B{}^2(T) = \begin{cases} 0, \ \ for\, T \ll \dfrac{1}{f_0} \\ B^2 \frac{2ln2}{\pi}, for\, T \gg \dfrac{1}{f_0} \end{cases}$$

f_0 is the cutoff frequency. As indicated in Figure C-5, Allan deviation starts with a slope of +1 for $T \ll \frac{1}{f_0}$ and reaches a segment that has slope of 0 with constant value at $0.664B$ for $T \gg \frac{1}{f_0}$.

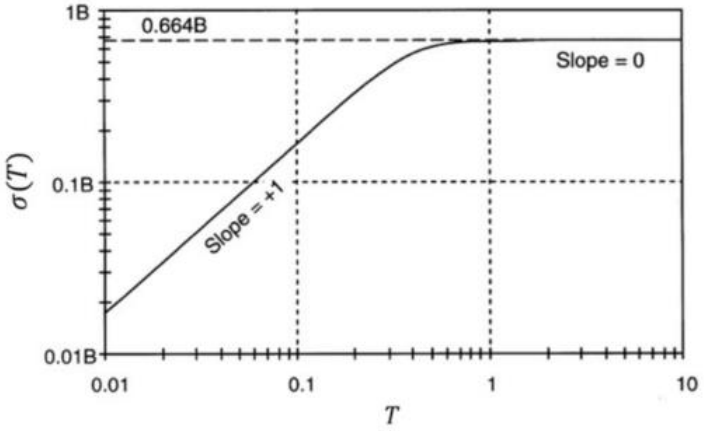

Figure C-5. Plot for Bias Instability [110]

D. INS Process Model

In this Appendix, the derivation process of the INS-only process model is detailed by conducting the perturbation analysis of the equations of motion. Each component of the final compact form will be detailed.

$$\begin{bmatrix} \delta\dot{\boldsymbol{p}}^{\boldsymbol{n}}_{\boldsymbol{nb}} \\ \delta\dot{\boldsymbol{v}}^{\boldsymbol{n}}_{\boldsymbol{nb}} \\ \delta\dot{\bar{\boldsymbol{\psi}}}_{\boldsymbol{nb}} \end{bmatrix} = \begin{bmatrix} \boldsymbol{F_{pp}} & \boldsymbol{F_{pv}} & \boldsymbol{0_3} \\ \boldsymbol{F_{vp}} & \boldsymbol{F_{vv}} & \boldsymbol{F_{ve}} \\ \boldsymbol{F_{ep}} & \boldsymbol{F_{ev}} & \boldsymbol{F_{ee}} \end{bmatrix} \begin{bmatrix} \delta\boldsymbol{p}^{\boldsymbol{n}}_{\boldsymbol{nb}} \\ \delta\boldsymbol{v}^{\boldsymbol{n}}_{\boldsymbol{nb}} \\ \delta\bar{\boldsymbol{\psi}}_{\boldsymbol{nb}} \end{bmatrix} + \begin{bmatrix} \boldsymbol{0_3} & \boldsymbol{0_3} & \boldsymbol{0_3} & \boldsymbol{0_3} \\ \boldsymbol{C^n_b} & \boldsymbol{0_3} & \boldsymbol{C^n_b F_b} & \boldsymbol{0_3} \\ \boldsymbol{0_3} & \boldsymbol{-C^n_b} & \boldsymbol{0_3} & \boldsymbol{-C^n_b W_b} \end{bmatrix} \begin{bmatrix} \delta\boldsymbol{b_a} \\ \delta\boldsymbol{b_g} \\ \delta\boldsymbol{S_a} \\ \delta\boldsymbol{S_g} \end{bmatrix} + \begin{bmatrix} 0_3 \\ \boldsymbol{C^n_b \eta_a} \\ \boldsymbol{-C^n_b \eta_g} \end{bmatrix}$$

$$\begin{cases} \delta\dot{\boldsymbol{b}}_{\boldsymbol{a}} = \dfrac{-1}{\boldsymbol{\tau}_{ba}} \delta\boldsymbol{b_a} + \boldsymbol{\eta_{ba}} \\ \delta\dot{\boldsymbol{b}}_{\boldsymbol{g}} = \dfrac{-1}{\boldsymbol{\tau}_{bg}} \delta\boldsymbol{b_g} + \boldsymbol{\eta_{bg}} \end{cases} \qquad \begin{cases} \delta\dot{\boldsymbol{s}}_{\boldsymbol{a}} = \dfrac{-1}{\boldsymbol{\tau}_{sa}} \delta\boldsymbol{s_a} + \boldsymbol{\eta_{sa}} \\ \delta\dot{\boldsymbol{s}}_{\boldsymbol{g}} = \dfrac{-1}{\boldsymbol{\tau}_{sg}} \delta\boldsymbol{s_g} + \boldsymbol{\eta_{sg}} \end{cases}$$

First of all, other than $\delta\boldsymbol{p}^{\boldsymbol{n}}_{\boldsymbol{nb}}$ the position error in local frame, the $\delta\boldsymbol{r}^{\boldsymbol{n}}_{\boldsymbol{nb}}$ geodetic position error in radian is considered, and the compact form in matrices is expressed as:

$$\begin{bmatrix} \delta\dot{\boldsymbol{r}}^{\boldsymbol{n}}_{\boldsymbol{nb}} \\ \delta\dot{\boldsymbol{v}}^{\boldsymbol{n}}_{\boldsymbol{nb}} \\ \delta\dot{\bar{\boldsymbol{\psi}}}_{\boldsymbol{nb}} \end{bmatrix} = \begin{bmatrix} \boldsymbol{F_{rr}} & \boldsymbol{F_{rv}} & 0_3 \\ \boldsymbol{F_{vr}} & \boldsymbol{F_{vv}} & \boldsymbol{F_{ve}} \\ \boldsymbol{F_{er}} & \boldsymbol{F_{ev}} & \boldsymbol{F_{ee}} \end{bmatrix} \begin{bmatrix} \delta\boldsymbol{r}^{\boldsymbol{n}}_{\boldsymbol{nb}} \\ \delta\boldsymbol{v}^{\boldsymbol{n}}_{\boldsymbol{nb}} \\ \delta\bar{\boldsymbol{\psi}}_{\boldsymbol{nb}} \end{bmatrix} + \begin{bmatrix} 0 \\ \boldsymbol{C^n_b} \delta\boldsymbol{f^b_{ib}} \\ \boldsymbol{-C^n_b} \delta\boldsymbol{w^b_{ib}} \end{bmatrix}$$

The second step is to construct the models of measurements error $\delta \boldsymbol{f}_{\boldsymbol{ib}}^{\boldsymbol{b}}$ and $\delta \boldsymbol{w}_{\boldsymbol{ib}}^{\boldsymbol{b}}$. Finally, with the need to avoid the computational singularity that may be caused by too small quantities in radian, a transformation from $\delta \boldsymbol{r}_{\boldsymbol{nb}}^{\boldsymbol{n}}$ to $\delta \boldsymbol{p}_{\boldsymbol{nb}}^{\boldsymbol{n}}$ will be made.

D1. Position Error Dynamics

In this section, the derivation process of the position error rate in following form will be detailed:

$$\delta \dot{\boldsymbol{r}}_{\boldsymbol{nb}}^{\boldsymbol{n}} = \boldsymbol{F}_{\boldsymbol{rr}} \cdot \delta \boldsymbol{r}_{\boldsymbol{nb}}^{\boldsymbol{n}} + \boldsymbol{F}_{\boldsymbol{rv}} \cdot \delta \boldsymbol{v}_{\boldsymbol{nb}}^{\boldsymbol{n}}$$

- $\boldsymbol{F}_{\boldsymbol{rr}} = \begin{bmatrix} 0 & 0 & \frac{-v_n}{(R_M+h)^2} \\ \frac{v_e sin\varphi}{(R_N+h)cos^2\varphi} & 0 & \frac{-v_e}{(R_N+h)^2 cos\varphi} \\ 0 & 0 & 0 \end{bmatrix}$ is the transformation matrix describing the relationship between the derivative of geodetic coordinates and themselves, with $R_N = \frac{a}{\sqrt{1-e^2 sin^2\varphi}}$ is the normal radius, $R_M = \frac{a(1-e^2)}{\sqrt{(1-e^2 sin^2\varphi)^3}}$ the meridian radius;
- $\boldsymbol{F}_{\boldsymbol{rv}} = \begin{bmatrix} 0 & \frac{1}{R_M+h} & 0 \\ \frac{1}{(R_N+h)cos\varphi} & 0 & 0 \\ 0 & 0 & 1 \end{bmatrix}$ is a transformation matrix describing the relationship between the derivative of geodetic coordinates and the velocity.

First of all, remind that the position error is defined as:

$$\delta \boldsymbol{r}_{\boldsymbol{nb}}^{\boldsymbol{n}} = \hat{\boldsymbol{r}}_{\boldsymbol{nb}}^{\boldsymbol{n}} - \boldsymbol{r}_{\boldsymbol{nb}}^{\boldsymbol{n}}$$

and the motion of the position is related to the velocity vector by

$$\dot{\boldsymbol{r}}_{\boldsymbol{nb}}^{\boldsymbol{n}} = \boldsymbol{F}_{\boldsymbol{rv}} \cdot \boldsymbol{v}_{\boldsymbol{nb}}^{\boldsymbol{n}}$$

with

- $\boldsymbol{r}_{\boldsymbol{nb}}^{\boldsymbol{n}} = (\varphi, \lambda, h)^T$ the geodetic coordinates of the moving object (herein, center of IMU);
- $\boldsymbol{v}_{\boldsymbol{nb}}^{\boldsymbol{n}} = (v_e, v_n, v_u)^T$ is the velocity vector in *n*-frame, consisting of east, north, up, three components;

Thus the time rate of the position error is

$$\delta \dot{\boldsymbol{r}}_{\boldsymbol{nb}}^{\boldsymbol{n}} = \hat{\dot{\boldsymbol{r}}}_{\boldsymbol{nb}}^{\boldsymbol{n}} - \dot{\boldsymbol{r}}_{\boldsymbol{nb}}^{\boldsymbol{n}}$$

By employing the first order approximation of Taylor series expansion,

$$\delta \dot{\boldsymbol{r}}_{\boldsymbol{nb}}^{\boldsymbol{n}} = \frac{\partial \dot{\boldsymbol{r}}_{\boldsymbol{nb}}^{\boldsymbol{n}}}{\partial \boldsymbol{r}_{\boldsymbol{nb}}^{\boldsymbol{n}}} \delta \boldsymbol{r}_{\boldsymbol{nb}}^{\boldsymbol{n}} + \frac{\partial \dot{\boldsymbol{r}}_{\boldsymbol{nb}}^{\boldsymbol{n}}}{\partial \boldsymbol{v}_{\boldsymbol{nb}}^{\boldsymbol{n}}} \delta \boldsymbol{v}_{\boldsymbol{nb}}^{\boldsymbol{n}} = \boldsymbol{F}_{\boldsymbol{rr}} \cdot \delta \boldsymbol{r}_{\boldsymbol{nb}}^{\boldsymbol{n}} + \boldsymbol{F}_{\boldsymbol{rv}} \cdot \delta \boldsymbol{v}_{\boldsymbol{nb}}^{\boldsymbol{n}}$$

$$\delta \dot{\boldsymbol{r}}_{\boldsymbol{nb}}^{\boldsymbol{n}} = \frac{\partial (\boldsymbol{F}_{\boldsymbol{rv}} \cdot \boldsymbol{v}_{\boldsymbol{nb}}^{\boldsymbol{n}})}{\partial \boldsymbol{r}_{\boldsymbol{nb}}^{\boldsymbol{n}}} \delta \boldsymbol{r}_{\boldsymbol{nb}}^{\boldsymbol{n}} + \frac{\partial (\boldsymbol{F}_{\boldsymbol{rv}} \cdot \boldsymbol{v}_{\boldsymbol{nb}}^{\boldsymbol{n}})}{\partial \boldsymbol{v}_{\boldsymbol{nb}}^{\boldsymbol{n}}} \delta \boldsymbol{v}_{\boldsymbol{nb}}^{\boldsymbol{n}}$$

$$\delta\dot{\boldsymbol{r}}_{\boldsymbol{nb}}^{\boldsymbol{n}} = \begin{bmatrix} 0 & \frac{-\delta h}{(R_M+h)^2} & 0 \\ \frac{sin\varphi \cdot \delta\varphi}{(R_N+h)cos^2\varphi} & 0 & 0 \\ 0 & 0 & 1 \end{bmatrix} \boldsymbol{v}_{\boldsymbol{nb}}^{\boldsymbol{n}} + \boldsymbol{F}_{\boldsymbol{rv}}\delta\boldsymbol{v}_{\boldsymbol{nb}}^{\boldsymbol{n}}$$

To display a product by the vector $\delta\boldsymbol{r}_{\boldsymbol{nb}}^{\boldsymbol{n}}$, the first term on the right of the equation can be rewritten as

$$\delta\dot{\boldsymbol{r}}_{\boldsymbol{nb}}^{\boldsymbol{n}} = \begin{bmatrix} 0 & 0 & \frac{-v_n}{(R_M+h)^2} \\ \frac{v_e sin\varphi}{(R_N+h)cos^2\varphi} & 0 & \frac{-v_e}{(R_N+h)^2 cos\varphi} \\ 0 & 0 & 0 \end{bmatrix} \cdot \delta\boldsymbol{r}_{\boldsymbol{nb}}^{\boldsymbol{n}} + \boldsymbol{F}_{\boldsymbol{rv}} \cdot \delta\boldsymbol{v}_{\boldsymbol{nb}}^{\boldsymbol{n}}$$

D2. Velocity Error dynamics

The final expression of the velocity error dynamics is in form:

$$\delta\dot{\boldsymbol{v}}_{\boldsymbol{nb}}^{\boldsymbol{n}} = \boldsymbol{F}_{\boldsymbol{vr}} \cdot \delta\boldsymbol{r}_{\boldsymbol{nb}}^{\boldsymbol{n}} + \boldsymbol{F}_{\boldsymbol{vv}} \cdot \delta\boldsymbol{v}_{\boldsymbol{nb}}^{\boldsymbol{n}} + \boldsymbol{F}_{\boldsymbol{ve}} \cdot \delta\bar{\boldsymbol{\psi}}_{\boldsymbol{nb}} + \boldsymbol{C}_{\boldsymbol{b}}^{\boldsymbol{n}}\delta\boldsymbol{f}_{\boldsymbol{ib}}^{\boldsymbol{b}}$$

with

- $\mathbf{F_{vr}} = \begin{bmatrix} 2\omega_{ie}(v_n \cos\varphi + v_u \sin\varphi) + \frac{v_e v_n}{(R_N+h)\cos\varphi} & 0 & \frac{v_e v_u}{(R_N+h)^2} - \frac{v_e v_n \tan\varphi}{(R_N+h)^2} \\ -2\omega_{ie} v_e \cos\varphi - \frac{v_e^2}{(R_N+h)\cos^2\varphi} & 0 & \frac{v_n v_u}{(R_M+h)^2} + \frac{v_e^2 \tan\varphi}{(R_N+h)^2} \\ -2\omega_{ie} v_e \sin\varphi & 0 & \frac{-v_e^2}{(R_N+h)^2} + \frac{-v_n^2}{(R_M+h)^2} + \frac{2g}{R+h} \end{bmatrix}$ the transformation matrix describing the relation between the derivative of velocity and the position;

- $\mathbf{F_{vv}} = \begin{bmatrix} \frac{v_n \tan\varphi - v_u}{R_N+h} & \frac{v_e \tan\varphi}{R_N+h} + 2\omega_{ie}\sin\varphi & -2\omega_{ie}\cos\varphi - \frac{v_e}{R_N+h} \\ \frac{-2v_e \tan\varphi}{R_N+h} - 2\omega_{ie}\sin\varphi & \frac{-v_u}{R_M+h} & \frac{-v_n}{R_M+h} \\ \frac{2v_e}{R_N+h} + 2\omega_e\cos\varphi & \frac{2v_n}{R_M+h} & 0 \end{bmatrix}$ the transformation matrix describing the relation between the derivative of velocity and itself;

- $\boldsymbol{F}_{\boldsymbol{ve}} = \left[\boldsymbol{C}_{\boldsymbol{b}}^{\boldsymbol{n}}\boldsymbol{f}_{\boldsymbol{ib}}^{\boldsymbol{b}} \times\right]$ a skew symmetric matrix describing the relation between the derivative of velocity and the attitudes, $\boldsymbol{f}_{\boldsymbol{ib}}^{\boldsymbol{b}}$ is the specific force measurements under *b*-frame;
- Attention on the modified version of attitudes errors in order $\delta\bar{\boldsymbol{\psi}}_{\boldsymbol{nb}} = [-\delta\theta_{nb}, -\delta\phi_{nb}, \delta\psi_{nb}]^T$;
- $\boldsymbol{\omega}_{\boldsymbol{ie}}$ is the Earth rotation speed; g is the nominal component of Earth gravity; R is the mean radius of the Earth.

Begin with the derivative of the velocity, the compact form's derivation of the velocity error dynamic is divided into three parts

$$\delta\dot{\boldsymbol{v}}_{\boldsymbol{nb}}^{\boldsymbol{n}} = ❶\delta\left(\boldsymbol{C}_{\boldsymbol{b}}^{\boldsymbol{n}}\boldsymbol{f}_{\boldsymbol{ib}}^{\boldsymbol{b}}\right) - ❷\delta\{(2\boldsymbol{\Omega}_{\boldsymbol{ie}}^{\boldsymbol{n}} + \boldsymbol{\Omega}_{\boldsymbol{en}}^{\boldsymbol{n}})\boldsymbol{v}_{\boldsymbol{nb}}^{\boldsymbol{n}}\} + ❸\delta(\boldsymbol{g}^{\boldsymbol{n}})$$

with

- $\boldsymbol{\Omega}_{\boldsymbol{ie}}^{\boldsymbol{n}} = [\boldsymbol{w}_{\boldsymbol{ie}}^{\boldsymbol{n}} \times]$, with $\boldsymbol{w}_{\boldsymbol{ie}}^{\boldsymbol{n}} = \begin{bmatrix} 0 \\ w_{ie}cos\varphi \\ w_{ie}sin\varphi \end{bmatrix}$ the notation of the Earth rotation rate vector under *n*-frame;
- $\boldsymbol{\Omega}_{\boldsymbol{en}}^{\boldsymbol{n}} = [\boldsymbol{w}_{\boldsymbol{en}}^{\boldsymbol{n}} \times]$, with the angular velocity of the *n*-frame w.r.t the *e*-frame expressed in *n*-frame.

$$\boldsymbol{w}_{\boldsymbol{en}}^{\boldsymbol{n}} = \begin{bmatrix} -\dot{\varphi} \\ \dot{\lambda}cos\varphi \\ \dot{\lambda}sin\varphi \end{bmatrix} = \begin{bmatrix} \frac{-v_n}{R_M + h} \\ \frac{v_e}{R_N + h} \\ \frac{v_e tan\varphi}{R_N + h} \end{bmatrix}$$

With the definition of $\delta(\boldsymbol{C}_{\boldsymbol{b}}^{\boldsymbol{n}}) = \boldsymbol{E}.\boldsymbol{C}_{\boldsymbol{b}}^{\boldsymbol{n}}$, the ❶ section expands as

$$❶\ \delta\left(\boldsymbol{C}_{\boldsymbol{b}}^{\boldsymbol{n}}\boldsymbol{f}_{\boldsymbol{ib}}^{\boldsymbol{b}}\right) = \delta(\boldsymbol{C}_{\boldsymbol{b}}^{\boldsymbol{n}})\boldsymbol{f}_{\boldsymbol{ib}}^{\boldsymbol{b}} + \boldsymbol{C}_{\boldsymbol{b}}^{\boldsymbol{n}}\delta\left(\boldsymbol{f}_{\boldsymbol{ib}}^{\boldsymbol{b}}\right) = -\boldsymbol{E}.\boldsymbol{C}_{\boldsymbol{b}}^{\boldsymbol{n}}\boldsymbol{f}_{\boldsymbol{ib}}^{\boldsymbol{b}} + \boldsymbol{C}_{\boldsymbol{b}}^{\boldsymbol{n}}.\delta\left(\boldsymbol{f}_{\boldsymbol{ib}}^{\boldsymbol{b}}\right)$$

Remind that $\boldsymbol{E}$ is the skew matrix of the attitudes errors in order $\delta\bar{\boldsymbol{\psi}}_{\boldsymbol{nb}} = [-\delta\theta_{nb}, -\delta\phi_{nb}, \delta\psi_{nb}]^T$. To display the vector $\delta\bar{\boldsymbol{\psi}}_{\boldsymbol{nb}}$, a re-ordering is made:

$$-\boldsymbol{E}.\boldsymbol{C}_{\boldsymbol{b}}^{\boldsymbol{n}}\boldsymbol{f}_{\boldsymbol{ib}}^{\boldsymbol{b}} = [\boldsymbol{C}_{\boldsymbol{b}}^{\boldsymbol{n}}\boldsymbol{f}_{\boldsymbol{ib}}^{\boldsymbol{b}} \wedge].\delta\bar{\boldsymbol{\psi}}_{\boldsymbol{nb}}$$

The final representation of the ❶ section in terms of error states is

$$❶\ \delta\left(\boldsymbol{C}_{\boldsymbol{b}}^{\boldsymbol{n}}\boldsymbol{f}_{\boldsymbol{ib}}^{\boldsymbol{b}}\right) = \left[\boldsymbol{C}_{\boldsymbol{b}}^{\boldsymbol{n}}\boldsymbol{f}_{\boldsymbol{ib}}^{\boldsymbol{b}} \wedge\right].\delta\bar{\boldsymbol{\psi}}_{\boldsymbol{nb}} + \boldsymbol{C}_{\boldsymbol{b}}^{\boldsymbol{n}}.\delta\left(\boldsymbol{f}_{\boldsymbol{ib}}^{\boldsymbol{b}}\right)$$

The ❷ section is disassembled into 2 parts:

$$❷\ -\delta\{(2\boldsymbol{\Omega}_{\boldsymbol{ie}}^{\boldsymbol{n}} + \boldsymbol{\Omega}_{\boldsymbol{en}}^{\boldsymbol{n}})\boldsymbol{v}_{\boldsymbol{nb}}^{\boldsymbol{n}}\} = -\delta\{2\boldsymbol{\Omega}_{\boldsymbol{ie}}^{\boldsymbol{n}} + \boldsymbol{\Omega}_{\boldsymbol{en}}^{\boldsymbol{n}}\}.\boldsymbol{v}_{\boldsymbol{nb}}^{\boldsymbol{n}} - (2\boldsymbol{\Omega}_{\boldsymbol{ie}}^{\boldsymbol{n}} + \boldsymbol{\Omega}_{\boldsymbol{en}}^{\boldsymbol{n}})\delta\boldsymbol{v}_{\boldsymbol{nb}}^{\boldsymbol{n}}$$

The second term in the right side is directly a product with the error state $\boldsymbol{v}_{\boldsymbol{nb}}^{\boldsymbol{n}}$, while the first term needs further analysis. After a re-ordering, we have

$$-\delta\{2\boldsymbol{\Omega}_{\boldsymbol{ie}}^{\boldsymbol{n}} + \boldsymbol{\Omega}_{\boldsymbol{en}}^{\boldsymbol{n}}\}.\boldsymbol{v}_{\boldsymbol{nb}}^{\boldsymbol{n}} = [\boldsymbol{v}_{\boldsymbol{nb}}^{\boldsymbol{n}} \wedge].\delta(2\boldsymbol{\omega}_{\boldsymbol{ie}}^{\boldsymbol{n}} + \boldsymbol{\omega}_{\boldsymbol{en}}^{\boldsymbol{n}})$$

$$\delta(2\boldsymbol{\omega}_{\boldsymbol{ie}}^{\boldsymbol{n}} + \boldsymbol{\omega}_{\boldsymbol{en}}^{\boldsymbol{n}}) = \delta\begin{bmatrix} -\dot{\varphi} \\ 2\omega_{ie}cos\varphi + \dot{\lambda}cos\varphi \\ 2\omega_{ie}sin\varphi + \dot{\lambda}sin\varphi \end{bmatrix} = \begin{bmatrix} -\delta\dot{\varphi} \\ -2\omega_{ie}sin\varphi.\delta\varphi + cos\varphi\delta\dot{\lambda} - \dot{\lambda}sin\varphi.\delta\varphi \\ 2\omega_{ie}cos\varphi.\delta\varphi + \delta\dot{\lambda}sin\varphi + \dot{\lambda}cos\varphi.\delta\varphi \end{bmatrix}$$

$$\delta(2\boldsymbol{\omega}_{\boldsymbol{ie}}^{\boldsymbol{n}} + \boldsymbol{\omega}_{\boldsymbol{en}}^{\boldsymbol{n}}) = \begin{bmatrix} 0 & 0 & 0 \\ -(2\omega_{ie} + \dot{\lambda})sin\varphi & 0 & 0 \\ (2\omega_{ie} + \dot{\lambda})cos\varphi & 0 & 0 \end{bmatrix}\delta\boldsymbol{r}_{\boldsymbol{nb}}^{\boldsymbol{n}} + \begin{bmatrix} -1 & 0 & 0 \\ 0 & cos\varphi & 0 \\ 0 & sin\varphi & 0 \end{bmatrix}\delta\dot{\boldsymbol{r}}_{\boldsymbol{nb}}^{\boldsymbol{n}}$$

Substitute herein the formulation of $\delta\dot{\boldsymbol{r}}_{\boldsymbol{nb}}^{\boldsymbol{n}}$,

$$\delta(\mathbf{2\omega_{ie}^{n}+\omega_{en}^{n}})=\begin{bmatrix}0 & 0 & \frac{v_n}{(R_M+h)^2}\\ -2\omega_{ie}sin\varphi & 0 & \frac{-v_e}{(R_N+h)^2}\\ 2\omega_{ie}cos\varphi+\frac{v_e}{(R_N+h)cos^2\varphi} & 0 & \frac{-v_e tan\varphi}{(R_N+h)^2}\end{bmatrix}.\delta\mathbf{r_{nb}^{n}}+\begin{bmatrix}0 & \frac{-1}{R_M+h} & 0\\ \frac{1}{R_N+h} & 0 & 0\\ \frac{tan\varphi}{R_N+h} & 0 & 0\end{bmatrix}\delta\mathbf{v_{nb}^{n}}$$

Thus the final formula of the ❷ section is obtained by expanding the matrix products

$$\begin{aligned}&❷\ -\delta\{(\mathbf{2\Omega_{ie}^{n}+\Omega_{en}^{n}})\mathbf{v_{nb}^{n}}\}\\&=\begin{bmatrix}2\omega_{ie}v_u sin\varphi+2\omega_{ie}v_n cos\varphi+\frac{v_e v_n}{(R_N+h)cos^2\varphi} & 0 & \frac{v_e v_u-v_e v_n tan\varphi}{(R_N+h)^2}\\ -2\omega_{ie}v_e cos\varphi-\frac{{v_e}^2}{(R_N+h)cos^2\varphi} & 0 & \frac{v_n v_u}{(R_M+h)^2}+\frac{{v_e}^2 tan\varphi}{(R_N+h)^2}\\ -2\omega_{ie}v_e sin\varphi & 0 & \frac{-{v_n}^2}{(R_M+h)^2}+\frac{-{v_e}^2}{(R_N+h)^2}\end{bmatrix}.\delta\mathbf{r_{nb}^{n}}\\&+\begin{bmatrix}\frac{-v_u+v_n tan\varphi}{R_N+h} & \frac{v_e tan\varphi}{R_N+h}+2\omega_{ie}sin\varphi & \frac{-v_e}{R_N+h}-2\omega_{ie}cos\varphi\\ \frac{-2v_e tan\varphi}{R_N+h}-2\omega_{ie}sin\varphi & \frac{v_u}{R_M+h} & \frac{v_n}{R_N+h}\\ \frac{2v_e}{R_N+h}+2\omega_{ie}cos\varphi & \frac{2v_n}{R_M+h} & 0\end{bmatrix}\delta\mathbf{v_{nb}^{n}}\end{aligned}$$

The final ❸ section is the perturbation of the gravity in local frame which is only related to the altitude:

$$❸\ \ \delta(\boldsymbol{g^{n}})=\left[0,0,\frac{2g}{R+h}\delta h\right]^{T}$$

D3. Attitudes Error Dynamics

The final expression of the attitude error dynamics is in form:

$$\delta\dot{\bar{\boldsymbol{\psi}}}_{\boldsymbol{nb}}=\boldsymbol{F_{er}}\cdot\delta\mathbf{r_{nb}^{n}}+\boldsymbol{F_{ev}}\cdot\delta\mathbf{v_{nb}^{n}}+\boldsymbol{F_{ee}}\cdot\delta\bar{\boldsymbol{\psi}}_{\boldsymbol{nb}}-\mathbf{C_{b}^{n}}\delta\mathbf{w_{ib}^{b}}$$

With

- $\boldsymbol{F_{er}}=\begin{bmatrix}0 & 0 & \frac{v_n}{(R_M+h)^2}\\ -\omega_{ie}sin\varphi & 0 & \frac{-v_e}{(R_N+h)^2}\\ \omega_{ie}cos\varphi+\frac{v_e}{(R_N+h)cos^2\varphi} & 0 & \frac{-v_e tan\varphi}{(R_N+h)^2}\end{bmatrix}$ the transformation matrix describing the relation between the derivative of attitudes and the position;

- $\boldsymbol{F_{ev}} = \begin{bmatrix} 0 & \frac{-1}{R_M+h} & 0 \\ \frac{1}{R_N+h} & 0 & 0 \\ \frac{tan\varphi}{R_N+h} & 0 & 0 \end{bmatrix}$ the transformation matrix describing the relation between the derivative of attitudes and the velocity;
- $\boldsymbol{F_{ee}} = -[(\boldsymbol{\omega_{ie}^n} + \boldsymbol{\omega_{en}^n}) \wedge], \boldsymbol{\omega_{ie}^n} + \boldsymbol{\omega_{en}^n} = \begin{bmatrix} \frac{-v_n}{R_M+h} \\ \frac{v_e}{R_N+h} + w_{ie}cos\varphi \\ \frac{v_e tan\varphi}{R_N+h} + w_{ie}sin\varphi \end{bmatrix}$ the transformation matrix describing the relation between the derivative of attitudes and themselves.

First of all, the relation between the matrix $\delta \boldsymbol{C_b^n}$ and the attitudes error $\delta \bar{\boldsymbol{\psi}}_{\boldsymbol{nb}} = [-\delta\theta_{nb}, -\delta\phi_{nb}, \delta\psi_{nb}]^T$ need to be established. Their definitions are respectively:

$$\delta \boldsymbol{\psi_{nb}} = \hat{\boldsymbol{\psi}}_{\boldsymbol{nb}} - \boldsymbol{\psi_{nb}}$$

$$\delta \boldsymbol{C_b^n} = \widehat{\boldsymbol{C}}_{\boldsymbol{b}}^{\boldsymbol{n}} - \boldsymbol{C_b^n}$$

Under the conception that the transformation matrix from *b*-frame to *n*-frame is actually 3 successive rotations around axes z^b, x^b and y^b, represented by $\boldsymbol{C_b^n}$, the expansion of $\widehat{\boldsymbol{C}}_{\boldsymbol{b}}^{\boldsymbol{n}}$ can be written as:

$$\widehat{\boldsymbol{C}}_{\boldsymbol{b}}^{\boldsymbol{n}} = \boldsymbol{R_z}(\psi_{nb} + \delta\psi_{nb})\boldsymbol{R_x}(-\theta_{nb} - \delta\theta_{nb})\boldsymbol{R_y}(-\phi_{nb} - \delta\phi_{nb})$$

with each rotation expressed as

$$\boldsymbol{R_z}(\psi_{nb} + \delta\psi_{nb}) = (I_3 + [(0, 0, -\delta\psi_{nb})^T \times]).\boldsymbol{R_z}(\psi_{nb})$$

$$\boldsymbol{R_x}(-\theta_{nb} - \delta\theta_{nb}) = (I_3 + [(\delta\theta_{nb}, 0, 0)^T \times]).\boldsymbol{R_x}(-\theta_{nb})$$

$$\boldsymbol{R_y}(-\phi_{nb} - \delta\phi_{nb}) = (I_3 + [(0, \delta\phi_{nb}, 0)^T \times]).\boldsymbol{R_y}(-\phi_{nb})$$

The approximation that the attitudes error $\delta \boldsymbol{\psi_{nb}}$ is a very small amount is always considered. When only first order terms of $\delta \boldsymbol{\psi_{nb}}$ are kept**,** the expansion of $\widehat{\boldsymbol{C}}_{\boldsymbol{b}}^{\boldsymbol{n}}$ can be approximated by

$$\widehat{\boldsymbol{C}}_{\boldsymbol{b}}^{\boldsymbol{n}} = \boldsymbol{C_b^n} - [\delta \bar{\boldsymbol{\psi}}_{\boldsymbol{nb}} \times].\boldsymbol{C_b^n}$$

$$\delta \boldsymbol{C_b^n} = -\boldsymbol{E}.\boldsymbol{C_b^n}$$

The perturbation analysis of attitudes error tries to establish its relations with other error states. First of all, we start from the two equal forms of the derivative of $\widehat{\boldsymbol{C}}_{\boldsymbol{b}}^{\boldsymbol{n}}$, one comes from the equation of motion and another comes from previous equations:

$$\dot{\widehat{\boldsymbol{C}}}_{\boldsymbol{b}}^{\boldsymbol{n}} = \widehat{\boldsymbol{C}}_{\boldsymbol{b}}^{\boldsymbol{n}}\widehat{\boldsymbol{\Omega}}_{\boldsymbol{nb}}^{\boldsymbol{b}} = (\boldsymbol{C_b^n} - \boldsymbol{E}.\boldsymbol{C_b^n})(\boldsymbol{\Omega_{nb}^b} + \delta\boldsymbol{\Omega_{nb}^b})$$

$$\dot{\widehat{\boldsymbol{C}}}_{\boldsymbol{b}}^{\boldsymbol{n}} = \dot{\boldsymbol{C}}_{\boldsymbol{b}}^{\boldsymbol{n}} - \dot{\boldsymbol{E}}.\boldsymbol{C_b^n} - \boldsymbol{E}.\dot{\boldsymbol{C}}_{\boldsymbol{b}}^{\boldsymbol{n}}$$

By having the equality of the two forms, we have

$$(\boldsymbol{C_b^n} - \boldsymbol{E}.\boldsymbol{C_b^n})\left(\boldsymbol{\Omega_{nb}^b} + \delta\boldsymbol{\Omega_{nb}^b}\right) = \dot{\boldsymbol{C}}_{\boldsymbol{b}}^{\boldsymbol{n}} - \dot{\boldsymbol{E}}.\boldsymbol{C_b^n} - \boldsymbol{E}.\dot{\boldsymbol{C}}_{\boldsymbol{b}}^{\boldsymbol{n}}$$

$$\boldsymbol{C_b^n}\boldsymbol{\Omega_{nb}^b} + \boldsymbol{C_b^n}\delta\boldsymbol{\Omega_{nb}^b} - \boldsymbol{E}.\boldsymbol{C_b^n}\boldsymbol{\Omega_{nb}^b} - \boldsymbol{E}.\boldsymbol{C_b^n}\delta\boldsymbol{\Omega_{nb}^b} = \dot{\boldsymbol{C}}_{\boldsymbol{b}}^{\boldsymbol{n}} - \dot{\boldsymbol{E}}.\boldsymbol{C_b^n} - \boldsymbol{E}.\dot{\boldsymbol{C}}_{\boldsymbol{b}}^{\boldsymbol{n}}$$

After removing identical terms on the both sides of the equation, and neglecting the second order effect of errors, we obtain

$$\dot{\boldsymbol{E}} = -\boldsymbol{C}_{\boldsymbol{b}}^{\boldsymbol{n}}\delta\boldsymbol{\Omega}_{\boldsymbol{nb}}^{\boldsymbol{b}}\boldsymbol{C}_{\boldsymbol{n}}^{\boldsymbol{b}}$$

and thus the vector from is

$$\delta\dot{\bar{\boldsymbol{\psi}}}_{\boldsymbol{nb}} = -\boldsymbol{C}_{\boldsymbol{b}}^{\boldsymbol{n}}\delta\mathbf{w}_{\boldsymbol{nb}}^{\boldsymbol{b}}$$

The next step is to expand $\delta\mathbf{w}_{\boldsymbol{nb}}^{\boldsymbol{b}}$ in a form of error states,

$$\delta\mathbf{w}_{\boldsymbol{nb}}^{\boldsymbol{b}} = \delta\mathbf{w}_{\boldsymbol{ib}}^{\boldsymbol{b}} - \delta(\boldsymbol{C}_{\boldsymbol{n}}^{\boldsymbol{b}}\mathbf{w}_{\boldsymbol{in}}^{\boldsymbol{n}}) = \delta\mathbf{w}_{\boldsymbol{ib}}^{\boldsymbol{b}} - \boldsymbol{C}_{\boldsymbol{n}}^{\boldsymbol{b}}\delta(\mathbf{w}_{\boldsymbol{in}}^{\boldsymbol{n}}) + (\boldsymbol{E}\boldsymbol{C}_{\boldsymbol{n}}^{\boldsymbol{b}})^{T}\mathbf{w}_{\boldsymbol{in}}^{\boldsymbol{n}}$$

$$\delta\mathbf{w}_{\boldsymbol{nb}}^{\boldsymbol{b}} = \delta\mathbf{w}_{\boldsymbol{ib}}^{\boldsymbol{b}} - \boldsymbol{C}_{\boldsymbol{n}}^{\boldsymbol{b}}\delta(\mathbf{w}_{\boldsymbol{in}}^{\boldsymbol{n}}) - \boldsymbol{C}_{\boldsymbol{n}}^{\boldsymbol{b}}\boldsymbol{E}.\mathbf{w}_{\boldsymbol{in}}^{\boldsymbol{n}}$$

$$\delta\mathbf{w}_{\boldsymbol{nb}}^{\boldsymbol{b}} = \delta\mathbf{w}_{\boldsymbol{ib}}^{\boldsymbol{b}} - \boldsymbol{C}_{\boldsymbol{n}}^{\boldsymbol{b}}\delta(\mathbf{w}_{\boldsymbol{in}}^{\boldsymbol{n}}) + \boldsymbol{C}_{\boldsymbol{n}}^{\boldsymbol{b}}\boldsymbol{\Omega}_{\boldsymbol{in}}^{\boldsymbol{n}}\delta\bar{\boldsymbol{\psi}}_{\boldsymbol{nb}}$$

By substituting the expression of $\delta\mathbf{w}_{\boldsymbol{nb}}^{\boldsymbol{b}}$ into the equation of $\delta\dot{\bar{\boldsymbol{\psi}}}_{\boldsymbol{nb}}$, we obtain

$$\delta\dot{\bar{\boldsymbol{\psi}}}_{\boldsymbol{nb}} = -\boldsymbol{C}_{\boldsymbol{b}}^{\boldsymbol{n}}(\delta\mathbf{w}_{\boldsymbol{ib}}^{\boldsymbol{b}} - \boldsymbol{C}_{\boldsymbol{n}}^{\boldsymbol{b}}\delta(\mathbf{w}_{\boldsymbol{in}}^{\boldsymbol{n}}) + \boldsymbol{C}_{\boldsymbol{n}}^{\boldsymbol{b}}\boldsymbol{\Omega}_{\boldsymbol{in}}^{\boldsymbol{n}}\delta\bar{\boldsymbol{\psi}}_{\boldsymbol{nb}})$$

$$\delta\dot{\bar{\boldsymbol{\psi}}}_{\boldsymbol{nb}} = \delta(\mathbf{w}_{\boldsymbol{in}}^{\boldsymbol{n}}) - \boldsymbol{\Omega}_{\boldsymbol{in}}^{\boldsymbol{n}}\delta\bar{\boldsymbol{\psi}}_{\boldsymbol{nb}} - \boldsymbol{C}_{\boldsymbol{b}}^{\boldsymbol{n}}\delta\mathbf{w}_{\boldsymbol{ib}}^{\boldsymbol{b}}$$

where the representation of $\delta(\mathbf{w}_{\boldsymbol{in}}^{\boldsymbol{n}})$ as an equation of $\delta\boldsymbol{r}_{\boldsymbol{nb}}^{\boldsymbol{n}}, \delta\boldsymbol{v}_{\boldsymbol{nb}}^{\boldsymbol{n}}$ is noted as, similar deterioration process as $\delta(\mathbf{2}\boldsymbol{\omega}_{\boldsymbol{ie}}^{\boldsymbol{n}} + \boldsymbol{\omega}_{\boldsymbol{en}}^{\boldsymbol{n}})$ in previous section,

$$\delta(\boldsymbol{\omega}_{\boldsymbol{ie}}^{\boldsymbol{n}} + \boldsymbol{\omega}_{\boldsymbol{en}}^{\boldsymbol{n}}) = \begin{bmatrix} 0 & 0 & \dfrac{v_n}{(R_M+h)^2} \\ -\omega_{ie}sin\varphi & 0 & \dfrac{-v_e}{(R_N+h)^2} \\ \omega_{ie}cos\varphi + \dfrac{v_e}{(R_N+h)cos^2\varphi} & 0 & \dfrac{-v_e tan\varphi}{(R_N+h)^2} \end{bmatrix}.\delta\boldsymbol{r}_{\boldsymbol{nb}}^{\boldsymbol{n}}$$

$$+\begin{bmatrix} 0 & \dfrac{-1}{R_M+h} & 0 \\ \dfrac{1}{R_N+h} & 0 & 0 \\ \dfrac{tan\varphi}{R_N+h} & 0 & 0 \end{bmatrix}\delta\boldsymbol{v}_{\boldsymbol{nb}}^{\boldsymbol{n}}$$

By so far,

$$\begin{bmatrix} \delta\dot{\boldsymbol{r}}_{\boldsymbol{nb}}^{\boldsymbol{n}} \\ \delta\dot{\boldsymbol{v}}_{\boldsymbol{nb}}^{\boldsymbol{n}} \\ \delta\dot{\bar{\boldsymbol{\psi}}}_{\boldsymbol{nb}} \end{bmatrix} = \begin{bmatrix} \boldsymbol{F}_{rr} & \boldsymbol{F}_{rv} & 0_3 \\ \boldsymbol{F}_{vr} & \boldsymbol{F}_{vv} & \boldsymbol{F}_{ve} \\ \boldsymbol{F}_{er} & \boldsymbol{F}_{ev} & \boldsymbol{F}_{ee} \end{bmatrix}\begin{bmatrix} \delta\boldsymbol{r}_{\boldsymbol{nb}}^{\boldsymbol{n}} \\ \delta\boldsymbol{v}_{\boldsymbol{nb}}^{\boldsymbol{n}} \\ \delta\bar{\boldsymbol{\psi}}_{\boldsymbol{nb}} \end{bmatrix} + \begin{bmatrix} 0 \\ \boldsymbol{C}_{\boldsymbol{b}}^{\boldsymbol{n}}\delta\boldsymbol{f}_{\boldsymbol{ib}}^{\boldsymbol{b}} \\ -\boldsymbol{C}_{\boldsymbol{b}}^{\boldsymbol{n}}\delta\boldsymbol{w}_{\boldsymbol{ib}}^{\boldsymbol{b}} \end{bmatrix}$$

D4. Sensor Error Dynamics

Additional states need to be added to model INS measurements errors $\delta\boldsymbol{f}_{\boldsymbol{ib}}^{\boldsymbol{b}}$ and $\delta\boldsymbol{w}_{\boldsymbol{ib}}^{\boldsymbol{b}}$, namely the bias drifts and the scale factors. For MEMS INS, they are normally modelled as a first-order Gauss-Markov process.

A general modelling of the accelerometer measurement and the gyroscope measurement is in form:

$$\tilde{\boldsymbol{f}}_{\boldsymbol{ib}}^{\boldsymbol{b}} = \boldsymbol{b}_{\boldsymbol{a}} + (\boldsymbol{I}_{\boldsymbol{3}} + \boldsymbol{S}_{\boldsymbol{a}})\boldsymbol{f}_{\boldsymbol{ib}}^{\boldsymbol{b}} + \boldsymbol{\eta}_{\boldsymbol{a}}$$

$$\tilde{\boldsymbol{\omega}}_{\boldsymbol{ib}}^{\boldsymbol{b}} = \boldsymbol{b}_{\boldsymbol{g}} + (\boldsymbol{I}_{\boldsymbol{3}} + \boldsymbol{S}_{\boldsymbol{g}})\boldsymbol{w}_{\boldsymbol{ib}}^{\boldsymbol{b}} + \boldsymbol{\eta}_{\boldsymbol{g}}$$

When only diagonal parameters are reserved, the matrix $\boldsymbol{S}_{\blacksquare}$ is actually

$$\boldsymbol{S}_{\boldsymbol{a}} = diag(\boldsymbol{s}_{\boldsymbol{a}})$$

$$\boldsymbol{S}_{\boldsymbol{g}} = diag(\boldsymbol{s}_{\boldsymbol{g}})$$

The specific force error can be expressed as a function of the bias drifts and the scale factor drifts:

$$\delta\boldsymbol{f}_{\boldsymbol{ib}}^{\boldsymbol{b}} = \hat{\boldsymbol{f}}_{\boldsymbol{ib}}^{\boldsymbol{b}} - \boldsymbol{f}_{\boldsymbol{ib}}^{\boldsymbol{b}} = \frac{\tilde{\boldsymbol{f}}_{\boldsymbol{ib}}^{\boldsymbol{b}} - \hat{\boldsymbol{b}}_{\boldsymbol{a}}}{\boldsymbol{I}_{\boldsymbol{3}} + \hat{\boldsymbol{S}}_{\boldsymbol{a}}} - \frac{\tilde{\boldsymbol{f}}_{\boldsymbol{ib}}^{\boldsymbol{b}} - \boldsymbol{b}_{\boldsymbol{a}}}{\boldsymbol{I}_{\boldsymbol{3}} + \boldsymbol{S}_{\boldsymbol{a}}} + \boldsymbol{w}_{\boldsymbol{a}} = \delta\boldsymbol{b}_{\boldsymbol{a}} + \boldsymbol{F}_{\boldsymbol{b}}\delta\boldsymbol{s}_{\boldsymbol{a}} + \boldsymbol{\eta}_{\boldsymbol{a}}$$

$$\delta\boldsymbol{w}_{\boldsymbol{ib}}^{\boldsymbol{b}} = \hat{\boldsymbol{w}}_{\boldsymbol{ib}}^{\boldsymbol{b}} - \boldsymbol{w}_{\boldsymbol{ib}}^{\boldsymbol{b}} = \frac{\tilde{\boldsymbol{w}}_{\boldsymbol{ib}}^{\boldsymbol{b}} - \hat{\boldsymbol{b}}_{\boldsymbol{g}}}{\boldsymbol{I}_{\boldsymbol{3}} + \hat{\boldsymbol{S}}_{\boldsymbol{g}}} - \frac{\tilde{\boldsymbol{w}}_{\boldsymbol{ib}}^{\boldsymbol{b}} - \boldsymbol{b}_{\boldsymbol{g}}}{\boldsymbol{I}_{\boldsymbol{3}} + \boldsymbol{S}_{\boldsymbol{g}}} + \boldsymbol{w}_{\boldsymbol{g}} = \delta\boldsymbol{b}_{\boldsymbol{g}} + \boldsymbol{W}_{\boldsymbol{b}}\delta\boldsymbol{s}_{\boldsymbol{g}} + \boldsymbol{\eta}_{\boldsymbol{g}}$$

with $\boldsymbol{F}_{\boldsymbol{b}} = diag(\tilde{\boldsymbol{f}}_{\boldsymbol{ib}}^{\boldsymbol{b}})$ and $\boldsymbol{W}_{\boldsymbol{b}} = diag(\tilde{\boldsymbol{w}}_{\boldsymbol{ib}}^{\boldsymbol{b}})$ **.**

A first order GM process is usually used to model $\delta\boldsymbol{b}_{\boldsymbol{a}}$, $\delta\boldsymbol{s}_{\boldsymbol{a}}$, $\delta\boldsymbol{b}_{\boldsymbol{g}}$ and $\delta\boldsymbol{s}_{\boldsymbol{g}}$ that

$$\delta\dot{\boldsymbol{b}}_{\boldsymbol{a}} = \frac{-1}{\boldsymbol{\tau}_{ba}}\delta\boldsymbol{b}_{\boldsymbol{a}} + \boldsymbol{\eta}_{\boldsymbol{ba}}$$

$$\delta\dot{\boldsymbol{s}}_{\boldsymbol{a}} = \frac{-1}{\boldsymbol{\tau}_{sa}}\delta\boldsymbol{s}_{\boldsymbol{a}} + \boldsymbol{\eta}_{\boldsymbol{sa}}$$

$$\delta\dot{\boldsymbol{b}}_{\boldsymbol{g}} = \frac{-1}{\boldsymbol{\tau}_{bg}}\delta\boldsymbol{b}_{\boldsymbol{g}} + \boldsymbol{\eta}_{\boldsymbol{bg}}$$

$$\delta\dot{\boldsymbol{s}}_{\boldsymbol{g}} = \frac{-1}{\boldsymbol{\tau}_{sg}}\delta\boldsymbol{s}_{\boldsymbol{g}} + \boldsymbol{\eta}_{\boldsymbol{sg}}$$

with $\boldsymbol{\tau}_{ba} = [\tau_{bax}, \tau_{bay}, \tau_{baz}]^T$, $\boldsymbol{\tau}_{sa} = [\tau_{sax}, \tau_{say}, \tau_{saz}]^T$, $\boldsymbol{\tau}_{bg} = [\tau_{bgx}, \tau_{bgy}, \tau_{bgz}]^T$, $\boldsymbol{\tau}_{sg} = [\tau_{sgx}, \tau_{sgy}, \tau_{sgz}]^T$ the corresponding 3-dimensional correlation times, $\boldsymbol{\eta}_{\boldsymbol{ba}}$, $\boldsymbol{\eta}_{\boldsymbol{sa}}$, $\boldsymbol{\eta}_{\boldsymbol{bg}}$ and $\boldsymbol{\eta}_{\boldsymbol{sg}}$ are GM process driving noises.

D5. Computational Transformation

Hence, the complete INS state propagation model is written as:

$$\delta\dot{\boldsymbol{x}}_{\boldsymbol{INS}} = \boldsymbol{F}_{\boldsymbol{INS}}\delta\boldsymbol{x}_{\boldsymbol{INS}} + \boldsymbol{G}_{\boldsymbol{INS}}\boldsymbol{u}_{\boldsymbol{INS}}$$

with

- $\delta\boldsymbol{x}_{\boldsymbol{INS}} = [\delta\boldsymbol{r}_{\boldsymbol{nb}}^{\boldsymbol{n}} \quad \delta\boldsymbol{v}_{\boldsymbol{nb}}^{\boldsymbol{n}} \quad \delta\overline{\boldsymbol{\psi}}_{\boldsymbol{nb}} \quad \delta\boldsymbol{b}_{\boldsymbol{a}} \quad \delta\boldsymbol{b}_{\boldsymbol{g}} \quad \delta\boldsymbol{s}_{\boldsymbol{a}} \quad \delta\boldsymbol{s}_{\boldsymbol{g}}]^{\boldsymbol{T}}$ the full INS error state model;
- the state transition matrix $\boldsymbol{F}_{\boldsymbol{INS}}$ is in form

$$\boldsymbol{F_{INS}} = \begin{bmatrix} \boldsymbol{F_{rr}} & \boldsymbol{F_{rv}} & 0_{3x3} & 0_{3x3} & 0_{3x3} & 0_{3x3} & 0_{3x3} \\ \boldsymbol{F_{vr}} & \boldsymbol{F_{vv}} & \boldsymbol{F_{ve}} & \boldsymbol{C_b^n} & 0_{3x3} & \boldsymbol{C_b^n F^b} & 0_{3x3} \\ \boldsymbol{F_{er}} & \boldsymbol{F_{ev}} & \boldsymbol{F_{ee}} & 0_{3x3} & -\boldsymbol{C_b^n} & 0_{3x3} & -\boldsymbol{C_b^n W^b} \\ 0_{3x3} & 0_{3x3} & 0_{3x3} & -\boldsymbol{\beta_{ba}} & 0_{3x3} & 0_{3x3} & 0_{3x3} \\ 0_{3x3} & 0_{3x3} & 0_{3x3} & 0_{3x3} & -\boldsymbol{\beta_{bg}} & 0_{3x3} & 0_{3x3} \\ 0_{3x3} & 0_{3x3} & 0_{3x3} & 0_{3x3} & 0_{3x3} & -\boldsymbol{\beta_{sa}} & 0_{3x3} \\ 0_{3x3} & 0_{3x3} & 0_{3x3} & 0_{3x3} & 0_{3x3} & 0_{3x3} & -\boldsymbol{\beta_{sg}} \end{bmatrix}$$

- the process driving noise and its control matrix are respectively

$$\boldsymbol{u_{INS}} = [\boldsymbol{\eta_a} \quad \boldsymbol{\eta_g} \quad \boldsymbol{\eta_{ba}} \quad \boldsymbol{\eta_{bg}} \quad \boldsymbol{\eta_{sa}} \quad \boldsymbol{\eta_{sg}}]^T$$

$$\boldsymbol{G_{INS}} = \begin{bmatrix} 0_{3x3} & 0_{3x3} & 0_{3x3} & 0_{3x3} & 0_{3x3} & 0_{3x3} \\ \boldsymbol{C_b^n} & 0_{3x3} & 0_{3x3} & 0_{3x3} & 0_{3x3} & 0_{3x3} \\ 0_{3x3} & -\boldsymbol{C_b^n} & 0_{3x3} & 0_{3x3} & 0_{3x3} & 0_{3x3} \\ 0_{3x3} & 0_{3x3} & I_{3x3} & 0_{3x3} & 0_{3x3} & 0_{3x3} \\ 0_{3x3} & 0_{3x3} & 0_{3x3} & I_{3x3} & 0_{3x3} & 0_{3x3} \\ 0_{3x3} & 0_{3x3} & 0_{3x3} & 0_{3x3} & I_{3x3} & 0_{3x3} \\ 0_{3x3} & 0_{3x3} & 0_{3x3} & 0_{3x3} & 0_{3x3} & I_{3x3} \end{bmatrix}$$

Denote $\boldsymbol{T}$ as the matrix to transform from $\delta\boldsymbol{x_{INS}}$ to the new error states vector with position error in meter

$$\delta\boldsymbol{x_{INS,new}} = \boldsymbol{T}\delta\boldsymbol{x_{INS}} = \begin{bmatrix} \delta\boldsymbol{p_{nb}^n} & \delta\mathbf{v}_{\boldsymbol{nb}}^{\boldsymbol{n}} & \delta\bar{\boldsymbol{\psi}}_{\boldsymbol{nb}} & \delta\boldsymbol{b_a} & \delta\boldsymbol{b_g} & \delta\boldsymbol{s_a} & \delta\boldsymbol{s_g} \end{bmatrix}^T$$

with $\boldsymbol{T} = \begin{bmatrix} \boldsymbol{F_{rv}^{-1}} & 0_{3x15} \\ 0_{15x3} & I_{15x15} \end{bmatrix} = \begin{bmatrix} \boldsymbol{A} & 0_{3x15} \\ 0_{15x3} & I_{15x15} \end{bmatrix}$.

The derivative of $\delta\boldsymbol{x_{INS,new}}$ is in form

$$\delta\dot{\boldsymbol{x}}_{\boldsymbol{INS,new}} = \dot{\boldsymbol{T}}\delta\boldsymbol{x_{INS}} + \boldsymbol{T}\delta\dot{\boldsymbol{x}}_{\boldsymbol{INS}} = \dot{\boldsymbol{T}}\boldsymbol{T^{-1}}\delta\boldsymbol{x_{INS,new}} + \boldsymbol{T}(\boldsymbol{F_{INS}}\boldsymbol{T^{-1}}\delta\boldsymbol{x_{INS,new}} + \boldsymbol{G_{INS}}\boldsymbol{u_{INS}})$$

$$\delta\dot{\boldsymbol{x}}_{\boldsymbol{INS,new}} = \left(\dot{\boldsymbol{T}}\boldsymbol{T^{-1}} + \boldsymbol{T}\boldsymbol{F_{INS}}\boldsymbol{T^{-1}}\right)\delta\boldsymbol{x_{INS,new}} + \boldsymbol{T}\boldsymbol{G_{INS}}\boldsymbol{u_{INS}}$$

Therefore,

$$\delta\dot{\boldsymbol{x}}_{\boldsymbol{INS,new}} = \boldsymbol{F_{INS,new}}\delta\boldsymbol{x_{INS,new}} + \boldsymbol{G_{INS,new}}\boldsymbol{u_{INS}}$$

with

$$\boldsymbol{F_{INS,new}} = \begin{bmatrix} \boldsymbol{F_{pp}} & \boldsymbol{F_{pv}} & 0_{3x3} & 0_{3x3} & 0_{3x3} & 0_{3x3} & 0_{3x3} \\ \boldsymbol{F_{vp}} & \boldsymbol{F_{vv}} & \boldsymbol{F_{ve}} & \boldsymbol{C_b^n} & 0_{3x3} & \boldsymbol{C_b^n F^b} & 0_{3x3} \\ \boldsymbol{F_{ep}} & \boldsymbol{F_{ev}} & \boldsymbol{F_{ee}} & 0_{3x3} & -\boldsymbol{C_b^n} & 0_{3x3} & -\boldsymbol{C_b^n W^b} \\ 0_{3x3} & 0_{3x3} & 0_{3x3} & -\boldsymbol{\beta_{ba}} & 0_{3x3} & 0_{3x3} & 0_{3x3} \\ 0_{3x3} & 0_{3x3} & 0_{3x3} & 0_{3x3} & -\boldsymbol{\beta_{bg}} & 0_{3x3} & 0_{3x3} \\ 0_{3x3} & 0_{3x3} & 0_{3x3} & 0_{3x3} & 0_{3x3} & -\boldsymbol{\beta_{sa}} & 0_{3x3} \\ 0_{3x3} & 0_{3x3} & 0_{3x3} & 0_{3x3} & 0_{3x3} & 0_{3x3} & -\boldsymbol{\beta_{sg}} \end{bmatrix}$$

$$\boldsymbol{F_{pp} = AF_{rr}A^{-1} + \dot{A}A^{-1}} = \begin{bmatrix} \frac{v_u}{R_N+h} - \frac{v_n tan\varphi}{R_M+h} & \frac{v_e tan\varphi}{R_M+h} & \frac{-v_e}{R_N+h} \\ 0 & \frac{v_u}{R_M+h} & \frac{-v_n}{R_M+h} \\ 0 & 0 & 0 \end{bmatrix}$$

$$\boldsymbol{F_{pv} = AF_{rv} = I_3}$$

$$\boldsymbol{F_{vp} = F_{vr}A}$$

$$= \begin{bmatrix} 0 & \frac{2\omega_{ie}(v_n cos\,\varphi + v_u\, sin\,\varphi)}{R_M+h} + \frac{v_e v_n}{(R_M+h)(R_N+h)cos^2\varphi} & \frac{v_e v_u}{(R_N+h)^2} - \frac{v_e v_n\, tan\,\varphi}{(R_N+h)^2} \\ 0 & \frac{-2\omega_{ie} v_e\, cos\,\varphi}{R_M+h} - \frac{v_e^2}{(R_N+h)(R_M+h)cos^2\varphi} & \frac{v_n v_u}{(R_M+h)^2} + \frac{v_e^2\, tan\varphi}{(R_N+h)^2} \\ 0 & -\frac{2\omega_{ie}\, v_e sin\,\varphi}{R_M+h} & \frac{-v_e^2}{(R_N+h)^2} + \frac{-v_n^2}{(R_M+h)^2} + \frac{2g}{R+h} \end{bmatrix}$$

$$\boldsymbol{F_{ep} = F_{er}A^{-1}} = \begin{bmatrix} 0 & 0 & \frac{v_n}{(R_M+h)^2} \\ 0 & \frac{-\omega_{ie}\sin\varphi}{R_M+h} & \frac{-v_e}{(R_N+h)^2} \\ 0 & \frac{\omega_{ie}\cos\varphi}{R_M+h} + \frac{v_e}{(R_N+h)(R_M+h)cos^2\varphi} & \frac{-v_e tan\varphi}{(R_N+h)^2} \end{bmatrix}$$

$$\boldsymbol{G_{INS,new} = G_{INS}}$$